UNIVERSITÀ DEGLI STUDI DI NAPOLI FEDERICO II

Scuola Politecnica e delle Scienze di Base

Area didattica di Scienze Matematiche, Fisiche e Naturali

Dipartimento di Scienze della Terra, dell'Ambiente e delle Risorse

DOTTORATO DI RICERCA IN SCIENZE DELLA TERRA, DELL'AMBIENTE E DELLE RISORSE

XXXVII ciclo

Relation between tectonics and crustal structures of Mercury

Salvatore Buoninfante

Supervisor

Prof. Luigi Ferranti

Co-Supervisors

Dr. Valentina Galluzzi

Dr. Maurizio Milano

Coordinator

Prof. Luigi Ferranti

Academic year 2024/2025

Thesis reviewers

Prof. Matteo Massironi,
Dipartimento di Geoscienze
Università degli Studi di Padova

Prof.ssa Cristina Pauselli,
Dipartimento di Fisica e Geologia
Università degli Studi di Perugia

Abstract

The main objective of this thesis was to study the relationship between tectonic and crustal structures of the planet Mercury, through the analysis of NASA MESSENGER imagery and gravity data. This project involved the production of a 1:3,000,000 scale geological map of the Michelangelo quadrangle (H12) of Mercury, based on the photointerpretation of the MDIS imagery. The funding for this study was planned to identify targets to be observed at high resolution during the ESA-JAXA BepiColombo mission.

Michelangelo appears as a densely cratered quadrangle dominated by degraded crater materials (c2) and intermediate plains. I identified two main regional thrust system trending NW-SE and NE-SW. I found that many lobed scarps developed at the edges of ancient, large impact basins. Clear examples of such tectonic structures in the Michelangelo quadrangle are provided by the Beethoven basin (20.8°S–236.1°E) or by the Vincente-Yakovlev basin (52.6°S–197.9°E). I propose a thick-skinned tectonic model according to which the lobate scarps were formed due to the positive reactivation of previous impact-related normal faults, as a consequence of the tectonic regime deriving from the global contraction. Morphological evidence of thick-skinned tectonics on Mercury is provided by the presence of fault systems reaching out of the basin rim (e.g., Beethoven basin). Beethoven basin is dated as a Tolstojan-Early Calorian (~4.0-3.8 Ga). The tectonic activity affecting Beethoven is more recent than the basin, the smooth plains covering the floor, and the subsequent impact craters.

Notwithstanding the low accuracy of XRS data at these latitudes, it appears that the NW-SE faults system in H12 broadly borders the southwestern edge of the high-Mg region (HMR).

I also analyzed the relation between volcanic vents and faults. Volcanic vents on Mercury are often associated with impact craters and/or tectonic structures, which can be considered as possible preferential areas for magma uprising. In some cases, vents are arranged along the peak-ring structure in impact craters, probably interacting with faults forming at peak-ring after the impact.

I analyzed the MESS160A gravity field model to model crustal heterogeneities in density. According to the flexural isostatic response curve, I assumed a flexural compensation model to first estimate a mean elastic thickness of 30 ± 10 km. I modeled the lithospheric flexure regardless of the gravity field and calculated the isostatic gravity anomalies, showing that considerable lateral density variations occur within Mercury's crust. I also estimated the crust-

mantle interface depth, finding that it varies from 19 to 42 km depth. Isostatic anomalies are mainly related to density variations in the crust: gravity highs mostly correspond to large-impact basins, suggesting intra-crustal magmatic intrusions as the main origin of these anomalies. Isostatic gravity lows prevail, instead, above intercrater plains and may represent the signature of a heavily fractured crust.

Bouguer gravity anomaly and crustal thickness data were analyzed to estimate the inner ring and main rim dimensions of peak-ring and multi-ring basins. Lunar impact basins are characterized by a one-to-one relationship between Bouguer diameter and crustal thinning diameter, estimated from regional background values, and the topographic peak-ring diameter. Mercury's peak-ring basins are instead characterized by a two-to-one relationship between Bouguer diameter and peak-ring size.

I evaluated the spatial relationship between mapped tectonic structures and crustal structures in the Victoria and Michelangelo quadrangles. Crustal structures are identified with gravity source edge detection methods: Total Horizontal Derivative (THD) and Enhanced Horizontal Derivative (EHD). Gravity data modelling shows that crustal structures can be spatially correlated with Carnegie, Larrocha systems and Victoria-Endeavour-Antoniadi array (Galluzzi et al., 2019), which partly border the HMR. These results suggest that the main thrust systems on Mercury may be characterized by a thick-skinned tectonic style.

Preamble

My thesis concerns the study of surface and subsurface tectonic structures of Mercury by integrating structural analysis and geophysics and dealt with two main topics. One topic is represented by geological mapping and the analysis of the tectonic structures of the Michelangelo quadrangle (H12), with a focus on the structures associated with impact basins and volcanic vents. The other topic concerned the analysis of gravity data to calculate and interpret intra-crustal sources and model the crust-mantle interface of Mercury. Gravity data were also used to develop a method of basin size quantification and estimate the geometry and position of crustal structures.

During the first year of my PhD, I dealt with the geological mapping of the Michelangelo quadrangle and the calculation of gravity isostatic anomalies of Mercury, the latter work leading to a paper published in Nature Scientific Reports. I have also been involved in the global characterization of volcanic vents on Mercury, in the ISSI #552 project "Wide-Ranging Characterization of Explosive Volcanism on Mercury: Origin, Properties, and Modifications of Pyroclastic Deposits" led by Anna Galiano (INAF). I am still involved in this project as an Early Career Researcher.

During the second year, I spent a period of 3 months as a visiting student at the Open University (Milton Keynes) collaborating with the planetary geology group led by David A. Rothery. During this period, I worked on the edges of the Michelangelo quadrangle, comparing my mapping with the current mapping of the contiguous quadrangles led by OU PhD students. Furthermore, I collaborated at the ISSI #552 project with David A. Rothery on the geological mapping of the Praxiteles crater area, with a focus on the *faculae* and hollow fields.

During the mapping work, I identified two new *rupēs* (Italica and Volasiga) and two *faculae* (Ngu and Ahas) in the Michelangelo quadrangle, whose names have been accepted and published by the International Astronomical Union (IAU).

I then contributed to the preparation of a scientific target list for the high-resolution observation that the SIMBIO-SYS instrumentation will provide during BepiColombo.

Subsequently, I worked on the development of gravity data modeling techniques to identify crustal structures and compare them with mapped surface structures.

Between the second and the third years, I moved to Paris to collaborate with Mark A. Wieczorek on the development of a new method, which exploits gravity data to estimate the size of peak-ring and multi-ring impact basins. This approach was successfully tested on lunar Gravity Recovery and Interior Laboratory (GRAIL) data, and subsequently used to estimate the size of some peak-ring basins on Mercury.

During the third year, I completed the geological mapping of H12 quadrangle and prepared the related paper, currently under review in Journal of Maps. I estimated the position of crustal structures in the Victoria quadrangle to provide spatial correspondence with the tectonic structures already mapped by Galluzzi et al. (2019) and indicate the position of newly discovered basins. At the end of the third year, I also started the study of terrestrial analogues of tectonic structures in intraplate tectonic settings. I am using Gravity Field and Steady-State Ocean Circulation Explorer (GOCE) and Gravity Recovery And Climate Experiment (GRACE) gravity data to identify the position of investigated structures and compare them with the identified Mercury's crustal structures. This work is part of the INAF minigrant "iMET", of which I am a Co-I.

During my PhD, I participated in several national and international conferences (National Congress of Planetary Sciences, Europlanet Science Congress, Lunar and Planetary Science Conference, Mercury Conference, BepiColombo SWT, IUGG General Assembly, EGU General Assembly).

I have been invited to hold a seminar by the School of Physical Science at the Open University and as an invited speaker at the EGU24 General Assembly and at the BepiColombo SWT#22 meeting in Münster. During the 55th Lunar and Planetary Science Conference (LPSC) this year, I have been awarded the Pierazzo Student Travel Award, which is won only by one non-U.S.-based graduate student involved in planetary science. I am currently an associate scientist in the BepiColombo Spectrometer and Imagers for MPO BepiColombo Integrated Observatory System (SIMBIO-SYS) and Jupiter Icy Moons Explorer (JUICE) JANUS teams, and I am currently collaborating with the BepiColombo MORE and JUICE 3GM teams. I am a member of the Europlanet Society. I am also member of the BepiColombo Surface and Composition, Geodesy and Geophsyics working groups (SCWG, GGWG), and member of the Young Scientists Study Group (YSSG), with the subgroup Surface and Environment Interaction Studies.

Table of Contents

1. Introduction

Planetary exploration represents a topic of increasing interest for the scientific community. The study of the geology of solid planets and small bodies plays a fundamental role in planetary research. In particular, an adequate geological and structural map of the body surfaces is fundamental to understanding their geological and tectonic activity, while a geophysical modeling approach is needed to investigate their internal structure.

In the last decades, Mercury was one of the most studied terrestrial planets from a geological and geophysical point of view, as this is fundamental to understanding the formation and the evolution of the planet itself and of the entire Solar System.

Mercury is the smallest planet in the Solar System and the closest to the Sun. It is characterized by a 3:2 spin/orbit resonance because of the tidal forces of the Sun (Colombo and Shapiro, 1966; Correia and Laskar, 2004). This means that Mercury rotates around its rotational axis three times while it orbits the Sun twice.

Mercury's internal structure is very peculiar. It is differentiated into a very large iron-rich core with a radius of ~2000 km (which covers about 80% of the entire volume), a ~400 km thick mantle made of iron-poor and magnesium-rich silicates, and a thin silicate crust with an average thickness of ~35 km (see Fig. 1.1). Mercury's core is divided into a solid inner core with a radius between 1000 km and 1500 km. The outer core is probably a convecting liquid of iron-sulfide that creates the magnetic field. The global planetary field can be represented by a dipole center on the spin axis, along which the magnetic field axis is aligned (Anderson et al., 2011). Above the core lies a thin, weak asthenosphere and thicker rigid lithosphere. Mercury has a tenuous exosphere made of ions temporarily removed from solids on the surface.

Mercury has a diameter of about 4880 km, just over 1/3 the size of the Earth, and it is characterized by a high density. Indeed, the average density value is 5.43 g/cm^3, slightly lower than the Earth density (5.52 g/cm^3). Such a density implies that iron is the main constituent in the composition of the planet. Since the measurements on the surface of Mercury (and probably also the mantle) indicate a low abundance of iron (~ 4 w%, Nittler et al., 2011), it is thought that Mercury is characterized by a ferrous core that occupies ~80% of the volume of the planet, with a radius of 2074 km. Several hypotheses have been formulated as to the reasons for the planet's high-density origin. The main hypotheses suggest an intense removal of silicates in an early phase of Mercury, which may be due to evaporation of the silicate surface in a hot solar nebula (Cameron, 1985), or following a giant impact (Benz et al., 1988; Stewart et al., 2013).

Hubbard (2014) attributed the formation of the large iron core to energetic magnetically mediated collisions during the protoplanetary disk phase, which led to the erosion of the non-magnetic silicate components and the enrichment in metallic iron. Some authors have also suggested the presence of a solid FeS layer at the base of the mantle, which could justify the high density of the solid outer shell as well (~ 3.65 g/cm3). However, recent studies have shown that the FeS layer is absent or less than 13 km thick (Cartier et al., 2020). The crustal thickness is about 35 km, while the mantle-core interface is located at a depth of about 400 km (Padovan et al., 2014; Genova et al., 2019; Solomon&Anderson, 2018; Fig. 1.1).

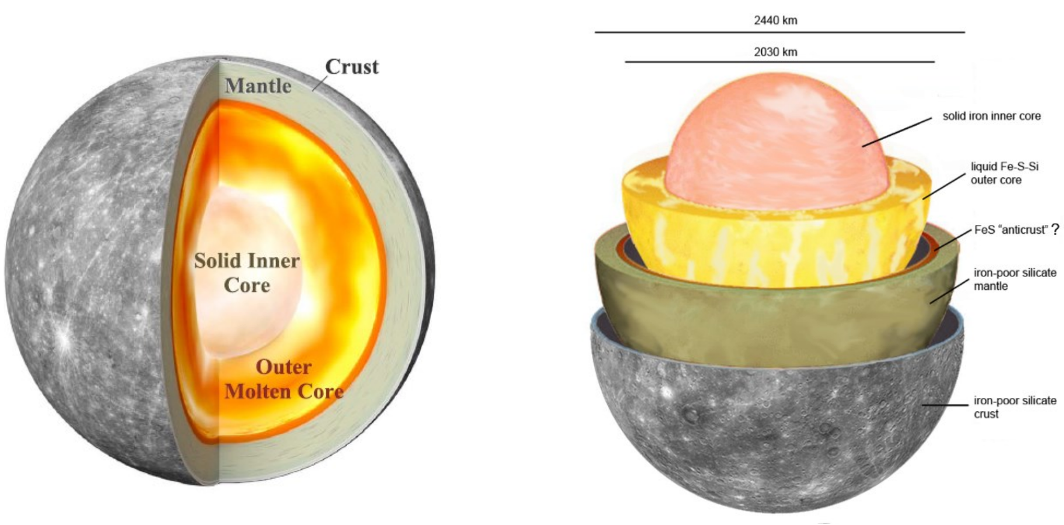

Figure 1.1. Internal structure of Mercury (modified from Genova et al., 2019 and from Rothery, 2015).

The exploration of Mercury began in 1973 when the NASA Mariner 10 (M10; Fig. 1.2a) mission was launched on November 3. Thirty years later, NASA planned the MErcury Surface, Space ENvironment, GEochemistry, and Ranging (MESSENGER) mission (Fig. 1.2b), launched on August 3, 2004. Nowadays, the exploration of Mercury continues with the ESA-JAXA BepiColombo mission (Fig. 1.2c), as the fifth Cornerstone mission of the Horizon 2000 Plus program. It was launched on 20 October 2018, and it is expected to reach the planet in November 2026 (differently from the previously planned date of December 2025 due to an issue that in April 2024 prevented electric thrusters of the Mercury Transfer Module (MTM) from operating at full power).

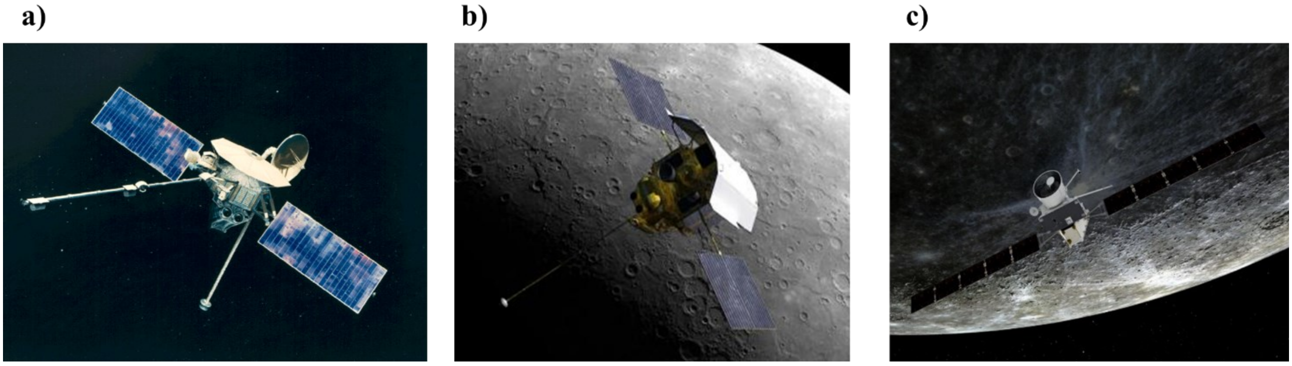

Figure 1.2. a) NASA Mariner 10 satellite (Credit: NASA/JPL); **b)** NASA MESSENGER satellite (Credit: NASA/Johns Hopkins Applied Physics Laboratory); **c)** ESA-JAXA BepiColombo satellite (Credit: ESA/ATG medialab).

During three flybys of the planet in 1974 and 1975, Mariner 10 was able to obtain images covering about 45% of Mercury's surface, at an average resolution of about 1 km. Mariner 10 measured ultraviolet signatures of H, He, and O in Mercury's exosphere, documented the time-varying magnetosphere, and determined some physical characteristics of surface materials (Solomon et al., 2007).

The M10 mission also identified the presence of a weak magnetic field (about 1% of the Earth's), probably deriving from the dynamo mechanism generated in the fluid outer core. In fact, studies on the longitudinal libration of great amplitude have confirmed the presence of a partially liquid core (Margot et al., 2007).

NASA's MESSENGER mission was the seventh mission of the Discovery Program and the second mission designed for the exploration of Mercury. The spacecraft performed the first three flybys of the planet (January 2008, October 2008, and September 2009), and then entered the orbit of Mercury on March 18, 2011 (Solomon et al., 2001; Solomon & Anderson, 2018). On April 30, 2015, it touched down on the surface of the planet, ending the mission. The main purpose of MESSENGER was to study the geology, magnetic field, and chemical composition of the planet. Six key objectives were indicated (Solomon et al., 2001):

1) to understand the formation processes that led to a high metal/silicate ratio, thus allowing a global mapping of the major chemical elements and surface mineralogy;

2) to reconstruct the geological history of Mercury, obtaining surface imaging coverage with a resolution of hundreds of meters together with spectral measurements of the major geological units;

3) to study the origin and nature of Mercury's magnetic field, by measuring the magnetic field near the planet and through Mercury's magnetosphere;

4) to understand the structure and state of Mercury's core, by measuring Mercury's obliquity, the amplitude of the physical libration (i.e. the periodic variation of the planet's rotation speed) and considering the second-order coefficients of the gravity field;

5) to understand which are the radar-reflecting materials at the planet's poles, with measurements obtained by ultraviolet spectrometry;

6) to understand the nature and source of the volatiles, identifying the main species present in the exosphere and in the magnetosphere.

The instrumentation on MESSENGER (Solomon et al., 2007; Fig. 1.3) included: the Mercury Dual Imaging System (MDIS), the Gamma Ray Spectrometer (GRS), the Neutron Spectrometer (NS), the X-Ray Spectrometer (XRS), the Magnetometer (MAG), the Mercury Laser Altimeter (MLA), the Mercury Atmospheric and Surface Composition Spectrometer (MASCS) with the subsystems UVVS (Ultraviolet and Visible Spectrometer) and VIRS (Visible and Infrared Spectrograph), the Energetic Particle and Plasma Spectrometer (EPPS), and the RadioScience experiment (RS).

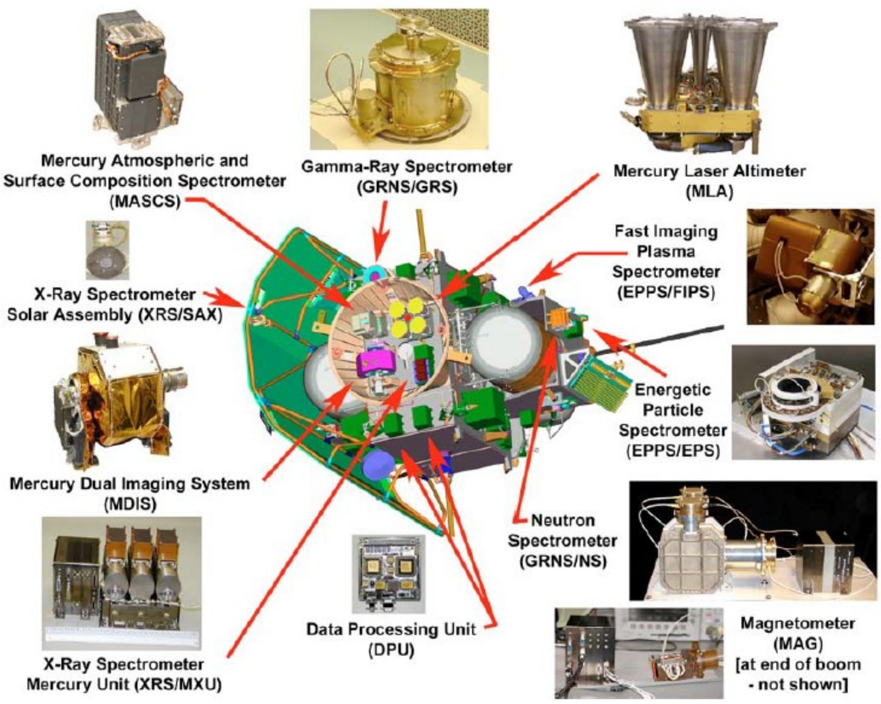

Figure 1.3. Instruments on the MESSENGER spacecraft and their respective position (from Solomon et al., 2007).

MDIS was used to image globally the surface through cameras data, allowing the recognition of geological units and structures. GRNS and XRS were used to map the surface elemental abundances. MASCS took spectral measurements of surface. MAG measured the magnetic field to study the internal field and the magnetosphere. EPPS measured thermal and low energy ions. MLA was mainly used to derive the topography through laser altimeter data. RS measured the libration amplitude and the gravity field, from the spacecraft position and velocity.

In my PhD project work I used data from the MDIS (Mercury Dual Imaging System), MLA (Mercury Laser Altimeter), XRS (X-Ray Spectrometer) and RS (Radioscience) instruments.
MDIS (Hawkins et al., 2007; Fig. 1.4) was developed by the Johns Hopkins University Applied Physics Laboratory, and it included a wide-angle camera (WAC) and a narrow-angle camera (NAC).

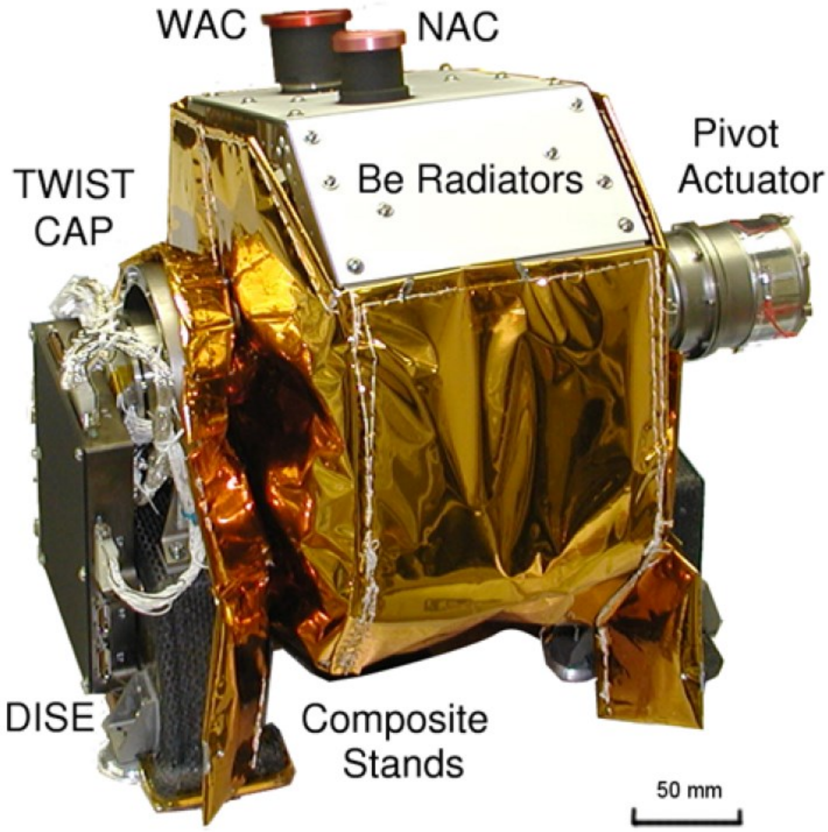

Figure 1.4. Mercury Dual Imaging System (MDIS) instrument, from Hawkins et al. (2007).

MLA (Cavanaugh et al., 2007; Fig. 1.5), developed by the NASA Goddard Space Flight Center, mapped Mercury's surface through an infrared laser transmitter, which sent laser pulses measured by a receiver. The laser transmitter operated at wavelengths of 1064 nm, sending 8 Hz pulses (eight pulses per second). The receiver consisted of four receiving telescopes with a photon-counting detector, and three matched low-pass electronic filters. MLA data was also used to measure the forced libration of the planet.

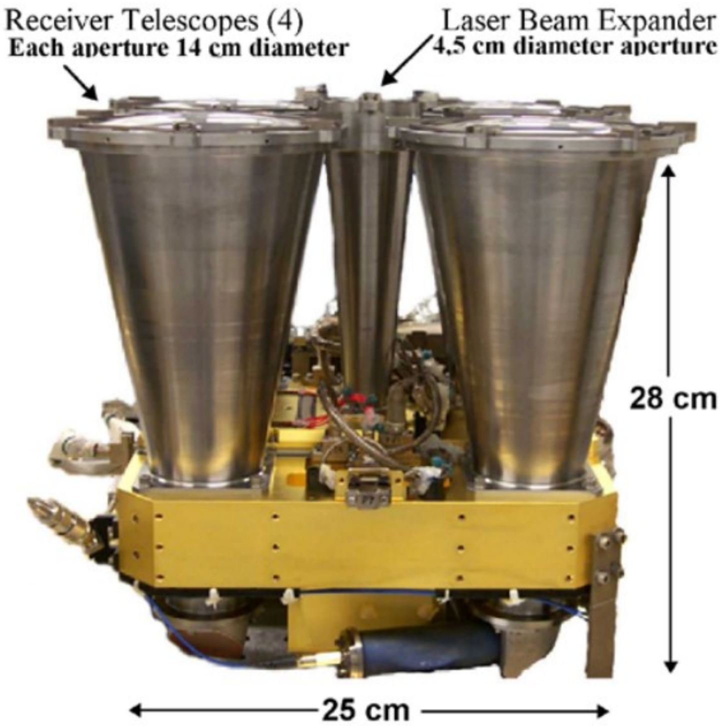

Figure 1.5. Mercury Laser Altimeter (MLA) instrument, from Cavanaugh et al. (2007).

XRS (Schlemm et al., 2007; Fig. 1.6) was developed by the Johns Hopkins University Applied Physics Laboratory. It mapped the elements on the Mercury's surface through three gas-filled detectors (Mercury X-ray Unit, MXU) which pointed to the planet, its associated electronics (Main Electronics for X-rays, MEX), and a silicon solid-state detector measuring the solar X-rays (Solar Assembly for X-rays, SAX).

Figure 1.6. Photography of the X-Ray Spectrometer (XRS), from Schlemm et al. (2007).

RS (Srinivasan et al., 2007) experiment was led by the NASA's Goddard Space Flight Center. Speed and distance of the spacecraft from the Earth were measured through a Radio Frequency (RF) Telecommunication Subsystem. These observations contained information on the gravity field of the planet. The RF Subsystem used for RS measurements included two opposing high gain phased-array antennas, two medium gain fanbeam antennas and four low gain antennas (Fig. 1.7). The RF signal was transmitted and received at X-band frequencies by the large ground-based antennas of the NASA Deep Space Network (DSN; Fig. 1.7). The DSN antennas measured the changes in frequency caused by the influence of the spacecraft in the Mercury's gravity field. RS observations were also used for planet's orbital ephemeris and rotation state estimates.

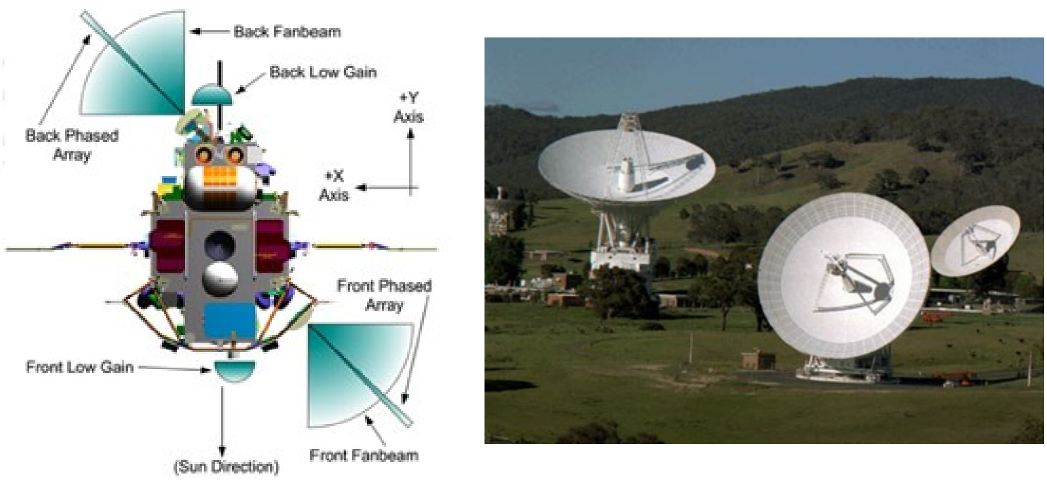

Figure 1.7. The MESSENGER spacecraft antenna suite on the left (Srinivasan et al., 2007) and the NASA Deep Space Communications Complex on the right (Credit: NASA/Johns Hopkins Applied Physics Laboratory).

MESSENGER provided fundamental information on the planet's geology and internal structure. In particular, MESSENGER data have enabled higher-resolution mapping of Mercury than Mariner 10, as well as improved understanding of its surface and chemical features. Surface features of greatest interest to study after MESSENGER are hollows. These are relatively young irregular rimless depressions, ranging in size from a few tens of meters to hundreds of meters, characterized by high reflectance with respect to the surrounding terrain (Blewett et al., 2011; Thomas et al., 2014a). They can usually be found in clusters or scattered, often associated with impact craters (Lucchetti et al., 2018). The hollows are probably formed by the loss of a volatile component present in the shallow crust (e.g., Rodriguez et al., 2023), probably via sublimation process (Blewett et al., 2011; Thomas et al., 2014a) or as a combination of processes which may involve also space weathering, volcanism, thermal desorption, and photon stimulated desorption (Blewett et al., 2011; Rothery, 2015).

BepiColombo is the current hermean mission. It derives from a collaboration between European Space Agency (ESA) and the Japan Aerospace Exploration Agency (JAXA), with the aim of studying Mercury to better understand the formation and evolution of the planet and of the Solar System. The spacecraft is composed of 4 modules: MMO or Mio, which is provided by JAXA (Japan Aerospace Exploration Agency); the protection shield (MOSIF); MPO, provided by ESA (European Space Agency); the MTM which transports the other modules (Benkhoff et al., 2021). The Mercury Magnetospheric Orbiter (MMO), also named Mio, is intended for in situ plasma and electromagnetic fields and waves measurements in Mercury orbit. The Mercury Planetary Orbiter (MPO) contains the following 11 scientific instruments: BepiColombo Laser Altimeter (BELA), Mercury Orbiter Radio Science Experiment (MORE), Italian Spring Accelerometer (ISA), Mercury Magnetometer (MPO-MAG), Mercury Thermal Infrared Spectrometer (MERTIS), Mercury Gamma-ray and Neutron Spectrometer (MGNS), Mercury Imaging X-ray Spectrometer (MIXS), Probing of Hermean Exosphere by Ultraviolet Spectroscopy (PHEBUS), Search for Exosphere Refilling and Emitted Neutral Abundances

(SERENA), Spectrometers and Imagers for MPO Integrated Observatory System (SIMBIO-SYS), Solar Intensity X-ray and particle Spectrometer (SIXS).

The instrumentation will provide a global characterization of Mercury through the investigation of the interior, surface, exosphere, and magnetosphere. A further objective will be to test Einstein's theory of general relativity (Benkhoff et al., 2021).

BELA is intended to characterize the topography and morphology of Mercury. MORE will determine the gravity field, the size and physical state of the core. The purpose of ISA is to study the interior structure and test Einstein's theory of relativity. MPO-MAG will study the magnetic field. MERTIS will focus on the mineralogical composition and surface temperature. MGNS will study the elemental composition of volatiles in the polar areas. MIXS will obtain a global map of the surface atomic composition. PHEBUS's aim is to analyze the composition and dynamics of the exosphere. Serena will study the relations between surface, exosphere, magnetosphere and solar wind. SIMBIO-SYS will provide cameras a global coverage data at high-resolution and infrared imaging of the surface. SIXS will study the solar X-rays and energetic particles.

The SIMBIO-SYS suite (Cremonese et al., 2020; Fig. 1.8) consists of three channels: STC, HRIC and VIHI. The STereo imaging Channel (STC) will provide global color coverage of the surface and Digital Terrain Model with an accuracy better than 80 m. Images are taken at a spectral band range of 400-950 nm and with spatial resolution up to 58 m/pixel. Its field of view (FOV) is 5º. The High Resolution Imaging Channel (HRIC) will provide high-resolution images in spectral bands range of 400-900 nm and spatial resolution up to 6 m/pixel. Its FOV is 1.47°. The Visible and near-Infrared Hyperspectral Imaging channel (VIHI) is a hyperspectral imager in the visible and near-infrared range. It will provide the global mineralogical composition of the surface, with high spectral resolution (up to 6 nm) in the 400-2000 nm range and spatial resolution at 480 m/pixel (up to 120 m/pixel).

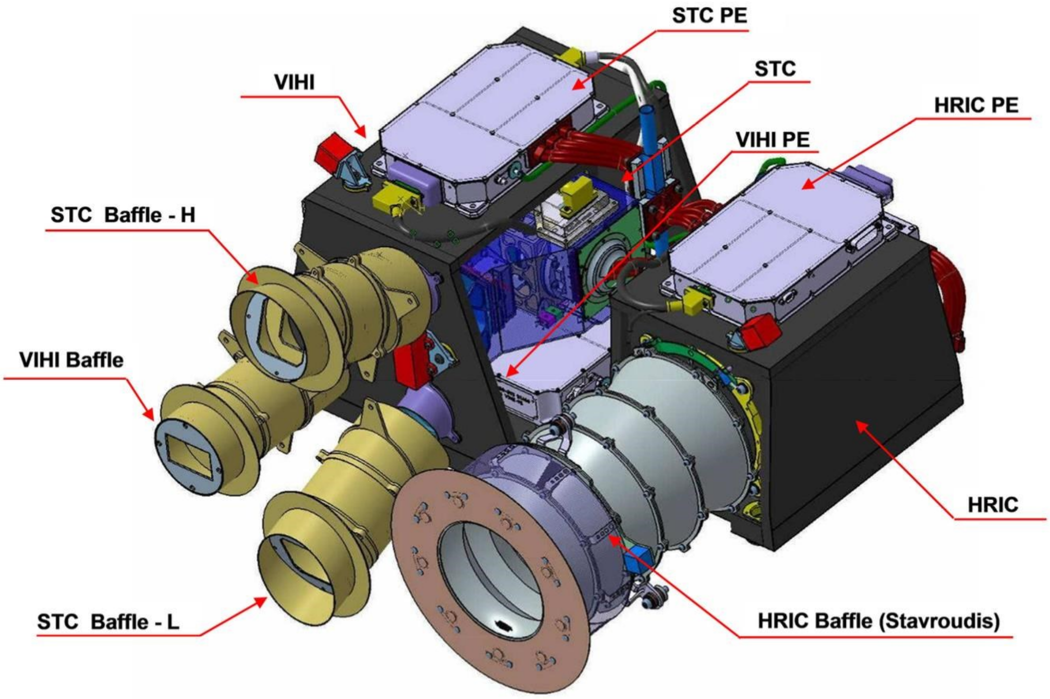

Figure 1.8. SIMBIO-SYS instrument suite, composed of STC, HRIC and VIHI channels (from Cremonese et al., 2020).

The BepiColombo Surface and Composition Working Group (SCWG) conducts further analysis of MESSENGER and BepiColombo data to study the topographical, surface and chemical features of Mercury's surface (Rothery et al., 2020). The Geodesy and Geophysics Working Group (GGWG) focuses on the study of Mercury's internal structure and its evolution (Genova et al., 2021).

During Mariner 10 mission, Mercury was divided into 15 quadrangles (Davies et al., 1978; Fig. 1.9) for mapping purposes at 1:5 million scale. Quadrangles were named after prominent topographic features, where M10 coverage data were available, and telescopic albedo features, where image coverage was not available (see Davies et al., 1978). The 0° longitude meridian was already defined as the longitude where the Sun was vertical when Mercury passed through its first perihelion in the 1950. Subsequently, new names were decided based on prominent features identified in each quadrangle (see Rothery, 2015; Fig. 1.10).

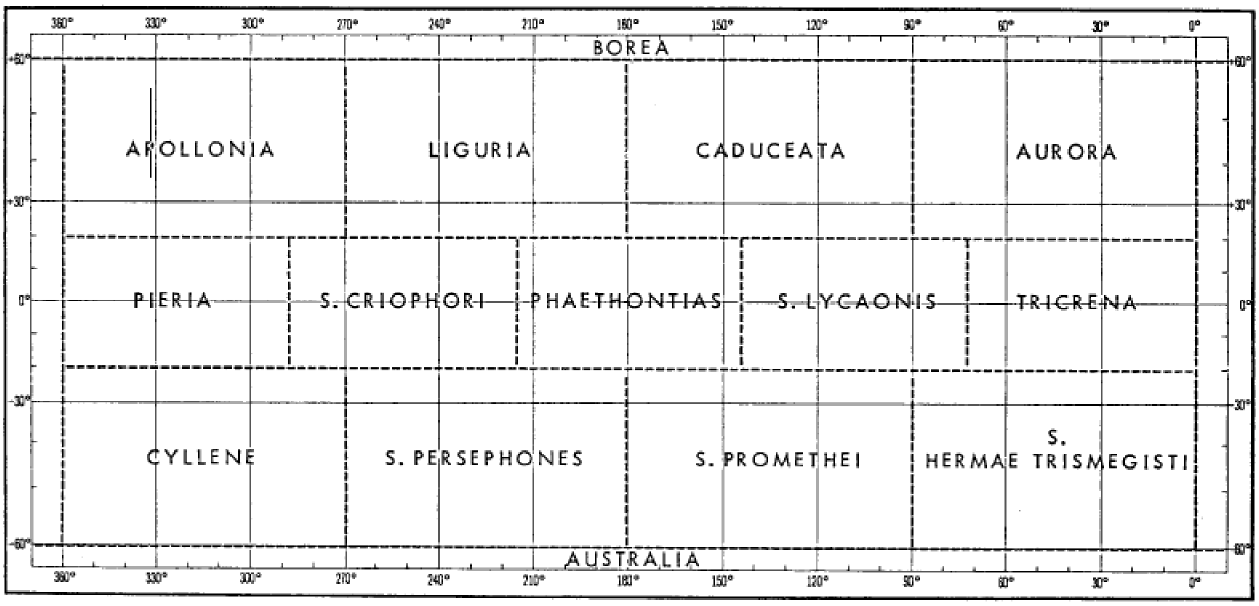

Figure 1.9. Mercury's quadrangles subdivision (see Davies et al., 1978) for the cartography program at 1:5 million scale, in equirectangular projection. Names derived from albedo and topographic features (from Dollfus et al., 1978).

Mariner 10 imaged only Caduceata, Solitudo Lycaonis, Solitudo Promethei, Solitudo Hermae Trismegisti, Tricrena, and partly Phaethontias, Aurora, Borea and Australia.

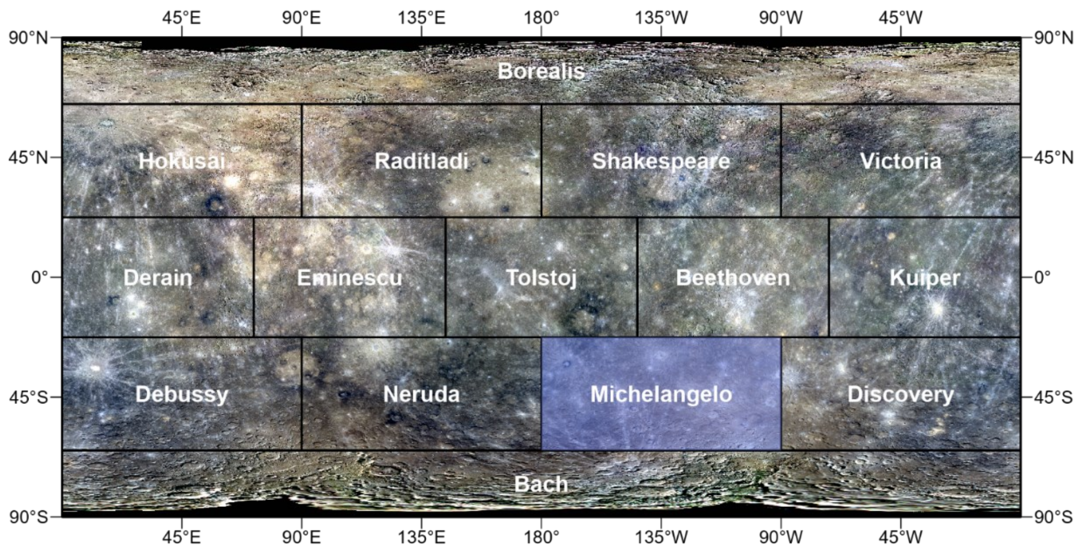

Figure 1.10. Mercury's quadrangles defined after Mariner 10 mission based on prominent features, on MDIS Color basemap in equirectangular projection. Michelangelo quadrangle (H12) is highlighted in blue.

Planet feature names are defined based on the IAU (International Astronomical Union) rules. Crater names are based on names of celebrated artists. *Faculae* (bright deposits) names are defined on the word snake in various languages. *Planitia* (large and low plains) are based on the names of Mercury in various languages. *Rupēs* (fault scarps) are defined after ships' names of scientific expeditions. Crater chains or *catenae* are named after radio telescope facilities. The others are less commonly used, for example there is only one *montes* feature (mountains), *Caloris montes*, named because of the hottest surface temperature in this area. *Fossae* (long, narrow depression) *and Valles* (valleys) are, instead, significant works of architecture and abandoned cities or towns of settlements, respectively.

The chronostratigraphy of Mercury is based on impact events determining the bases of each Mercurian system. The geochronology of Mercury was established based on a comparison with Lunar chronology and is therefore divided into five periods. The Pre-Tolstojan period includes units older than 4 Ga. The Tolstojan period follows the Pre-Tolstojan and its base is defined by the Tolstoj basin deposits. Tolstojan period ends around 3.8 Ga, delimiting the base of the following Calorian period, defined by the Caloris basin deposits. The Mansurian period is defined by Mansur crater deposits, whose base is estimated at 3-3.5 Ga. The Kuiperian period is the most recent period on Mercury and its base is established at ~1 Ga, which is the age of the young Kuiper crater materials.

The main purposes of this thesis can be summarized as follows:

- to provide a complete geological map of the Michelangelo quadrangle (Fig. 1.11a) at 1: 3M scale.
- to map the tectonic structures bordering a geochemical terrain which extends from the southern hemisphere to the northern hemisphere, and characterized by a high concentration of Mg, defined as High-Mg region (Fig. 1.11b). This geological investigation will contribute to the 1:3M geological map series campaign that constitutes a basic work to identify targets proposed for science observations during the ESA-JAXA BepiColombo mission.
- to verify the spatial correlation between mapped tectonic structures and the edges of the High-Mg region, aimed at understanding the origin of this geochemical anomaly.

- To study the relationship between tectonic structures and crustal structures identified by means of geophysical modeling of satellite gravity data.

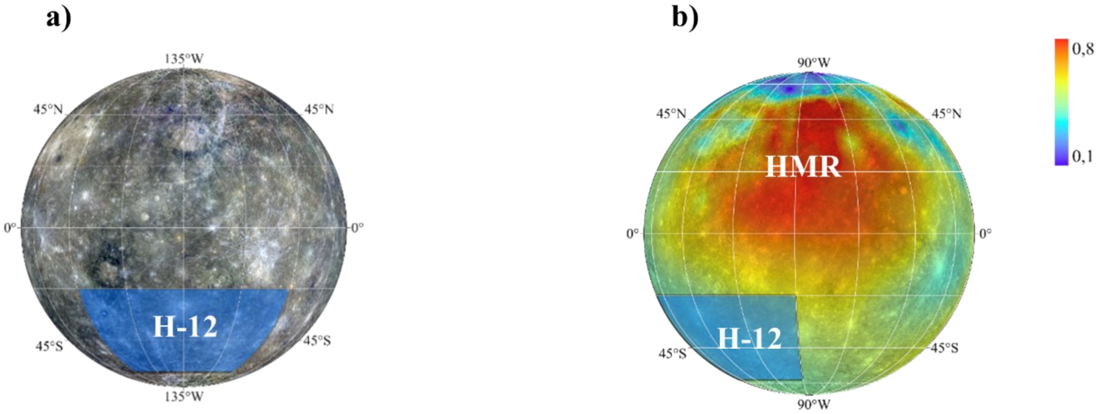

Figure 1.11. a) Location of the Michelangelo quadrangle (H12), on the MDIS color basemap in orthographic projection; **b)** Location of the High-Mg region, on the XRS Mg/Si abundance map in orthographic projection.

1.1 Mercury's surface

The surface of Mercury is very similar to that of the Moon, characterized by impact craters and with no signs of aeolian, fluvial or glacial processes. These features are essentially due to the absence of an atmosphere, which is usually the main cause of surface alteration of a planet. There is a tendency to divide the surface of Mercury into three different units on the basis of their degradation degree and age: intercrater plains, intermediate plains and smooth plains. Intercrater plains (icp; Fig. 1.12) are the most widespread units on the surface of Mercury, characterized by a high density of craters. The origin of the intercrater plains is attributed to the formation of lava flows or fluidized material expelled (ejecta) by the impacts. Intercrater plains are mainly composed of low reflectance materials. Intermediate plains (imp; Fig. 1.13) are planar or wavy surfaces that have a higher density of craters than smooth plains, but a lower crater intensity than intercrater plains. The smooth plains (sp; Fig. 1.14) are morphologically flat and slightly cratered surfaces. Smooth plains were originally interpreted as deriving from effusive volcanism or fluidized ejecta. Recent studies seem to confirm the volcanic nature of these materials, highlighting the presence of sharp color contrasts with the surrounding materials. Smooth plains cover approximately 27% of Mercury's surface (Denevi et al., 2013). It is well known that the planet was also affected by a global resurfacing around (4.0–4.1 Ga) due to volcanism, after LHB (Marchi et al., 2013).

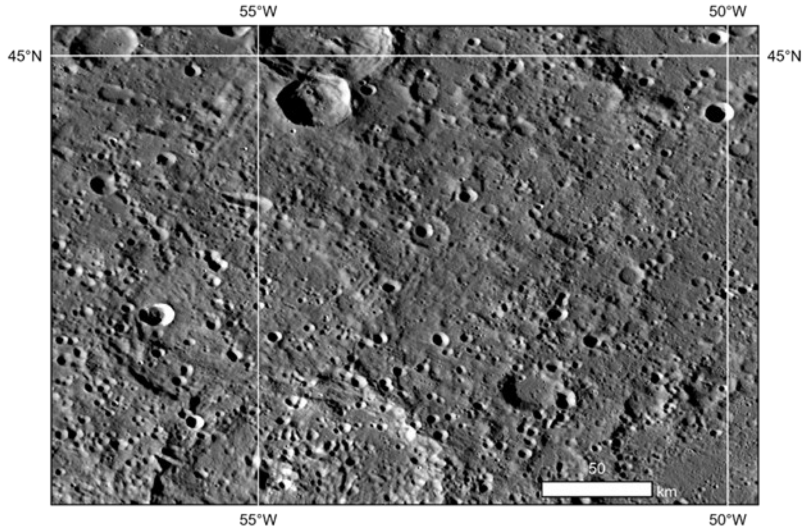

Figure 1.12. Example of Mercury’s intercrater plains from MESSENGER MDIS BDR basemap, in equirectangular projection.

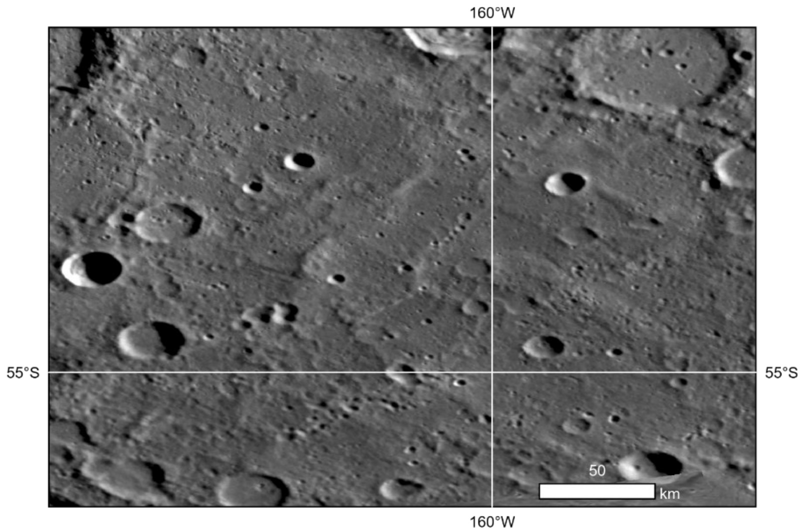

Figure 1.13. Example of Mercury’s intermediate plains from MESSENGER MDIS BDR basemap, in equirectangular projection.

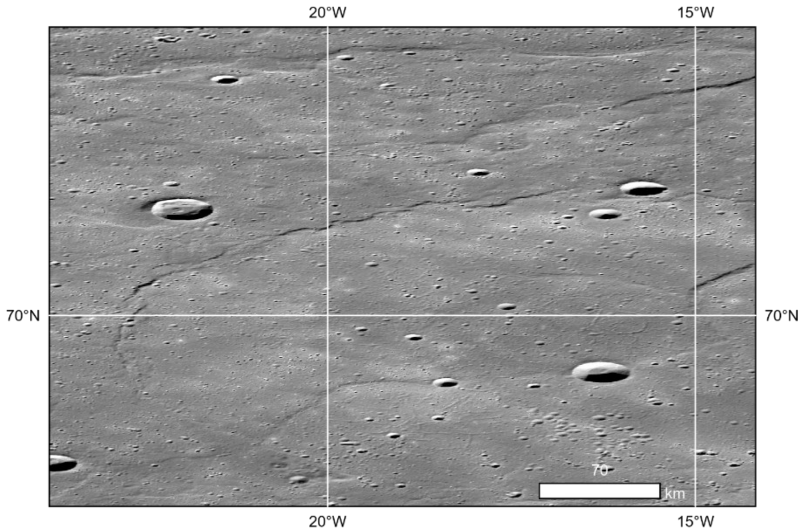

Figure 1.14. Example of Mercury's smooth plains (Northern Smooth Plains) from MESSENGER MDIS BDR basemap, in equirectangular projection.

1.2 Geological maps

Mariner 10 was the first mission leading to the mapping of Mercury's surface. M10 television experiment (Murray, 1975) observed the ~40–45% planet's surface during three flybys between 1974 and 1975. Previous works provided both complete and partial geological map at 1:5 million scale (DeHon et al., 1981; Grolier & Boyce, 1984; Guest & Greeley, 1983; King & Scott, 1990; McGill & King, 1983; Schaber & McCauley, 1980; Spudis & Guest, 1988; Spudis & Prosser, 1984; Strom et al., 1990; Trask & Dzurisin, 1984; Trask & Guest, 1975). The Michelangelo quadrangle of Mercury (H12) encompasses the area between latitudes 22.5°S-65°S and longitudes 180°E-270°E (Fig. 1.15). It was previously named Solitudo Promethei (180°E-270°E; 20°S-60°S) from the dark-hued albedo feature (Dollfus et al., 1978), then changed in Michelangelo after the homonymous crater (109.69°E; 44.92 °S), which itself was named by IAU in 1979. Spudis & Prosser (1984) produced the first geological map of the Michelangelo quadrangle at 1:5 million scale (Fig. 1.16), also including part of the nearby Neruda quadrangle (H-13) as insufficient data were available to provide a separate geological map for H13 (see also Man et al., 2023b). They identified and mapped five classes of craters and four main plain units: intercrater, intermediate, smooth and very smooth plains.

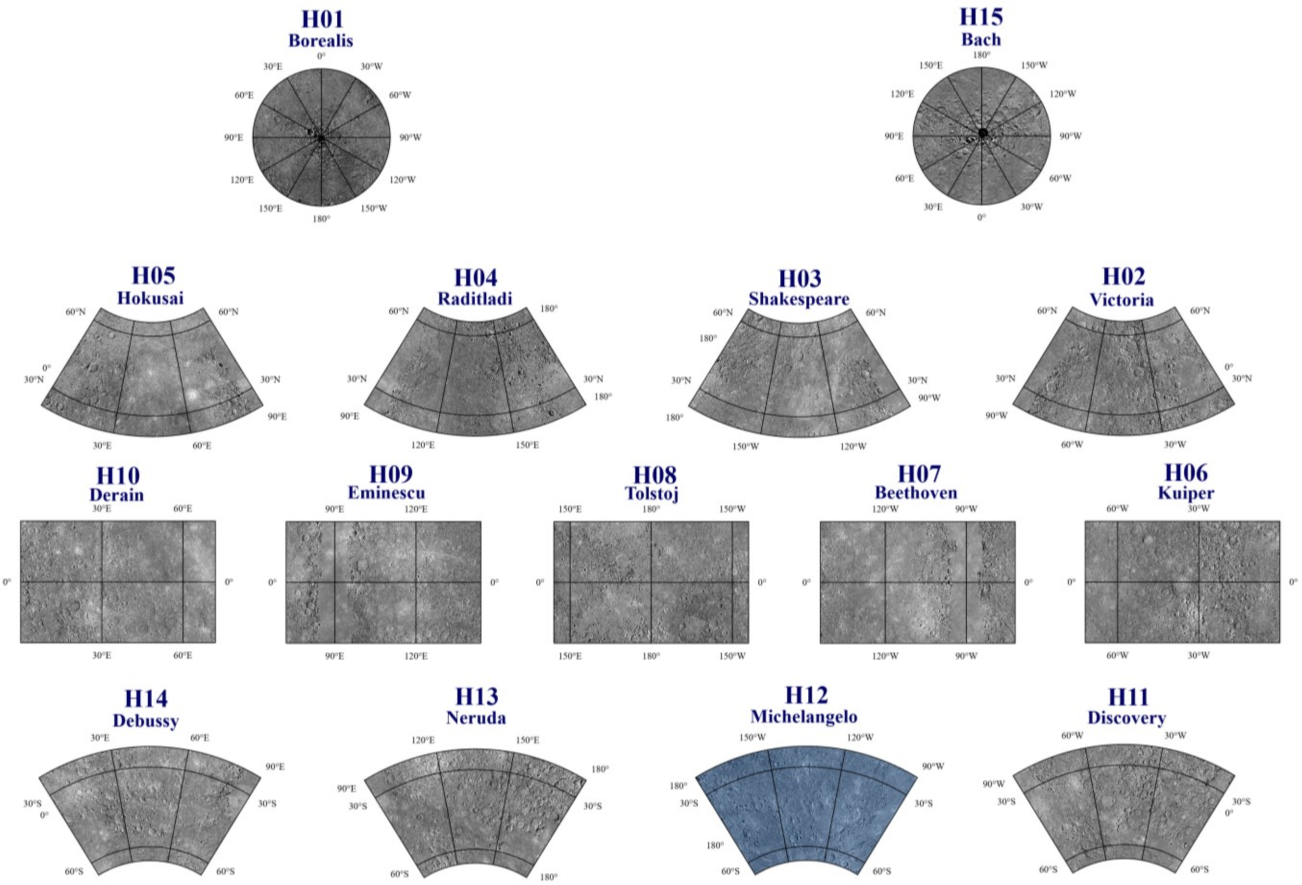

Figure 1.15. Mercury quadrangles on the MESSENGER MDIS BDR mosaics. The location of the H12 Quadrangle (180°E-270°E; 22.5°S-65°S) is highlighted in blue.

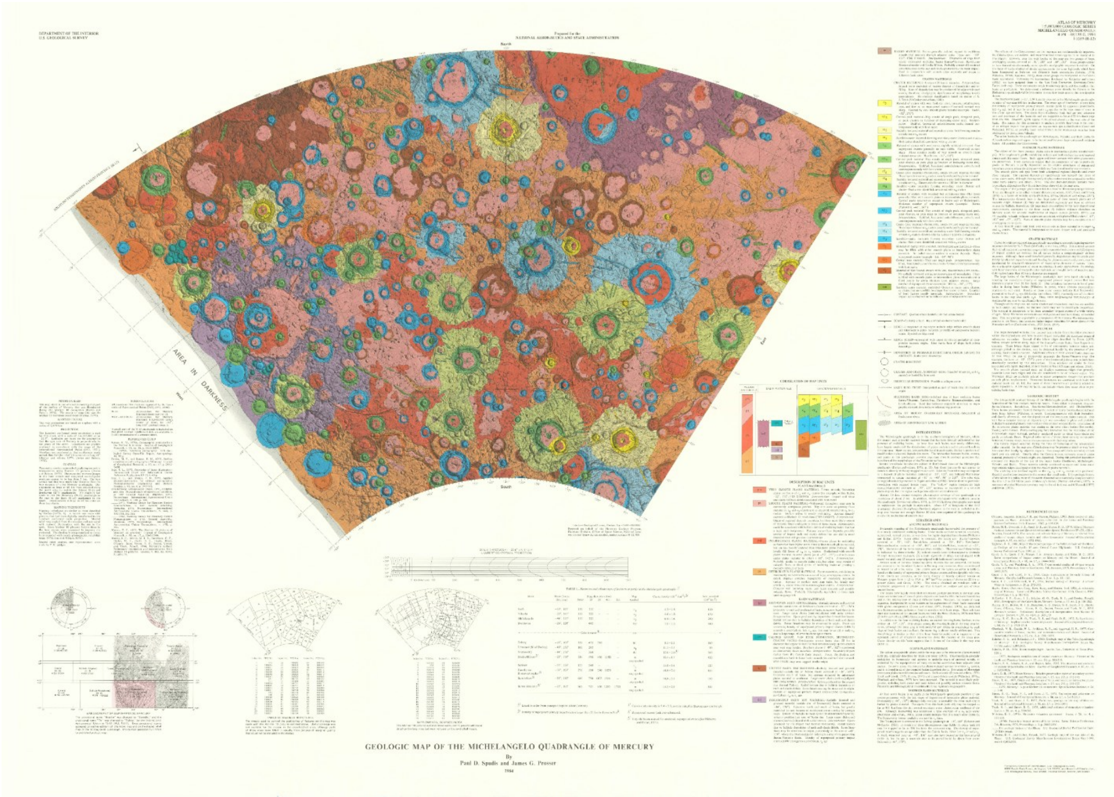

Figure 1.16. First geological map of H12 produced by Spudis and Prosser (1984) at 1:5M scale using Mariner 10 data. Figure map by Spudis and Prosser (1984).

MESSENGER data allowed mapping at a larger scale (1:3M) than the mapping work based on Mariner 10 data (1:5M). So far, several quadrangle maps at 1:3 million scale have been published (Galluzzi et al., 2016; Giacomini et al., 2022; Guzzetta et al., 2017; Malliband et al., 2023; Man et al., 2023b; Mancinelli et al., 2016; Pegg et al., 2021b; Wright et al., 2019; see Fig. 1.16). MESSENGER obtained global image coverage, allowing the production of the first global geological map at a scale of 1:15M (Kinczyk et al., 2019).

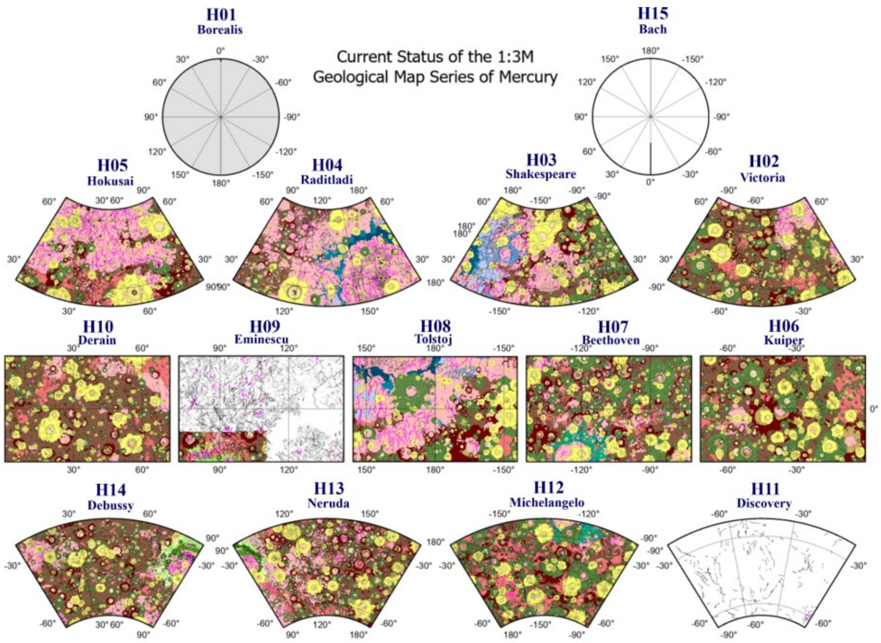

Figure 1.16. Status of the 1:3M geological map series of Mercury (Galluzzi et al., 2024). Modified from Galluzzi et al. (2024).

1.3 Mercury's tectonics

The hermean tectonics has been explained by three main tectonic models: global contraction (Strom et al., 1975), tidal despinning (Melosh & Dzurisin, 1978) and mantle convection (King, 2008).

Global contraction, due to planetary cooling, which generated a compressive tectonic regime leading to a radial contraction, is viewed as the dominant tectonic process on Mercury. This tectonic activity began before the end of the Late Heavy Bombardment (~3.9 billion years ago) and continued until at least 300 Ma. Global contraction derives from the planet's interior cooling (see also Solomon, 1976; Hauck et al., 2004).

Tidal despinning is generated by gravitational force that the Sun exerts on Mercury. With this model, Melosh (1977) suggested a distribution of NW-SE and NE-SW strike-slip faults at mid-latitudes, E-W normal faults at high latitudes and N-S thrusts at low latitudes. Pechmann & Melosh (1979) and Matsuyama & Nimmo (2009) suggested an extensive distribution of N-S thrusts also at higher latitudes. Later, Klimczak et al. (2015) proposed that a combination of tidal despinning and global contraction could cause N-S thrusts in the equatorial region.

The mantle convection proposed by King (2008) is based on convection cells which may regulate the distribution of faults. Nevertheless, convection cells, derived from the updated interior structure models (Smith et al., 2012; Hauck et al., 2013; Michel et al., 2013; Tosi et al., 2013), are not spatially consistent with the current fault distribution. Watters et al. (2015) found that the contractional structures are concentrated in longitudinal bands and between the north and south hemispheres, with a preferential north-south trend at low-mid latitudes and east-west trend at high latitudes. They explained the nonrandom trends because of the effect of tidal despinning combined with the global contraction. The nonuniform distribution of the tectonic structures was attributed to mantle downwelling or heterogeneities in lithospheric strength.

Tectonic structures on Mercury include prevailing contractional faults and subordinately extensional faults. Previous authors mapped up to almost 7000 contractional tectonic structures (Byrne et al., 2014; Watters et al., 2021; Man et al., 2023a; Fig. 1.17). Contractional faults on Mercury are subdivided into two main categories: lobate scarps and wrinkle ridges. Both are interpreted to be the surface expression of thrust faults. The wrinkle ridges (Fig. 1.18a) are typically found within the smooth plains and are defined as wide arches in low relief and superimposed by narrow ridges (Byrne et al., 2014). These may represent the surface expression of fault-propagation folding or fault bend folding. The lobate scarps (Fig. 1.18b) are steep scarps, asymmetrical in section and interpreted as the surface expression of thrusts (Crane & Klimczak, 2019; Massironi et al., 2015). Lobate scarps are mainly located in the intercrater plains and can be hundreds of kilometers long and have large offsets of 1-3 km. High-relief ridges (Fig. 1.18c) are less common contractional structures, symmetrical in section, which often common combine with lobate scarps (Watters & Nimmo, 2010). High-relief ridges may be interpreted as anticlines formed above steeply dipping reverse faults (e.g., Watters et al., 2001). However, recent studies demonstrate that division into such morphological categories can be misleading, since the contractional structures conform more to a range of structures whose ideal endmembers can be identified in the lobate scarps and wrinkle ridges structures (e.g., Byrne et al., 2018; Crane & Klimczak, 2019; Loveless et al., 2024).

Extensional faults can be normal or oblique faults, usually mapped as grabens. They are mainly identified in large basins (e.g., Caloris basin) or within large contractional system (Man et al., 2023a). Grabens may have formed radially or concentrically from the basin center (Strom et al., 1975; Dzurisin, 1978; Murchie et al., 2008; Watters et al., 2009). More recently, Man et al. (2023a) discovered extensional activity superposed on large compressional tectonic structures. This led to the formation of young grabens, which must be ~300 million years old or younger.

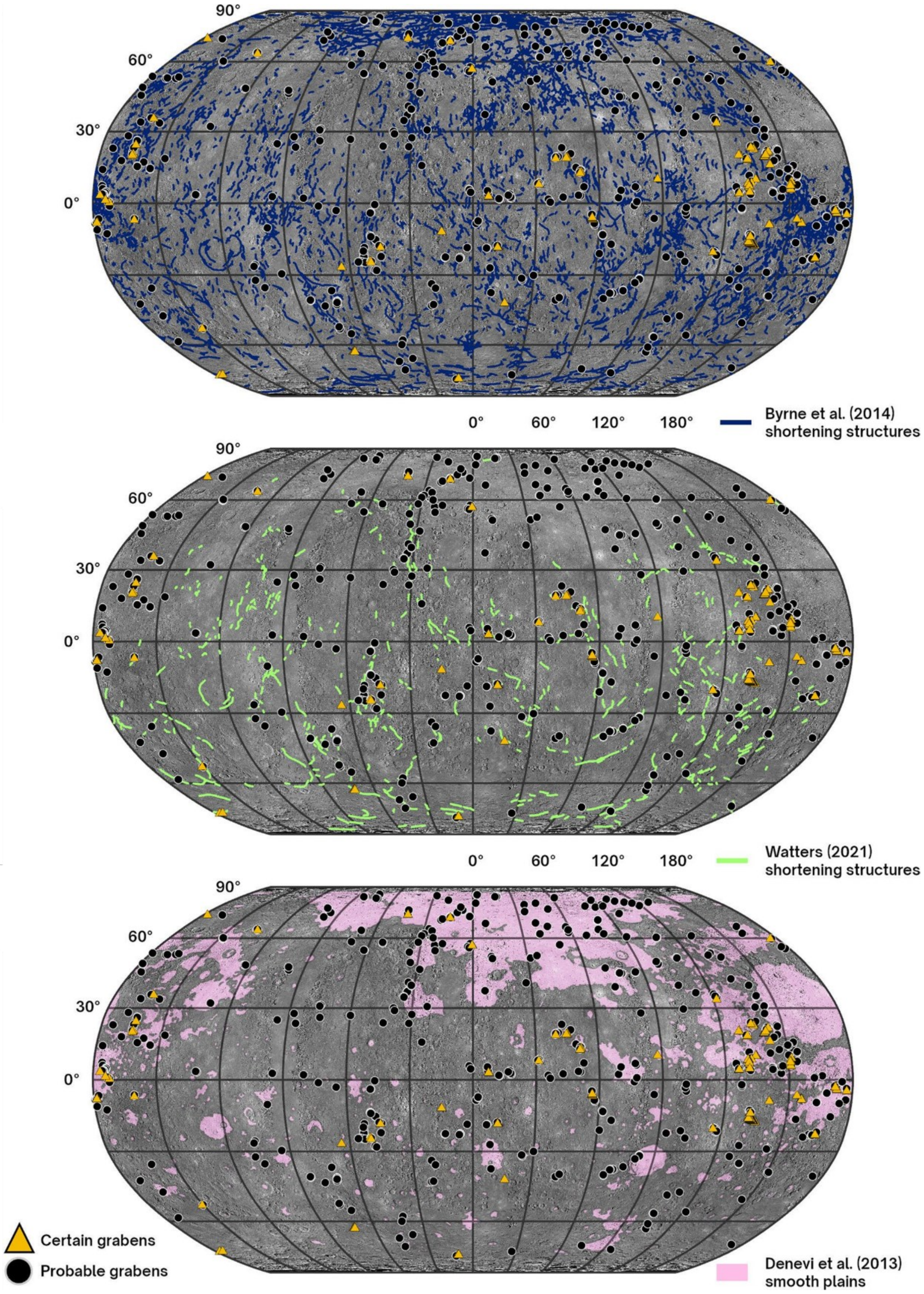

Figure 1.17. Mercury's contractional and extensional tectonic structures in Robinson projection, by Man et al. (2023a). Contractional tectonic structures are from Byrne et al. (2014) and Watters et al. (2021). Grabens are from Man et al. (2023a).

The amount of global radial contraction was first estimated during the Mariner 10 mission, suggesting a ~ 1-2 km radius change (Strom et al., 1975; Watters et al., 1998; Watters & Nimmo, 2010). After the MESSENGER mission, a radial contraction up to ~ 4 km (Di Achille et al., 2012) and ~7 km (Byrne et al., 2014, 2018). Later, Watters et al. (2021) estimated a radius change of 1-2 km at most.

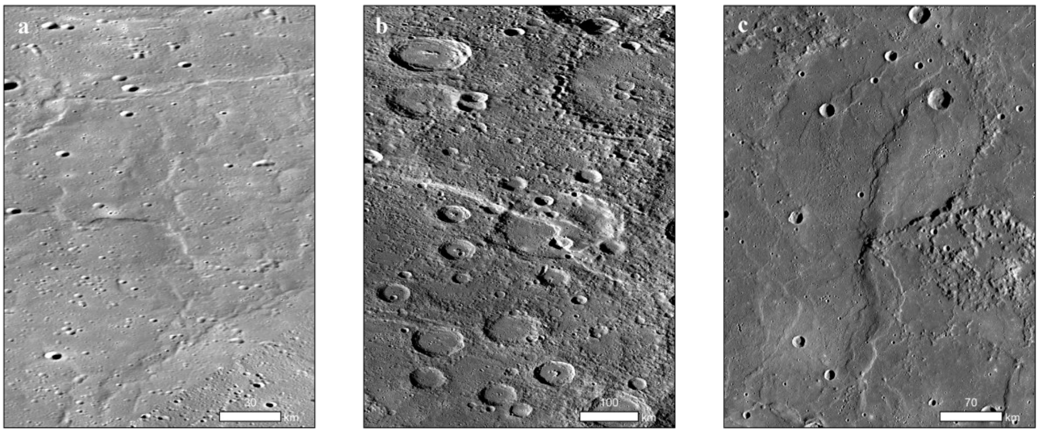

Figure 1.18. Examples of the three main contraction structures on Mercury: a) wrinkle ridges; b) lobate scarp (*Carnegie Rupes*); c) high-relief ridge (Schiaparelli Dorsum). Images are taken from MESSENGER MDIS BDR basemap, in equirectangular projection.

The major thrusts are thought to represent thick-skinned structures, since a depth of faulting of ~35-40 km was estimated for Discovery Rupes and Soya Rupes (Watters et al., 2002; Ritzer et al., 2010). Watters et al. (2002) considered planar thrust faults, modeling a dip angle of 30–35°. Later, Rothery and Massironi (2010) analyzed Beagle Rupes as a listric fault, estimating a more feasible dip angle of ~20°.

Victoria quadrangle (H02) is instead characterized by three fault systems, namely the trending NNW-SSE Victoria, the NW-SE trending Carnegie, and the NE-SW trending Larrocha systems (Galluzzi et al., 2019). These fault systems were coeval and active until ~3.7 Ga. The Victoria-Endeavour-Antoniadi (VEA) array seems to be characterized by low dip angles (6°-10°; Galluzzi et al., 2019), although previous estimates provided dip angles of ~25°-35° (Watters & Nimmo, 2010). *Carnegie Rupes* dip angles estimates are higher (28°–52°; Galluzzi et al., 2019), probably because it represents a left-transpressional activity in an ENE-WSW regional compressional stress.

1.4 High-Mg region

The high-Mg region (HMR; Fig. 1.19) shows a particularly high concentration in Mg, that can be observed in the Mg/Si abundance map derived from the XRS (X Ray Spectrometer) data.

According to most studies, this region could have formed following a large impact event preceding the global resurfacing (4.0-4.1 Ga; Marchi et al., 2013), which has led to the emergence of Mg-rich material due to excavation of the crust and involvement of the upper mantle (Weider et al., 2015; Galluzzi et al., 2019). The large impact event could also have led to intense crustal fracturing and modification of the underlying mantle with consequent intense volcanic activity through dikes or plumes. Alternatively, this region could have formed from highly viscous ultramafic lavas not necessarily related to the impact model (see also Frank et al., 2017 and references therein).

Other works suggest that the HMR may have originated either due to chemical heterogeneity in the mantle, or from a high degree of heterogeneous mantle melting (Frank et al., 2017; Namur & Charlier, 2017; Padovan et al., 2017; Beuthe et al., 2020). This heterogeneity may be due to a thin mantle, which may limit the size of convective cells, thus preventing chemical homogeneity (Evans et al., 2015). However, chemical heterogeneity in the mantle may also be due to incomplete mixing of multiple impactors that have excavated the entire crust (Rivera-Valentin and Barr, 2014). Frank et al. (2017) simulated the large impact showing that it would have excavated the entire crust of Mg-rich mantle material and easily distributed it far from the formed basin. However, the authors assert that subsequent erosion and modification that would have hidden the evidence for an impact should have obscured the geochemical evidence. Therefore, they suggest that the HMR is much more likely the result of mantle heterogeneity and intense volcanic activity generating Mg-rich melts.

More recently, Beuthe et al. (2020), considering a variable crustal density, found that the HMR is characterized by a crust thicker than what was previously estimated, thus excluding the model of the large impact event and suggesting the mantle melting as responsible of the Mg- enrichment.

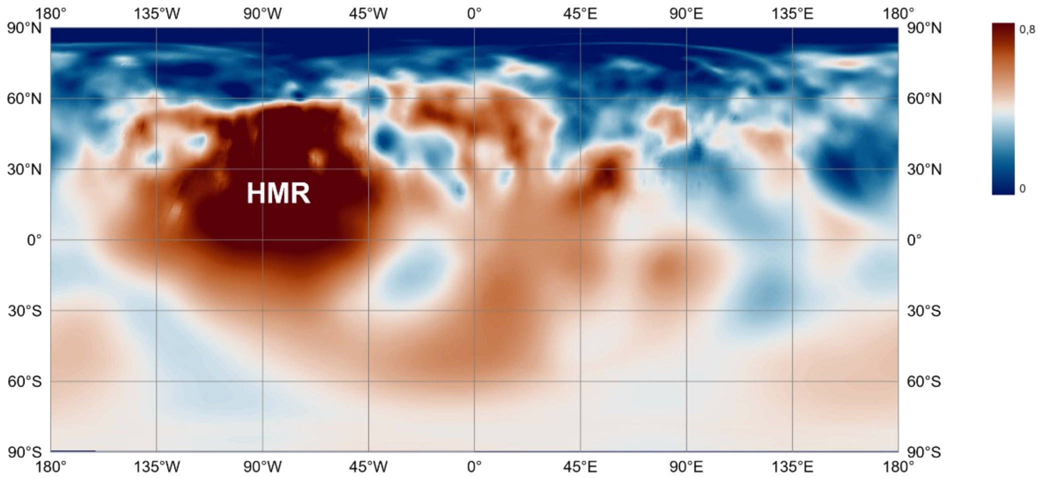

Figure 1.19. Location of the high-Mg region, on the XRS Mg/Si abundance map, in equirectangular projection.

1.5 Impact craters and basins

The surface and crust of terrestrial planets have been influenced by large and energetic impact events during the evolution of the solar system. Impact basins on terrestrial planets have long been recognized and studied through different datasets, including satellite images, topographic data, and gravity data.

Craters and basins form after an impact event, which can be usually differentiated into three stages: contact and compression stage, excavation stage, and modification stage (Gault et al., 1968; Melosh, 1989; Kenkmann et al., 2014). Craters may be mainly subdivided into simple and complex craters. Simple craters are generally characterized by a bowl-shaped morphology, while complex craters are composed of terraced rims and of an uplifted central structure (Kenkmann et al., 2014). Pike (1988) identified four crater classes: (1) simple crater, (2) modified simple crater, (3) immature complex craters, and (4) mature complex craters (see Fig. 1.20). Simple craters are characterized by a bowl-shaped interior, with a smooth and circular rim. Modified simple craters may be characterized by small slump deposits. Immature complex craters are usually characterized by large slump deposits, weak terracing and small central peaks. Mature complex craters may exhibit a prominent central peak or a cluster of central peak elements and well-defined terraces.

Impact basins can be subdivided, with increasing diameter, into protobasins, peak-ring basins, and multi-ring basins (Pike, 1988; Baker et al., 2011a; Fig. 1.20). Protobasins are intermediate structures between complex crater and multiring, as they exhibit a main rim, an inner ring, and a central peak. Peak-ring basins are characterized by a rim crest and an interior peak-ring, while multi-ring basins are larger and defined by more concentric topographic rings (e.g., Pike, 1988; Baker et al., 2011a). The inner peak-ring of a basin is believed to form by the collapse of the central peak, as initially developed after the impact (Melosh, 1989; Collins et al., 2002).

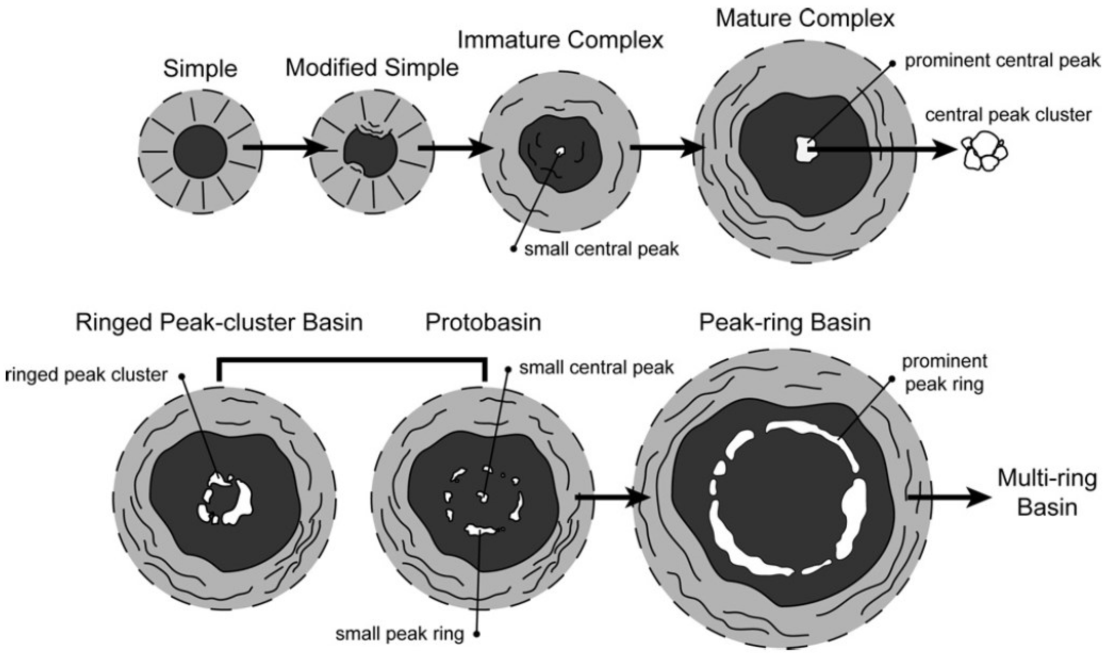

Figure 1.20. Scheme representing the transition from simple to complex crater, and from protobasin to multi-ring basins, as also explained by Pyke (1988). Figure by Baker et al. (2011a).

The formation of the peak-ring structure goes along with the development of thrust faults, which accommodate the structural uplift (e.g., Chicxulub crater; see Collins et al., 2002; Gulick et al., 2013; Fig. 1.21). According to Collins et al. (2002) the peak-ring formed as material that was originally part of the central uplift, which collapsed outward while thrusting over the inwardly collapsing transient crater rim.

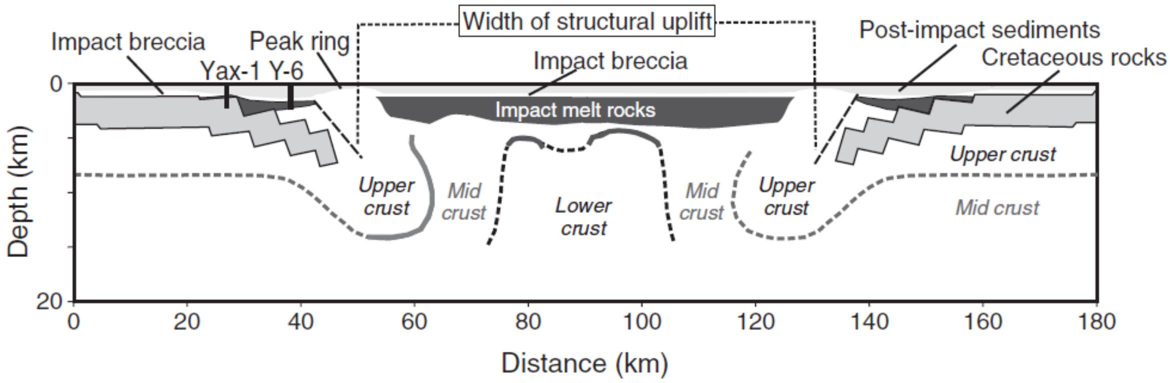

Figure 1.21. Cross section of Chicxulub impact structure with main structural elements. Figure by Gulick et al., 2013.

Previous works have also shown that the cut-off rim crest diameter (D) of peak-ring basins is 80 km for Mercury (Baker et al., 2011a), 100 km for Mars (Baker, 2016), and 200 km for the Moon (Baker et al., 2011b).

Peak-ring basins (like Rachmaninoff crater on Mercury; Fig. 1.22) and multiring basins are widespread on terrestrial planets and can be characterized by their gravity signature. GRAIL data showed that large lunar basins are characterized by a central gravity anomaly. The size of the central Bouguer gravity anomaly corresponds closely to the diameter of the inner peak-ring of a basin, while the main ring is approximatively twice the diameter of the peak-ring (Neumann et al., 2015). This finding allows us to confirm the existence of previously proposed basins on the Moon, but also to correctly estimate the size of the main crater and detect new basins that were not yet identified.

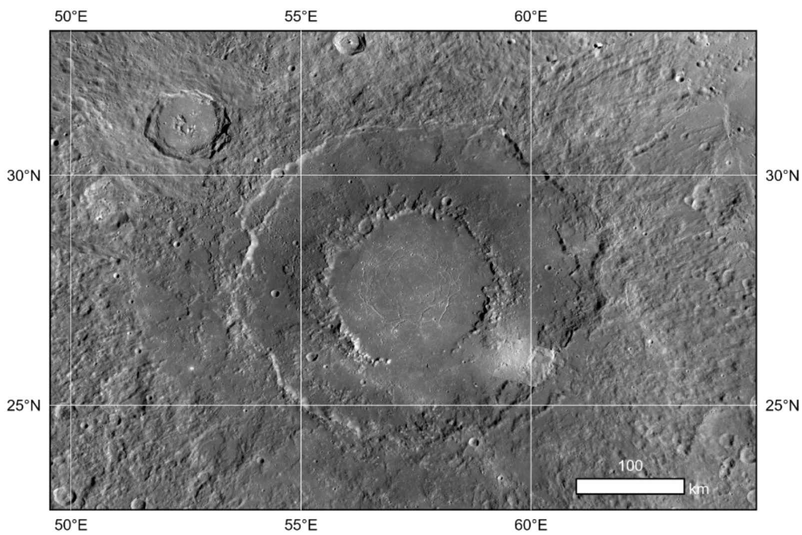

Figure 1.22. Example of peak-ring basin on Mercury (Rachmaninoff basin), characterized by an external topographic rim and an internal ring structure. Equirectangular projection.

It has already been shown that large impact basins on Mercury are often affected by a reactivation process as indicated by the thrust structures bordering the basin rims internally (see Rothery, 2015; Fegan et al., 2017). Rothery (2015) suggested that the compressive tectonic regime could have supported the development of thrusts along an interface between the basin floor and the lava filling. According to Fegan et al. (2017) the thrusts may form along the interface between the basin floor and the younger smooth plains units covering the floor. The impact that forms the basin leads to the fracturing of the crust with consequent formation of regolith. The basin floor is then filled with lava, and the compressive tectonic regime causes the development of thrusts along the weakness plane between the floor and the younger lava (Fig. 1.23).

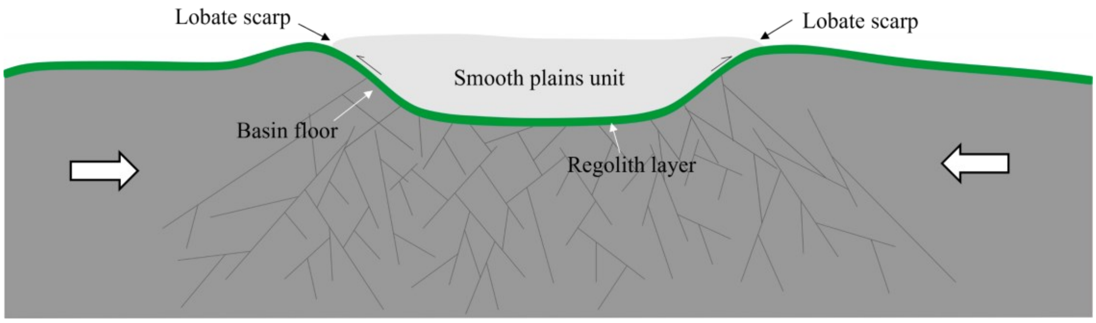

Figure 1.23. Schematic illustration representing the basin reactivation process as suggested by Fegan et al. (2017). Faults nucleate due to compressive tectonic regime along the interface between the basin floor and the infilled lava. White arrows indicate the direction of maximum lithospheric compression. Modified from Fegan et al. (2017).

1.6 Fault-vent interaction

On Mercury, volcanic vents are usually associated with morphologically irregular pits and with *faculae* (see Besse et al., 2020), pyroclastic deposits which are normally bright or very bright in the MDIS Enhanced color basemap.

Thomas et al. (2014b) showed that pits and pyroclastic deposits are usually associated with weakness zones within impact craters and/or with the surface expressions of individual thrust faults (e.g., Geddes crater; Fig. 1.24). The collocation of sites of explosive volcanism with near-surface faults and crater-related fractures is likely a result of such structures acting as conduits for volatile and/or magma release from shallow reservoirs, with volatile overpressure in these reservoirs could be a key trigger for eruption in some cases. Thus, widespread, long-lived explosive volcanism on Mercury may have been facilitated by the interplay between impact cratering, tectonic structures, and magmatic fractionation. Jozwiak et al. (2018) discussed the interaction between thrust segments and magmatic uprise. In their model a dike propagating from depth intersects an existing thrust fault causing the magma to continue propagating along the thrust fault and to erupt explosively when it reaches the surface.

There are several earth analogues of volcanic activity in contractional and strike-slip to transpressional tectonic settings (see Tibaldi et al., 2010). Classic examples of volcanism in compressional tectonic setting are volcanic arcs overlying subduction zones. The Japan volcanic arc develops from the subduction of the Pacific Plate under the Eurasiatic plate (Tibaldi et al., 2010). In the Southern Central Andes Volcanic Zone, the Nazca plate is subducting under the South American plate, where thrust fault systems affect the early stages of the volcanic arc and where volcanic vents form along thrusts or in linkage zones (Naranjo et al., 2018).

Within intra-plate contexts, volcanoes are present in the Great Caucasus-Lesser Caucasus thrust zone. Similarly in the Black Mountain Zone, a fault segment of the San Andreas fault system in California, there is evidence of eruption during tectonic activity (Glazner & Bartley, 1994). In southern Sicily, volcanic vents developed along important transpressional fault segments at the front of the Sicilian orogen (Montanari et al., 2017).

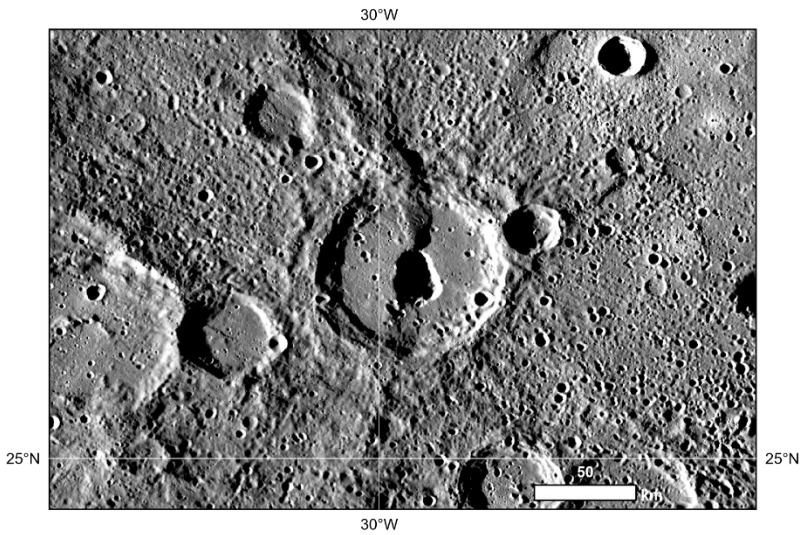

Figure 1.24. Geddes crater characterized by a central volcanic vent, developed along a contractional structure (Antoniadi Dorsum), probably interacting with the explosive volcanic activity. Equirectangular projection.

1.7 Comparative planetology

In planetary sciences, planetary bodies are often compared to analyse surfaces and interpret geological features, taking into account the physical parameters that vary for different planetary bodies (Chahine et al., 2013; Sauro et al., 2020). The Moon has often been used as a reference for comparing Mercury's tectonic processes, volcanism, geological features, and exosphere. The chronology of Mercury is based on the comparison with the Moon’s chronology (e.g., Marchi et al., 2009). Tectonism and volcanism of the Moon have been used as comparison with the tectonic and volcanic activity of Mercury (Thomas et al., 1982). Gault et al. (1975) compared impact crater morphology of Moon and Mercury to infer main differences in their gravity fields and interpret impact processes. Mercury’s chemical composition of exosphere and thermal features were compared with exosphere and thermal characteristics of the Moon (e.g., Sprague, 1990; Killen and Ip, 1999).

Peak-ring basins and multiring basins are widespread on terrestrial planets and can be characterized by their gravity signature. After Gravity Recovery and Interior Laboratory (GRAIL) mission, Neumann et al. (2015) showed that lunar basins were characterized by a central gravity anomaly that was caused by the excavation of crustal materials and their replacement by denser mantle materials. The size of the central Bouguer gravity anomaly corresponds closely to the diameter of the inner peak-ring of a basin, while the main ring is approximately twice the diameter of the peak-ring (Neumann et al., 2015; Fig. 1.25). This allowed to confirm the existence of previously proposed basins on the Moon, but also to correctly estimate the size of the main crater and detect new basins that were not yet identified. In this thesis, I present an improved technique based on the analysis of gravity and crustal thickness data to estimate the inner ring and rim crest diameters. This technique expands upon the work of Neumann et al. (2015) and allows one to better identify highly degraded basins. From this analysis, I also quantify how lower resolution gravity, and crustal thickness datasets (such as for Mars or Mercury) might bias the peak-ring and main rim diameter estimates. In this thesis, the approach has been applied to Mercury's impact basins to provide an estimate of the diameter of the peak-rings or inner rings.

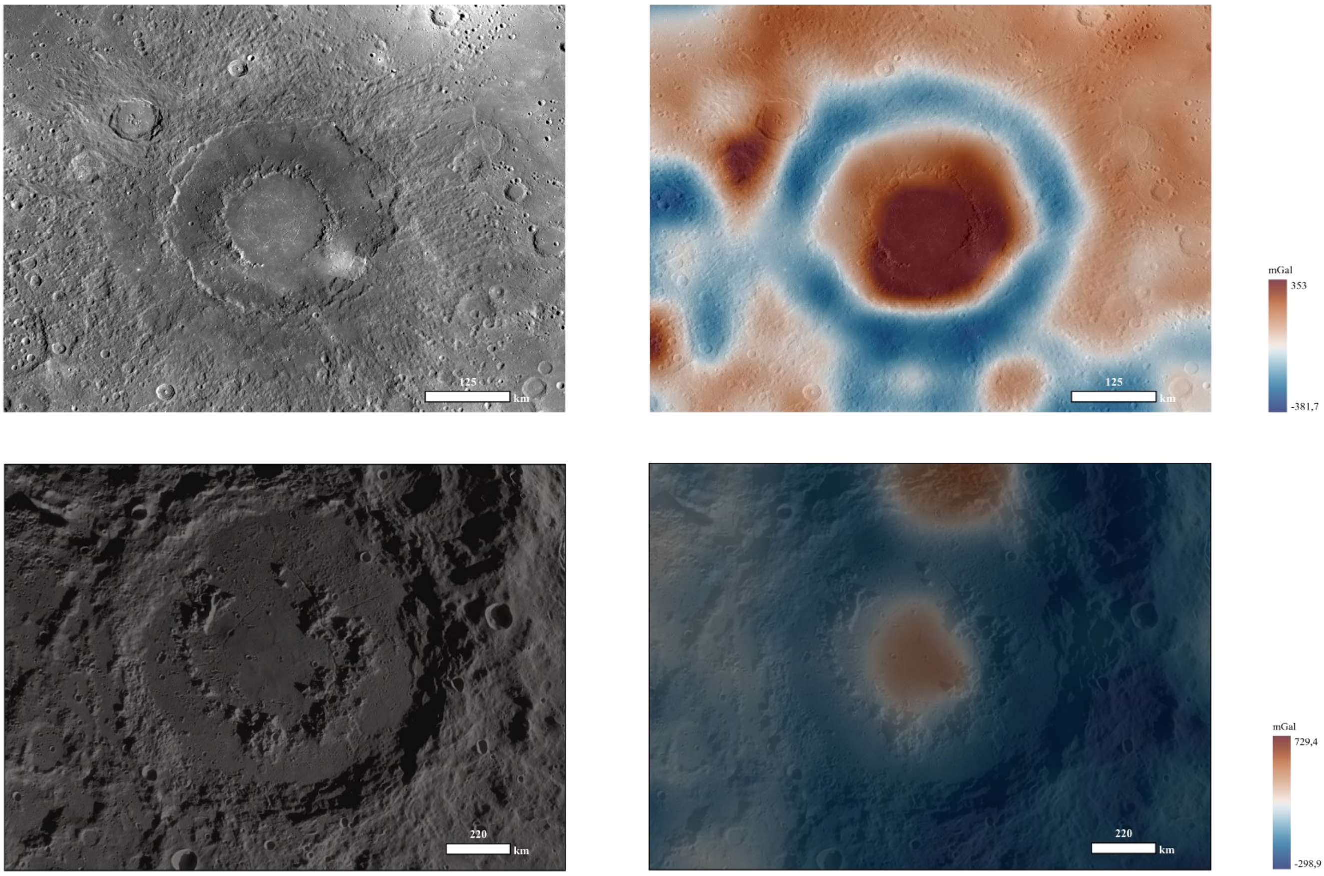

Figure 1.25. Example of peak-ring basin on Mercury (top; Rachmaninoff basin) and Moon (bottom; Schrödinger basin) characterized by an external topographic rim and an internal ring structure. Morphological basemaps derived from MESSENGER MDIS and LRO LROC imagery, for Mercury and Moon respectively, are shown on the left. Bouguer gravity anomaly maps derived from MESSENGER Radio Science and GRAIL data, for Mercury and Moon respectively, are shown on the right.

1.8 Gravity modelling

The spacecraft's range and range-rate observations are inverted to determine the planet's gravity field, improve the planet's orbital ephemeris, and improve knowledge of the rotational state, including obliquity and forced physical libration of the investigated planet.

Gravity data are often used to investigate the internal structure of planets at large scales, and to estimate densities or geometries of bodies at smaller scales. Satellite gravity data have been extensively used for the Earth, terrestrial planets and icy satellites with the intent of studying the internal structure and the characteristics of shallow or deep sources and structures (Ebbing et al., 2013; Wieczorek, 2015a; De Marchi et al., 2022). Bouguer gravity anomalies are usually studied for modelling and investigating the subsurface. The Bouguer anomalies in planetary studies are obtained by removing the gravity effect of topography from the observed free-air anomalies (see Methods section). To calculate gravity effect of the topography, the method basically consists of a power expansion of the coefficients of the topography in a Taylor series, with reference to a radial distance (Wieczorek and Phillips, 1998; Wieczorek, 2015a).

In planetary geophysics, the Bouguer gravity anomalies are usually associated with the only contribution of the crust-mantle interface, neglecting other crustal or deeper sources (e.g., Wieczorek, 2015a). As a results previous authors derived the crustal thickness and the crust-mantle interface of the planet by assuming the average crustal and mantle densities (e.g., Genova et al., 2019). The crust-mantle surface is in fact determined by continuing downwards the Bouguer gravity field down to the average radial distance between the center of the planet and the crust-mantle surface. By minimizing the difference between the surface coefficients obtained from the observed Bouguer coefficients and the calculated surface coefficients, the crust-mantle interface is thus determined using an iterative approach (Wieczorek and Phillips, 1998). The average bulk density can be usually estimated by minimizing the correlation between the topography and the Bouguer anomalies or exploiting the relationship between gravity and topography in the frequency domain. Assuming a constant crustal density of the topography, according to Wieczorek et al. (2013) and Goossens et al. (2017) the bulk density can be estimated from the cross-spectrum ratio between observed gravity and topographic effect and the power spectral density of the topographic effect.

Regarding Mercury's internal structure, previous works modelled the crust-mantle interface and estimated mean crustal and elastic lithosphere thickness.

James et al. (2015) estimated a crustal thickness in the range 0-90 km. Phillips et al. (2018) estimated a 0-70 km crustal thickness. Watters et al. (2021) estimated two different crustal thickness models with depths ranging ~11-73 km and ~7-74 km, respectively.

Other authors estimated the mean crustal and elastic thicknesses of Mercury, or computed them in limited areas, by a spectral approach. Their method is based on the calculation of the admittance or correlation functions between gravity and topography (see Wieczorek, 2015a). The average crustal thickness can be estimated, for example, by equating the observed geoid-topography ratio (GTR) to the calculated one. Padovan et al. (2015) assumed the Airy isostatic model for $9<l<15$ degrees and derived a mean crustal thickness of 35 ± 18 km for the Mercury's northern hemisphere using geoid-topography ratios; Sori (2018) calculated a mean crustal thickness of 26 ± 11 km, again using the Airy model. Konopliv et al. (2020) computed a crustal thickness ranging 23-50 km (see table 1).

Regarding the mean elastic thickness (T_e) of Mercury, James et al. (2016) estimated T_e = 31 ± 9 km; Watters et al. (2002) derived T_e= 40 km from the maximum depth of faulting; Nimmo and Watters (2004) calculated T_e= 25-30 km equating the elastic-plastic bending moment to the elastic bending moment. Very different values, $T_e \cong$ 110-180 km, were estimated by Tosi et al. (2015), for degrees l= [2,4] of geoid and topography (see also table 1). Differently from the above methods, some authors considered also crustal heterogeneities, in areas where surface and internal loads can be assumed to be in phase, i.e., when the two are related linearly by a degree-independent constant (e.g., Wieczorek, 2015a; Grott and Wieczorek, 2012; Broquet and Wieczorek, 2019). For these restricted areas, Goossens et al. (2022) estimated a crustal thickness ranging between 36 ± 14 and 112 ± 17 km and an elastic thickness between 11 ± 7 and 28 ± 7 km, while Genova et al. (2023) estimated crustal thickness varying between 51 ± 37 and 91 ± 22 km, and an elastic thickness varying between 5 ± 4 and 102 ± 35 km (see also table 1). Beuthe et al. (2020) utilized the crustal densities derived from XRS data (Nittler et al., 2020) and obtained an 8-97 km crustal thickness model. In their model, crustal heterogeneity vs. depth is modelled by an exponential decrease of porosity and a smoothing out of lateral density variations.

Table 1. Existing estimates of Mercury's crustal parameters.

Elastic thickness, T_e		**Crustal thickness models**		**Mean crustal thickness, T_c**	
Value	**Reference**	**Value**	**Reference**	**Value**	**Reference**
31 ± 9 km	James et al. (2016)	0-90 km	James et al (2015)	35 ± 18 km	Padovan et al. (2015)
		0-70 km	Phillips et al. (2018)		
40 km	Watters et al. (2002)			26 ± 11 km	Sori (2018)
25-30 km	Nimmo & Watters (2004)	~11-73 km	Watters et al. (2021)		
		~7-74 km	Watters et al. (2021)	23-50 km	Konopliv et al. (2020)
~110-180 km	Tosi et al. (2015)	8-97 km	Beuthe et al. (2020)		

1.9 Boundary analysis

The map location of horizontal boundaries of gravity anomalies sources has been the subject of numerous studies in different applications of potential fields, from engineering applications to planetary studies. Gravimetric data enhancement techniques are indeed very useful to estimate the horizontal position at depth of sources and crustal structures (e.g., Fedi and Florio, 2001).

Several boundary analysis techniques based on derivatives of various orders of the field have been developed and used so far (Miller and Singh, 1994; Fedi and Florio, 2001; Fedi, 2002a; Verdzuco et al., 2004; Wijns et al., 2005; Cooper and Cowan, 2006; Ma and Li, 2012). One of the most exploited methods is based on the calculation of the first- or second-order vertical derivative of the gravity field, to identify the horizontal position of the sources through the zero contour (e.g., Evjen, 1936; Nabighian, 1984), although it has been demonstrated that the estimated boundaries are shifted with respect to the real position (e.g., Thurston and Smith, 1997).

Cordell (1979) developed the total horizontal derivative (THD) method, showing that the maxima of the horizontal gradient of potential field anomalies are located in correspondence of density contrasts or changes of magnetization. Another useful approach based on Euler's equation was developed to identify the boundaries and estimate sources depths of magnetic and gravity anomalies (Thompson, 1982; Reid et al., 1990).

Pedersen and Rasmussen (1990) proposed to calculate invariants of the gradient tensor to mainly emphasize large volumetric sources.

Later, the total gradient analysis was used in order to better estimate position and depths of investigated sources (Roest et al., 1992; Hsu et al., 1996, 1998). Roest et al. (1992) derived the absolute value of the analytic signal as the square root of the squared sum of the vertical and the two horizontal derivatives.

Fedi and Florio (2001) developed a new high-resolution boundary analysis technique named Enhanced Horizontal Derivative (EHD), based on the horizontal derivative of a sum of weighted vertical derivatives of the field having increasing order (see also Cella et al., 2009; Fig. 1.26). The maxima correspond to the horizontal boundaries of the sources (see also Methods section).

Fedi (2002a) proposed the Multiscale Derivative Analysis (MDA), based on the EHD of the field, but using different weights for different derivatives, depending on the contributions to be enhanced.

Satellite gravity gradients and curvature components are also used to study the global Earth's structure (Ebbing et al., 2018; Pappa et al., 2019).

On terrestrial planets, similar approaches have already been implemented and used. For example, Andrews-Hanna et al. (2013) calculated the second horizontal derivative of the Bouguer potential to identify short-wavelengths structures in the lunar crust.

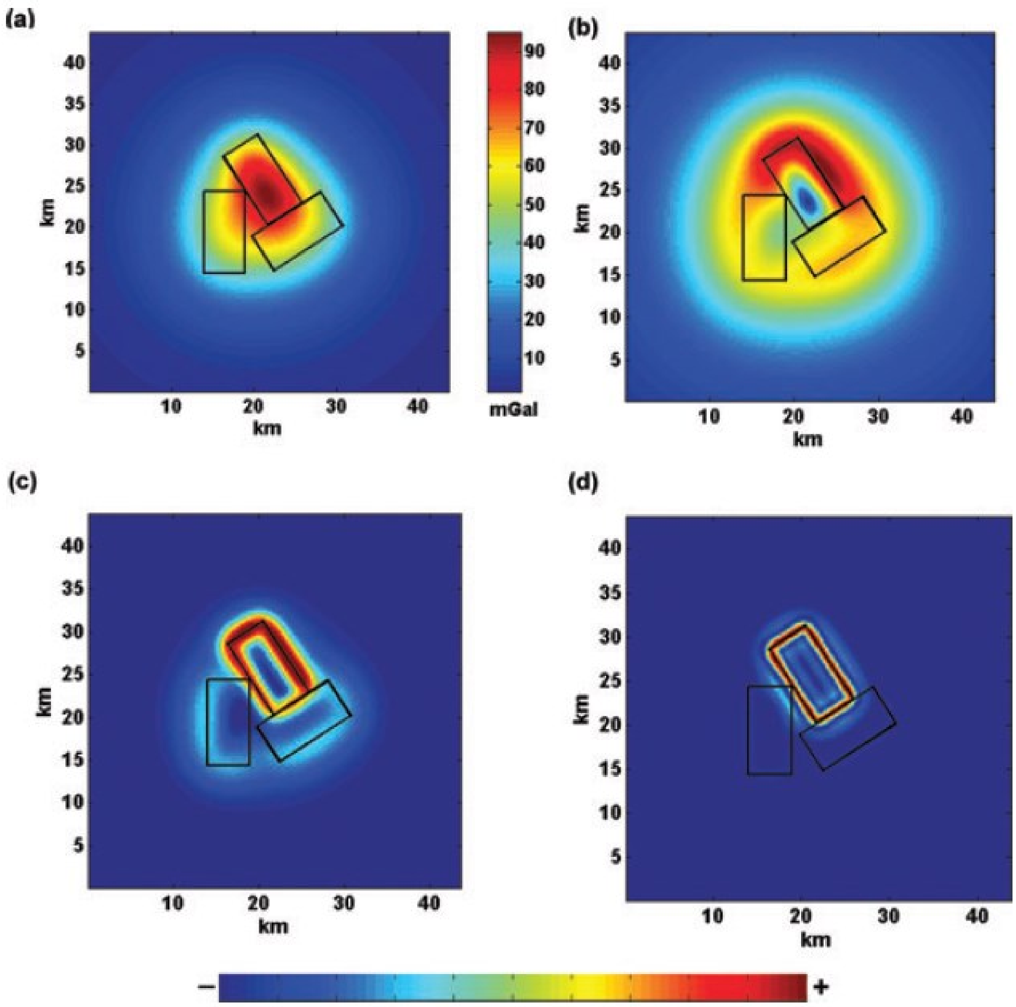

Figure 1.26. a) Gravity field generated by three different prismatic sources. The northernmost prism has its top at a depth of 2 km; the others are 4 km deep. **b)** Enhanced horizontal derivative computed with derivatives up to the second order, which enhances large-scale structures. **c)** Enhanced horizontal derivative computed with derivatives up to the third order, which enhances the intermediate-scale sources. **d)** Enhanced horizontal derivative computed with derivatives up to the fourth order, enhancing short-scale sources (modified after Cella et al.,2009).

1.10 Thesis structure

This thesis work focuses on the geological and structural analysis of the Michelangelo quadrangle (H12) and the Beethoven basin, on the analysis of the tectonic structures that border and reactivate ancient impact basins, on the interaction of volcanic vents and thrust faults, on the calculation of gravity anomalies related to crustal and intra-crustal sources, on the assessment of tectonic models that mainly affects large impact basins and the high-Mg region through morphological observations and gravity data enhancing techniques, and finally on the development of a new method to estimate the size of impact basins for terrestrial planets.

The structure of the thesis develops in the following chapters: Data, Methods, Results, Discussion and Conclusions.

In the Data section, I will present the MESSENGER datasets used for the production of the geological map and for Mercury's crustal structure modelling, but also the dataset used for the study of lunar peak-ring or multi-ring basins.

In the Methods section, I will provide the criteria used for geological mapping and analysis of tectonic structures, and the techniques developed in this thesis for the geophysical analysis of crustal structures, and the estimation of the size of impact basins.

In the Results paragraph, I will i) present the geological map of Michelangelo quadrangle (H12) at 1:3 million scale with a specific focus on the Beethoven basin; ii) explain how faults can interact with explosive volcanism on Mercury; iii) illustrate a new model for the reactivation of impact basins; iv) show the main gravity anomalies generated by intra-crustal sources, highlighting those related to impact basins and large tectonic structures; and v) provide the size estimates of some lunar and Mercury basins.

In the Discussion section, I will discuss i) the nature of Michelangelo terrains; ii) the interaction mechanisms between faults and vents; iii) a geological interpretation of the main calculated isostatic gravity anomalies; iv) a possible thick-skinned tectonic style, with specific regard to large impact basins and to the high-Mg region of Mercury. Finally, I will demonstrate the validity of boundary analysis techniques in identifying new impact basins.

Part of the following chapters derives from the following works: Buoninfante et al. (2023), and Buoninfante et al. (in review in Journal of Maps).

2. Data

The planets and celestial bodies of the solar system can generally be studied through satellite measurements and observations. In recent decades, several satellite missions have been organized by government space agencies, each dedicated to the study of a specific planetary body.

2.1 MESSENGER datasets

As already mentioned, the most complete products and datasets for Mercury come from the latest completed mission, MESSENGER. Thanks to MESSENGER, we obtained fundamental information on the planet's gravity field, geological structure, and history. In particular, the MESSENGER Mercury Dual Imaging System (MDIS) provided images of the surface of the planet (Hawkins et al., 2007), allowing the recognition of geological units and structures. The Mercury Laser Altimeter (MLA) returned the surface topography (see for instance Manheim et al., 2022), while Radio Science (RS) provided gravity field data from the spacecraft position and velocity (see Konopliv et al., 2020). The NASA Planetary Data System (PDS) provides the MESSENGER dataset that was used in this thesis.

2.1.1 MDIS data

For the geological mapping, I mainly used MESSENGER MDIS products. In this project, I used basemaps (Fig. 2.1) produced by the MESSENGER team and derived from the Mercury Dual Imaging System (MDIS) Wide-Angle Camera (WAC) and Narrow-Angle Camera (NAC) data (Hawkins et al., 2007; Denevi et al., 2018). These cameras covered the planet with a mean resolution of ~200 m/pixel, reaching a maximum of ~8 m/pixel for a total of more than 270,000 images.

The NAC is an off-axis reflective telescope with a 550-mm focal length and a collecting area of 462 mm^2. The NAC has a single medium-band filter (50 nm wide), centered at 750 nm to match the corresponding WAC filter for monochrome imaging (Hawkins et al., 2007; Denevi et al., 2018).

The WAC consists of a 4-element refractive telescope with a focal length of 78 mm and a collecting area of 48 mm^2. It is characterized by eleven spectral filters in the range from 395 to 1040 nm, in order to cover wavelengths indicative of several surface materials.

The detector located at the focal plane was an Atmel (Thomson) TH7888A frame-transfer CCD with a 1024x1024 format and 14-micron pitch detector elements providing a 179-microrad pixel field-of-view (IFOV). The 12-position filter wheel gave color imaging over the spectral range of the CCD detector (Hawkins et al., 2007; Denevi et al., 2018).

The PDS Imaging Node (NASA-USGS-JPL) provided all the information through the MDIS Experiment Data Record (EDR) Software Interface Specification (SIS) and the MDIS Calibrated Data Record/Reduced Data Record (CDR/RDR) SIS.

EDR consists of single-frame almost-raw images, which are the primary data coming from MESSENGER MDIS with information attached on the PDS labels, about spacecraft position at the time of frame shot.

CDR consists of single-frame images calibrated in units of radiance (RA), radiance factor (I/F, IF) or photometrically corrected reflectance (RE). Radiance factor is defined as the ratio between measured radiance and a calculated radiance, which would be measured from an ideal diffusely-reflecting surface (Lambertian surface). CDRs are not geometrically corrected.

The Derived Data Record (DDR) consists of single images containing geometrical information about latitude, longitude, incidence angle (i, the angle between the sun and the surface), emission angle (e, the angle between the spacecraft and the surface) and phase angle (g, the angle between the incident and reflected light) at the equipotential surface.

RDR data can be subdivided into: Map Projected Basemap (BDR), 8-color Map Projected Multispectral (MDR), 3-color Map Projected Multispectral (MD3), 5-color Map Projected Multispectral (MP5), Map Projected High-Incidence Angle Basemap Illuminated from the East (HIE), Map Projected High-Incidence Angle Basemap Illuminated from the West (HIW), Map Projected Low-Incidence Angle Basemap (LOI), Regional Targeted Mosaic (RTM).

Map Projected Basemap RDR (Fig. 2.1a; BDR) consists of a global monochrome map, with photometrical correction to $i = 30º$, $e = 0º$, $g = 30º$ at a resolution of 256 pixels per degree (ppd, ~166 meters/pixel at the equator). In this product the NAC and WAC 750-nm images were used (Denevi et al., 2018). WAC images were preferentially taken at the periapse where

MESSENGER reached its minimum altitude of 200 km, while NAC images were specially taken at apoapse where the spacecraft reached 13100 km of altitude.

The BDR dataset is divided into 54 tiles, each representing the NW, NE, SW, or SE quadrant of each quadrangle. This dataset mainly includes moderate solar incidence angle (~74°) images, useful for morphological interpretation. MESSENGER MDIS BDR is the main reference basemap used in this work.

The 8-color Map Projected Multispectral RDR (MDR) dataset consists of a mosaicked global color map of 8-color image sets, corrected to i = 30º, e = 0º, and g = 30° and sampled at 64 ppd.

The 3-color Map Projected Multispectral RDR (MD3) dataset consists of a mosaicked global color map of 3-color image sets, corrected to i = 30º, e = 0º, and g = 30° at a resolution of 128 ppd.

The 5-color Map Projected Multispectral RDR (MP5) data set consists of a mosaicked regional color map of 5-color image sets, corrected to i = 30º, e = 0º, and g = 30° at a resolution of 128 ppd.

The LOI basemap (Fig. 2.1b) consists of a mosaic composed of low incidence angle NAC and WAC 750-nm images with a resolution of 166 m/pixel (Denevi et al., 2018). This product tends to highlight albedo variations and minimize obscuration by shadows.

The HIE and HIW mosaics (Fig. 2.1c, d) are derived from NAC and WAC 750-nm images illuminated at high angle of solar incidence (~78°) from the East and West, respectively, with a resolution of 166 m/pixel (Denevi et al., 2018). These basemaps were mainly used to identify morphological features in BDR shadowed regions.

The MESSENGER MDIS 3-color map-projected Multispectral reduced Data record (Fig. 2.1e; MD3) was created using MDIS-WAC 1000-nm, 750-nm, 430-nm, filters in the red, green, and blue channels, respectively, at a resolution of ~665 m/pixel. The Enhanced color basemap is a derived product that emphasizes color differences by means of principal component analysis. The second principal component is placed in the red, the first principal component in the green, and the ratio of 430/1000 nm filters in the blue channel, respectively (Denevi et al., 2018). These products were mainly used to identify strongly-colored surface features (i.e., pyroclastic deposits, bright deposits, dark materials, and hollows).

The RTM dataset consists of regional maps corrected to i = 30º, e = 0º, g = 30° at resolutions optimized to each mosaic, from images taken as NAC strips or WAC color observations.

In this thesis work I used the MDIS BDR, LOI, HIW, HIE, Global Color and Enhanced Color mosaics (Fig. 2.1).

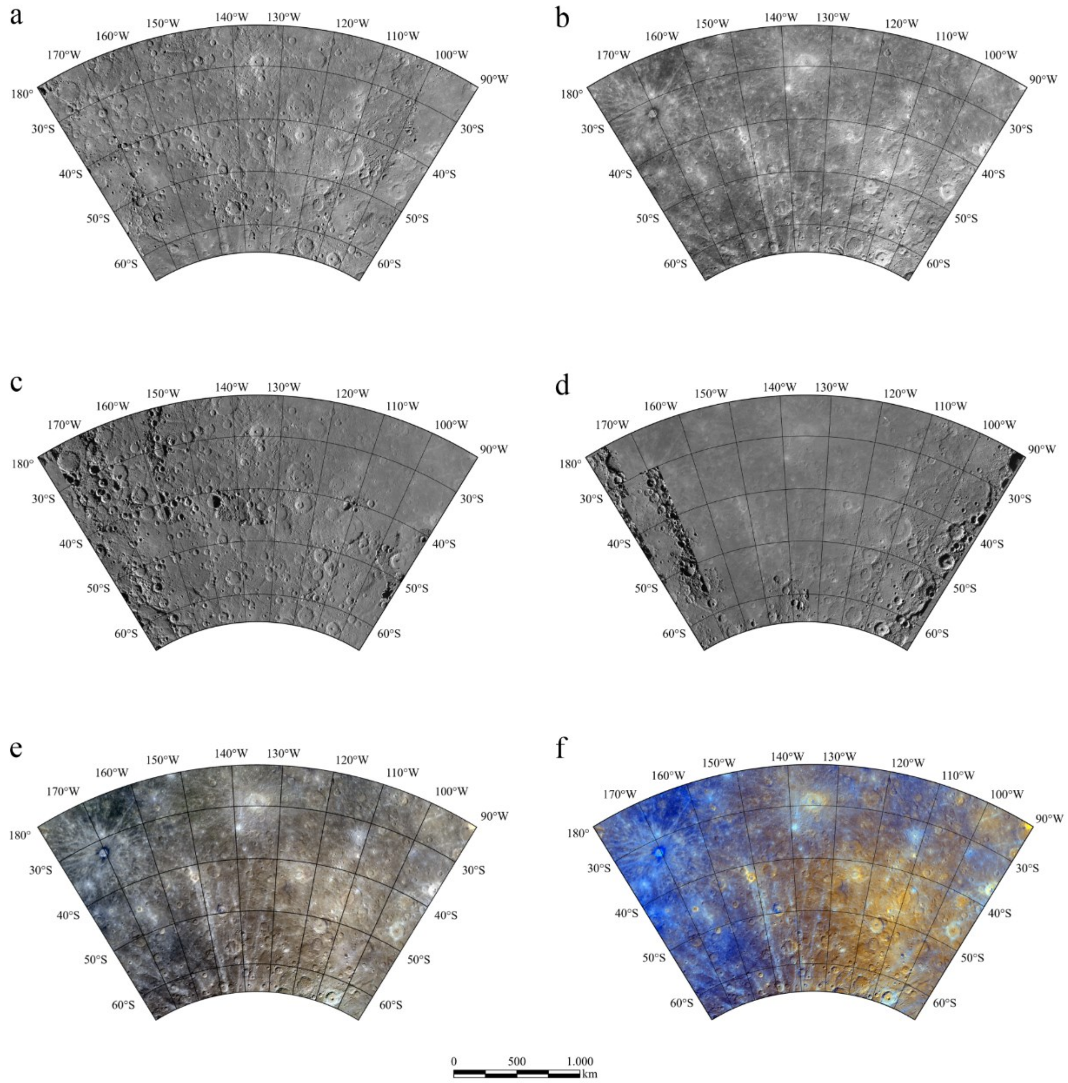

Figure 2.1. H12 MDIS data used as basemaps for the geological cartography: **a)** Basemap reduced Data Record (BDR) mosaic; **b)** Low Incidence angle (LOI) mosaic; **c)** High Incidence angle from East

(HIE) mosaic; **d)** High Incidence angle from West (HIW) mosaic; **e)** Global Color Basemap mosaic; **f)** Enhanced Color Basemap mosaic. Lambert conformal conic projection.

2.1.2 Topography data

Topographic data is necessary for correct geological interpretation, as it provides important information on the surface processes, internal structure, and on the thermal and geological evolution of the planet. Mariner 10 data already allowed stereo coverage (e.g., Jet Propulsion Laboratory, 1976; Davies et al., 1978; Cook & Robinson, 2000). During MESSENGER mission, Preusker et al. (2011) produced three digital terrain models from stereo images taken in three flybys. After MESSENGER, Zuber et al. (2012) derived a topographic model of the northern hemisphere from Mercury Laser Altimeter (MLA) measurements. Elgner et al. (2014) derived global shape and topography models of Mercury from limb images. Later, Perry et al. (2015) derived a spherical harmonic model by combining MLA measurements from the northern hemisphere and radio frequency occultations data of southern hemisphere.

Digital Terrain Models (DTMs) at resolution ~222 m/pixel (192 pixels per degree) of specific quadrangles were produced by DLR (see Preusker et al., 2017a), based on stereo photogrammetry using WAC, mainly for the northern hemisphere, and NAC images, covering also the southern hemisphere. The process involves multi-image matching to derive tie-points, which are used to perform a photogrammetric block adjustment. Then, interpolation was used to derive a DTM (see Oberst et al., 2010; Preusker et al., 2011; Preusker et al., 2017a). DTMs for the quadrangles Shakespeare (H03; Preusker et al., 2017b), Hokusai (H05; Stark et al., 2017), Kuiper (H06; Preusker et al., 2017a), Beethoven (H07; Oberst et al., 2017) were provided and available on the USGS PDS Imaging Node Server. Later, Preusker et al. (2018) derived DTMs also for the quadrangles Discovery (H11), Michelangelo (H12; Fig. 2.2), Neruda (H13), Debussy (H14). To produce H12 DTM, Preusker et al. (2018) selected about 5500 NAC images, identifying about 40,000 independent stereo combinations. 75,000 tie point observation were used for the bundle block adjustment. 10.3 billion surface points with a mean accuracy of about ±40m were derived from image matching. The final DTM has a vertical accuracy of ~35 m.

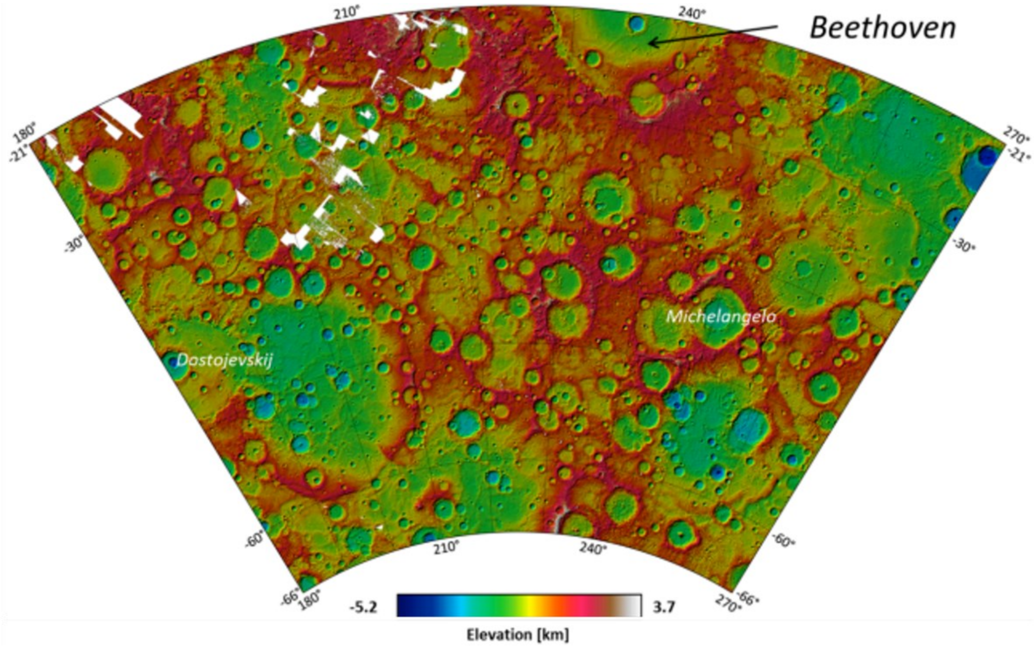

Figure 2.2. H12 DLR DTM (~222 m/pixel; from Preusker et al., 2018). Lambert conformal conic projection.

The topographic model used in this work is the global United States Geological Survey (Fig. 2.3; USGS) stereo-DEM (665 m/pixel; 64 pixels/degree) derived from stereo matching of NAC and WAC 750-nm data with elevations calibrated with the MESSENGER's Mercury Laser Altimeter data (Becker et al., 2016). The global DEM was created from a least-squares bundle adjustment (jigsaw in ISIS3; Edmundson et al., 2012) of features, measured as tie point coordinates in overlapping NAC and WAC-G filter images (see Becker et al., 2016).

The global DEM was used in support of monochrome images to better identify tectonic structures and crater rims.

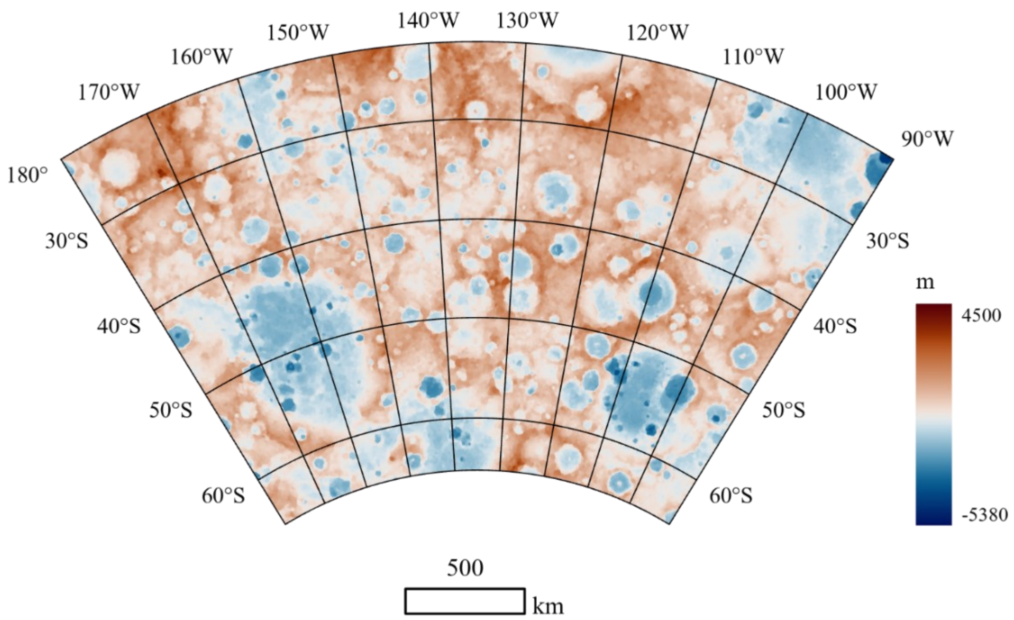

Figure 2.3. USGS DEM of the Michelangelo quadrangle (~665 m/pixel). Lambert conformal conic projection.

2.1.3 Radioscience data

Satellite potential field data play an important role in studying a planet, especially at large scales. Satellite measurements can be used to produce maps of regional magnetic and gravity anomalies. Gravimetric measurements derive for example from the analysis of satellite movements (see also Appendix). By observing the movements of satellites with ground-based tracking systems, the spherical harmonics coefficients of the gravitational potential can be determined using various techniques. For planetary studies, the estimate of the planet's gravity field is normally obtained with radioscience techniques (e.g., Milani et al., 2001, Iess and Boscagli, 2001). Usually, the ground station sends a high-frequency radio signal which is received by the probe. The probe decodes the commands, encodes the telemetry data and transmits the signal back to the ground station. The variation in frequency of the signal caused by the Doppler effect, generated by the relative motion between the satellite and the planet itself, is recorded (Srinivasan et al., 2007). Then, the gravitational attraction is derived from the recording obtained with the used instrumentation (Transponder).

First estimates of the Mercury's gravity field were determined during and after MESSENGER mission. Smith et al. (2012) computed the first global gravity field model HgM002, using the radio tracking data acquired by MESSENGER up to August 23rd, 2011. Despite the limited spectral resolution, up to spherical harmonic degree and order 20, this model allowed estimating the crustal thickness, the elastic lithosphere thickness of the Northern Rise region and the polar moment of inertia (Smith et al., 2012). Later, Mazarico et al. (2014) and Mazarico et al. (2016) improved the gravity field models, up to spherical harmonic degree and order 50 (HgM005) and 100 (HgM007), respectively. It provides a better relationship with the surface topography resulting from the measurements of MESSENGER's Mercury Laser Altimeter (Zuber et al., 2012). Genova et al. (2019) elaborated the HgM008 model, which defines the gravity field up to spherical harmonic degree and order 100. The latest gravity field models (Konopliv et al., 2020; Genova et al., 2023), respectively named MESS160A and HgM009, are defined up to spherical harmonic degree and order 160. Previous works also provided maps of the free-air and Bouguer gravity anomalies (e.g., Smith et al., 2012; Mazarico et al., 2014; Genova et al., 2019; Konopliv et al., 2020; Genova et al., 2023; Verma et al., 2016).

The gravity field used in this thesis work is the MESS160A model (Konopliv et al., 2020; Fig. 2.4). The model includes the complete MESSENGER tracking data from March 2011 to April 2015. Considering l_{max}=160 and the radius of Mercury, the minimum wavelength that can be resolved with the MESS160A field is ~50 km (see eq. A.11). Konopliv et al. (2020) also determined the spine-pole axis, the rotation period, the Love number, and ephemeris. Although the model is expressed up to 160 degrees, the actual resolution (degree strength) of the MESS160A model varies from l=12 in the southern hemisphere (half-wavelength spatial resolution of 640km) to a maximum resolution in the northern hemisphere of l =154 (half-wavelength spatial resolution of 50km). The degree strength (see Fig. 4 in Konopliv et al., 2020) gives the model local resolution in spherical harmonic degrees, defined from the intersection between the gravity signal of the coefficients and the gravity uncertainty (Konopliv et al., 1999).

More recently, Genova et al. (2023) derived the HgM009 solution through a reprocessing of the entire MESSENGER radio tracking dataset. They also analysed the localized spectral admittance to study the lateral variations of the crustal bulk density. They estimated a bulk density of 2540 ± 60 kg/m^3 in the northern hemisphere and a crustal porosity of 15 ± 2%.

The topography model GTMES_150v05 (Fig. 2.5; archived on the NASA Planetary Data System, PDS, at https://pds-geosciences.wustl.edu/messenger/mess-h-rss_mla-5-sdp-v1/messrs_1001/data/shadr/gtmes_150v05_sha.tab) is defined up to a spherical harmonic degrees of 150. The model defines the shape of Mercury and is expressed in terms of radial distance from the center of mass. It is more accurate in the northern hemisphere but not well resolved in the southern hemisphere (see Neumann et al., 2016), as it is derived from the MESSENGER's Mercury Laser Altimeter (MLA) measurements in the northern hemisphere and from radio occultations measurements (see also Perry et al., 2015) in the southern hemisphere. The gravity field model is also better resolved in the northern hemisphere due to the lower orbital distance of the satellite instrumentation. However, the topography model has a resolution similar to the resolution of the latest gravity field models. It can be noted that the free-air gravity anomalies correlate well with the topography, especially in the northern hemisphere, where both have good data resolution. In the southern hemisphere the correlation between free-air gravity anomalies and topography is worse as the data resolution is low.

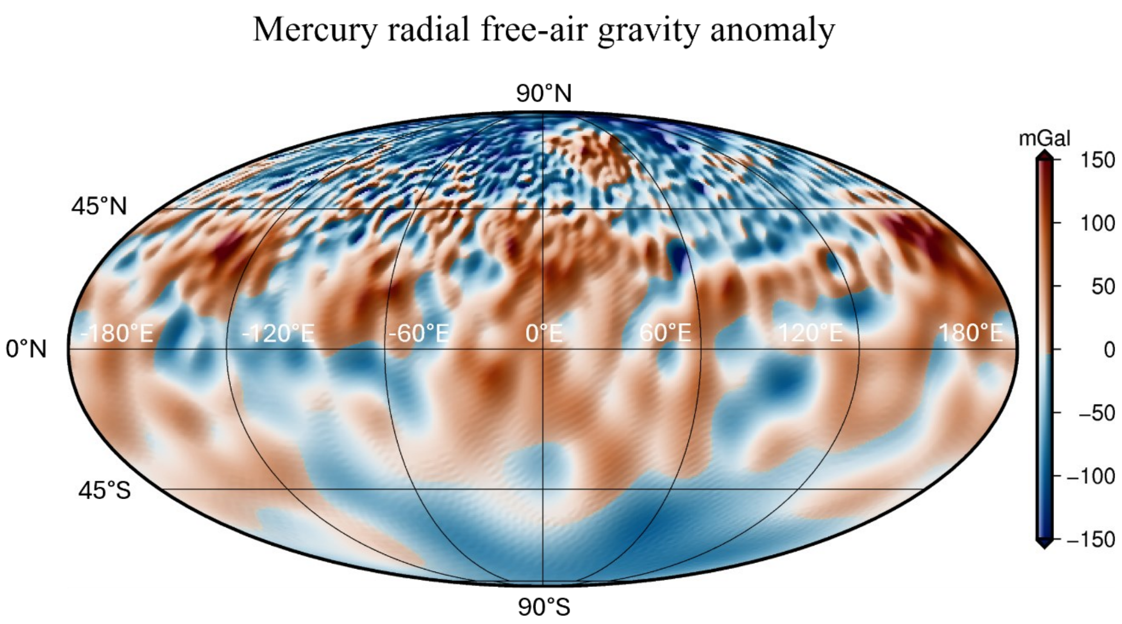

Figure 2.4. MESS160A (Konopliv et al., 2020) radial component of free-air anomaly of Mercury, in Mollweide projection.

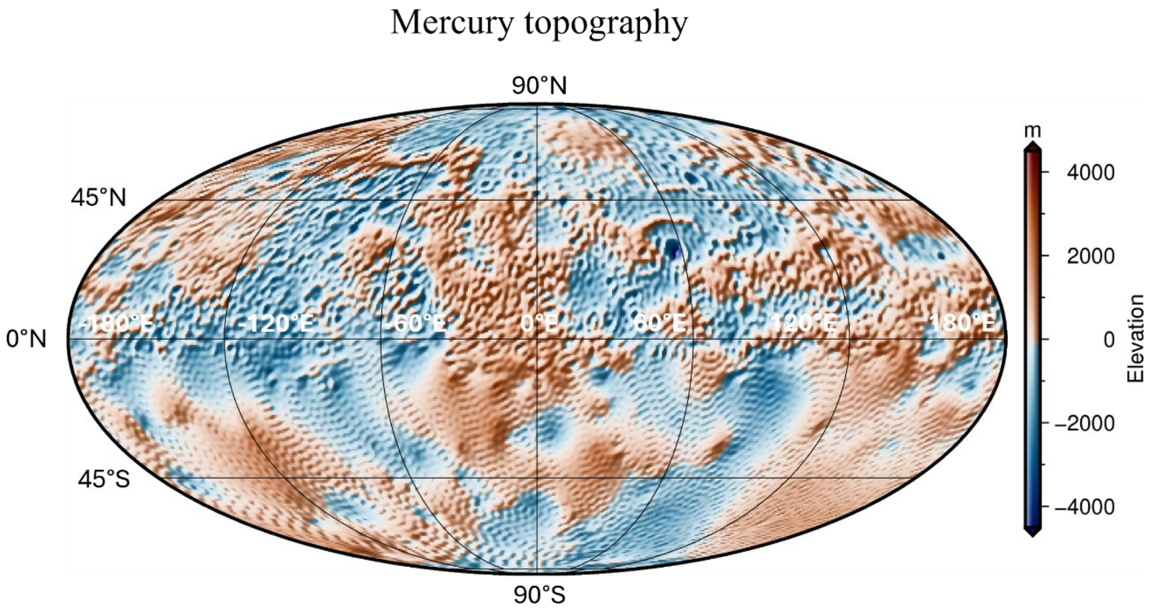

Figure 2.5. Topography of Mercury derived from the GTMES_150v05 model (Neumann et al., 2016), in Mollweide projection.

2.2 GRAIL datasets

To investigate the gravity signature of lunar impact basins, I used the gravity field model, and the crustal thickness model derived after GRAIL mission.

Gravity Recovery and Interior Laboratory (GRAIL) was a spacecraft-to-spacecraft tracking mission whose aim was to map the gravity field of the Moon to study its interior structure and to investigate its thermal evolution (Zuber et al., 2013). The spacecrafts include the Lunar Gravity Ranging System (LGRS) instrument, which measured the variations in distance between the two spacecrafts as Ka-band range-rate (KBRR) tracking (Asmar et al., 2013; Klipstein et al., 2013). The first lunar gravity field model produced after GRAIL was GL0420A, defined to spherical harmonic degree and order 420 (Zuber et al., 2013). Subsequently, GRAIL data led to higher resolution models. Lemoine et al. (2013) and Konopliv et al. (2013) derived models up to degree and order 660. These solutions were updated, leading to models to degree and order 900 (Lemoine et al., 2014; Konopliv et al., 2014). Later, models up to degree and order 1200 (Goossens et al., 2016) and 1500 (Park et al., 2015) were derived.

More recently, Goossens et al. (2020) produced the GRGM1200B (Fig. 2.6), defined up to degree and order 1200 and based on topography constraint. This work resulted in a model showing a high correlation with topography and in maps of vertical and lateral density structure of the Moon's crust. Topography data used in this work derives from the MoonTopo2600p model (Fig. 2.7; Wieczorek, 2015b).

GRAIL data was also used to derive the Moon's crustal thickness constrained by the Apollo seismic data (Fig. 2.8; Wieczorek et al., 2013). These results showed that the average density of the highlands crust is 2550 kg/m^3, and that the average crustal thickness varies between 34 and 43 km.

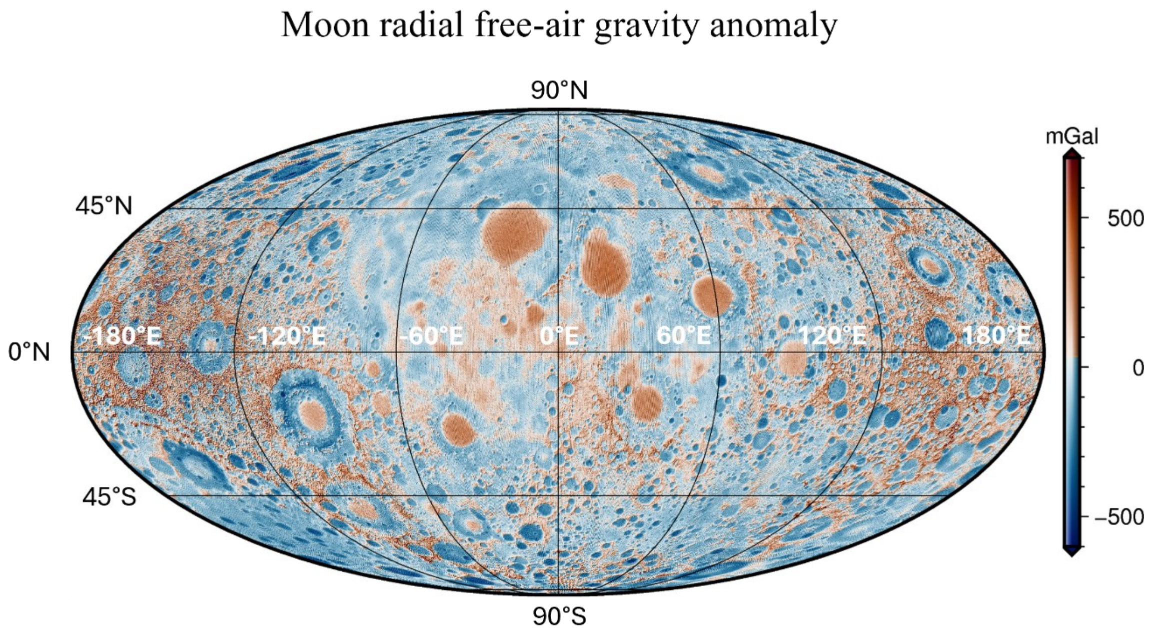

Figure 2.6. GRGM1200B (Goossens et al., 2020) radial component of free-air anomaly of the Moon, in Mollweide projection.

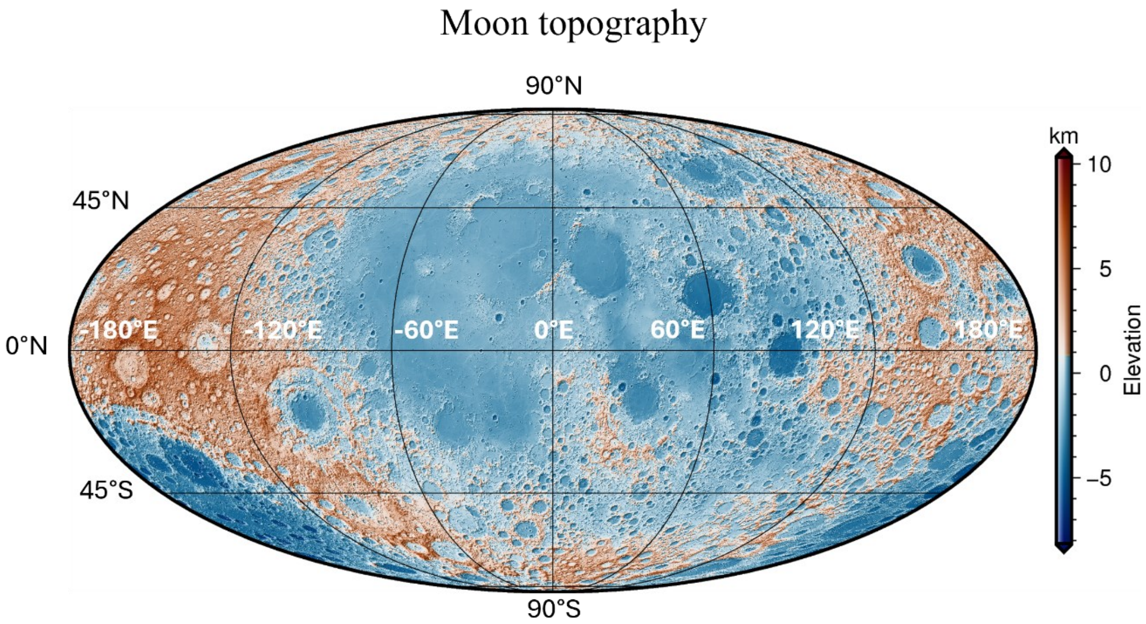

Figure 2.7. Topography of Moon derived from the MoonTopo2600p model (Wieczorek, 2015b), in Mollweide projection.

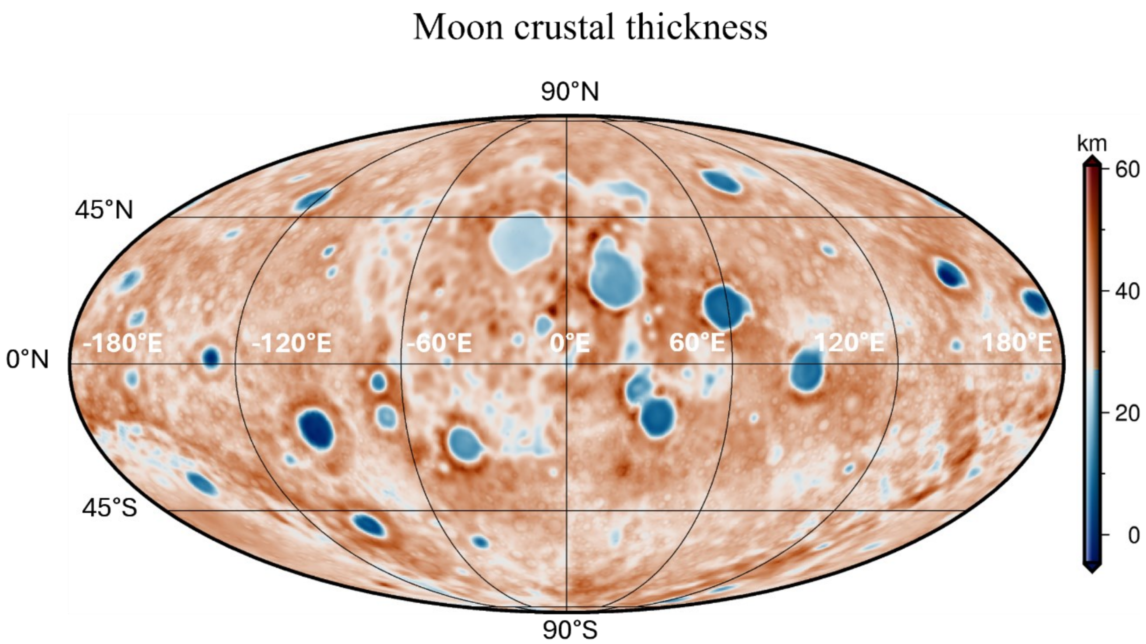

Figure 2.8. GRAIL (Wieczorek et al., 2013) crustal thickness of the Moon. Crustal density used is 2500 kg/m^3, in Mollweide projection.

3. Methods

In this chapter, I will first describe the method, and the workflow used to map the Michelangelo quadrangle of Mercury. Then, I will explain the gravity data analysis techniques developed and exploited to model Mercury's crustal heterogeneities and crustal structures geometries.

3.1 Geological mapping

This section reports and partly expands the paper Buoninfante et al., in review in Journal of Maps.

3.1.1 Map projection

Following previous mid-latitude geological maps (Galluzzi et al., 2016; Mancinelli et al., 2016; Guzzetta et al., 2017; Wright et al., 2019; Pegg et al., 2021a; Man et al., 2023b) and standard cartographic guidelines (Davies et al., 1978), the projection used in this work is the Lambert conformal conic (see also Fig. 2.1). This projection superimposes a cone on the planet sphere, with two standard parallels that represent the secants between the sphere and the cone of projection, conventionally at 1/6 and 5/6 of the latitudinal range (30°S and 58°S in H12). It is characterized by constant linear deformation and zero angular deformation. The scale of features is true along the standard parallels, slightly smaller between them and slightly larger beyond them (Kennedy & Kopp, 2004).

3.1.2 Scale

Standard cartographic rules suggest using a mapping scale Sm = Rr x 2000, where Rr is the raster resolution (Tobler, 1987). Considering the available spatial resolution of the MESSENGER MDIS BDR reference basemap (~166 m/pixel), the Tobler rule allowed us to recognize features up to 1:300,000-scale. The USGS guidelines recommend mapping at a scale two to five times larger than the final output scale (Tanaka et al., 2011). More recently, Hauber et al. (2020) and Skinner et al. (2022) proposed a mapping scale 4x the publication scale. To exploit MESSENGER basemaps at their best resolution, I drew contacts at a variable scale between ~1:300,000 and ~1:600,000 for a final map-output at 1:3 million scale. I avoided drawing features smaller than 5 km, to avoid feature excesses at the chosen output-scale.

3.1.3 Geodatabase structure and mapping process

Following the USGS recommendations and previous mapping works (e.g., Galluzzi et al., 2016; Guzzetta et al., 2017; Giacomini et al., 2022; Malliband et al., 2022; Man et al., 2023b), I used a geographic information system (GIS) to organize vector layers for the digitization. I created four main feature classes in an ArcGIS Pro 3.2.2 geodatabase: (1) geologic contacts (polyline layer), (2) linear features (polyline layer), (3) geological units (polygon layer), and (4) surface features (polygon layer).

In H12, the linear features include faults, wrinkle ridges, crater rims and irregular pits. I interpreted lobate scarps (e.g., Massironi et al., 2015) and high-relief ridges (e.g., Massironi & Byrne, 2015) as underlain by thrust-faults. Regarding crater rims, I mapped all craters with diameter larger than 5 km.

I classified the degradation state and mapped the ejecta of craters exceeding 20 km in diameter. Geological maps produced using Mariner 10 data (see McCauley et al., 1981) divided craters into five degradation states, from the most degraded class c1 to the least degraded c5, directly correlating them to each of the 5 time-periods of Mercury (pre-Tolstojan, Tolstojan, Calorian, Mansurian, Kuiperian). This 5-class system was later updated by Kinczick et al. (2020) for craters larger than 40 km. Here I follow the approach of Galluzzi et al. (2016), who used a 3-class system, from heavily degraded units (c1) to well-preserved units (c3). The latter approach was devised to resolve rare morphological uncertainties and inconsistencies found when mapping craters larger than 20 km. The 3-class system also allows integration of crater materials into the correlation of map units without implying correspondence to the five chronostratigraphic periods of Mercury. Indeed, by sticking to superposition relationships, this classification enhances the readability of the map at the 1:3M output scale and better frames the stratigraphy of the main volcanic events that shaped the surface in the first billion years of Mercury's history. The three-class system is currently being used globally in the 1:3M geological map series (Galluzzi et al., 2024), although several maps also use a five-class system in parallel.

Plains units were divided into smooth, intermediate, and intercrater based on the morphological appearance and crater density of the terrains (i.e., from very smooth to rough, respectively). Crater materials and plains units are defined by closed and topographically controlled geological contacts that were subdivided into certain and approximate.

Finally, as surface features I mapped crater chains (or *catenae*), hollows, *faculae*, bright deposits, and dark deposits locally covering the main units.

3.2 *Gravity data analysis*

In planetary studies, the gravity field is analysed through a spherical harmonic expansion (see Appendix). Usually for geodetic studies we conventionally refer to gravity disturbances or gravity anomalies as anomalies of the gravity field with respect to the normal gravity (GM/R^2) of the planet considered (see Appendix). In this work I describe such anomalies as gravity anomalies. This section reports and partly expands the paper Buoninfante et al. (2023).

3.2.1 Topographic gravity effect and Bouguer anomalies

Free-air gravity anomalies are normally defined as the radial component of the gravity field (see also Appendix). After computing the free-air gravity anomalies of Mercury, I used the *SHTools* software (Wieczorek & Meschede, 2005; https://shtools.oca.eu/shtools/public/) to estimate the gravity effect of the topography g^{TE} as:

$$g^{TE}(r,\varphi,\theta) = \frac{GM}{r^2}\sum_{l=0}^{l_{max}}\left(\frac{R}{r}\right)^l (l-1)\sum_{m=0}^{l} P_{lm}(\sin\theta)\,[\,H_{lm}\cos m\varphi + K_{lm}\sin m\varphi] \quad (3.1)$$

with the topographic effect coefficients $\{H_{lm}, K_{lm}\}$ defined as (Wieczorek and Phillips, 1998):

$$\{\,H_{lm}, K_{lm}\} = \frac{4\pi\,\Delta\rho\,B^3}{M(2l+1)}\sum_{n=1}^{l+3}\frac{\{h_{lm}^n, k_{lm}^n\}}{B^n n!}\frac{\prod_{j=1}^{n}(l+4-j)}{(l+3)}, \quad (3.2)$$

where $\{h_{lm}, k_{lm}\}$ are the topography model coefficients, B is the zero-degree term of the topography coefficients (i.e., the Mercury radius), n=5 the order of the Taylor series expansion. A $\Delta\rho$ = 2800 kg/m^3 density is assumed for the underlying crust (Genova et al., 2019).

The Bouguer anomalies are calculated by subtracting the topographic gravity effect from the free-air anomalies (see Appendix).

3.2.2 *Elastic thickness*

The isostatic gravity effect can be calculated assuming a local compensation model, i.e., a crust without rigidity that is effectively floating on a denser lower mantle (Airy, 1855; Pratt, 1855). However, I assumed a complex model, according to which the crust has an elastic behavior and the lithosphere flexes in response to surface loads (Vening Meinesz, 1931; Turcotte et al., 1981). According to the Vening Meinesz theory (Vening Meinesz, 1931), isostatic compensation occurs as a regional phenomenon, so that small topographic loads do not deform the lithosphere. The lithosphere acts as an elastic shell, whose strength distributes the topographic load over a wider horizontal distance. The elastic thickness (T_e) is a parameter with which the flexural rigidity, or the strength of the lithosphere to the applied loads, is commonly expressed. According to Tesauro et al. (2012), T_e is "the thickness of an elastic layer that would respond to applied loads in the same way as the heterogeneous lithospheric plate". The greater the elastic thickness, the greater the resistance of the lithosphere, and the lower the bending (Lowrie, 2007). Following Turcotte et al. (1981), in this work I have considered a model in which the plate strength is defined in terms of flexural rigidity or elastic thickness rather than radius of regionality. To estimate the elastic thickness, I used 1-dimensional profiles oriented in different directions. For each profile, and assuming different T_e values, I compared the observed free-air gravity anomalies with the calculated free-air gravity anomalies (see also section 4.3), which are given by:

$$\mathrm{FA}=\mathrm{IE}+\mathrm{TE}+\mathrm{IA}, \tag{3.3}$$

where IE is the calculated isostatic gravity effect, TE the topography gravity effect and IA the isostatic gravity anomalies.

3.2.3 *Lithospheric deflection*

The lithospheric deflection and its gravity effect are dependent on the topography and on the crustal and mantle densities. Following the Turcotte et al. (1981) approach, the crust-mantle interface mainly depends on the crust-mantle density contrast considered. It is also implicitly assumed that the crust with density ρ_c fills the flexured region (Turcotte et al., 1981). Thus, the lithospheric deflection coefficients w_{lm}, u_{lm} can be obtained considering that the ratio between these coefficients and the topography coefficients h_{lm}, k_{lm} is:

$$\frac{w_{lm}}{h_{lm}} = \frac{u_{lm}}{k_{lm}} =$$

$$= \frac{\rho_c}{\rho_m - \rho_c}\left\{1 - \frac{3\rho_m}{(2l+1)\bar{\rho}}\right\}\left\{\frac{\sigma[l^3(l+1)^3 - 4l^2(l+1)^2] + \tau[l(l+1)-2] + l(l+1) - (1-v)}{l(l+1)-(1-v)} - \frac{3\rho_m}{(2l+1)\bar{\rho}}\right\}^{-1}, \tag{3.4}$$

where ρ_m is the mantle density, $\bar{\rho}$ is the mean density (5429 $\frac{kg}{m^3}$) and τ is the rigidity of the lithosphere if the bending resistance is neglected (Turcotte et al., 1981; Johnson et al., 2000), given by:

$$\tau = \frac{ET_e}{{R_l}^2 g(\rho_m - \rho_c)}\,. \tag{3.5}$$

where R_l is the mean radius of the lithospheric shell and σ is the resistance of the lithosphere to bending:

$$\sigma = \frac{\Upsilon}{{R_l}^4 g(\rho_m - \rho_c)} = \frac{\tau}{12(1-v^2)}\left(\frac{T_e}{R}\right)^2, \tag{3.6}$$

where Υ is the effective flexural rigidity.

3.2.4 Crust-mantle interface

Wieczorek and Phillips (1998) and Wieczorek (2015a) suggested modelling the crust-mantle interface by first performing a regularized downward continuation of the Bouguer anomalies down to an average depth and then converting it into the relief along the crust-mantle interface using an iterative approach. It follows that previous studies used such approach to provide a global crustal thickness map for Mercury (Phillips et al., 2018; Genova et al., 2019; Watters et al., 2021). However, instabilities due to the downward continuation occur, especially for continuations greater than the data sampling step (e.g., Wieczorek, 2015a; Bouman, 2000; Fedi and Florio, 2002). With this approach, an inherent instability occurs when the continuation is close to the top of intra-crustal sources. In fact, if the crust is assumed not to be homogeneous, the Bouguer gravity anomaly can no longer be continued downwards to the crust-mantle interface, because Laplace equation applies (e.g., Blakely, 1996; Fedi and Florio, 2002) only in the harmonic region, that is in a source-free volume. To address this issue, prior studies have suggested applying low-pass filtering (Wieczorek & Phillips, 1998; Phipps Morgan & Blackman, 1993). However, these approaches are limited by the arbitrary selection of a cut-off wavelength. Consequently, this study focuses on the assumption of a heterogeneous crust to distinguish between the gravitational contributions from the crust-mantle interface and intra-crustal sources. I used the previously calculated lithospheric deflection coefficients to model the crust-mantle interface (Fig. 4.38) by means of a spherical harmonic expansion, considering a mean elastic thickness of 30 km and assuming densities for crust and mantle of 2800 kg/m^3 and 3200 kg/m^3 (Genova et al., 2019), respectively.

3.2.5 Isostatic gravity anomalies

Bouguer gravity anomalies are often used to analyse crustal sources and model the crust-mantle interface in planetary studies. However, Bouguer gravity anomalies are usually associated with the exclusive contribution of the crust-mantle interface, neglecting intra-crustal density heterogeneities. Furthermore, they arise from the removal of the topographic gravity effect that is dominant with respect to free-air gravity anomalies. However, discrepancies in spatial resolution between topographic and gravity datasets, along with inaccuracies in selecting the appropriate topographic density, can lead to errors in calculating Bouguer gravity data. Thus, to study more appropriately the crustal properties and structures, it is necessary to take into account the lithospheric flexure and the isostatic compensation of the topography and to correct the Bouguer anomalies for their gravity effect. In this section, I show how to calculate isostatic anomalies (see Fig. 3.1), which are fundamental to analyse and interpret intra-crustal sources.

Isostatic gravity anomalies are obtained by removing the gravity effect caused by the lithospheric flexure to the Bouguer anomalies. In fact, neglecting the weaker contributions from mantle or deep sources, the isostatic anomalies mainly refer to intra-crustal density contrasts.

The isostatic gravity effect can be, then, modelled assuming a local compensation model (e.g., Airy compensation), or a regional compensation model (e.g., Vening-Meinesz compensation, flexural compensation).

According to the Airy compensation model (Airy, 1855), the crust without rigidity can float on a denser lower mantle. In this case the compensating crustal roots lie directly under topographic masses, and the mass deficiency of the root equals the excess load on the surface (Lowrie, 2007).

Assuming the Airy compensation model, Hirt et al. (2012) derived the topographic and isostatic gravity effect as a third-order series expansion (see Appendix).

Assuming a heterogeneous crust and a regional or flexural compensation model, the lithosphere acts as an elastic shell, distributing the topographic loads over a wide horizontal distance. The greater the elastic thickness (T_e), the greater the rigidity of the lithosphere, and the lower the flexure (Lowrie, 2007). We know that the gravity effect of the topography may be evaluated by equation 3.1. This equation can also be used to compute the isostatic gravity effect, by replacing the h_{lm}, k_{lm} coefficients of the topography in equation 3.2 with the lithospheric deflection coefficients of the crust-mantle interface w_{lm}, u_{lm}. Considering equation 3.3, we can easily obtain the isostatic anomalies by removing the contribution of topography and crustal roots (isostatic gravity effect).

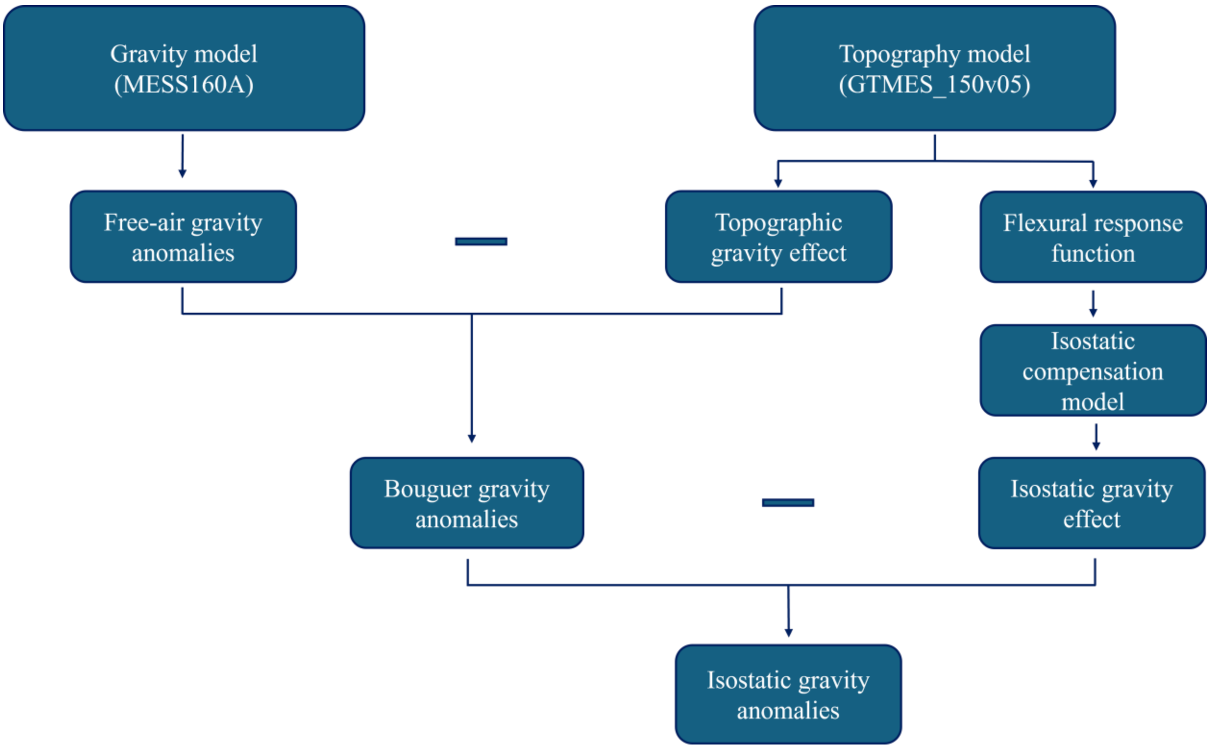

Figure 3.1. Schematic representation of the calculation of isostatic gravity anomalies, obtained as the Bouguer gravity anomalies corrected of the isostatic gravity effect, i.e., the gravity effect of the isostatic compensation. The Bouguer gravity anomalies are derived from the subtraction of the topographic gravity effect, calculated using the GTMES_150v05 model, from the free-air gravity anomalies (see section 3.2.1), calculated with a spherical harmonic expansion of the gravity field MESS160A. The topography model is also used to derive the flexural response function, which is basic to deduce which compensation model should be considered (see section 3.2.6).

3.2.6 Flexural response function

The flexural response function is useful to understand where the lithosphere flexes, as a function of the applied topographic load. According to Watts and Moore (2017), the flexural compensation, or flexural response function $\Phi(l)$, depends on the spherical harmonic degrees of the topography. This function is given by:

$$\Phi(l) = \left[1 + \frac{\Upsilon}{(\rho_m - \rho_c)g}\left(\frac{2l+1}{2R}\right)^4\right]^{-1}, \quad (3.7)$$

where ρ_c is the crustal density, ρ_m is the mantle density, R is the planet radius, and D the effective flexural rigidity which is defined as:

$$\Upsilon = \frac{ET_e^3}{12(1-v^2)}, \quad (3.8)$$

where E is the Young's modulus, v is the Poisson's ratio, T_e is the elastic thickness, g is the gravitational acceleration.

When the flexural response function curve flattens and is ~ 1, the flexural rigidity $\Upsilon \to 0$, and we may assume the local compensation Airy model. If the flexural response function tends to zero, the flexural rigidity $\Upsilon \to \infty$, and the topographic loads are considered too weak to cause isostatic compensation. In the intermediate range, topographic loads cause a lithospheric flexure, and a regional compensation model (flexural model) can be assumed (Watts and Moore, 2017). In table 2, I provide the parameters used to calculate the flexural response function for Mercury.

Table 2. Mercury's parameters used in this work.

Parameter	Value	Reference
Crustal density, r_c	2800 kg/m^3	Genova et al. (2019)
Mantle density, r_m	3200 kg/m^3	Genova et al. (2019)
Planetary radius, R	2439.4 km	NASA Fact Sheet
Young's modulus, E	100 GPa	Johnson et al. (2000); Dombard & Hauck (2008); Hauck et al. (2004)
Poisson's ratio, n	0.25	Johnson et al. (2000); Hauck et al. (2004); Klimczak et al. (2013)
Elastic thickness, T_e	30 km	Buoninfante et al. (2023)
Crustal thickness, T_c	35 km	Padovan et al. (2015); Buoninfante et al. (2023)
Gravitational acceleration, g	3.70 m/s^2	NASA Fact Sheet

3.2.7 Heat flux

Assuming a linear temperature gradient, the heat flux q can be calculated using the Fourier's law of heat conduction (e.g., Goossens et al., 2022; Turcotte & Schubert, 2002):

$$q = \kappa \frac{T_{base} - T_{surf}}{T_e}, \tag{3.9}$$

where κ is the coefficient of thermal conductivity, T_{base} is the temperature at the base of the lithosphere and T_{surf} the surface temperature.

4. Results

In this chapter, I will report the results obtained from my thesis work. I will first illustrate the complete geological map and the structural setting of Michelangelo quadrangle, which represents the core of this work, and of the Beethoven basin partially contained in H12. The geological mapping has highlighted the strong influence of impact basins and geochemical terrains in the arrangement of tectonic structures and the frequent interaction of faults with volcanic and volatile-driven processes, especially in peak-ring basins (e.g., Praxiteles basin). I will then show a globally valid model that can explain the formation of faults bordering impact basins and examples of volcanic activity or hollow fields that could have been affected or supported by faults.

Consequently, I have globally interpreted intra-crustal gravity sources and applied boundary analysis techniques to show the relationship of possible shallow or deep crustal structures interacting with tectonic structures mapped at the surface. In this work I will show the results obtained for both Michelangelo quadrangle and Victoria quadrangle, which is characterized by a better data resolution.

Finally, I will illustrate the estimates of some peak-ring sizes Mercury's basins and Beethoven basin, obtained from the analysis of Bouguer gravity anomaly and crustal thickness data, appropriately tested on certain lunar peak-ring and multi-ring basins.

4.1 Geological map of the Michelangelo quadrangle

This section reports and partly expands the paper Buoninfante et al., in review in Journal of Maps.

The Michelangelo quadrangle appears as a densely cratered quadrangle, mainly dominated by intermediate plains and by c2 crater materials. The intermediate plains can be usually found inside large ancient basins, interpreted as post-impact infilling by effusive volcanism, and degraded by later small impacts and by their ejecta materials. Clear examples can be seen in Dostoevskij crater (44.7°S-181.9°E), Vincente-Yakovlev basin (52.6°S-197.9°E, Orgel et al., 2020) and the b2 basin (38.9°S-258.6°E, Orgel et al., 2020). The Michelangelo crater and the Beethoven basin are characterized by smooth plains units covering the basin floors. Smooth and intermediate plains in H12 are frequently affected by wrinkle ridges with various orientations. The quadrangle is also characterized by the significant presence of younger craters with well-preserved materials (c3). Intercrater plains represent the second most extensive terrain within H12, while smooth plains are mainly confined to some crater interiors, and to some patches interpreted as fluidized ejecta deposits (see also Denevi et al., 2013). Based on the Enhanced color basemap, I identified a dark blue terrain in the western side (180-200°E), and bright reddish and yellow terrains covering almost all the rest of the quadrangle.

The map in figure 4.1 represents the geological interpretation at 1:3 million scale of the Michelangelo quadrangle. I produced the map in A0 size (841 x 1189mm), in a consistent way with all the other maps of the Mercury quadrangles already published at the 1:3 million scale (Galluzzi et al., 2016; Mancinelli et al., 2016; Guzzetta et al., 2017; Wright et al., 2019; Pegg et al., 2021a; Giacomini et al., 2022; Malliband et al., 2023; Man et al., 2023b). The main geological map is set to transparency on the MDIS map projected Basemap Reduced Data Record (BDR; ~166 m/pixel). I used a Lambert conformal conic projection since the quadrangle is located at mid-southern latitudes. A Lambert conformal conic 1:3 million scalebar is added to show what is the actual projection distortion in km as a function of latitude. The main map symbology for contacts, geologic units, linear features, and surface features is based on the symbology defined by the United States Geological Survey (USGS) Federal Geographic Data Committee (FGDC; https://ngmdb usgs.gov/fgdc_gds /geolsymstd/download.php). The main map is accompanied by a map key which describes in detail the symbology used. I have added a figure of the Mercury MESSENGER MDIS Global Color Mosaic (MDR; ~665 m/pixel) in orthographic projection centered on the meridian passing through the center of the Michelangelo quadrangle (225°E), to show the location of H12. Michelangelo edges are highlighted in yellow. This is accompanied by another global map outlining all of Mercury's quadrangles, in equirectangular projection. The Michelangelo quadrangle is highlighted with a yellow background to focus on its location relative to the other quadrangles. Finally, a scheme on the correlation of the mapped geological units and their respective ages is presented, allowing readers to also better understand their stratigraphic relationships.

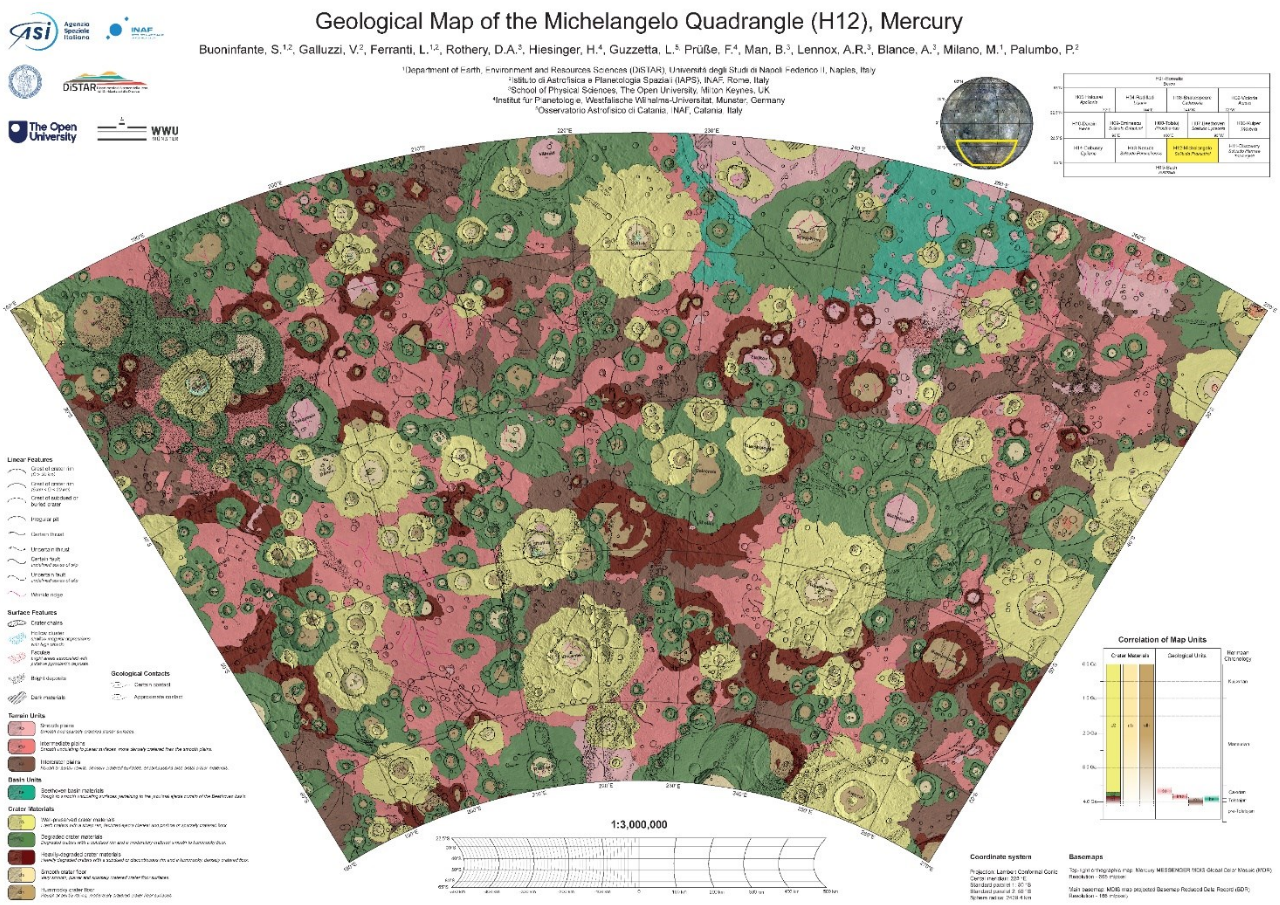

Figure 4.1. Geological map of Michelangelo (H12) of Mercury, at 1:3 million scale (from Buoninfante et al., in review). Map in Lambert conformal conic projection.

4.1.1 Geological contacts

The geological contacts define the boundaries between the geological units, based on morphological, textural, color, and crater density differences. In this work we subdivided contacts into (a) certain, where there was a clear and sharp contrast between terrain textures or morphologies and (b) approximate, where there was an uncertain, unclear or a gradational transition between terrains.

4.1.2 Linear features

Linear features include crater rims, tectonic structures and irregular pits. Crater rims are subdivided into (a) 'small' (≥ 5 km and < 20 km in diameter), (b) 'large' (≥ 20 km in diameter) and (c) 'subdued or buried' (≥ 20 km in diameter). 'Subdued or buried' crater rims refer to craters heavily degraded or covered by other units, but whose rim is still morphologically visible.

Tectonic structures include thrusts and faults with uncertain sense of slip. These structures are related to morphological features known as lobate scarps and high-relief ridges. We mapped separately the wrinkle ridges, which are commonly found in smooth plains or intermediate plains and are interpreted as the surface expression of fault-propagation folds (see Byrne et al., 2018; Klimczak et al., 2019). Fault types are subdivided into: (a) certain, if the faults are very clear and recognizable, and (b) uncertain, if they are inferred or difficult to identify.

Finally, we mapped rims of irregular pits, which are commonly interpreted as the vents formed after explosive eruptions (Jozwiak et al., 2018; Pegg et al., 2021b; Rothery et al., 2014; Thomas et al., 2014a).

4.1.3 Surface features

Surface features include secondary crater chains (or *catenae*), *faculae*, hollow clusters, bright and dark deposits.

Secondary craters are craters formed by ejecta from larger craters, which can be arranged radially from the crater center, as chains or clusters.

Faculae are very bright features, spectrally red and with diffuse margins. They are thought to represent pyroclastic deposits emplaced by explosive volcanism (Gillis-Davis et al., 2009; Kerber et al., 2011; Pegg et al., 2021b; Thomas et al., 2014a).

Hollows are peculiar features characterized by flat-floored irregular and rimless depressions, surrounded by high-reflectance material, probably caused by volatile loss (Blewett et al., 2011; Thomas et al., 2014b; Wang et al., 2020), and usually occurring in clusters.

Bright deposits mainly correspond to the ejecta rays of freshest craters. Dark deposits identified in H12 may indicate proximal ejecta enriched in low-reflectance material (e.g., Bashō crater; Klima et al., 2018) and exposure of excavated LRM-rich material (e.g., Sibelius crater; Canale et al., 2024).

4.1.4 Geological units

4.1.4.1 Plains units

We recognized and mapped three different plains in H12: smooth, intermediate and intercrater plains, from younger to older respectively.

Smooth plains (sp) are defined as flat or sparsely cratered surfaces with a smooth texture (Strom et al., 1975; Trask & Guest, 1975; Spudis & Guest, 1988) and they may encompass well recognizable ghost craters (see Head et al., 2008; Klimczak et al., 2012). In H12 smooth plains are uncommon and mostly confined to impact basins and craters or formed as patches of ejecta (Figs. 4.2a-b). Clear examples of smooth plains inside H12 can be found inside the Michelangelo crater (44.9°S-250.3°E), Takayoshi crater (37.2°S-196.2°E) and the Beethoven basin (20.9°S-235.8°E). Patches of smooth plains were mainly detected in the proximal ejecta of the Beethoven basin. Based on the Enhanced color basemap observations, smooth plains in the H12 quadrangle seem to be characterized by consistent reflectance characteristics, implying compositional homogeneity. Wrinkle ridges can be frequently identified inside smooth plains. At the planet scale, most smooth plains are interpreted as the result of effusive volcanism that affected Mercury during the Calorian (~3.8–3.5 Ga; Byrne et al., 2016; Denevi et al., 2013; Ostrach et al., 2015). Within ancient craters and basins, these units represent the most recent effusive event, as later impact craters on the floor of these basins embayed or covered by the infilling lavas. Patches of smooth plains identified in the proximal ejecta of craters or basins are interpreted as ponds of impact melt (see also Wright et al., 2019).

The intermediate plains (imp) are plains with characteristics intermediate between intercrater and smooth plains. They are represented by smooth undulating to planar surfaces and are more cratered than smooth plains, but less cratered than the intercrater plains (Spudis & Prosser, 1984). This unit is characterized by smooth to hummocky terrain, overprinted by sharp to degraded crater rims. The intermediate plains represent the most widespread unit in H12. In many cases intermediate plains cover the floor of large ancient basins, and were probably formed by later infilling, then, degraded by younger impacts (Figs. 4.2c-d). The transition between intermediate and intercrater plains is usually subdued and of gradational nature. The identification of wrinkle ridges was useful as a distinction, because intermediate plains may be characterized by the presence of these structures, even if not so commonly as in smooth plains (e.g., Galluzzi et al., 2016). Intermediate plains may include embayed craters, which is a key characteristic of units younger than intercrater plains. The imp unit shows spectral characteristics very similar to the intercrater plains in H12 and tend to correspond with darker areas observed in the Enhanced color basemap mainly in the western sector of the quadrangle. In some mapped quadrangles, imp is interpreted as a thin layer of smooth plains covering intercrater plains thus preserving the underlying roughness (Wright et al., 2019). However, since in our work we also consider the stratigraphic interpretation of the geological units, intermediate plains are mapped where these are thought to be a defined unit of intermediate age and intermediate texture between smooth plains and intercrater plains. Areas texturally consistent with imp, but with superposing crater density lower than average imp crater density, are considered as thin layer of sp and thus mapped as such by sticking to stratigraphic laws. Instead, where crater density cannot be easily assessed because of morphological uncertainties, the unit is mapped as imp.

The intercrater plains (icp) are densely cratered surfaces, considered as the most widespread unit on Mercury (e.g., Kinczyk et al., 2018; Trask & Guest, 1975; Whitten et al., 2014). The texture is rough and hummocky, previously described by Trask & Guest (1975) as "level to gently rolling ground between and around large craters and basins". They are globally characterized by isostatic gravity anomaly lows (see Buoninfante et al., 2023). A pre-Tolstojan to Tolstojan age (4.5-3.9 Ga; Whitten et al., 2014) is assigned to this unit, which is considered as the oldest surface on Mercury. In H12 icp represent the second most widespread unit (Figs. 4.2e-f). The intercrater plains can be superposed by all three crater classes (c1-c3), and frequently by degraded secondary impact craters (Whitten et al., 2014). They lack distinct spectral characteristics and specific colors. These plains may have a volcanic origin, although heavily degraded and reworked by later impacts (Marchi et al., 2013; Whitten et al., 2014).

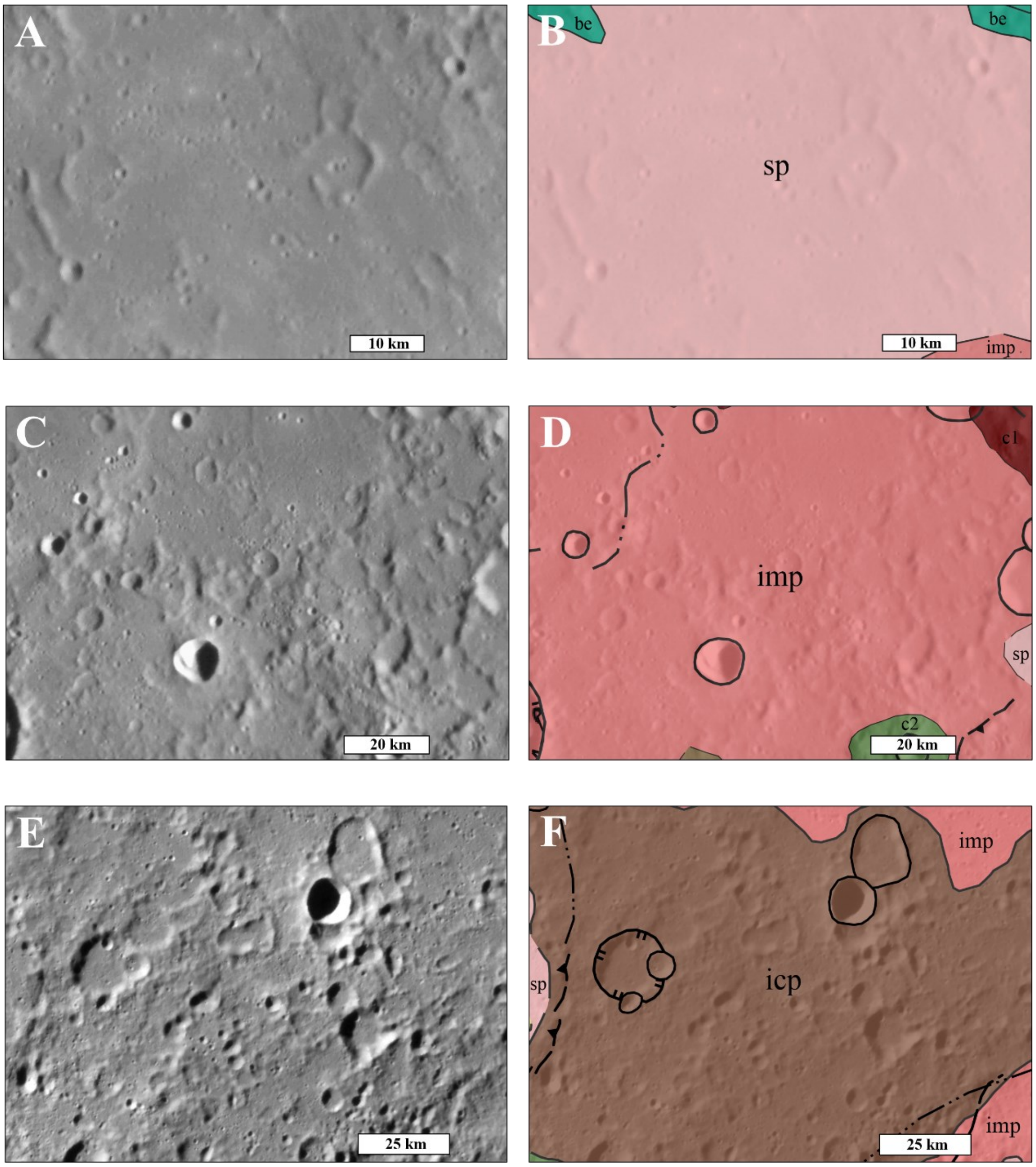

Figure 4.2. Examples of plains units (BDR mosaic basemap on the left side and the geological interpretation on the right side): A), B): smooth plains (sp); C), D): intermediate plains (imp); E), F): intercrater plains (icp).

4.1.4.2 Crater materials units

According to the three degradation-class system we identified three classes of crater materials (Fig. 4.3): fresh craters (c3), degraded craters (c2) and heavily degraded craters (c1), from the youngest and well-preserved showing fresher morphology to the oldest and most degraded. The floors of impact craters were also mapped based on its degradation and texture as smooth crater floor (cfs) or hummocky crater floor (cfh).

Fresh craters (Figs. 4.3a-b) are craters with sharp and intact rims. When complex, they can be characterized by a well-preserved central peak or peak-ring, and by well-defined terraces and textured ejecta blankets. Contacts between the crater floor and the wall or internal structures are also well-defined. Ejecta are usually very distinct and bright, and recognizable up to one diameter, sometimes wider, from the crater rim. Evident striations, crater chains, or even rays can be locally detected, and distal ejecta are well-identified by small secondary craters.

Degraded craters (Figs. 4.3c-d) are craters that are moderately degraded, with complete or partially subdued rims, usually not sharp. In complex craters, wall terraces can be present, but not well-defined. Central peaks or peak-rings appear subdued. Ejecta can still be distinct, but often they are less than one diameter away from the rim. Also, distal ejecta are more difficult to discern.

Heavily degraded craters (Figs. 4.3e-f) are degraded craters with eroded or erased rims. These are usually larger in size and therefore likely formed as complex craters. Central peaks or peak-rings are usually degraded or absent. The contact between the crater floor and the wall or internal structures is usually approximate. Only proximal ejecta close to the rim can be discerned. These craters are often degraded by several later impacts of all sizes. They may also present ruptures of crater rims and be embayed by sp or imp.

Smooth crater floors are smooth and planar crater floors, scarcely affected by later impacts. Smooth floors may represent the original and likely young floor of fresher impact craters (c3), volcanic infilling or impact melt following the impact (e.g., Canale, 2024).

Hummocky crater floors are crater floors with rough texture or gently rolling material. In c3 or c2 craters, these materials represent crater wall debris, mass wasting deposits or the original floor. In more degraded craters, this unit represents a degraded floor caused by subsequent small impacts.

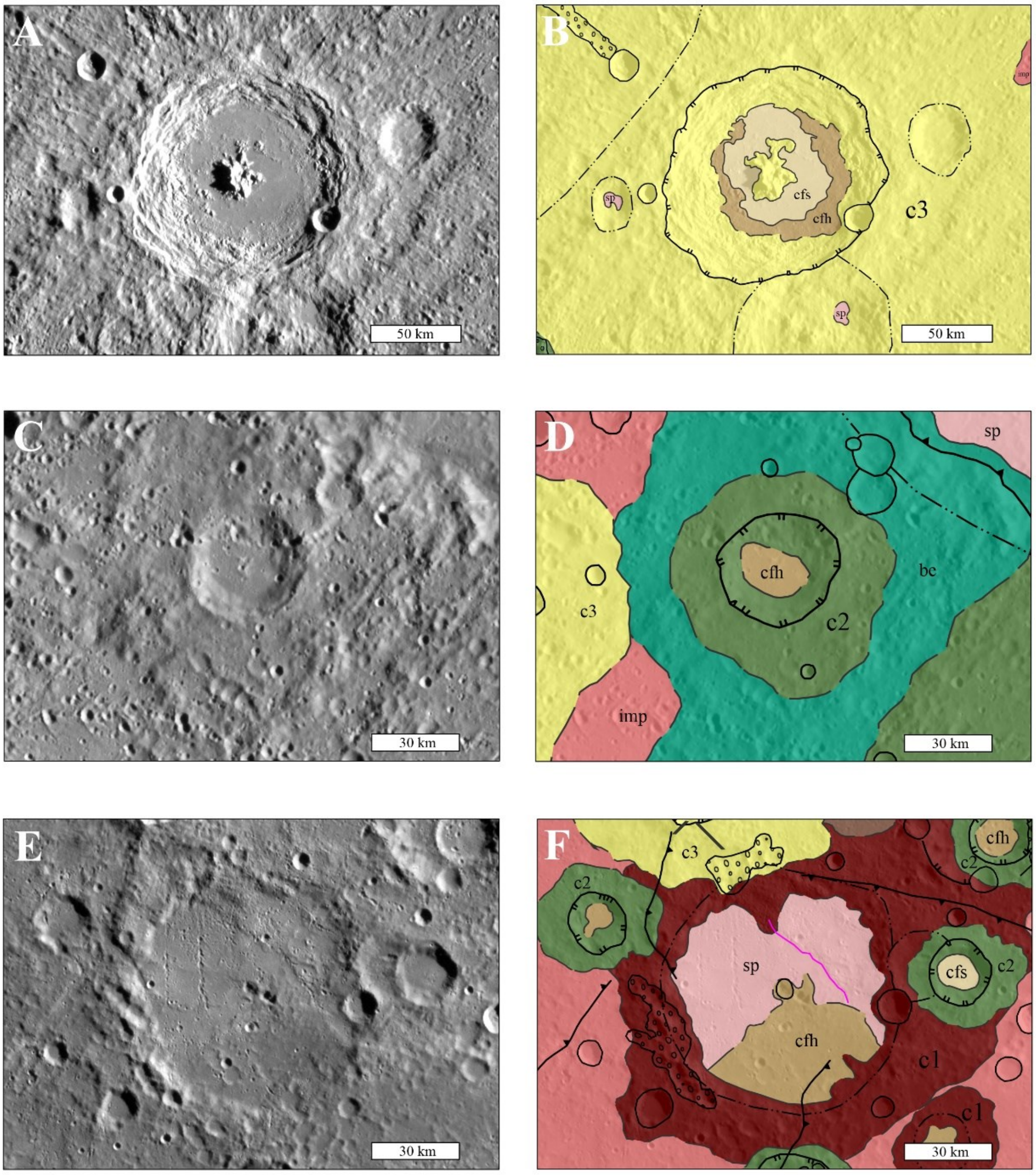

Figure 4.3. Examples of crater materials based on degradation degree (BDR mosaic basemap on the left side and the geological interpretation on the right side): fresh crater (Bartók crater; c3), degraded crater (c2), heavily degraded crater (c1) from top to bottom, respectively. Smooth crater floors are indicated as 'cfs'; hummocky crater floors are indicated as 'cfh'.

4.1.5 The Beethoven basin

The Beethoven basin (20.9°S-235.8°E; Fig. 4.4) extends between H12 and H07 quadrangles, with a diameter of ~640 km, and is thought to have a Tolstojan age (Spudis & Guest, 1988). The basin has a subdued rim (Fig. 4.5; Strom et al., 1975; Spudis & Prosser, 1984; Spudis & Guest, 1988; King & Scott, 1990). The basin floor is constituted by smooth plains materials formed by later infilling (Fig. 4.5; Spudis and Prosser, 1984; Spudis and Guest, 1988; King and Scott, 1990), with estimated age of 3.7-3.9 Ga (Massironi et al., 2009; Byrne et al., 2016). The sp unit may have buried internal rings (Spudis and Guest, 1988). Beethoven is superposed by five main c3 to c2 craters, especially Bello crater (c3, 18.9°S-239.8°E) and Sayat-Nova crater (c2, 28.0°S-237.3°E), and their respective ejecta materials. In H12, I mapped Beethoven basin ejecta as a separate geological unit (Fig. 4.6) because they have spectral characteristics slightly different to the adjacent terrains, appearing with darker colors in the Enhanced Color Basemap. This suggests that they are characterized by a different composition. The ejecta extend almost one diameter from the basin rim, but on the western side they appear almost completely covered by more recent units (intermediate plains, degraded or fresh crater materials). On the eastern side, the basin ejecta unit is superimposed by multiple patches of smooth plains, which in some cases fill subdued impact craters.

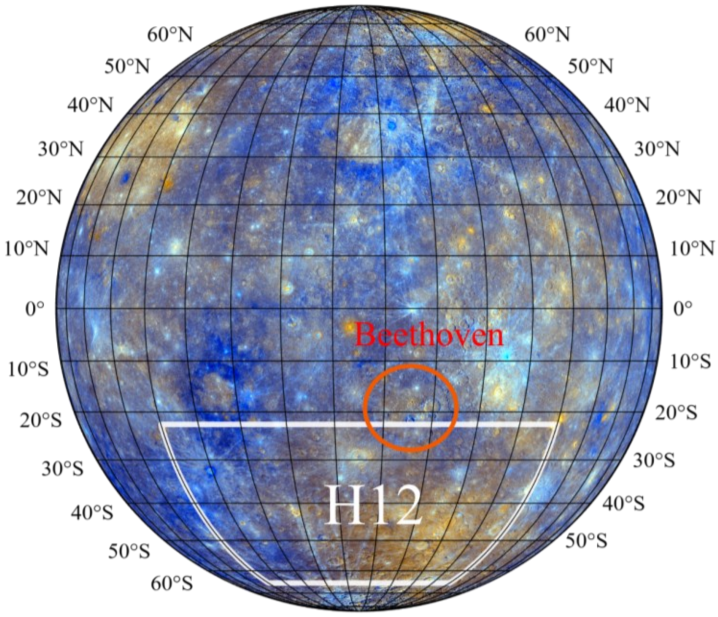

Figure 4.4. Location of H12 and Beethoven basin on the MDIS color basemap in orthographic projection, centered at 135°W.

It is noteworthy that the main tectonic structures within the basin display a concentric pattern (Fig. 4.5). *Duyfken Rupes* (20.9 °S-228.1 °E) is the main concentric thrust segment and lies close to and inside the basin rim. This structure is part of a major thrust system trending NW-SE. Important thrust segments are also identified in the southern and eastern edges of the Beethoven basin, partly or completely cutting the superposed craters, thus showing that the tectonic activity is younger than the basin and most craters. The mapped concentric faults bordering the inner depression of the basin can be interpreted as normal or oblique faults developed after the impact due to gravitational subsidence (e.g., Melosh, 1996). Wrinkle ridges inside the basin affect the sp units and developed mostly concentrically. Our mapping shows that the Beethoven basin materials must be older than the intermediate plains and c2 craters. Stratigraphic relationships confirm a probable Tolstojan-Early Calorian age for Beethoven, between 4.0 and 3.8 Ga.

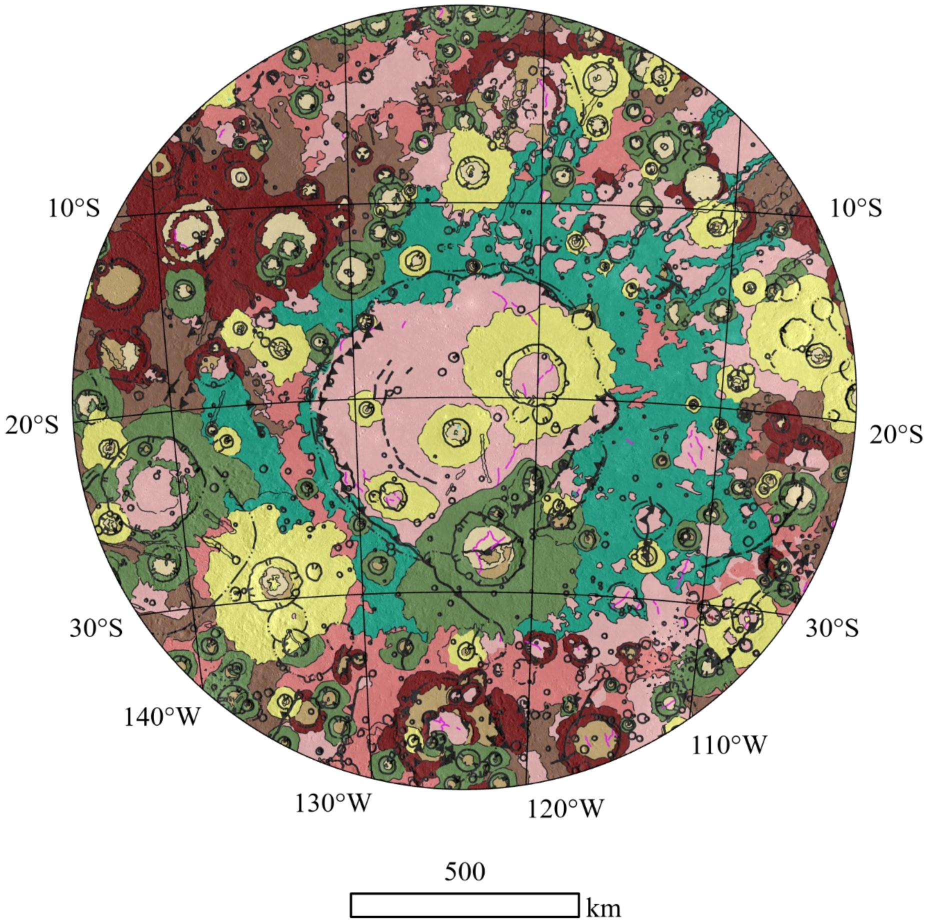

Figure 4.5. Preliminary geological map of Beethoven basin at 1:3 million scale (see also Lewang et al., 2018), in stereographic projection. See legend in Fig. 4.1.

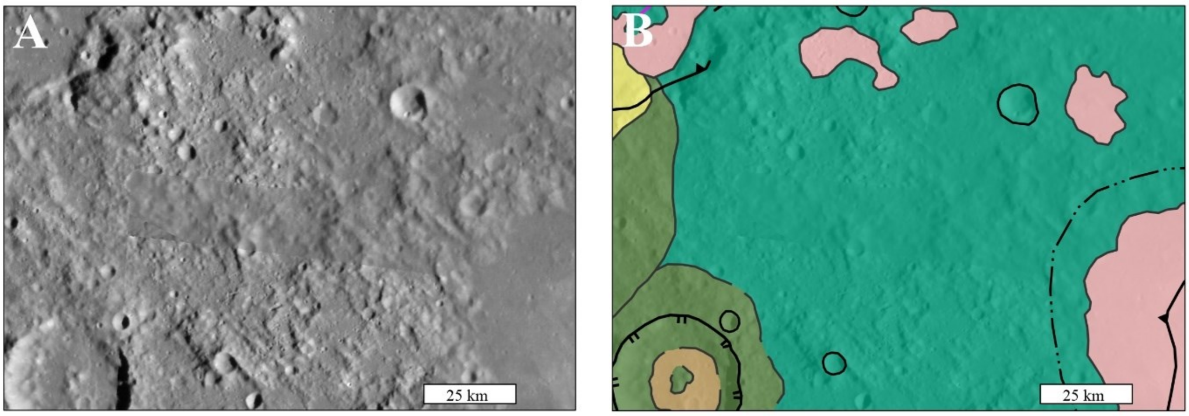

Figure 4.6. Example of Beethoven basin ejecta (Be). A) BDR mosaic; B) Interpreted geological map.

The schematic stratigraphy shown in figure 4.7 represents the correlation between H12 geological units, based on the superposition relationships observed and on previously estimated absolute model ages (Byrne et al., 2016; Giacomini et al., 2022; Marchi et al., 2013; Neukum et al., 2001; Ostrach et al., 2015; Whitten et al., 2014). A complete schematic correlation of map units is shown in figure 4.1.

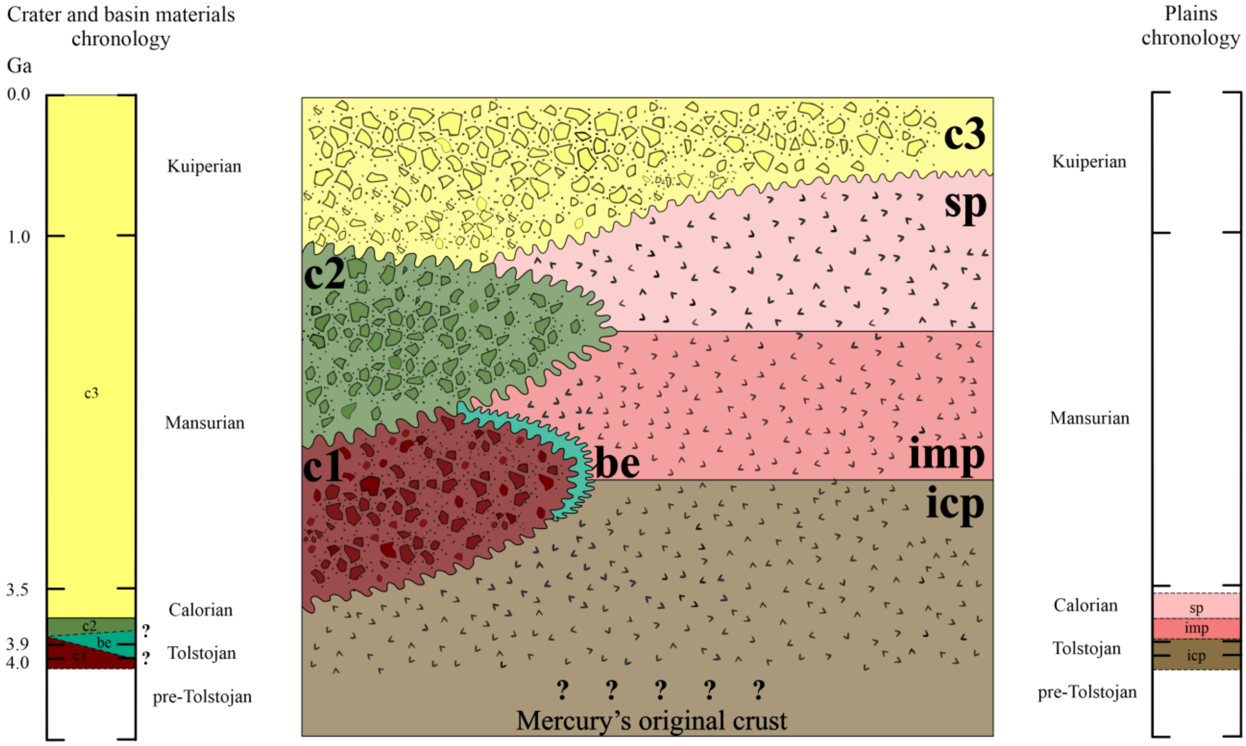

Figure 4.7. Chronostratigraphic scheme of Mercury (see also Galluzzi et al., 2016) related to plains units (icp, imp, sp; right) and crater and basin materials (be, c1, c2, c3; left). Mercury's geochronology from Spudis and Guest (1988). The stratigraphic column (not to scale) shows the correlation of H12 geological units based on superposition criteria and absolute model ages (Byrne et al., 2016; Giacomini et al., 2022; Marchi et al., 2013; Neukum et al., 2001; Ostrach et al., 2015; Whitten et al., 2014). The undulating lines represent erosional contacts. Brecciated texture is used for crater materials symbology, while arrow heads indicate plains units.

4.1.6 New rupēs and faculae in H12

Following the geological mapping of H12, I identified two new *rupees* and two *faculae* in Michelangelo quadrangle, accepted by the International Astronomical Union (IAU). The tectonic structures were named *Italica* (42.31 °S, 137.96 °W) and *Volasiga* (34.97 °S, 145.15 °W), respectively shown in figures 4.8 and 4.9. The two *faculae*, shown in figures 4.10 and 4.11, were named as *Ngu* (22.80 °S, 90.80 °W) and *Ahas* (21.33 °S, 89.41 °W).
See also https://planetarynames.wr.usgs.gov/Page/MERCURY/target.

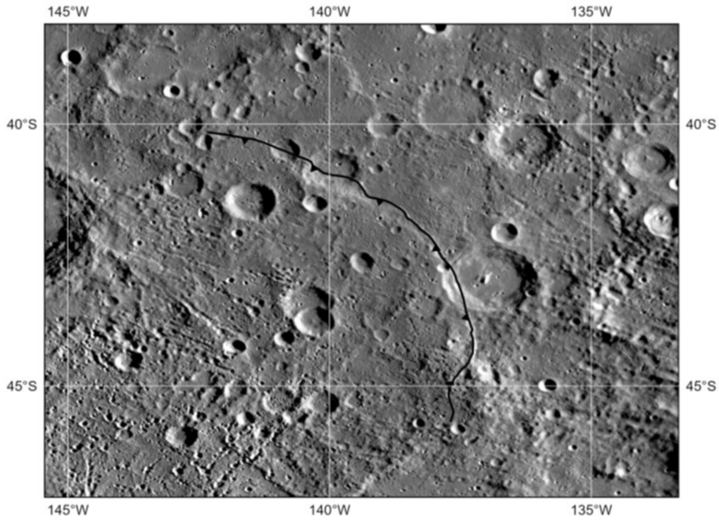

Figure 4.8. *Italica Rupes*, in equirectangular projection.

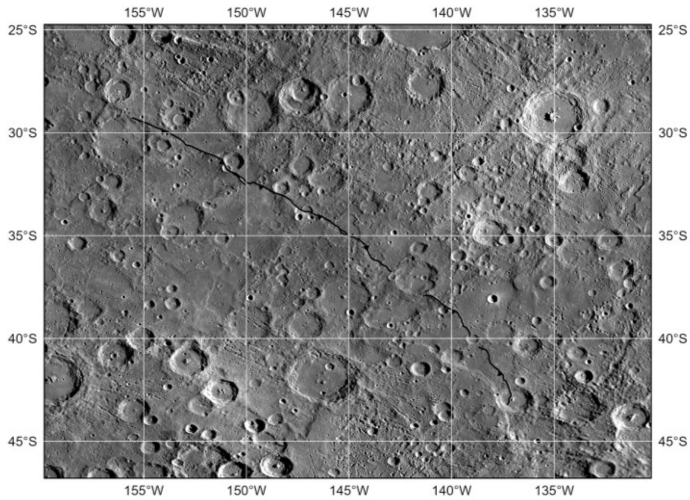

Figure 4.9. *Volasiga Rupes*, in equirectangular projection.

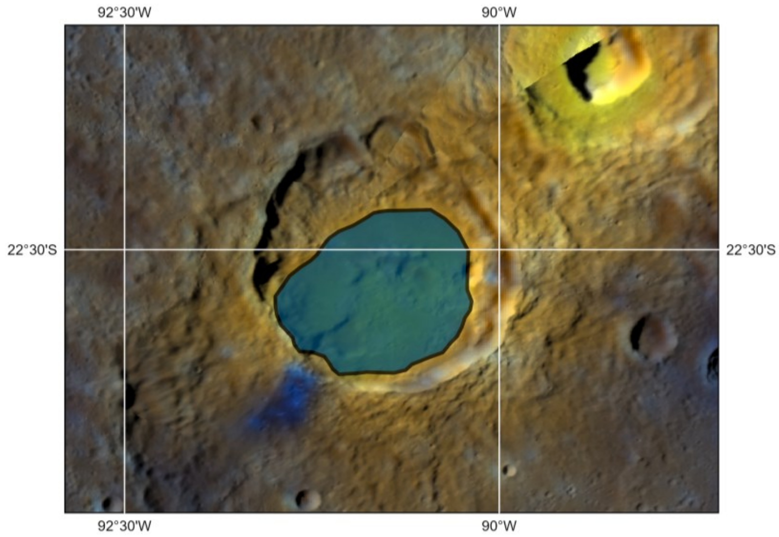

Figure 4.10. *Ngu Facula*, in equirectangular projection.

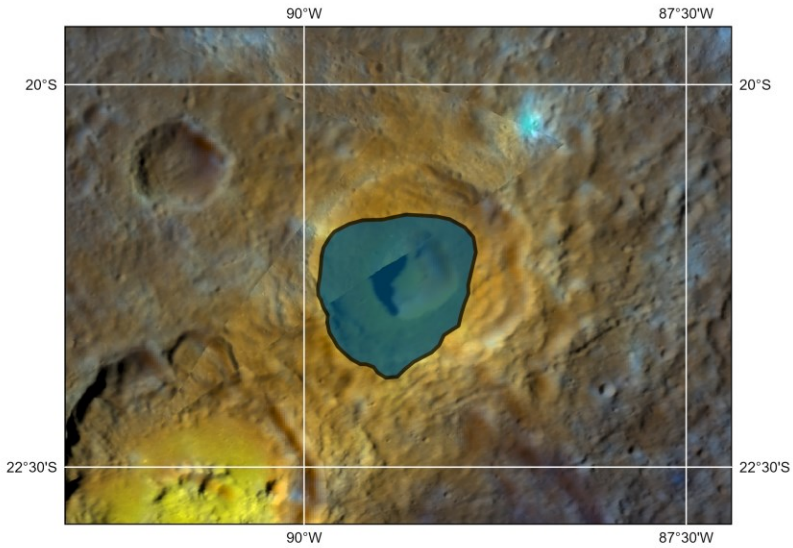

Figure 4.11. *Ahas Facula*, in equirectangular projection.

4.2 Tectonic structures and their interaction with volcanic and volatile-driven processes

4.2.1 Structural analysis of the Michelangelo quadrangle

The H12 quadrangle is characterized by two main fault trends, with NW-SE and NE-SW orientation as shown in figure 4.12. Figure 4.13 provides a comprehensive overview of the craters and basins in H12 affected by tectonic structures. Faulted craters are indicated with solid red circles, while craters or basins affected only by wrinkle ridges are shown with solid black circles. Reactivated basins with lobate scarps bordering their rim are indicated with solid orange circles. Finally, smaller craters with reactivated floors, i.e., characterized by faults cutting the crater floor and bordering the crater rim, are denoted with solid green circles. H12 is characterized by 165 faulted craters and basins, of which 131 are generic faulted craters, 20 are craters affected only by wrinkle ridges, 12 are reactivated basins, and 2 are small craters characterized by a reactivated floor.

Rose diagrams for thrusts, wrinkle ridges and normal/oblique faults, and for the reactivated faults, (Fig. 4.14) were created using GeoRose software, setting 5° trend bins. Main thrust faults trend NW-SE and NE-SW. Wrinkle ridges are more randomly oriented, although they show preferential trends NNW-SSE and NNE-SSW in H12. Reactivated faults are randomly oriented, while normal or oblique faults show a preferential NE-SW trend.

Moreover, I identified tectonic structures arranged concentrically with respect to large old basins. As already suggested by Fegan et al. (2017), some lobate scarps form concentrically to the basins as a result of reactivation of previous discontinuity planes in response to global contraction. They suggested a model where faults nucleate along the interface between the basin floor and the base of the smooth plains unit, with the shortening of the crust.

The model suggested here is, instead, based on a thick-skinned tectonic style (Fig. 4.15), involving deep thrust faults (down to 35-40 km). According to this model, tectonic structures bordering the basins are basically affected by a reactivation process due to the compressive tectonic regime of Mercury, started around 4 Ga ago (see Crane & Klimczak, 2017), which reversed the pre-existing normal faults formed after the impact and which leads to the formation of lobate scarps. This could be the case of the Beethoven basin (20.8°S-236.1°E;

Fig. 4.16) and Vincente-Yakovlev basin (52.6°S-197.9°E, Orgel et al., 2020; Fig. 4.17). In the Beethoven basin, the reactivated faults arranged concentrically and bordering the rim are represented in orange, while the thrust segment in blue is tangent to the basin and is part of the NW-SE system, which also seems to border the high-Mg region. Similarly, Vincente-Yakovlev basin, in the southwestern area of the quadrangle, is mainly characterized by evident concentric reactivation structures, also in the southern part of Vincent-Yakovlev for the presence of another smaller ancient basin.

Some evidence of thick-skinned tectonics can be provided by the presence of fault systems whose trace exceeds the basin edges. In this case, long, regional thrust systems could reactivate pre-existing tectonic structures located at the edges of the basins if they are favorably oriented. For the case of Beethoven basin, the NW-SE thrust segment is linked to the concentric structures inside the basin. However, it cannot be completely ruled out that the fault plane may continue along a horizontal plane of weakness within the basin, leading to a thin-skinned tectonic style. Further evidence can be provided by the estimated depth of faulting of some lobate scarps bordering the basins (Fig. 4.18). Watters et al. (2002) estimated a depth of faulting of 35–40 km for *Discovery Rupes*, bordering Andal-Coleridge basin (Fassett et al., 2012; Orgel et al., 2020; Szczech et al., 2024). Later, Ritzer et al. (2020) estimated a 35 km depth of faulting for *Soya Rupes*, bordering b56 basin (Fassett et al., 2012; Orgel et al., 2020; Szczech et al., 2024).

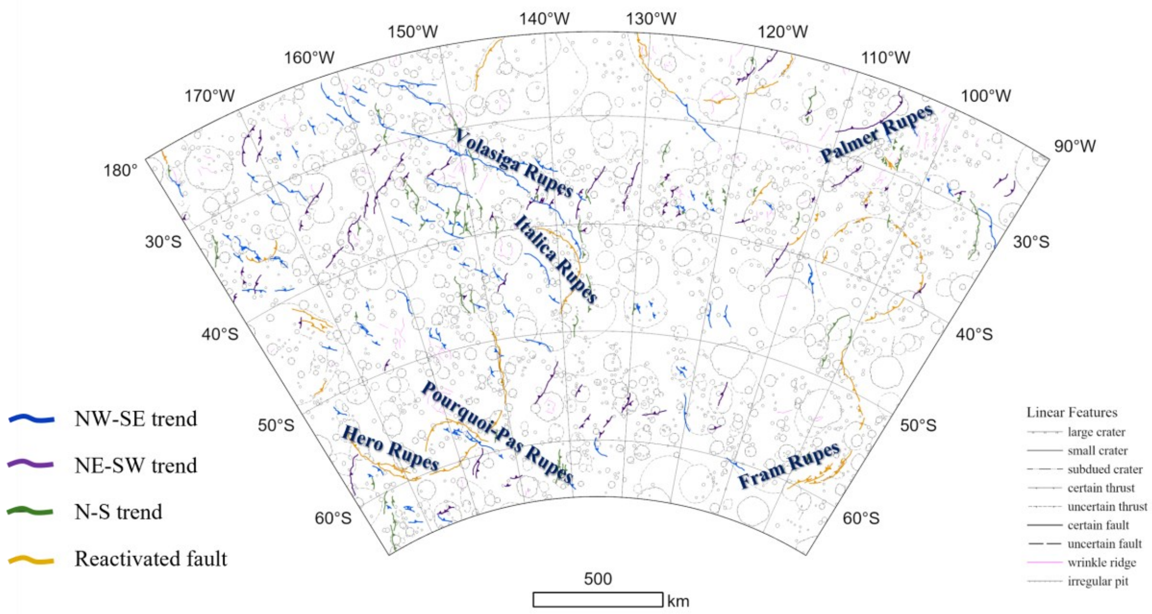

Figure 4.12. Linear features of the Michelangelo quadrangle (H12) in Lambert conformal conic projection. Blue lines indicate NW-SE fault trend; purple lines indicate NE-SW fault trend; green lines indicate N-S trend; orange lines indicate reactivated faults bordering the basins.

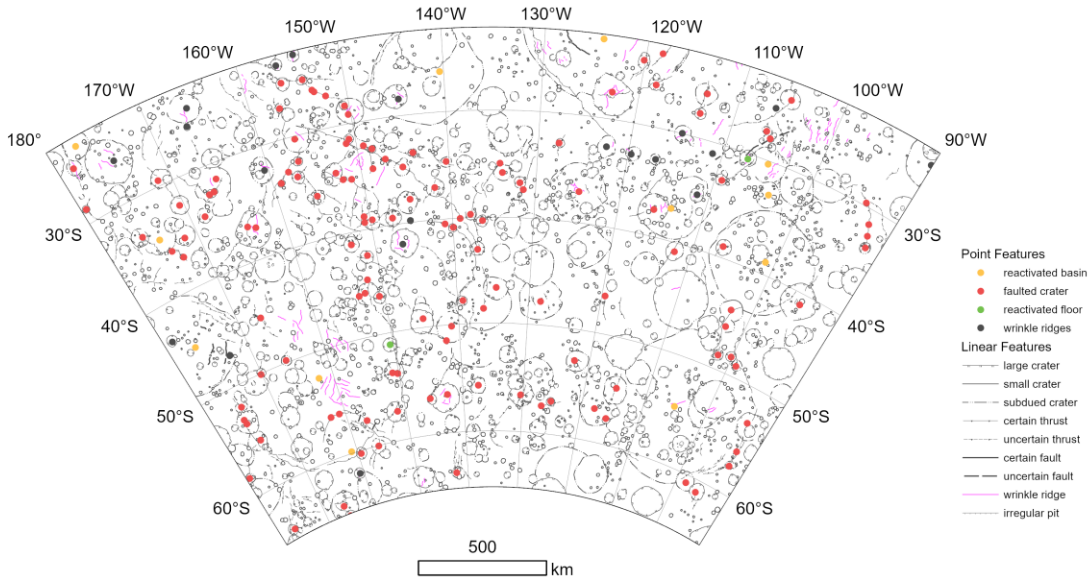

Figure 4.13. H12 point features indicating generic faulted craters (solid red circles), craters or basins affected only by wrinkle ridges (solid black circles), reactivated basins (solid orange circles), craters with reactivated floors (solid green circles), and linear features, in Lambert conformal conic projection.

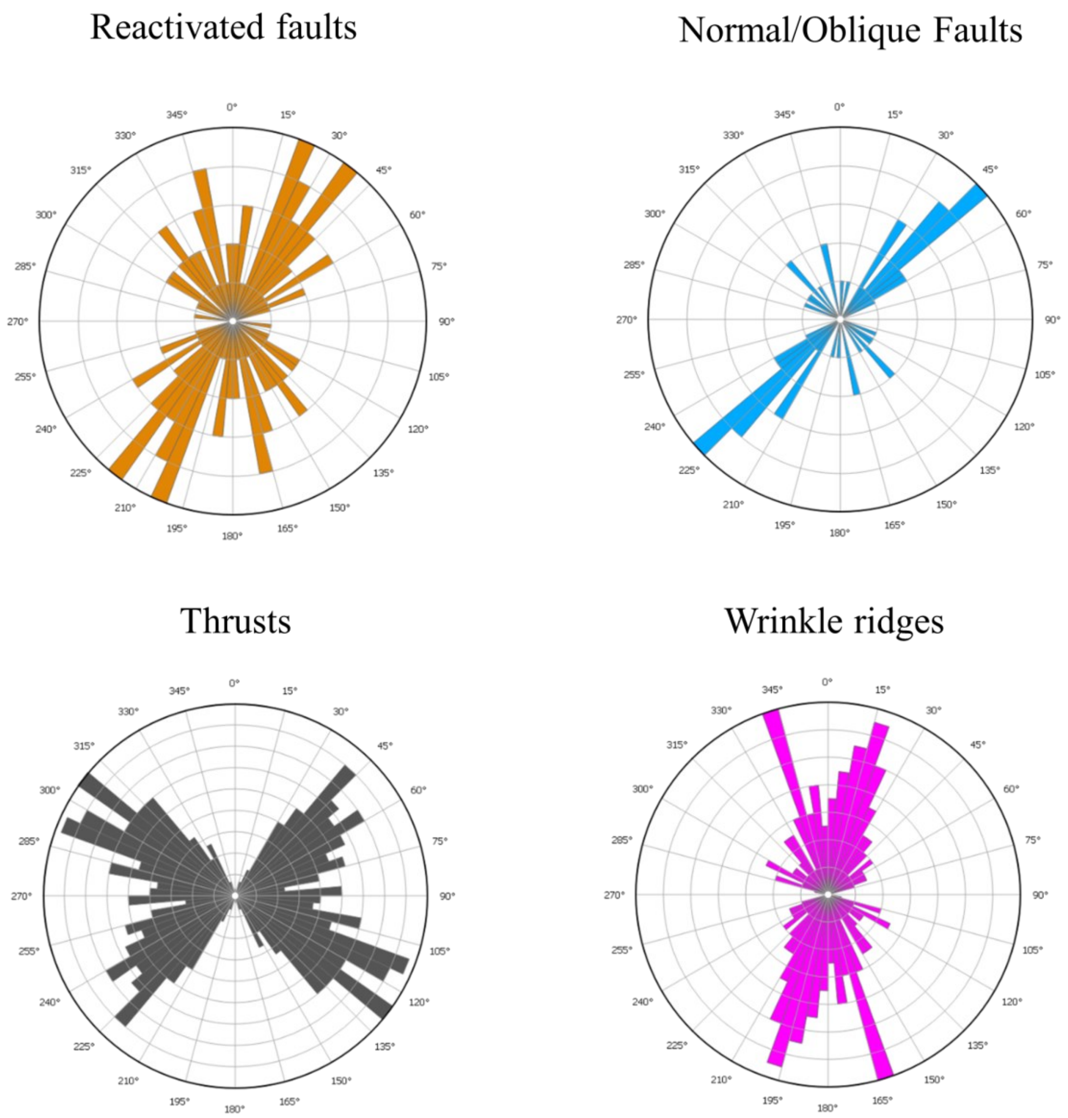

Figure 4.14. Rose diagrams for thrusts, wrinkle ridges and normal/oblique faults, and for the reactivated faults, created from GeoRose software, setting 5° trend bins.

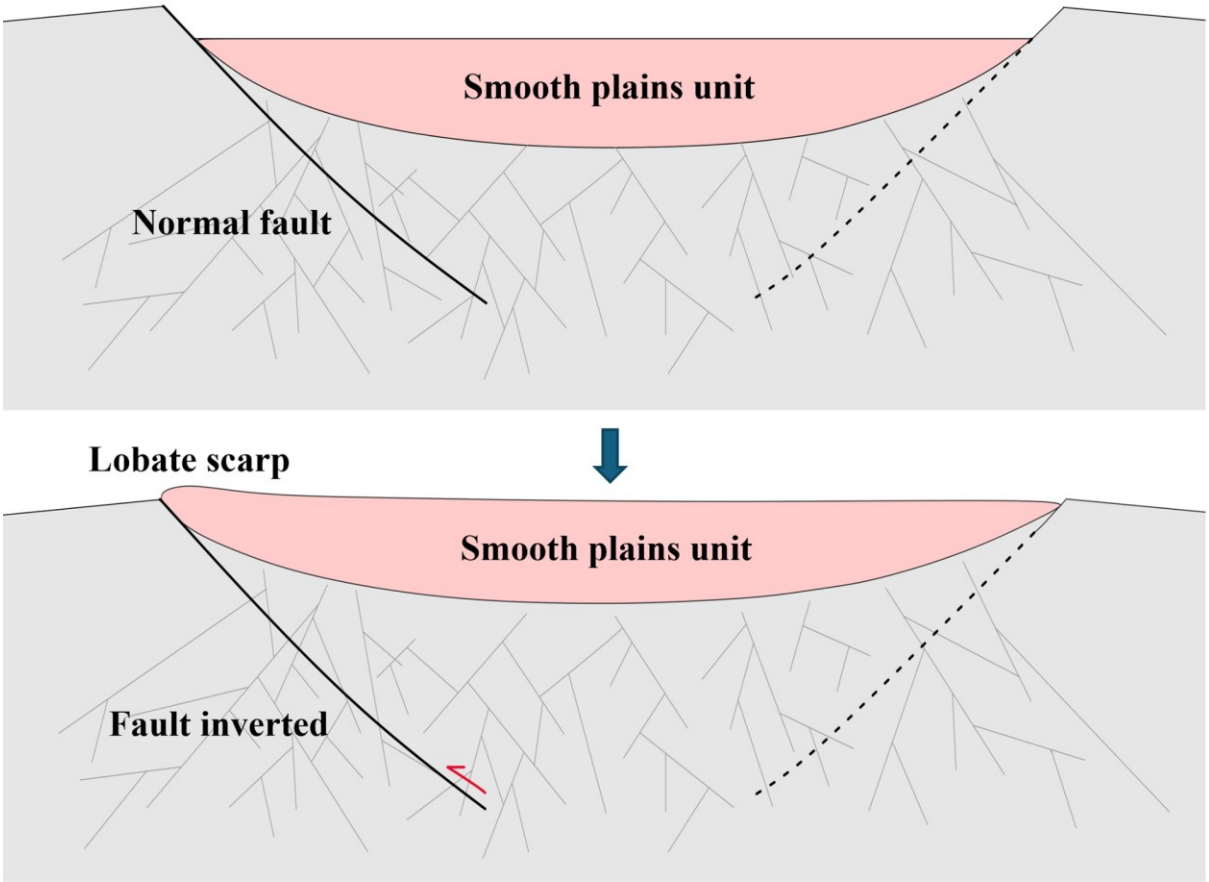

Figure 4.15. Schematic representation of the reactivation of faults bordering the old basins, as result of the contractional tectonic regime.

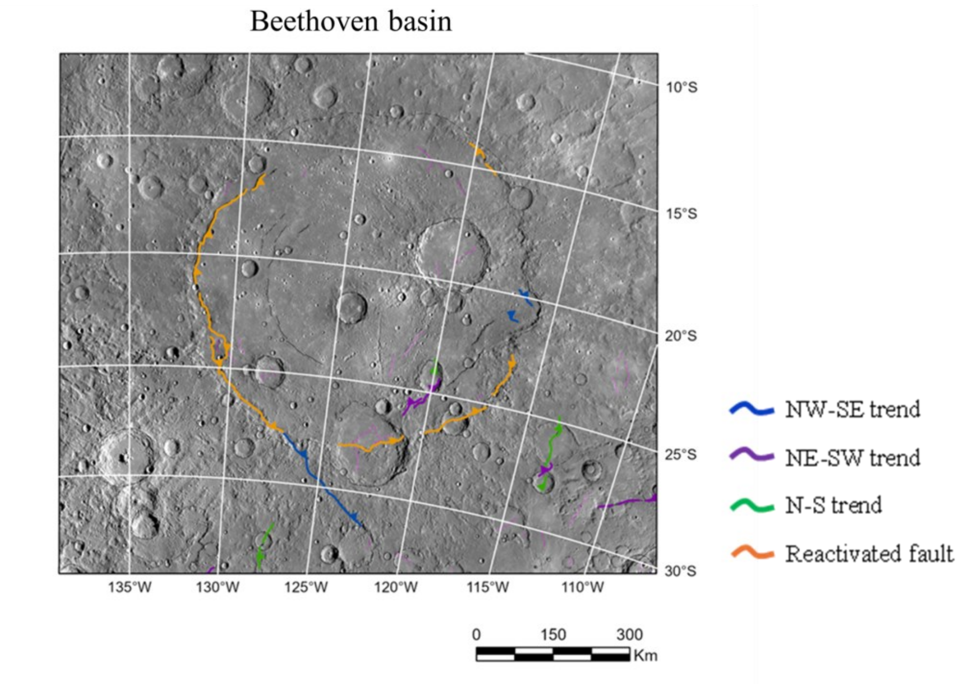

Figure 4.16. Beethoven basin seen from the MDIS BDR basemap. Orange lines represent the concentric reactivated structures. Blue line represents the tangent reactivated structures, which are also part of the NW-SE fault system. Lambert conformal conic projection.

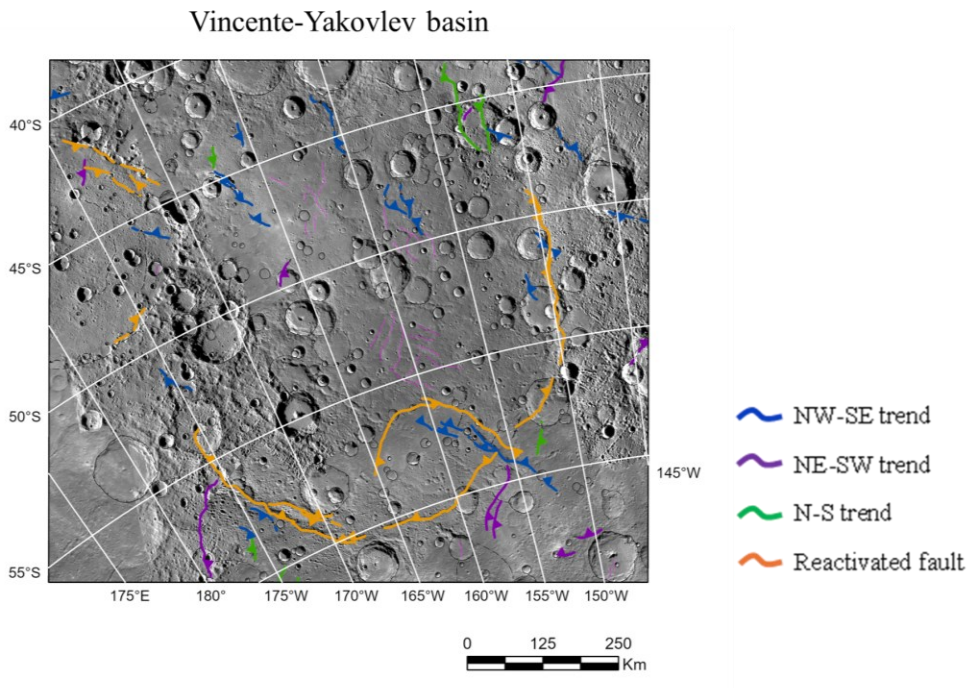

Figure 4.17. Vincente-Yakovlev basin seen from the MDIS BDR basemap. Orange lines represent the concentric reactivated structures. Lambert conformal conic projection.

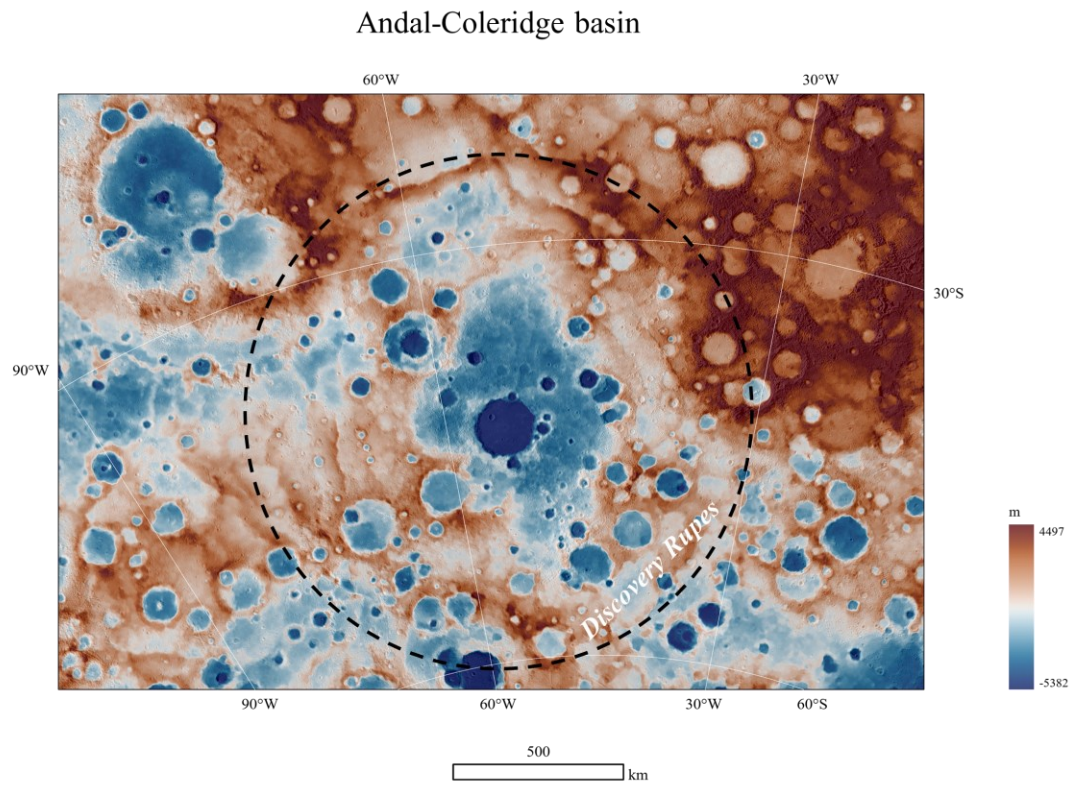

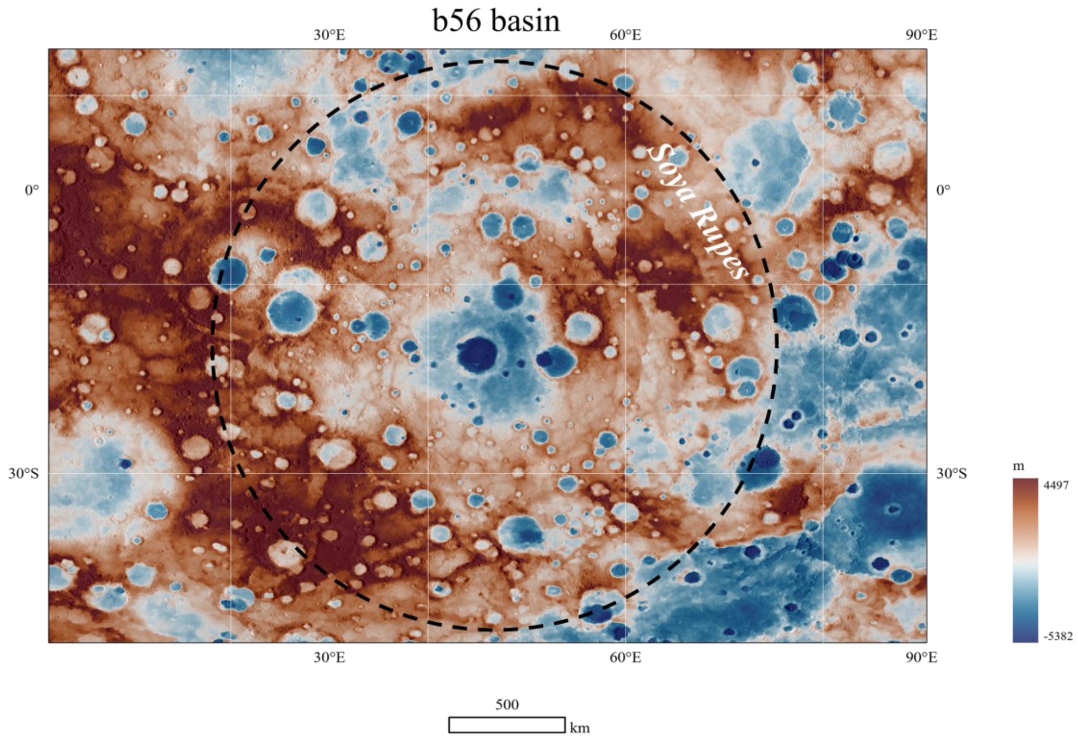

Figure 4.18. The *Discovery Rupes* (top) and *Soya Rupes* (bottom) bordering Andal-Coleridge and b56 basin rims, respectively in Lambert conformal conic projection and equirectangular projection, on the

topography map. Thrust faults have an estimated depth of ~35-40 km and likely represent thick-skinned reactivated structures.

In figure 4.19, I show all the certain and probable basins/craters affected by reactivation at their rims in Michelangelo quadrangle. Certain reactivated craters are indicated with red names, while probable ones with grey names. Crater and basin names derive from IAU nomenclature, and from Fassett et al. (2012) and Orgel et al. (2020). Unknown craters are named in this work RC1-RC17. This analysis clearly shows that fault reactivation on Mercury is common for both basins (D>100km) and impact craters (D<100km). Thrust segments that reactivate the edges of craters in H12 mainly dip inward, while smaller segments can be also characterized by outward dips (see also table 5).

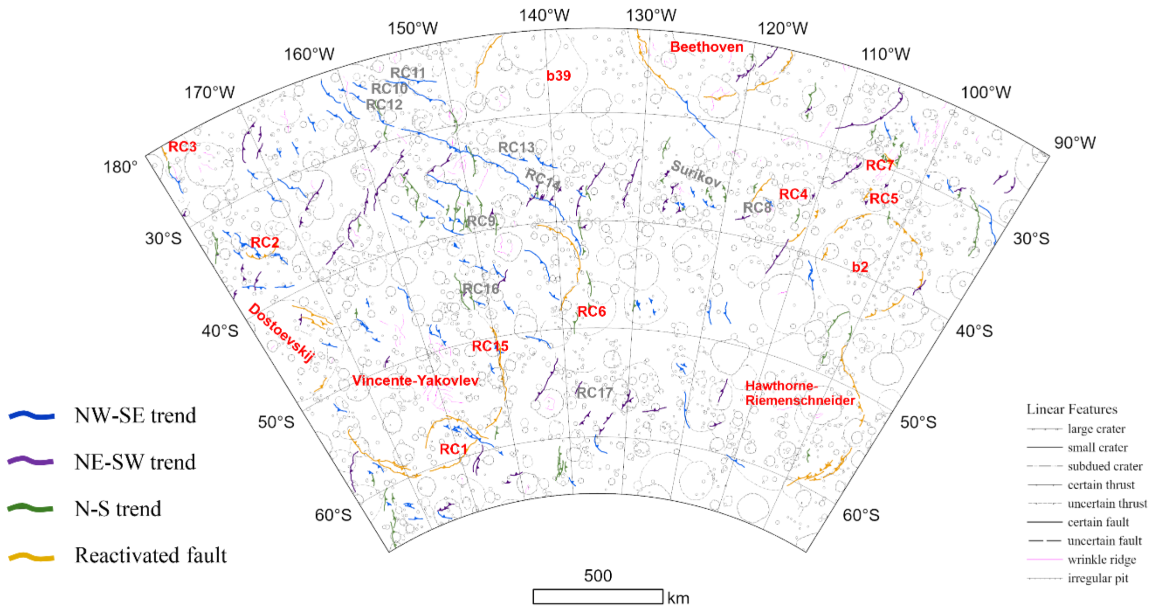

Figure 4.19. Certain (red names) and probable (grey names) craters reactivated in H12 quadrangle, in Lambert conformal conic projection.

Table 5. Certain and probable craters reactivated in H12 quadrangle.

NAME	SOURCE	LAT - LON	DIAMETER (km)	THRUST DIP	NOTES
Beethoven	IAU	20.8°S - 236.1°E	650	INWARD	Presence of thrust segment with locally outward dip; Radial thrust outside the basin
b2	Fassett et al. (2012); Orgel et al. (2020)	39°S - 258.6°E	419	INWARD	Presence of thrust segment with locally outward dip
Vincente-Yakovlev	IAU	52.6°S - 197.9°E	690	INWARD	
Dostoevskij	IAU	44.7°S - 181.9°E	454	INWARD	
Hawthorne-Riemenschneider	Fassett et al. (2012); Orgel et al. (2020)	55.9°S - 74.1°E	620	INWARD	Presence of thrust segment with locally outward dip
b39	Fassett et al. (2012); Orgel et al. (2020)	26.5°S - 218°E	435	INWARD	
Surikov	IAU	37°S - 235.1°E	227	OUTWARD	Presence of thrust segment with locally inward dip in the inner ring
RC1	/	58.5°S - 209.2°E	177	INWARD and OUTWARD	Radial thrust outside the basin
RC2	/	34.2°S - 185.8°E	138	INWARD	
RC3	/	23.2°S - 182.8°E	103	INWARD	
RC4	/	36.7°S - 246.9°E	283	INWARD	
RC5	/	32.9°S - 256°E	105	INWARD	Presence of thrust segment with locally outward dip
RC6	/	48.4°S - 223.5°E	208	INWARD	
RC7	/	30.3°S - 254.9°E	144	INWARD	Presence of thrust segment with locally west dip
RC8	/	37.3°S - 244°E	130	OUTWARD	
RC9	/	39.2°S - 210.1°E	71	OUTWARD	
RC10	/	25.1°S - 103.9°E	52	INWARD	
RC11	/	25.2°S - 205.8°E	41	INWARD	
RC12	/	27.2°S - 202.9°E	37	INWARD	
RC13	/	33.6°S - 215.9°E	34	INWARD	
RC14	/	37°S - 218.2°E	75	OUTWARD	
RC15	/	51.2°S - 209.4°E	56	INWARD	
RC16	/	46.1°S - 207.9	97	OUTWARD	
RC17	/	55.8°S - 222.5°E	67	INWARD	

Galluzzi et al. (2019) showed that the location of some thrust systems in the Victoria quadrangle (H02) is broadly correlated with the edges of the high-Mg region. Similarly, in the Michelangelo quadrangle, I mapped fault systems that appear to border this geochemical terrain. Comparing the fault systems mapped with the map of Mg/Si abundance, derived from the XRS data (X-ray spectrometer), the NW-SE system seems to coincide broadly with the southwestern edge of the high-Mg region (Fig. 4.20), although the accuracy of XRS data at these latitudes is much lower than the accuracy of data acquired in the northern hemisphere.

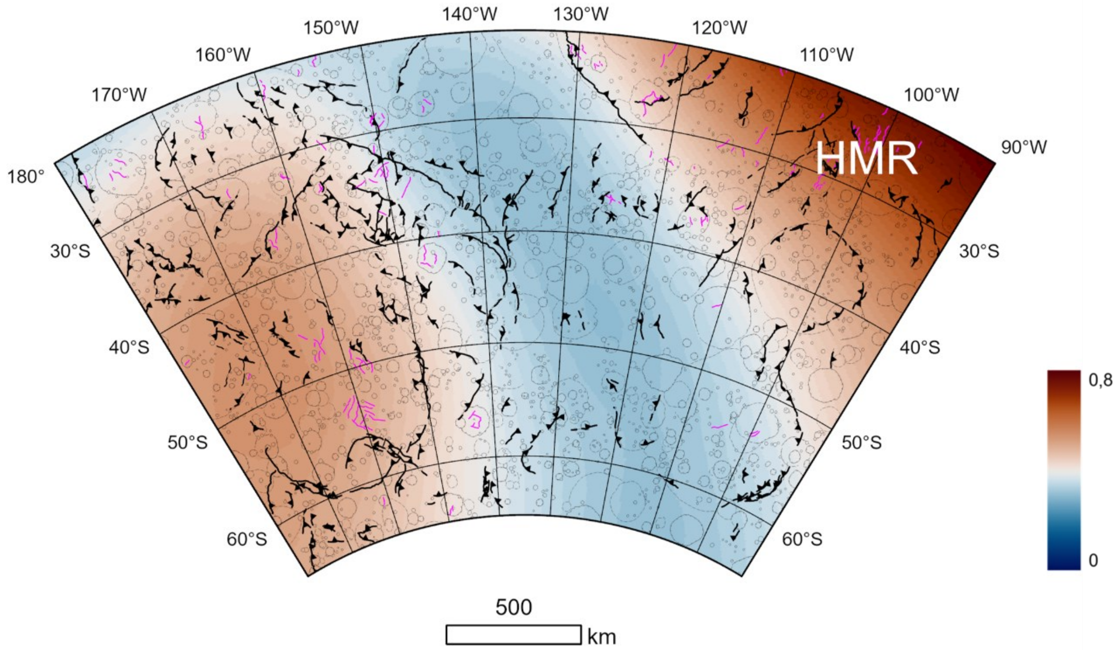

Figure 4.20. Linear features on the Mg/Si abundance map, derived from the XRS data, in Lambert conformal conic projection. Red lines represent the NW-SE system, which seems to border the southwestern edge of the high-Mg region.

4.2.2 Explosive volcanism and influence of tectonic structures

The volcanic vents on Mercury are usually associated with irregular morphological depressions. In this work, I first analysed 120 volcanic vents on Mercury (Fig. 4.21) indicated in the latest catalogues of Thomas et al. (2014b) and Galiano et al. (2022) and characterized by the best MESSENGER MASCS data coverage. I subdivided the vents into five main categories: (1) single vent, (2) compound vents, when characterized by multiple mouths, (3) cluster of simple vents, (4) vent with mound, and (5) pitted ground. By assessing the degradation stage of the vents visually from the MDIS basemaps, I further subdivided the pits as fresh, slightly degraded, degraded and heavily degraded. Similarly, I assessed the brightness of pyroclastic deposits (*faculae*) related to vents with a visual inspection from the Enhanced Color basemap. I considered four categories for the brightness: very bright, bright, slightly bright and dark deposits. The graph in figure 4.22 represents a frequency distribution for each class defined by each couple of brightness and degradation stage values, with different colors representing the identified vent types. The vents with the best MASCS coverage are mostly characterized by bright *faculae* associated with low degradation stages. But at the same time there are various fewer cases of vents characterized by bright or very bright *faculae* with a high degradation stage, as well as vents with lower brightness intensity and with a fresh morphology.

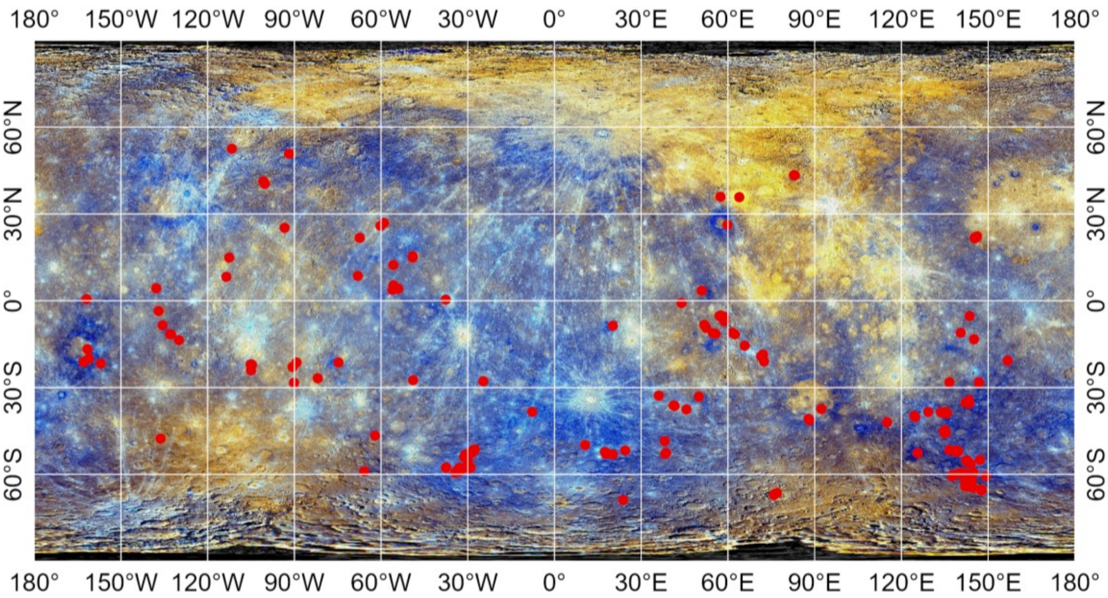

Figure 4.21. Volcanic vents in red from the catalogues of Thomas et al. (2014b) and Galiano et al. (2022). Equirectangular projection.

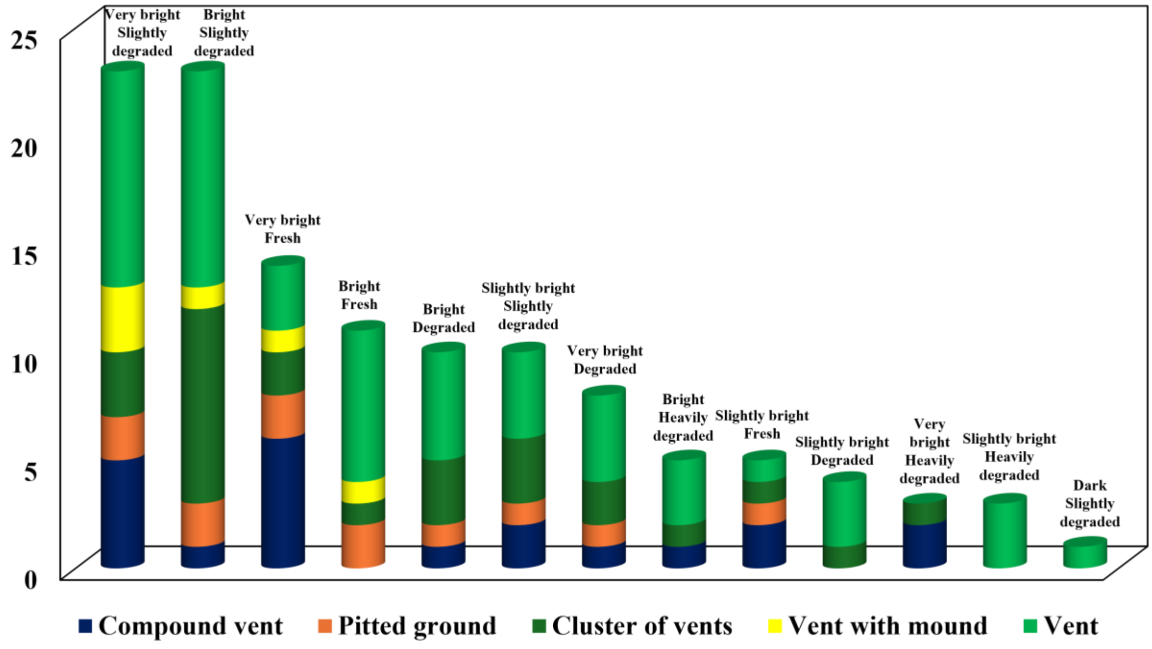

Figure 4.22. Frequency distribution for vent classes defined by each couple of brightness and degradation stage values. Colors represent the vent types (single vent, compound vents, cluster of vents, vent with mound and pitted ground).

Volcanic vents identified in the Michelangelo quadrangle are shown in figure 4.23. At a first glance, morphological pits related to volcanic activity are often found along lobate scarps (see Fig. 4.24a; see also Galluzzi et al., 2019; Jozwiak et al., 2018; Thomas et al., 2014b) or in soft-linkage zones between the thrust segments (see Fig. 4.24b), which, on Earth (see Tibaldi et al., 2009) are considered possible preferential areas for magma uprise. The presence of craters itself can represent a further weakness zone supporting the magmatic uprise. Globally, ~58% of the studied vents are linked to tectonic structures.

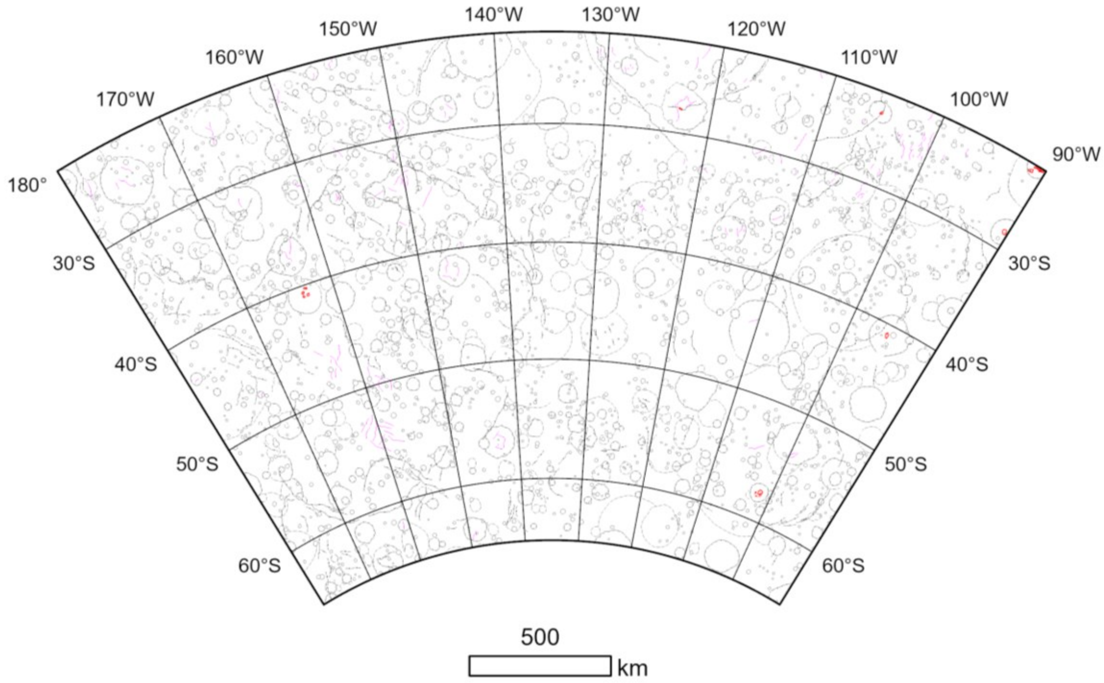

Figure 4.23. H12 Linear features and irregular pits representing probable volcanic vents highlighted in red, in Lambert conformal conic projection.

A clear example of a volcanic vent associated with a thrust fault is shown in the inner part of the Sayat-Nova crater (Fig. 4.24a), where the vent is located along the lobate scarp, suggesting that the mapped faults act as preferential pathways for the magma uprise (e.g., see also Galluzzi et al., 2019; Jozwiak et al., 2018; Thomas et al., 2014b). Another example is shown at the b2 basin rim (Fig. 4.24b), where the volcanic vent is found in the soft-linkage zone between the thrust segments bordering the basin. The crater south-east of the basin acts as a further weakness zone supporting the magma and volatiles rising. In addition, the crater can affect thrust vergence. The two thrust segments have opposite vergence: the segment inside the basin, formed by reactivation at the basin rims, verges toward NW, while outside the basin the thrust has a SE vergence. It's important to note that the thrust segment bordering Beethoven basin and the one bordering b2 basin with NW vergence may be interpreted as reactivated faults located at the edges of the basins. Thrust faults may more likely be controlled by previous normal faults located at the basin edges, as the smaller craters above the rim of the basins do not strongly affect the thrust segment orientation. This also suggests that reactivation itself can be associated with magmatic activity.

a)

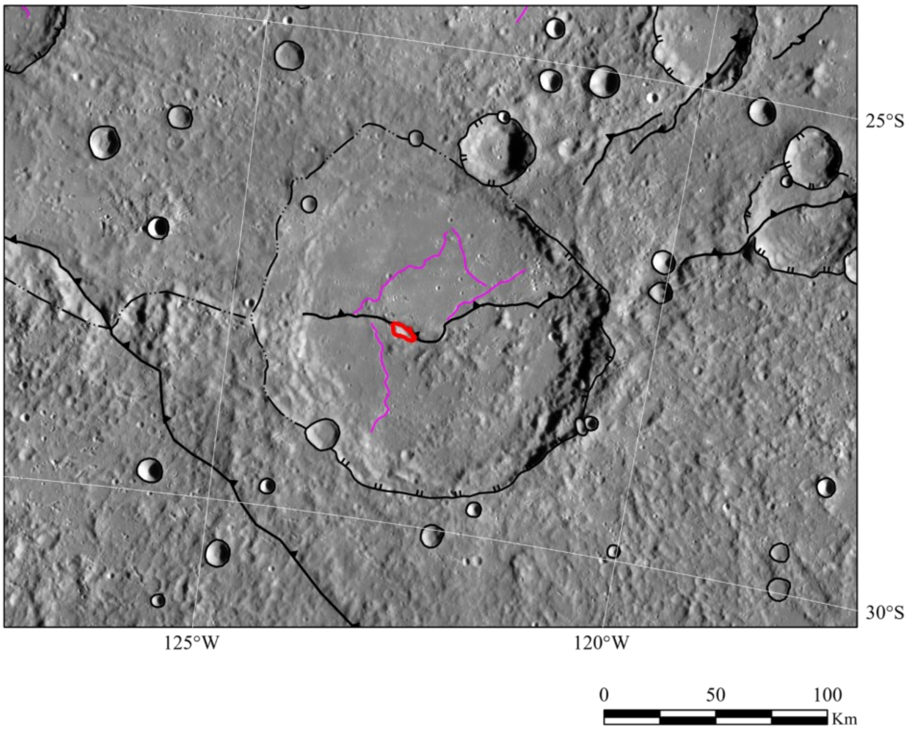

b)

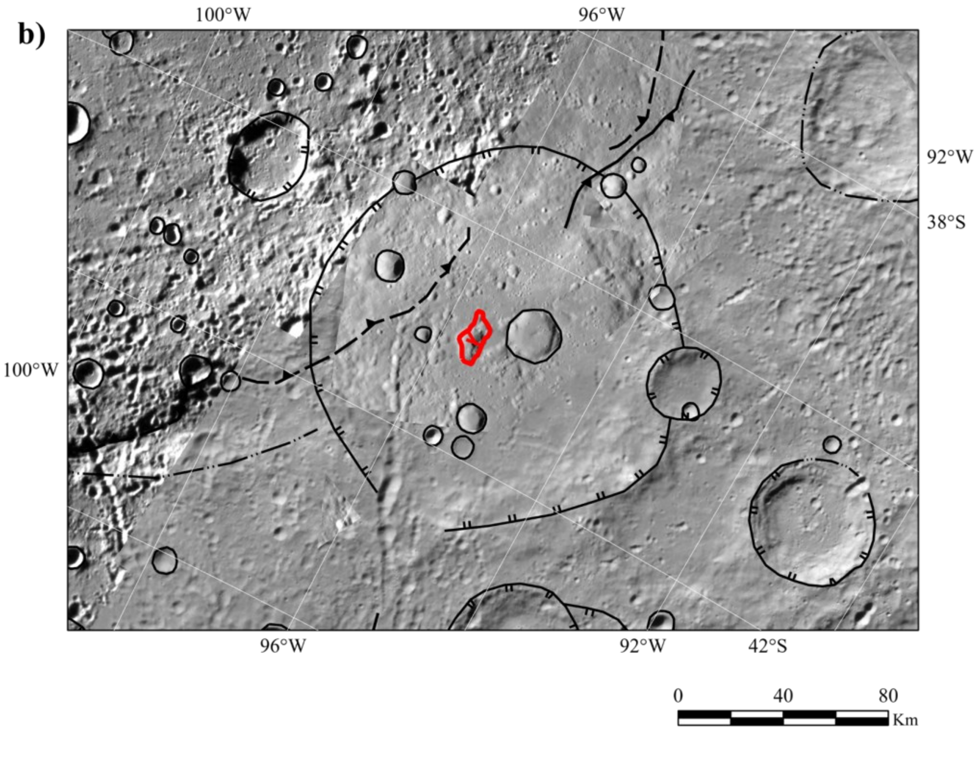

Figure 4.24. a) Volcanic vent along the thrust segment cutting the Sayat Nova crater, on the MDIS H12 BDR mosaic; **b)** Volcanic vent in the relay zone between thrust segments at the b2 basin rim, on the MDIS H12 HIW mosaic. Lambert conformal conic projection.

Other examples of interaction between volcanic vents and faults on Mercury are represented by peak-ring craters, where vents can be found close to the peak-ring. They may form preferentially along the peak-ring structure, suggesting a feasible interaction with the faults accommodating the structural uplift following the central collapse (e.g., Collins et al., 2002; Gulick et al., 2013). Some examples of peak-ring craters with volcanic vents close to peak-rings on Mercury are Scarlatti (40.7°N;-101.2°E) and Praxiteles (27.1°N;-60.3°E) craters (Fig. 4.25).

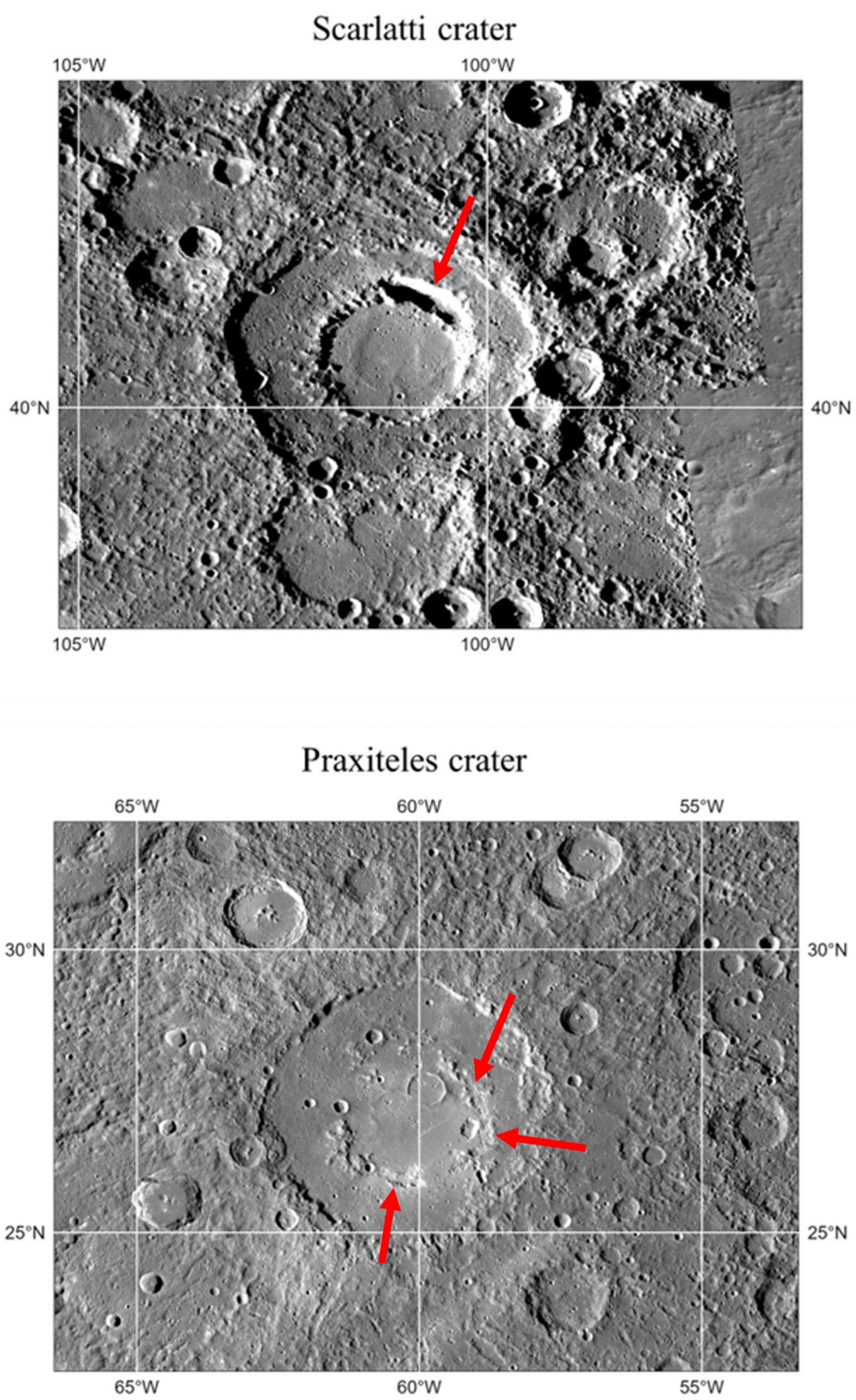

Figure 4.25. Examples of peak-ring craters on Mercury: Scarlatti crater (top) and Praxiteles crater (bottom), with volcanic vents located along the intact or destroyed peak-ring, indicated by red arrows. Equirectangular projection.

4.2.3 *Praxiteles basin: a case example of peak-ring basin affected by explosive volcanism*

A geomorphological and spectral analysis of vents and peak-ring structure inside Praxiteles crater was conducted in this work, to assess and study the interaction mechanisms between peak-ring structures and volcanic activity in the peak-ring basins.

Praxiteles is a peak-ring basin (diameter ~ 180 km) located in the Victoria quadrangle (Fig. 4.26). It has been classified as a degraded crater (Galluzzi et al., 2016) of early-Calorian age (see also Kinczyck et al., 2020). Kinczyck et al. (2020) evaluated Praxiteles as a c3 basin in the 5 classes scheme, since it is characterized by a continuous and degraded rim and slumped wall terraces. In Galluzzi et al. (2016), the original floor has been mapped as smooth crater floor. Volcanic vents and hollow fields were identified inside the floor and along the peak-ring structure. The 1:3M geological map of the Victoria quadrangle (Galluzzi et al., 2016) also showed that Praxiteles is mainly surrounded by intercrater and intermediate plains. The enhanced color mosaic indicates that Praxiteles is mainly surrounded by blue terrains. Moreover, it is entirely contained in the high-Mg region (HMR; see also Hall et al., 2021) and hosts low-reflectance-material (LRM; Klima et al., 2018).

In this work I first updated the 1:3 million geological map by Galluzzi et al. (2016), based on the photointerpretation of MESSENGER MDIS basemaps and of the USGS DEM. I then used high-resolution NAC images (mostly 18-20 mpp) and produced new mosaics to map in detail irregular pits and hollow fields within Praxiteles floor.

Figure 4.26 shows a geological map of Praxiteles crater at 1:3 million scale. According to the 3 crater classes classification, I mapped Praxiteles as an early-Calorian c2 crater, being characterized by a degraded morphology and a slightly sharp rim. The map shows that its floor is almost entirely covered by smooth plains, indicating subsequent effusive volcanic activity which covered some younger impact craters in Praxiteles, still observable as ghost craters (see Klimczak et al., 2012 and references therein). Pits representing mainly compound volcanic vents (see also Pegg et al., 2021) developed along the peak-ring structure, which was partly destroyed by explosive eruptions and partly covered by the smooth plains unit. Magma began to rise long after crater formation, as later impact craters on the crater floor were flooded by the secondary infilling that, in turn, is pierced by explosive eruptions. The faults related to the peak-ring may have acted as pathways for magma rising from a deeper source. In addition to the pyroclastic deposits covering the floor of the crater, hollows and a few dark deposits have formed close to the peak-ring. Following Rodriguez et al. (2023), hollows may form due to a sublimation process from a shallow crustal volatile-rich layer (VRL), ~1-2.5 km deep. The presence of hollows along the peak-ring could therefore suggest that this layer was exposed following the impact, right at the peak-ring.

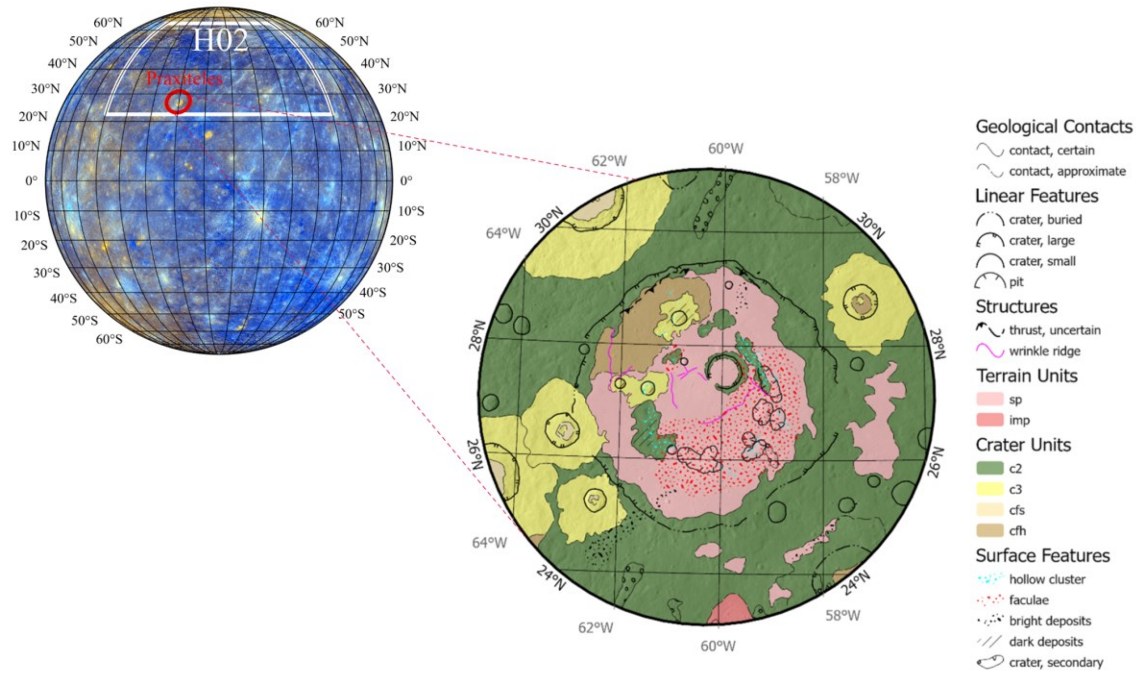

Figure 4.26. Location of H02 quadrangle and Praxiteles crater (27.1 °N; -60.3 °E) on the enhanced color basemap, in ortographic projection centered at 45°W (left) and geological map of the Praxiteles crater at 1:3 million scale, in a stereographic projection (right).

4.3 Mercury's gravity data analysis

This section reports and partly expands the paper Buoninfante et al. (2023).

4.3.1 Mercury's gravity anomalies

I present the gravity field maps calculated using the MESS160A model coefficients (see Methods). Figure 4.27a shows the free-air gravity anomalies of Mercury at an altitude of 50 km from the surface, as it is representative of the last period (April 2014 - January 2015) of the

MESSENGER radioscience measurements (Genova et al., 2019; Solomon and Anderson, 2018). Figure 4.27b shows the topography of Mercury derived from the *GTMES_150v05* model, defined up to spherical harmonic degree and order 150 (Neumann et al., 2016). The model defines the shape of Mercury and is expressed in terms of radial distance from the center of mass. It is worth noting that the topography model *GTMES_150v05* exhibits a spectral resolution comparable to the MESS160A gravity field model. At first, I estimated the Bouguer gravity anomalies (Fig. 4.27d) by subtracting the topographic gravity effect (Fig. 4.27c) to the free-air anomalies (see also the Methods chapter).

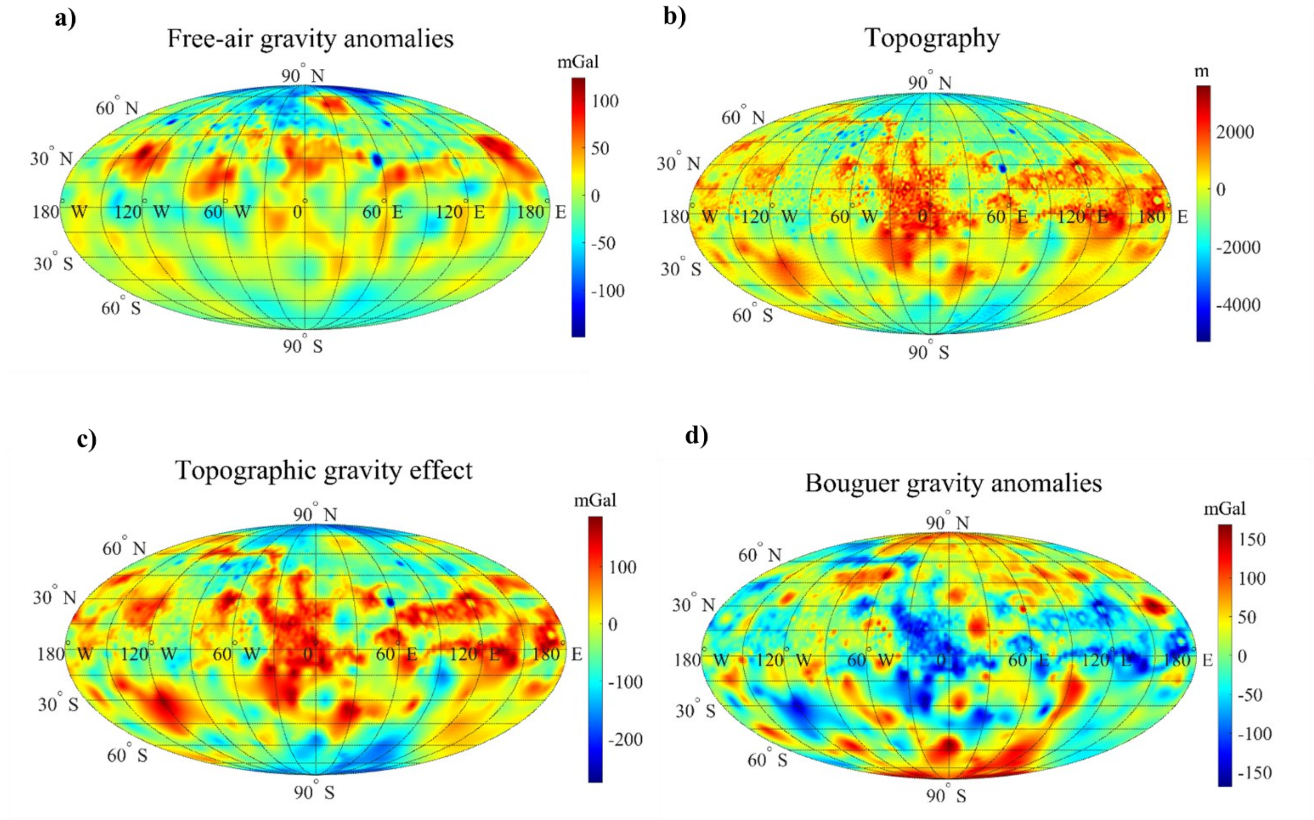

Figure 4.27. a) Free-air gravity anomalies, from the spherical harmonic model MESS160A**; b)** Global topography of Mercury from the spherical harmonic model *GTMES_150v05*; **c)** Topographic gravity effect; **d)** Bouguer gravity anomalies. The anomalies are computed at 50 km altitude from the mean surface. Maps in Mollweide projection.

4.3.2 Lithosphere elastic thickness

The estimation of the elastic thickness is crucial to understand the elastic behaviour of the lithosphere and to model the isostatic compensation surface. Following Watts (2010), I estimated the average elastic lithosphere thickness as the one giving the best fit between observed and calculated free-air anomalies along a series of 1-dimensional profiles. In Fig. 4.28, I show the results obtained along a NW-SE trending profile (Figure 4.28a-b). The L_2 misfit between the observed and calculated data (Fig. 4.29c) reaches its minimum at the elastic thickness of 30 km (see also Fig. 4.29). By evaluating the results obtained for all the chosen profiles, I assumed T_e= 30 $\pm$ 10 km as representative of the mean elastic lithosphere thickness. This value is consistent with previous estimates (e.g., James et al., 2016; Nimmo and Watters, 2004; Goossens et al., 2022). RMS plots of the other chosen profiles are shown in figures 4.30.

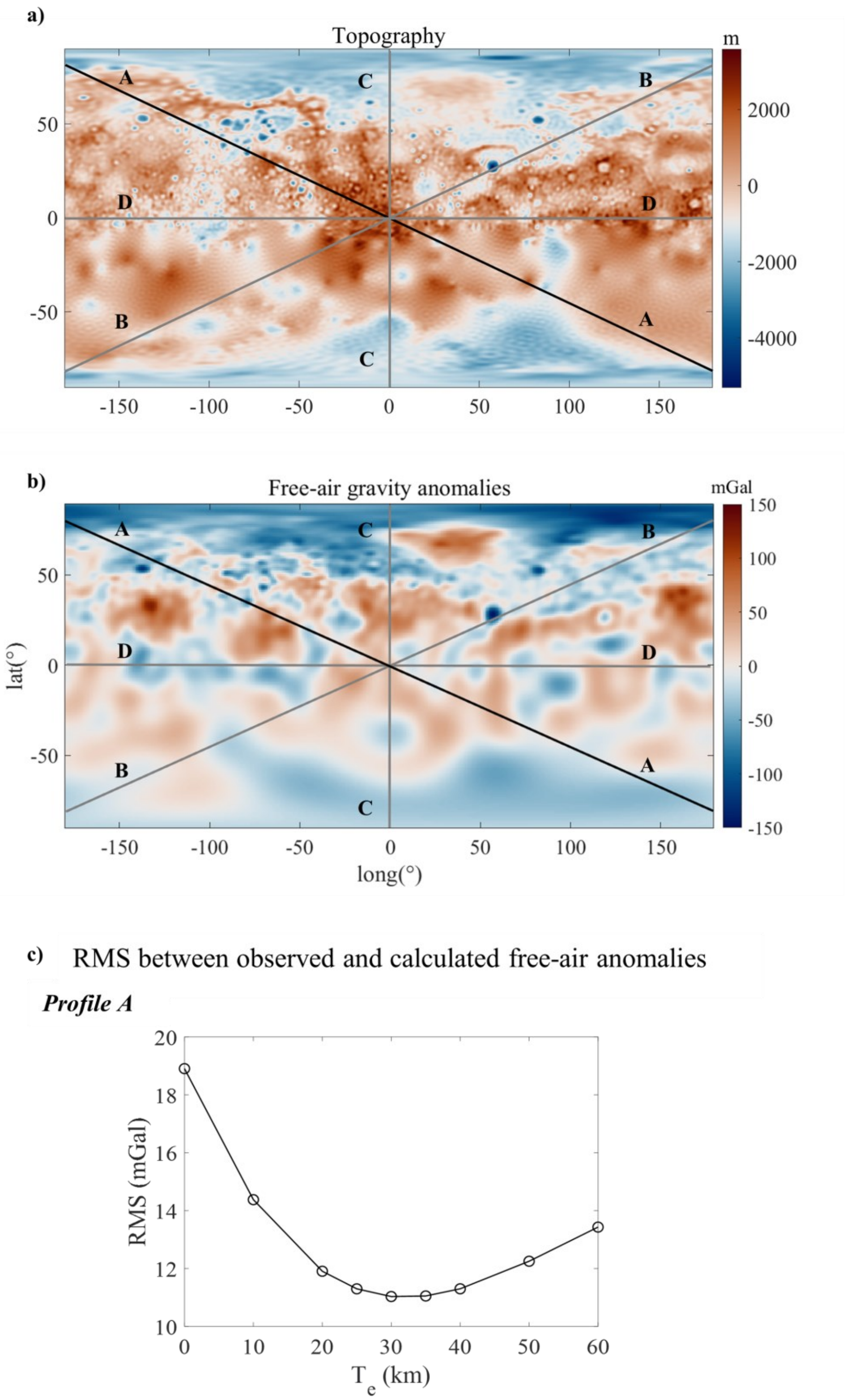

Figure 4.28. a) Global topography of Mercury derived from the *GTMES_150v05* model, in equirectangular projection. The black line indicates the representative global profile (*A*) among others (in gray) chosen to calculate the average elastic thickness; **b)** Free-air gravity anomalies derived from the spherical harmonic model MESS160A, in equirectangular projection. In Figures 4.27a and 4.27b I

used the Vik (Crameri, 2018) colormap to prevent ambiguity and visual distortion of the data; **c)** Plot of the root mean square difference (RMS) between observed and calculated free-air gravity anomalies vs T_e, for the representative profile (A).

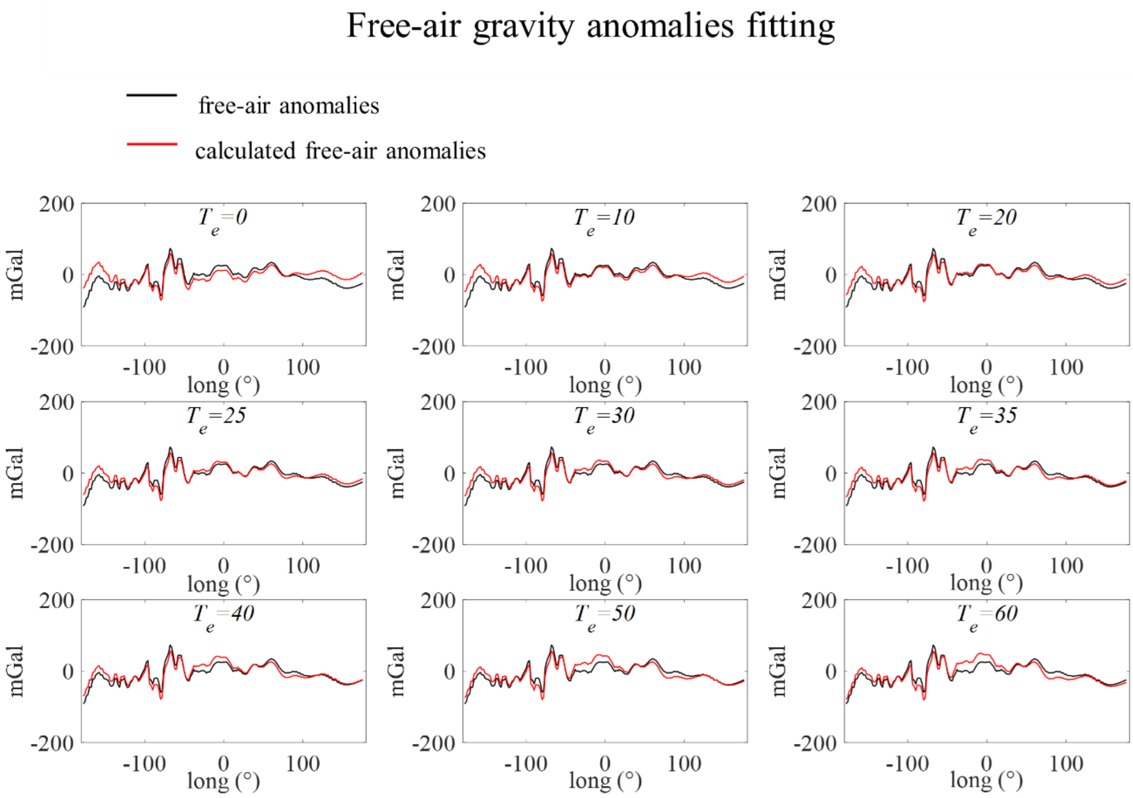

Figure 4.29. Comparison between observed and calculated free-air gravity anomalies along a global profile NW-SE, for different elastic lithosphere thickness T_e.

Profile B

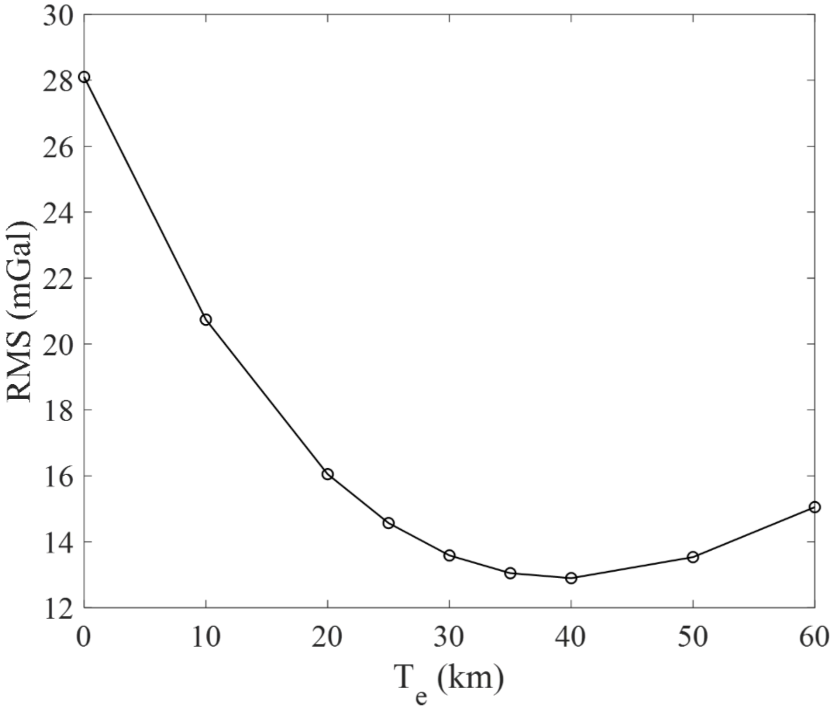

Profile C

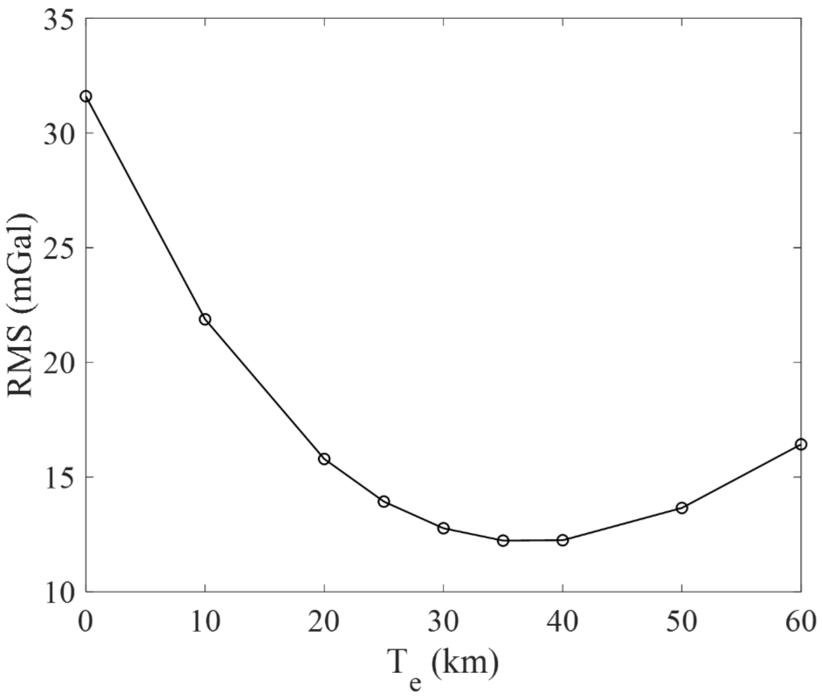

Profile D

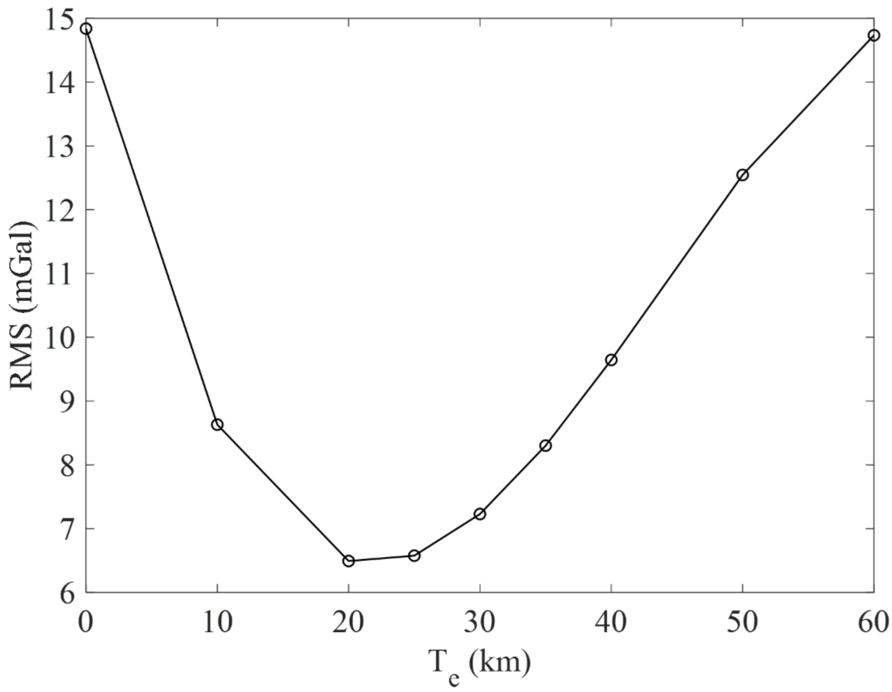

Figure 4.30. Root mean square difference (RMS) between observed and calculated free-air gravity anomalies vs T_e for profiles *B, C* and *D* (see figure 4.28b).

4.3.3 Flexural compensation model

The Airy isostatic compensation model (Airy, 1855) assumes that the lithosphere has no rigidity, and that, therefore, the elastic thickness T_e=0. A flexural compensation model, instead, assumes that the lithosphere has an elastic behavior (T_e>0) and flexes in response to surface loads.

The flexural response function (see Methods) represents the flexural response of the lithosphere to loading and allows understanding what type of isostatic model should be considered for a given spherical harmonic degree range. By analysing the flexural response (Fig. 4.31), it is possible to determine the wavelength range corresponding to the Airy compensation model (very low flexural rigidity), to the flexural compensation model (flexural rigidity), or to a non-compensation (very high flexural rigidity). The flexural response curve in figure 4.31 shows that the lithosphere of Mercury flexes for spherical harmonic degrees of the topography in the range $5<l<80$, i.e., or topography wavelengths ranging $190<\lambda<2800$ km. For spherical harmonics up to degree 5 and wavelengths longer than 2800 km, the flexural rigidity $\varUpsilon \to 0$, and the Airy compensation model can be assumed. For surface features with wavelengths shorter than 190 km (l>80), $\varUpsilon \to \infty$, and no lithospheric flexure occurs since the rigidity of the lithosphere is such to resist the topographic load.

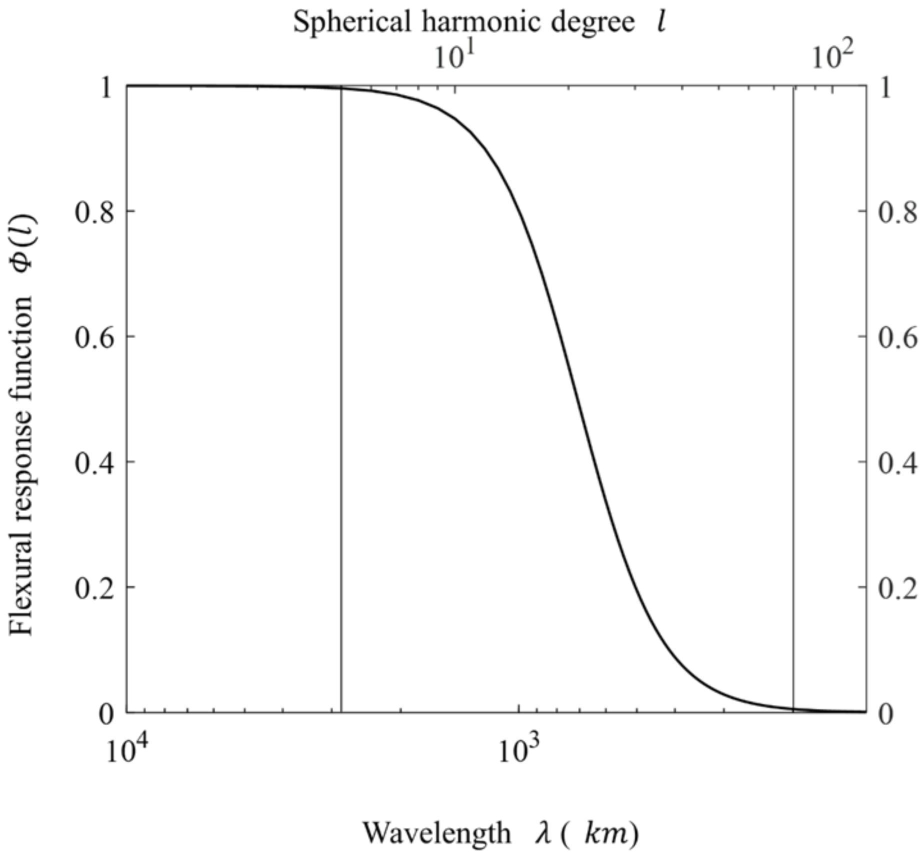

Figure 4.31. Flexural response function $\Phi(l)$ as a function of spherical harmonic degree l and the effective Cartesian wavelength $\lambda = \frac{2\pi R}{\sqrt{l(l+1)}}$, for an elastic thickness $T_e = 30$ km. For degrees l<5, the model approximates Airy compensation ($\varUpsilon \to 0$). For degrees l>80 topography is essentially uncompensated, approaching the Bouguer infinite rigidity case ($\varUpsilon \to \infty$). Flexural isostasy prevails in the spherical harmonic degree range 5<l<80. The range of spherical harmonic degree 5<l<80 corresponds to the range of wavelengths 190<λ<2800 km.

While the Airy compensation model is valid for $l < 5$, components up to $l = 4$ are associated with the polar mass deficit and to the morphological contrast between the lowlands and elevated regions (Tenzer et al., 2019). Hence, I decided to subtract the terms up to degree 4.

4.3.4 Isostatic gravity anomalies

If we assume an Airy compensation model, the T_e can be considered negligible, and the Airy isostatic anomalies can be calculated (Fig. 4.32), adapting the method proposed by Hirt et al. (2012) for Mercury (see Appendix). I assumed the crustal thickness T_c=35 km, crust and mantle density ρ_c=2800 kg/m^3 and ρ_m=3200 kg/m^3, respectively (Genova et al., 2019), and the mean density $\bar{\rho}$=5429 kg/m^3.

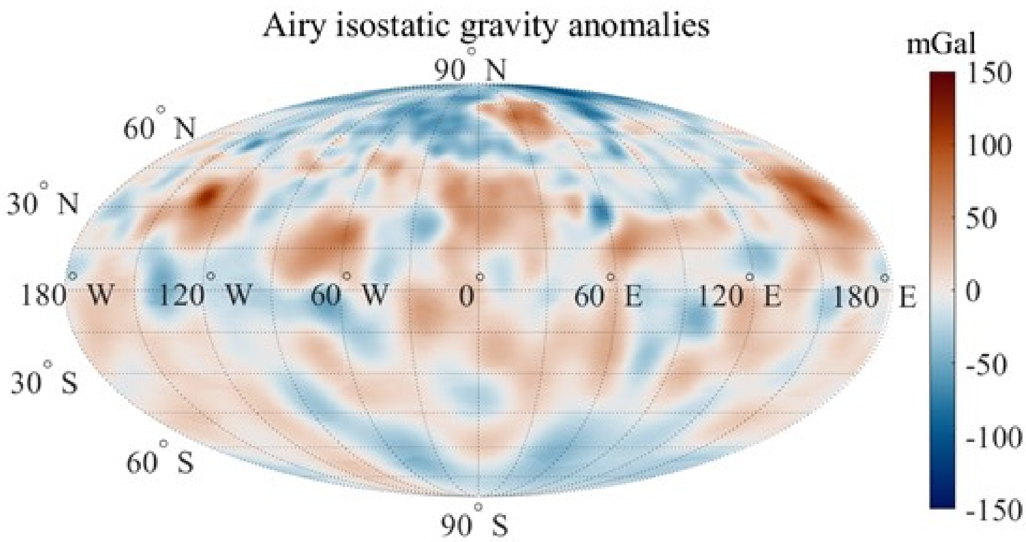

Figure 4.32. Isostatic gravity anomalies calculated using the degree strength of the MESS160A gravity field model, according to the Airy compensation model. The anomalies are computed at 50 km altitude. Map in Mollweide projection.

In this work I assumed a flexural compensation model (Turcotte et al., 1981), considering the estimated elastic thickness T_e=30 km. The map of the isostatic gravity effect, i.e., the isostatic correction assuming a flexural model, is shown in figure 4.33.

In figure 4.34, I show the isostatic gravity anomalies calculated assuming the flexural compensation model. The isostatic anomalies are obtained by subtracting the topographic and the isostatic gravity effects from the free-air anomalies and constrained by the MESS160A degree strength map (Fig. 4 in Konopliv et al., 2020), which shows the local resolution of the gravity field, i.e., the maximum acceptable degree of the gravity field model for given latitudes and longitudes. It is derived at the intersection between the expected acceleration at the Mercury surface and the surface acceleration uncertainty (Konopliv et al., 1999; 2020).

Figure 4.35 shows the map of isostatic anomalies without constraints on the degree strength. As expected, the isostatic gravity anomalies in Figure 4.34 get smoother where the degree strength is lower, compared to the anomalies constrained with the degree strength.

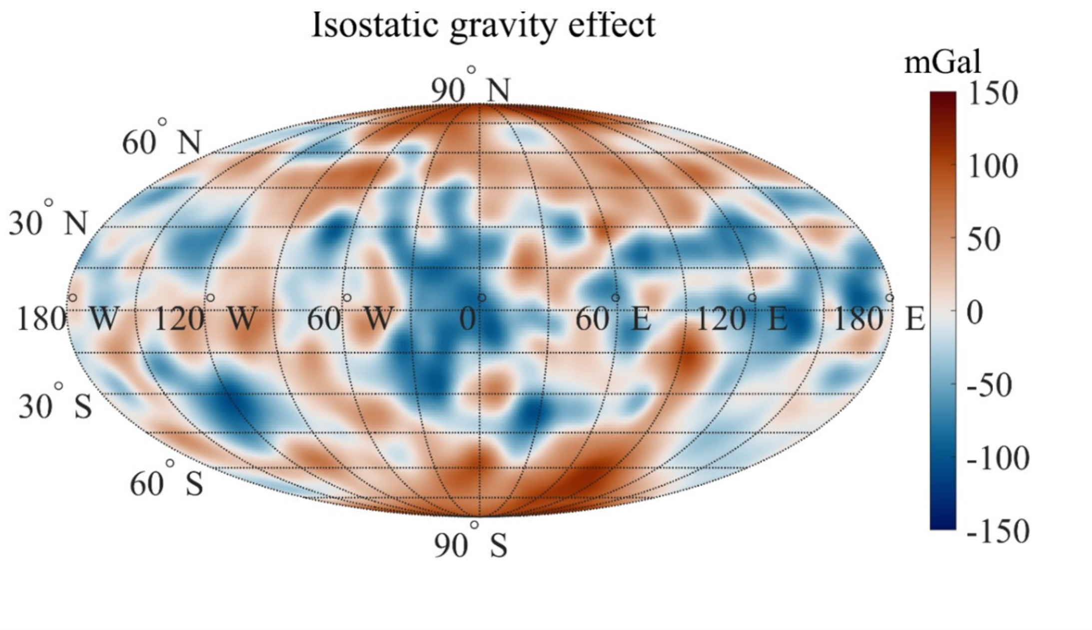

Figure 4.33. Isostatic gravity effect calculated assuming a flexural compensation model, in Mollweide projection.

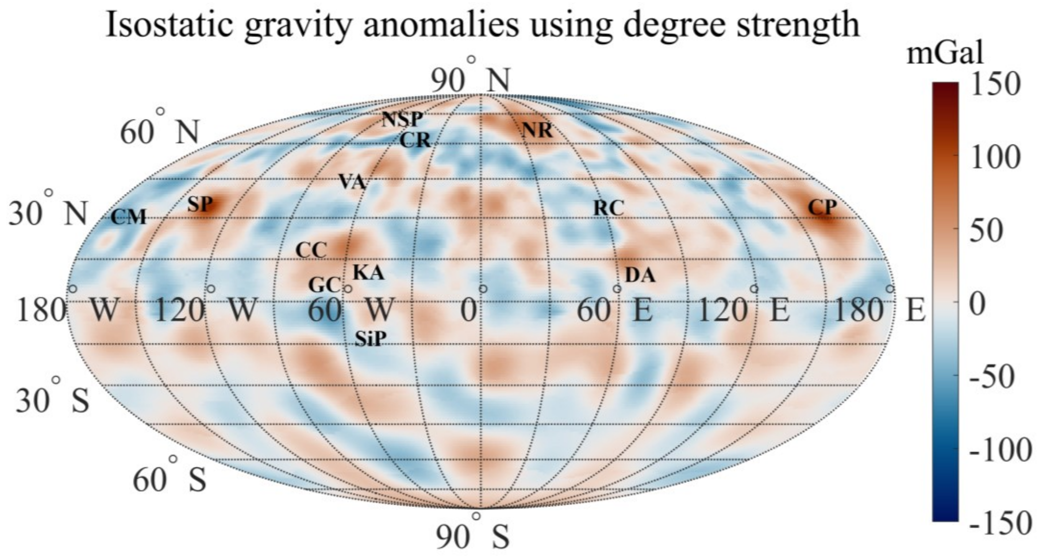

Figure 4.34. Isostatic gravity anomalies, after correcting the free-air anomalies with the topographic and isostatic gravity effects. For each point, the gravity is evaluated up to a maximum spherical harmonic degree that corresponds to the degree strength of the model MESS160A. Major features indicated are: **CM** = *Caloris Montes*; **CP** = *Caloris Planitia*; **CR** = *Carnegie Rupes*; **DA** = Derain anomaly; **KA** = Kuiper anomaly; **NR** = Northern Rise; **NSP** = Northern Smooth Plains; **RC** = Rachmaninoff Crater; **SiP** = *Sihtu Planitia*; **SP** = *Sobkou Planitia*; **VA** = Victoria Anomaly; **CC** = Catullus Crater; **GC** = Giotto Crater. The anomalies are computed at 50 km altitude (see Supplementary Information). Map in Mollweide projection.

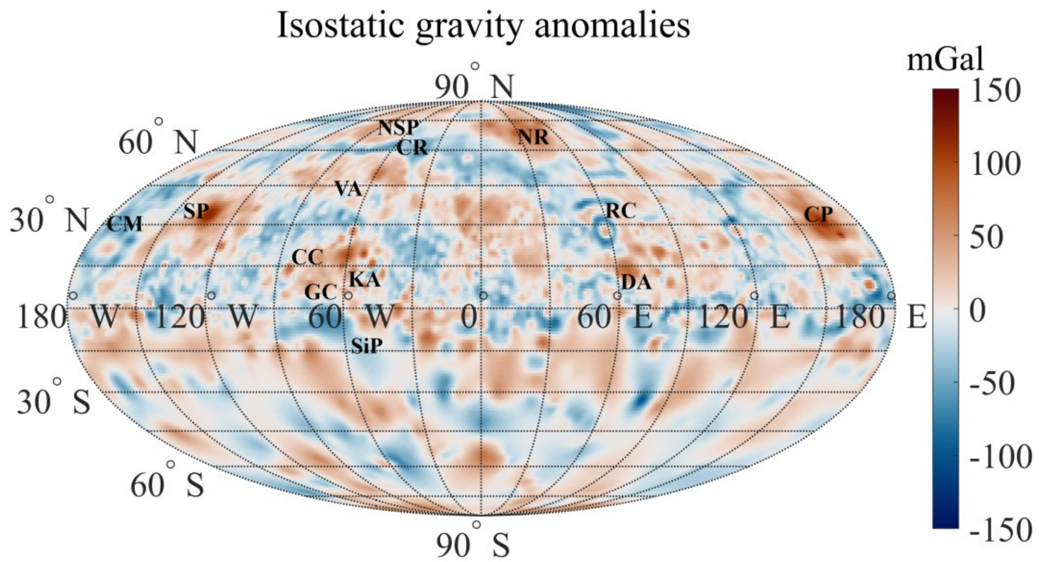

Figure 4.35. Isostatic gravity anomalies computed considering the maximum spherical harmonic degree (150). Major features indicated are: **CM** = *Caloris Montes*; **CP** = *Caloris Planitia*; **CR** = *Carnegie Rupes*; **DA** = Derain anomaly; **KA** = Kuiper anomaly; **NR** = Northern Rise; **NSP** = Northern Smooth Plains; **RC** = Rachmaninoff Crater; **SiP** = *Sihtu Planitia*; **SP** = *Sobkou Planitia*; **VA** = Victoria Anomaly; **CC** = Catullus Crater; **GC** = Giotto Crater. The anomalies are computed at 50 km altitude. Map in Mollweide projection.

4.3.5 Gravity anomalies spectral correlation

The map in figure 4.32 shows higher correlation to the free-air gravity map, with respect to the isostatic gravity map obtained assuming a flexural compensation model. This is clearly due to the excessive simplification imposed by the Airy model, which does not consider the effect of lithospheric rigidity and leads to an overestimation of the compensating crustal roots. The excessive correlation between free-air anomaly and Airy isostatic anomaly is also clear by analysing their spectral contribution. The correlation between gravity and topography may be defined as a dimensionless quantity based on their cross-power spectra (Wieczorek, 2015a). Here, I replaced these cross-power spectra with the cross-power spectra of the free-air anomaly and isostatic anomaly fields:

$$\gamma(l) = \frac{S_{fi}(l)}{\sqrt{S_{ff}(l)S_{ii}(l)}}, \tag{4.1}$$

where $S_{fi}(l)$ is the cross-power spectrum between the free-air anomaly and isostatic anomaly fields, $S_{ff}(l)$ is the power spectrum of the free-air anomaly fields and $S_{ii}(l)$ is the power spectrum of the isostatic anomaly fields.

I calculated and compared the spectral correlation $\gamma(l)$ between free-air and Airy isostatic anomalies and between free-air and flexural isostatic anomalies (Fig. 4.36). In both cases the correlation decreases as the spherical harmonic degree increases. However, the spectral correlation curve between free-air anomaly and flexural isostatic anomaly tends to zero over a much wider spherical harmonic degree range than the spectral correlation between free-air anomaly and Airy isostatic anomaly. This further confirms that a model considering lithospheric rigidity is necessary to isolate anomalies deriving from intra-crustal sources.

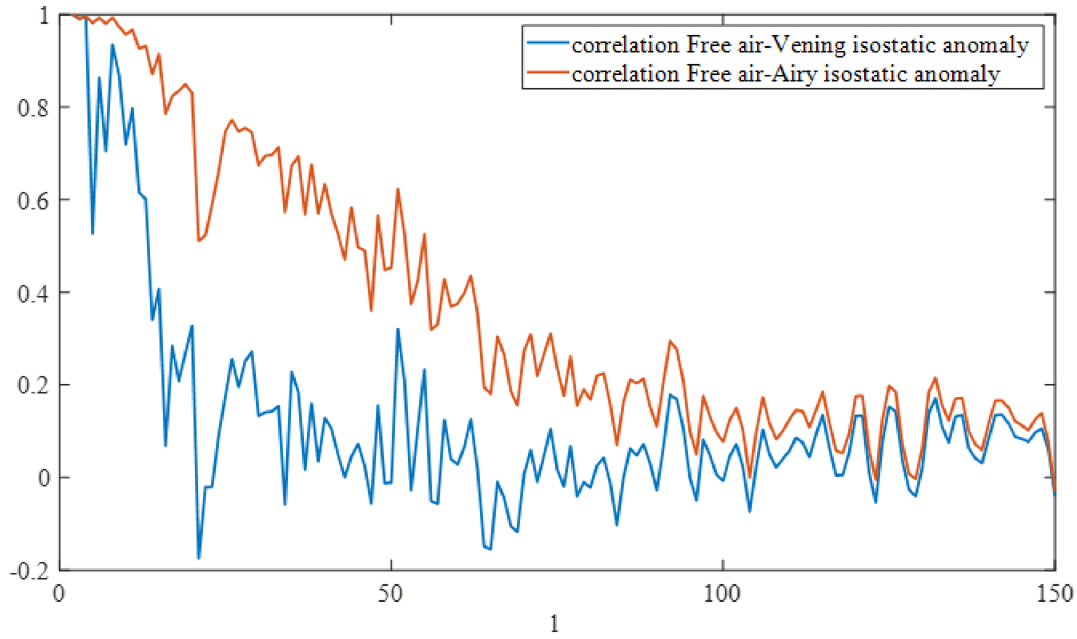

Figure 4.36. Spectral correlation between free-air and isostatic anomalies considering the lithospheric deflection model (blue curve) and spectral correlation between free-air and isostatic anomalies considering the Airy model (orange curve).

4.3.6 Mercury's crust-mantle interface

I considered lithospheric deflection coefficients (see Methods) to model the crust-mantle interface (Fig. 4.37) by means of a spherical harmonic expansion. I used the previously estimated mean elastic thickness of 30 km and assumed densities for crust and mantle of 2800 kg/m^3 and 3200 kg/m^3, respectively.

I neglected compensating the roots of sub-surface loads, since the intra-crustal sources (intrusions, dikes, sills) are bodies with limited extent. Indeed, the flexural response function $\Phi(l)$ (Fig. 4.38) shows that, for intra-crustal sources at ~15 km depth with lateral extension ≲500 km, and ~300 kg/m^3 density contrast, the lithospheric flexure tends to be negligible and does not generate any compensation roots effect. By a visual inspection of the extent of the isostatic anomalies in figure 4.34, which roughly accounts for the maximum size of the related source, sub-surface loads would thus hardly involve a crustal deepening that could affect the crust-mantle interface.

The result shows that the crust-mantle interface has a depth variable between 19 and 42 km. This estimate is included in a narrower range of values than the previous estimates (see table 1; Genova et al., 2019; James et al., 2015; Watters et al., 2021; Phillips et al., 2018; Beuthe et al., 2020), because the lithospheric rigidity effect has a strong influence on the crustal thickness modelling. I used the topography model uncertainties and their average value (9.5% of the model values) to compute the sensitivity on the result (see Appendix). The estimated sensitivity (see eq. A.30) with this approach is 5%.

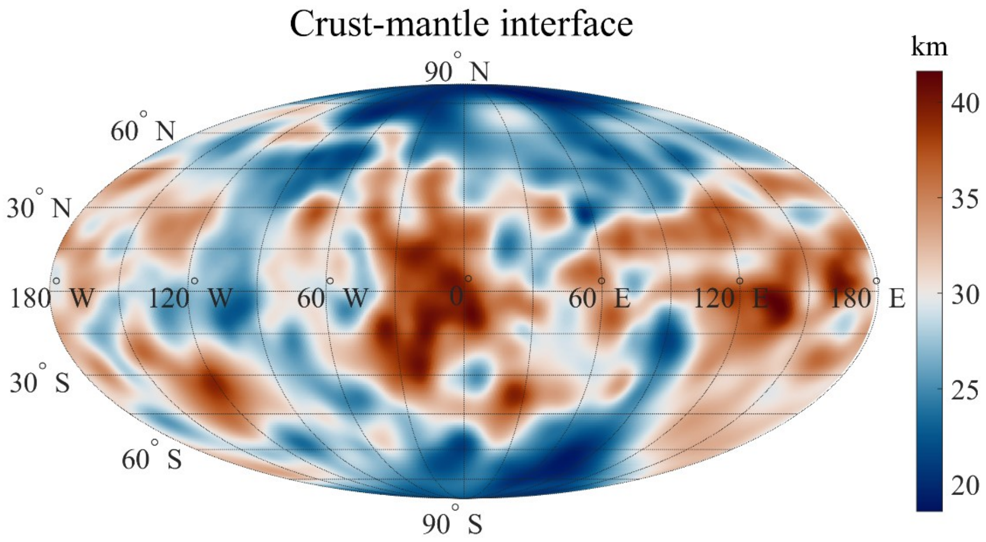

Figure 4.37. Map of the crust-mantle interface of Mercury predicted from a lithospheric flexure model, expressed as depth (km) with respect to the reference surface, in Mollweide projection. I modelled the deflection of the crust-mantle interface using the estimated elastic lithosphere thickness of 30 km, the crustal thickness (T_c) of 35 km and the densities of 2800 kg/m^3 and 3200 kg/m^3, for crust and mantle respectively.

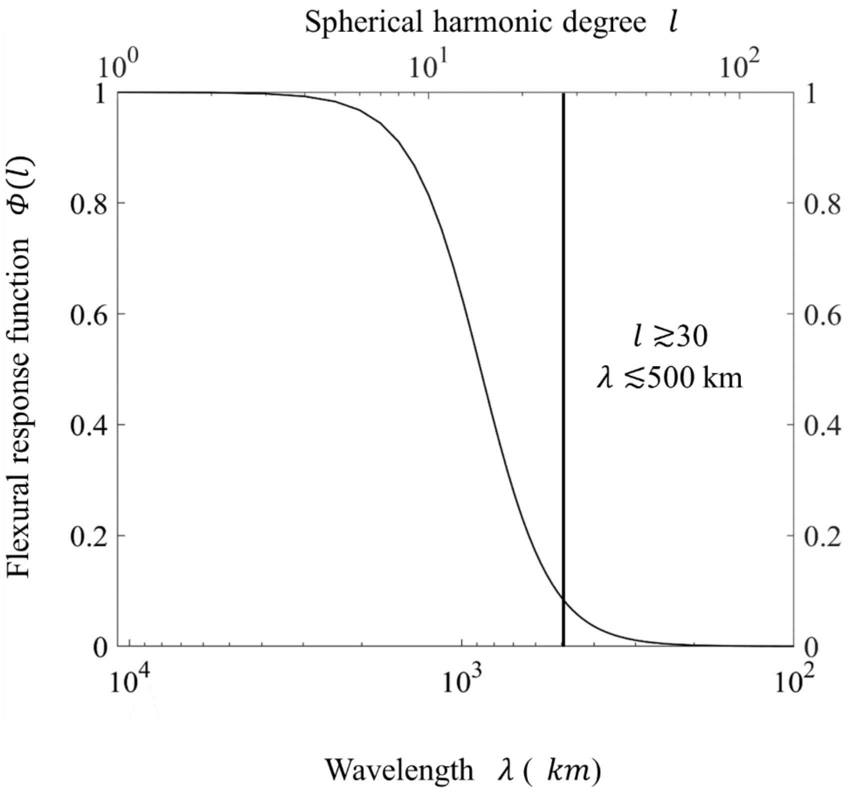

Figure 4.38. Flexural response function $\Phi(l)$ calculated for subsurface loads 15 km deep, producing a density contrast of 300 kg/m^3, and for the elastic thickness T_e =30 km. Intra-crustal sources, with $\lambda \lesssim 500$ km, do not cause significant lithospheric flexure and their compensation roots hardly develop.

4.3.7 Heat flux estimation

Following Goossens et al. (2022), the elastic thickness is related to heat flux through the equation 3.9. Elastic thickness is related to the time of topography formation during the LHB and to later resurfacing (e.g., Marchi et al., 2013; Byrne et al., 2016), in the period between 4.2 and 3.5 Ga. I assumed that the temperature at the base of the lithosphere T_{base} is 1050 K (e.g., Breuer & Moore, 2007; Goossens et al., 2022), the surface temperature T_{surf} is 440 K (e.g., Padovan et al., 2014, Goossens et al., 2022) and the thermal conductivity κ is 3 W m^{-1} K^{-1} (e.g., Michel et al., 2013; Goossens et al., 2022). The resulting heat flux q for T_e= 30 km is 61 mW m^{-2}. Watters et al. (2002) and Nimmo & Watters (2004) found that the heat flux ranges between 10-50 mW m^{-2}. Later, Goossens et al. (2022) calculated a value of 105 mW m^{-2} for the planet heat flux. Our results present relatively high values of heat flux, although lower than Goossens et al. (2022), which however may be expected for Mercury, as a planet partially molten at the end of accretion and subsequently rapidly cooling.

5. Discussion

In this chapter I will discuss the results presented previously. I will treat the geology of the terrains identified in Michelangelo and the role of tectonic structures in volcanic processes. I will provide a geological interpretation of the calculated crustal gravity sources. I will then discuss the thick-skinned tectonic style of Mercury, comparing the tectonic structures and the crustal structures identified by the calculation of isostatic gravity anomalies and by boundary analysis techniques. Finally, I will show the potential of boundary analysis techniques in the identification of degraded impact basins on Mercury.

5.1 The nature of H12 terrains

Results of this thesis show that Michelangelo quadrangle consists mainly of intermediate plains and reddish terrains that distinguish it from adjacent quadrangles (H11 and H13) of the southern hemisphere, which are instead characterized by large extension of darker surfaces. The bright reddish terrains show the same spectral characteristics of the high-reflectance plains (HRP), which represent red volcanic deposits with spectral properties (steep spectral slope) consistent with magma depleted in opaque materials (Robinson et al., 2008). The reddish area in H12 appears, then, spectrally consistent with some of the larger *planitiae* on Mercury, such as *Caloris Planitia*, *Utaridi Planitia*, *Borealis Planitia*, *Apārangi Planitia* and *Sobkou Planitia*. Comparing the mapped geological units and the Enhanced color basemap, it emerges that the c3 craters and smooth plains tend to overlap with the bright yellow areas. On the other hand, the dark blue terrains seem to have a good match with the imp covering ancient basin floors and the be. The XRS measurements seem to confirm these compositional differences, as the reddish terrains correspond to areas depleted in Ca and Mg, of typical basalt composition, respect to the surrounding dark terrains, maybe characterized by a more ultramafic composition (Nittler et al., 2011; Weider et al., 2012). This also suggests a possible compositional difference between the "dark" infilling (imp) of ancient basins, such as Vincente-Yakovlev and probably b73 (Orgel et al., 2020), and the "bright" infilling (sp) of younger basins and craters such as Beethoven and Michelangelo.

5.2 Fault-vent interaction

The analysis of the distribution of faults and volcanic vents both at global scale and in the Michelangelo quadrangle highlights the significant contribution of tectonic structures in the explosive volcanism of Mercury, because the faults represent preferential pathways that support the ascent of magma and volatiles. Figure 5.1 shows two conceptual schemes of fault-vent interaction. In case 1, the volcanic vent is located along a thrust cutting a crater, which represents a weakness zone. In case 2, the volcanic vent is found in the soft-linkage zone between the thrust segments bordering the basin. Moving from the first to the second case, there is an increased probability of volcanic vent formation, due to the increased fracturing (Fig. 5.1).

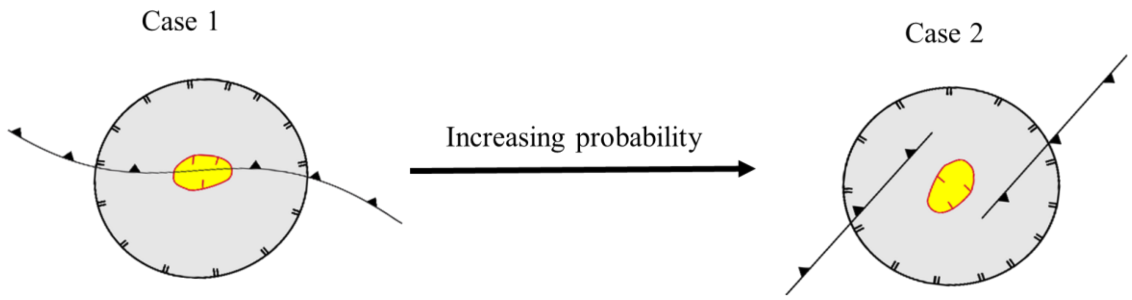

Figure 5.1. Case 1: schematic representation of volcanic vent along a lobate scarp; Case 2: schematic representation of volcanic vent in the relay zone between thrust segments.

Regarding the explosive activity in Mercury's peak-ring basins, I consider two possible models explaining the formation of volcanic vents close to the peak-ring structure (Fig. 5.2). According to the first model, the gravitational collapse of the central uplift results in the development of inward-dipping extensional faults (Osinski and Spray, 2005). Normal faults can act as preferential routes for the upwelling of magma and volatiles, which leads to explosive eruption at the surface along the direction of the faults. As a result, volcanic vents form close to the peak-ring.

In the second model, thrust faults are responsible for peak-ring formation (Collins et al., 2002). Again, the uprise of magma and volatiles may occur along the thrust faults forming the peak-ring and accommodating the structural uplift.

Magma and volatiles sources are not necessarily a crustal magma chamber, as any magma chamber below craters on Mercury could be deeper than on the Moon, as Mercury has no floor-fractured craters (Thomas et al., 2015), although this could also be due to insufficient data resolution.

The Chicxulub crater represents a reliable Earth analog for peak-ring basins on Mercury. Previous works on Chicxulub demonstrated that the formation of the peak-ring is accompanied by the development of thrust faults (see also Fig. 1.21; e.g., Collins et al., 2002; Gulick et al., 2013). Inside Chicxulub there is no evidence of volcanic activity, but hydrothermal activity has been recognized (Kring et al., 2020), which is particularly vigorous adjacent to the melt pool, near the peak-ring.

a)

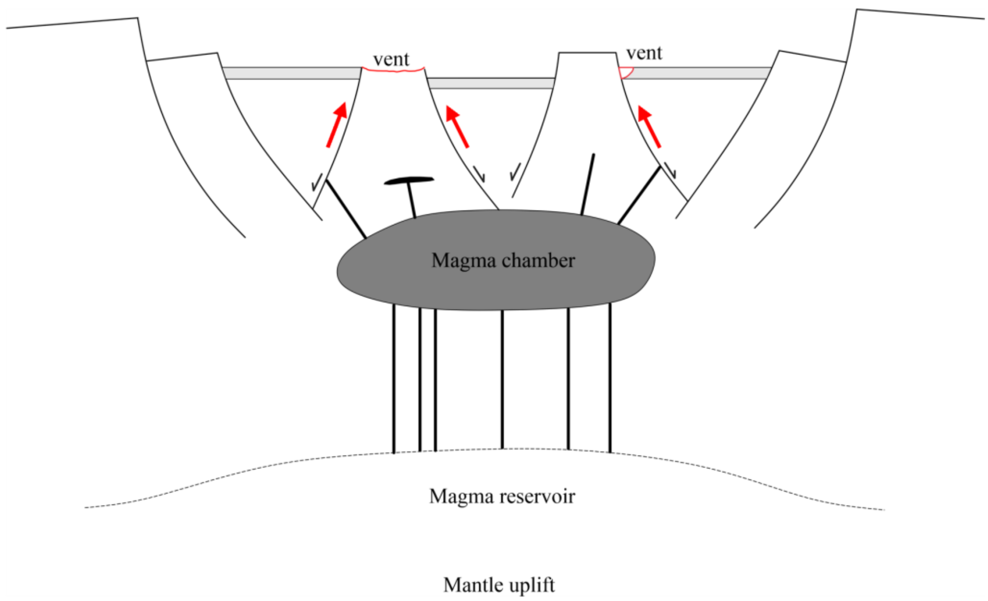

b)

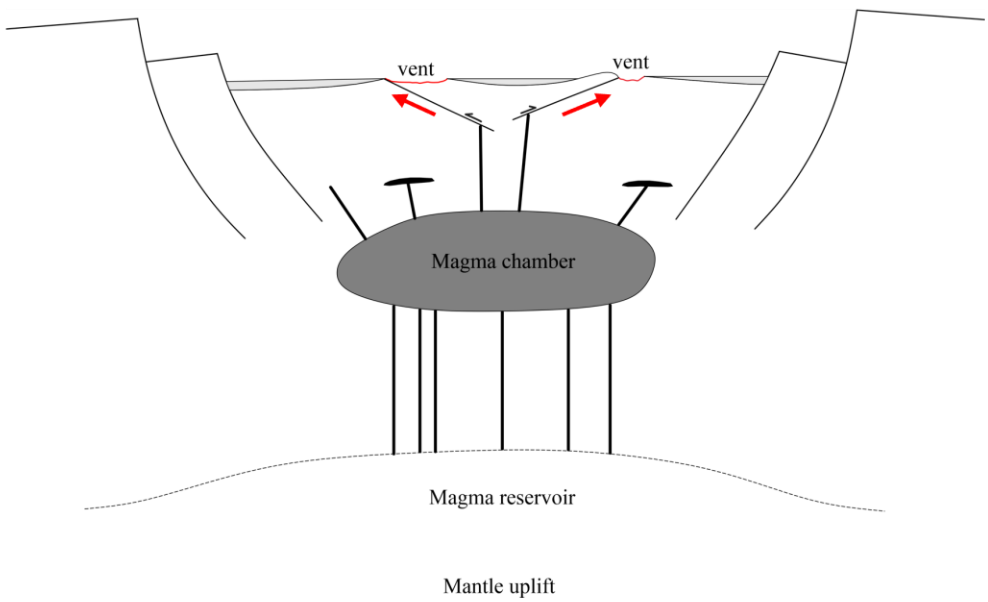

Figure 5.2. a) First proposed model explaining the formation of volcanic vents close to the peak-ring structure. Magma and volatiles rise from a deeper source, along normal faults formed during the gravitational collapse of the central uplift. **b)** Second proposed model explaining the formation of volcanic vents close to the peak-ring structure, where magma and volatiles rise from a deeper source along thrust faults accommodating the structural uplift. Red arrows indicate the ascent of magmatic material towards the emission centers.

5.3 Geological interpretation of isostatic anomalies

This section reports and expands what discussed in the paper Buoninfante et al. (2023).

The identification of isostatic gravity anomalies is crucial for better understanding Mercury's internal structure. I have distinguished isostatic anomalies in highs and lows. Isostatic anomaly highs are mainly identified above large basins, which originated after huge meteoritic impacts and are mostly characterized by smooth plains on the surface (Fassett et al., 2012; Denevi et al., 2013; Strom, 1997). These anomalies can represent the effect of intra-crustal magmatic intrusions (Head et al., 2009) caused by the regional extensional regime following the impact, as also observed for the Moon and Mars (Thomas et al., 2015). On the other hand, isostatic anomaly lows are mainly found above intercrater plains regions, also named heavily cratered terrains (Strom, 1997). These regions are likely characterized by a highly fractured crust with respect to the impact basins, since the icp are the oldest terrains on Mercury (4.5-3.9 Ga), affected by numerous impacts and strong fracturing over time resulting in a lower crustal bulk density. In principle, isostatic anomaly lows could also be explained by the presence of voids, interpreted as empty lava tubes or caves, as identified on Earth, Moon and Mars (Sauro et al., 2020). Examples are Schröter's Rille (Chappaz et al., 2017) and Marius Hills Hole (Kaku et al., 2017). However, these effects are expected not to be important at the scale considered. So, the origin of the isostatic lows is better explained with the highly fractured crust below the ancient icp terrains.

In general, detection of isostatic anomalies provides a significant contribution for the geological interpretation of Mercury because it highlights smaller-scale buried geological features that were not revealed by free-air and Bouguer anomaly maps. Indeed, a significant part of the anomalies in the isostatic gravity anomaly map (Fig. 5.3) was not evident in the free-air and Bouguer anomaly maps, because of the interference with the effect of the topography and of the crust-mantle interface. Above the Northern Smooth Plains (**NSP** in Fig. 5.3), many anomalies characterized by wavelengths of a few hundred km and clearly visible in the isostatic anomaly map, are difficult or not at all detectable in the free-air and in the Bouguer anomaly maps (Fig. 4.26a and Fig. 4.26d, respectively). Similarly, in the southern polar area the isostatic anomaly map highlights a gravity high extending in latitude from 57°S to 90°S, and flanked towards the west by a low, which corresponds to a depressed region of the southern hemisphere. An extended free-air gravity low is, instead, observed in the same area, while the Bouguer anomaly map is dominated by anomaly highs. In the Rachmaninoff crater (**RC**) area, within which lies the lowest elevation on Mercury (Tenthoff et al., 2020), the free-air anomaly map shows an intense low. The Bouguer anomaly map shows a high, probably due to the mantle uplift following the formation of the crater (Ding et al., 2021). On the other hand, the isostatic anomaly map in Fig. 5.3 does not present significant anomalies. This implies that rare magmatic intrusions probably occurred, or the model resolution is not sufficient to sample any intrusions.

The isostatic anomaly map shows several anomalies associated with the highest topographic area of Mercury, between latitude 45°S-35°N and longitude 300°E-30°E. Here the Bouguer anomaly map shows an intense low, which does not allow us to identify and interpret other shorter wavelength anomalies. On the contrary, the free-air anomaly map is characterized by overlapping anomalies which hide the effects associated with intra-crustal sources.

Previous studies interpreted the Bouguer gravity anomaly in the Caloris basin (**CP**) and the Sobkou basin (**SP**) areas as associated with topographic lows and mass concentrations (mascons; Konopliv et al., 2020; Mazarico et al., 2014); however, the presence of isostatic anomaly highs in the same areas seem to suggest the occurrence of diffuse intra-crustal magmatic intrusions.

Regarding the Northern Rise (**NR**) anomaly, two main hypotheses have been made about its origin. The first hypothesis considers a crustal or even deeper source related to the mantle uplift, following a meteoritic impact (Zuber et al., 2012). The second hypothesis considers a source in the core or at core-mantle boundary interface (Plattner et al., 2021). Once again, the concurrent presence of an isostatic anomaly may suggest the occurrence of magmatic intrusions.

The isostatic anomaly high named Victoria anomaly (**VA**) is found in the more depressed area of the Victoria Quadrangle (301°E, 49°N), which is associated with an impact basin (b55 in figures 5.4-5.5). As indicated in figure 5.4, isostatic anomaly highs are frequently associated with impact basins and, therefore, they can be interpreted by possible intrusive bodies.

Other anomaly highs such as the anomaly observed in the region between the Catullus (**CC**) and Giotto (**GC**) craters, in the Kuiper Quadrangle (**KA**), and the anomaly south of the Rachmaninoff crater (**RC**), the Derain anomaly (**DA**) (see Fig. 5.3), do not show any correlations with the topography and do not seem associated with known impact basins, but they can be attributed to intrusive bodies.

East of the Caloris Basin (**CP**) anomaly, the isostatic anomaly map shows an alignment of gravity lows, corresponding to the Caloris Montes (**CM**), probably due to the negative contrast given by the basin rim at depth with the denser crustal material filling the basin.

In the northern polar region, a large isostatic anomaly low extends from 77°N to 90°N latitude, and from 110°E to 200°E longitude and spatially corresponds to smooth plains, because characterized by younger and less fractured crustal materials respect to the surrounding terrains.

The isostatic anomaly low west of Sihtu Planitia (**SiP**) (293°E, 5.5°S), included within the high-Mg region, shows no correlation with the topography, thus suggesting that it is caused by a probable less dense and fractured crust material generating a negative density contrast with the denser basin material.

Finally, an alignment of isostatic anomaly lows runs along the tectonic structure known as *Carnegie Rupes* (**CR**) (250°E-325°E, 55°N-65°N), one of the largest lobate scarps in the northern hemisphere of Mercury, suggesting the presence of crustal density discontinuities along this structure.

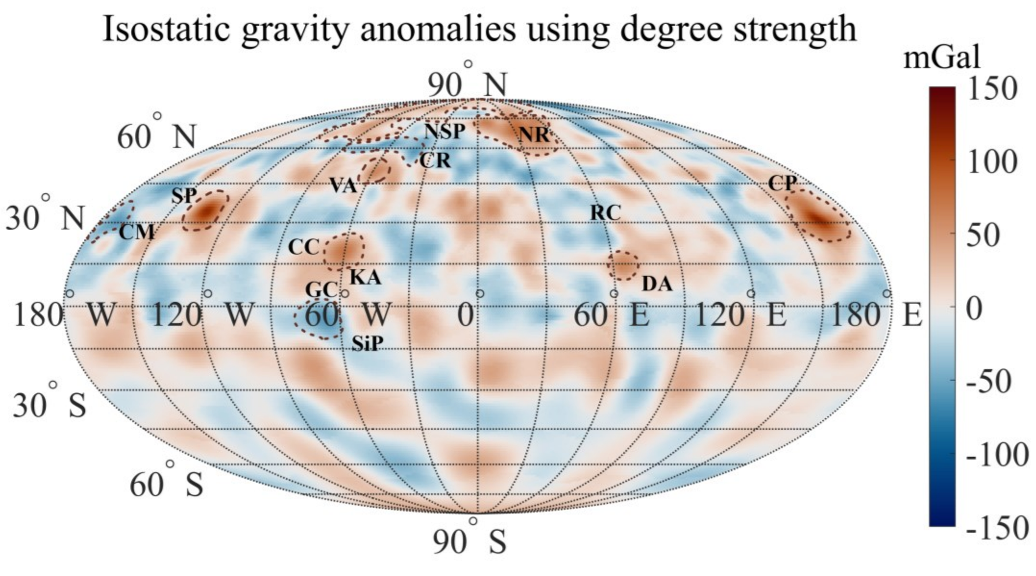

Figure 5.3. Isostatic gravity anomalies, after correcting the free-air anomalies with the topographic and isostatic gravity effects. For each point, the gravity is evaluated up to a maximum spherical harmonic degree that corresponds to the degree strength of the model MESS160A. Dark red dashed lines indicate discussed isostatic anomalies. Major features indicated are: **CM** = *Caloris Montes*; **CP** = *Caloris*

Planitia; **CR** = *Carnegie Rupes*; **DA** = Derain anomaly; **KA** = Kuiper anomaly; **NR** = Northern Rise; **NSP** = Northern Smooth Plains; **RC** = Rachmaninoff Crater; **SiP** = *Sihtu Planitia*; **SP** = *Sobkou Planitia*; **VA** = Victoria Anomaly; **CC** = Catullus Crater; **GC** = Giotto Crater. The anomalies are computed at 50 km altitude (see Supplementary Information). Map in Mollweide projection.

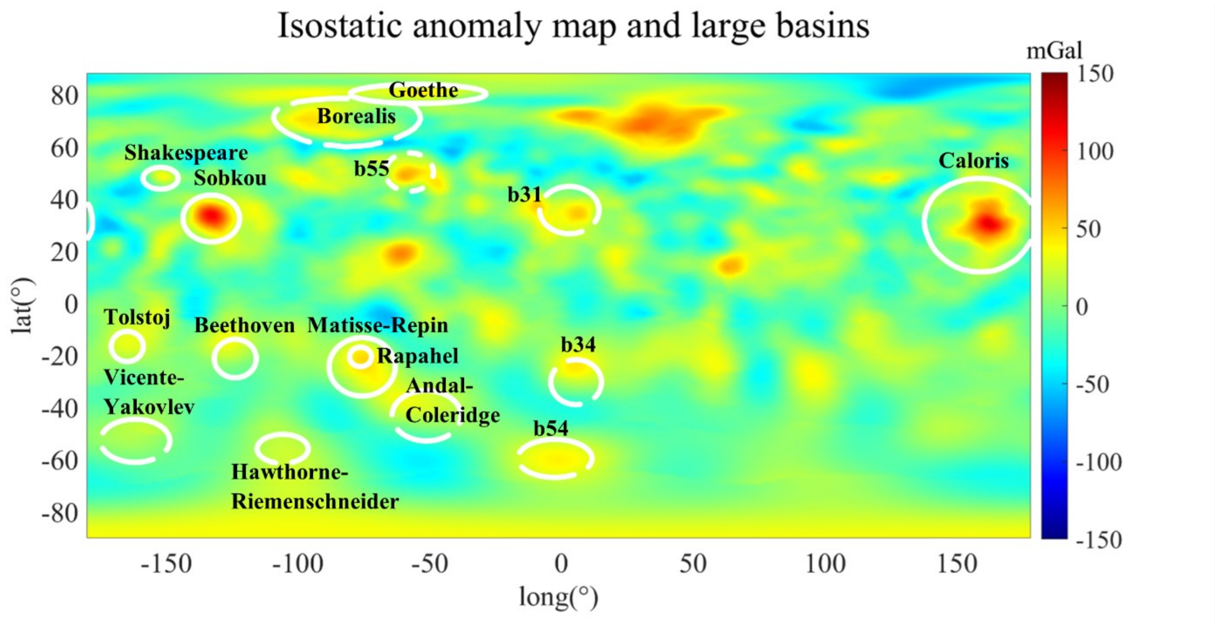

Figure 5.4. Large certain basins (solid white circles) and large suggested basins (dashed white circles; Orgel et al., 2020) associated with isostatic anomaly highs interpreted as intra-crustal magmatic intrusions. Equirectangular projection.

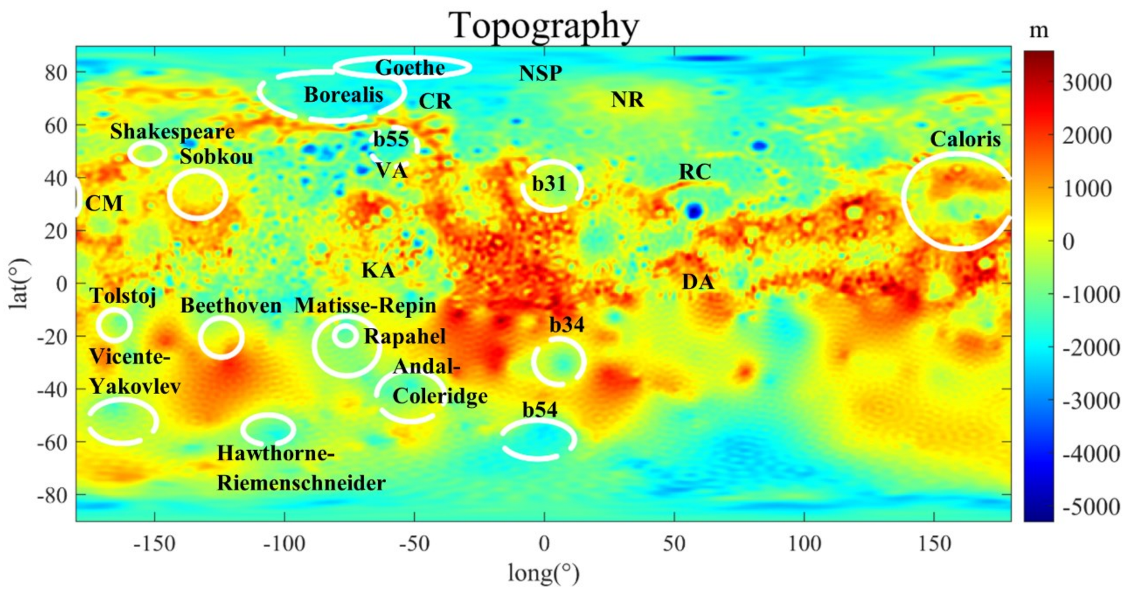

Figure 5.5. Large certain basins (solid white circles), large suggested basins (dashed white circles) and major features identified on the topography map. Equirectangular projection.

Appendix

Satellite tracking

The principle of physical geodesy that is based on tracking a satellite from a ground base station can be described by the following equation (e.g., Reigber, 2005):

$$\mathbf{x_T} + \mathbf{r_d} = \mathbf{x_S}, \tag{A.1}$$

where $\mathbf{x_T}$ represents the position vector of the base station, $\mathbf{r_d}$ is the distance vector between station and satellite resulting from the tracking data and $\mathbf{x_S}$ is the position vector of the satellite. Considering the principles of Newton's dynamics, in an inertial reference system:

$$m_S \ddot{\mathbf{x}}_\mathbf{S} = \mathbf{g_S} + \mathbf{f_S}, \tag{A.2}$$

where m_S is the satellite mass, $\mathbf{g_S}$ represents the sum of the gravitational forces acting on the satellite and $\mathbf{f_S}$ is the sum of the non-gravitational forces (see Reigber, 2005).

Gravity field

The gravity field is expressed through a spherical harmonic expansion. The spherical harmonic analysis provides a way to synthesize an equation applicable to a sphere, starting from discrete measurements made on the sphere itself. This equation can therefore be used to understand the behaviour of the field even in areas of the sphere where there are no measurements (Blakely, 1996).

The spherical harmonics are the solutions of the Laplace equation in spherical coordinates, that is, they essentially represent the adaptation of the Fourier analysis to a spherical surface.

The stationary part of the gravitational potential, therefore, at each point (r, φ, θ) of its surface is expressed on a global scale with spherical harmonic expansion. The coefficients of spherical harmonics (Stokes coefficients) are used to study the global structure and irregularities of the field in the spectrum domain.

The Newtonian gravitational potential W of a planet can be represented as the sum of a normal potential U, and a disturbing potential T. At a global scale, it is common to express the gravity field through a series of spherical harmonics, which are the solutions of the Laplace equation in spherical coordinates (e.g., Barthelmes, 2013):

$$W(r,\varphi,\theta) = \frac{GM}{R}\sum_{l=0}^{\infty}\sum_{m=0}^{l}\left(\frac{R}{r}\right)^{l+1} P_{lm}(\sin\theta)[\,C_{lm}\cos m\varphi + S_{lm}\sin m\varphi], \qquad \text{(A.3)}$$

where (r,φ,θ) are the geocentric coordinates of the satellite; G is the gravitational constant; M and R are the mass and mean radius of the planet; C_{lm}, S_{lm} are the Stokes coefficients; P_{lm} are the normalized Legendre functions of degree l and order m. The spherical harmonic coefficients (Stokes coefficients) are used to study the overall structure and the irregularities of the field in the spectral domain. The spherical harmonic expansion is truncated to a degree l_{max}, depending on the data resolution (Wieczorek, 2015a). The normal potential is the potential of a rotating ellipsoid that has an equipotential surface. This potential is represented by a series in spherical harmonics using only the coefficients $\bar{C}_{20}$ and $\bar{C}_{40}$, determined by the parameters of the reference ellipsoid. The disturbing potential can always be defined as a series in spherical harmonics and is the difference between the geopotential, whose field is measured, and the normal potential.

The disturbing potential is defined as:

$$T(r,\varphi,\theta) = \frac{GM}{r}\sum_{l=2}^{l_{max}}\left(\frac{R}{r}\right)^{l}\sum_{m=0}^{l} P_{lm}(\sin\theta)\,[\,C_{lm}^{T}\cos m\varphi + S_{lm}^{T}\sin m\varphi]. \qquad \text{(A.4)}$$

A spherical approximation is often used for the disturbing potential T (Hofmann-Wellenhof & Moritz, 2006); in addition, if the origin of the reference system coincides with the planet center of mass, the potential has no terms of degree $l = 1$. Therefore, the sum of T starts from $l = 2$.

The Stokes coefficients C_{lm}^{T} and S_{lm}^{T} are related to mass distribution, defined as:

$$C_{lm}^{T}\;(o\;S_{lm}^{T}) = \frac{1}{(2l+1)M}\int_V \left(\frac{r'}{R}\right)^{l} \rho(r',\varphi',\theta')P_{lm}(\sin\theta')\cos(or\;\sin)m\varphi'\;dV, \qquad \text{(A.5)}$$

integrating over all density anomalies $\rho(r',\varphi',\theta')$ within the planet of volume V.

The approximation in spherical harmonics of the field up to a maximum degree $lmax$ consists of $(lmax + 1)^2$ coefficients. The accuracy of the field depends on the accuracy of the coefficients themselves (C_{lm}, S_{lm}) and the spatial resolution depends on the maximum degree lmax.

One of the techniques used to estimate the coefficients consists of a numerical integration of the orbital equations of motion and the use of differential correction techniques (Martin et al., 1976). In other cases, analytical techniques are used to evaluate the orbital elements of the satellite and the coefficients in spherical harmonics (Gaposchkin, 1974).

The geoid variations can be calculated from Brun's formula:

$$N = T/\Omega, \tag{A.6}$$

where T is the disturbing potential and Ω the gravitational force calculated from the normal potential.

Satellite altimetry is very useful to obtain information on the shorter wavelength components of the gravity field. For the Earth, by measuring the satellite distance from sea level and subtracting this measurement from the spacecraft altitude above a reference ellipsoid, a direct measurement of the geoid undulations is obtained. Another commonly used technique involves tracking the movements of a satellite from another nearby satellite. In this case the gravitational perturbation of the spacecraft at lower altitude is observed more continuously than with the ground tracking system (Regan et al., 1979). Gravity anomalies in geodesy are, therefore, used to mainly define the shape of the geoid.

In geophysics, however, anomalies are associated with density contrasts in the subsurface and specific geological structures. Conventionally we talk about gravity anomaly in geophysical applications and gravity disturbances in geodetic applications.

The gravity disturbance vector $\boldsymbol{\delta}g$ at a given altitude h is defined as the gradient of the disturbing potential T:

$$\boldsymbol{\delta}g(h, \varphi, \theta) = \nabla T(h, \varphi, \theta) = \nabla W(h, \varphi, \theta) - \nabla U(h, \theta). \tag{A.7}$$

The gravity disturbance δg is, then, given by the difference between the modulus of the geopotential gradient and the modulus of the normal potential gradient:

$$\delta g(h, \varphi, \theta) = |\nabla W(h, \varphi, \theta)| - |\nabla U(h, \theta)|. \tag{A.8}$$

The gravity anomaly is defined, however, as the modulus of the field at a given point (h, φ, θ) minus the modulus of the normal field taken at the same longitude φ and latitude θ, but at the height $h - z_g$, where z_g represents a certain height anomaly:

$$\Delta g(h, \varphi, \theta) = |\nabla W(h, \varphi, \theta)| - \left|\nabla U\left(h - z_g, \varphi, \theta\right)\right|. \tag{A.9}$$

The height anomaly $z_g(\varphi, \theta)$ is defined as the distance between the planet's surface and the point where the normal potential U has the same value as the geopotential W on the surface (Molodensky et al., 1962; Hofmann-Wellenhof & Moritz, 2005).

The main difference is that, while in the case of gravity disturbance, the geoid surface is taken as the reference surface, for the gravity anomaly the reference level can be chosen at an arbitrary altitude, such as the average altitude of the area of interest (Hackney & Featherstone, 2003).

Tenzer et al. (2019) also defined the gravity disturbance as the difference between effective gravity and normal gravity, in the same point of the surface for which normal gravity is calculated based on the geometric altitude with respect to the reference geometric surface. On the other hand, the gravity anomaly is expressed as the difference between the actual gravity at a point on the surface and the normal gravity calculated at a point for which the vertical distance with respect to the geometric reference surface is defined by the physical height.

The wavelength on the surface of a sphere of radius R asymptotically equivalent to a spherical harmonic degree l is given by the Jeans relation (Wieczorek & Simons, 2005):

$$\lambda = \frac{2\pi R}{\sqrt{l(l+1)}} \approx \frac{2\pi R}{(l+1/2)}. \tag{A.10}$$

A simple estimate of the minimum half-wavelength ψ_{min} (as spherical distance) that can be resolved from the coefficients C_{lm}, S_{lm} is, therefore (Barthelmes, 2013):

$$\psi_{min}(l_{max}) \approx \frac{\pi R}{l_{max}}. \quad \text{(A.11)}$$

The gravity disturbance can be expressed as:

$$\delta g(r,\varphi,\theta) = \frac{GM}{r^2}\sum_{l=0}^{lmax}\left(\frac{R}{r}\right)^l (l+1)\sum_{m=0}^{l} P_{lm}(\sin\theta)\,[\,C_{lm}^T\cos m\varphi + S_{lm}^T\sin m\varphi]. \quad \text{(A.12)}$$

Mathematically, the free air gravity disturbance δg^{FA} is given by the negative radial derivative of the disturbing potential T:

$$\delta g^{FA} \cong -\frac{\partial T}{\partial r}. \quad \text{(A.13)}$$

The free air gravity anomaly Δg^{FA} is, however, defined as:

$$\Delta g^{FA} \cong -\frac{\partial T}{\partial r} + \frac{1}{\gamma(H,\theta)}\frac{\partial \gamma}{\partial r}\,T, \quad \text{(A.14)}$$

where γ is normal gravity, $\frac{\partial \gamma}{\partial r}$ is the gradient of normal gravity, θ indicates the latitude and H the physical altitude. Then, the free air gravity anomaly Δg^{FA} can be written as (Qingyun et al., 2018; Tenzer et al., 2019):

$$\Delta g^{FA}(r,\varphi,\theta) = -\frac{\partial T}{\partial r} - \frac{2T}{r} =$$

$$= \frac{GM}{r^2}\sum_{l=2}^{l_{max}}\left(\frac{R}{r}\right)^l (l-1)\sum_{m=0}^{l} P_{lm}(\sin\theta)\,[\,C_{lm}^T\cos m\varphi + S_{lm}^T\sin m\varphi]. \quad \text{(A.15)}$$

The Bouguer anomaly is calculated by applying a topographic correction to the free air anomaly. So, the Bouguer gravity disturbance δg^{BA} is obtained as (Tenzer et al., 2019):

$$\delta g^{BA} = \delta g^{FA} - g^T \cong -\frac{\partial T}{\partial r} + \frac{\partial V^T}{\partial r}, \quad \text{(A.16)}$$

where the topographic correction is defined as the radial derivative of the topographic gravitational potential V^T.

The corresponding Bouguer anomaly will be (Tenzer et al., 2019):

$$\Delta g^{BA} \cong -\frac{\partial T}{\partial r} + \frac{\partial V^T}{\partial r} - \frac{2}{r}T + \frac{2}{r}V^T = \delta g^{BA} - \frac{2}{r}T + \frac{2}{r}V^T. \quad \text{(A.17)}$$

Tesseroids

Tesseroids, or spherical prisms, are used in this work to model the sources and crustal structures of Mercury and to test the boundary analysis methods. Tesseroids are very useful in planetary studies as they allow us to model crustal or deep bodies taking into account the sphericity of the planet. A tesseroid is a volume defined in geocentric spherical coordinates and bounded by two meridians, two parallels and two concentric circles. Grombein et al. (2013) define the potential V and the gravity field Δg of a tesseroid, with constant density ρ, respectively as:

$$V(r, \varphi, \theta) = G\rho \int_{\varphi_1}^{\varphi_2} \int_{\theta_1}^{\theta_2} \int_{r_1}^{r_2} \frac{1}{l} t dr' d\theta' d\varphi', \quad \text{(A.18)}$$

$$\Delta g\ (r, \varphi, \theta) = G\rho \int_{\varphi_1}^{\varphi_2} \int_{\theta_1}^{\theta_2} \int_{r_1}^{r_2} \frac{\Delta_{(x,y,z)}}{l^3} t dr' d\theta' d\varphi', \quad \text{(A.19)}$$

where G is the gravitational constant, r is the radius, θ and φ are latitude and longitude, and (x,y,z) are the local coordinate system (Fig. A1), and

$$\Delta_x = r'(\cos\theta \sin\theta' - \sin\theta \cos\theta' \cos(\varphi' - \varphi)), \quad \text{(A.20)}$$

$$\Delta_y = r' \cos\theta' \sin(\varphi' - \varphi), \quad \text{(A.21)}$$

$$\Delta_z = r' \cos\zeta - r, \quad \text{(A.22)}$$

$$t = {r'}^2 \cos\theta', \quad \text{(A.23)}$$

$$\mathrm{d} = \sqrt{{r'}^2 + r^2 - 2r'r\cos\zeta}, \quad \text{(A.24)}$$

$$\cos \zeta = \sin \theta \sin \theta' + \cos \theta \cos \theta' \cos(\varphi' - \varphi). \tag{A.25}$$

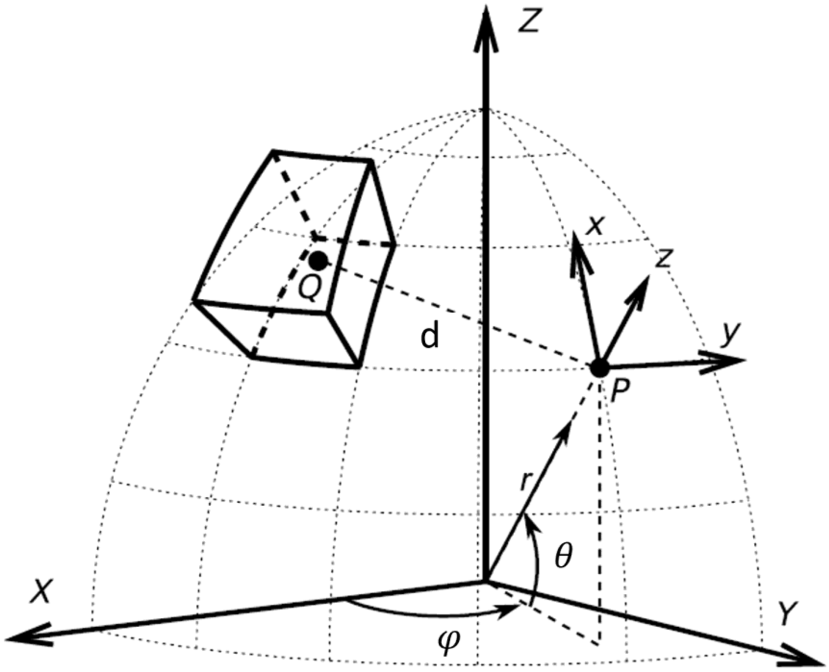

Figure A1. Geometric representation of a tesseroid. Q: integration point inside the tesseroid; (X,Y,Z): geocentric coordinate system; P: calculation point; (x, y, z): local coordinate system; r,θ,φ: radius, latitude and longitude, respectively, of the point P; d: distance between Q and P. Modified from Uieda et al. (2015).

To model the internal structure of the planet and to calculate the field and derivatives in spherical coordinates, I used the Tesseroids codes included in the Fatiando a Terra toolbox (http://tesseroids.leouieda.com/en; Uieda et al., 2015), which I modified to conform it to the study of Mercury.

Figure A2 shows an example of the radial component of the field (g_r) of a single tesseroid with lateral extension of 2° and its derivatives $g_{rr}, g_{r\theta}, g_{r\varphi}$ in spherical coordinates, calculated with the Tesseroids code. The top is placed at a depth of 10 km from the surface, while the bottom is placed at 50 km. The density ρ is set to 200 $\frac{kg}{m^3}$.

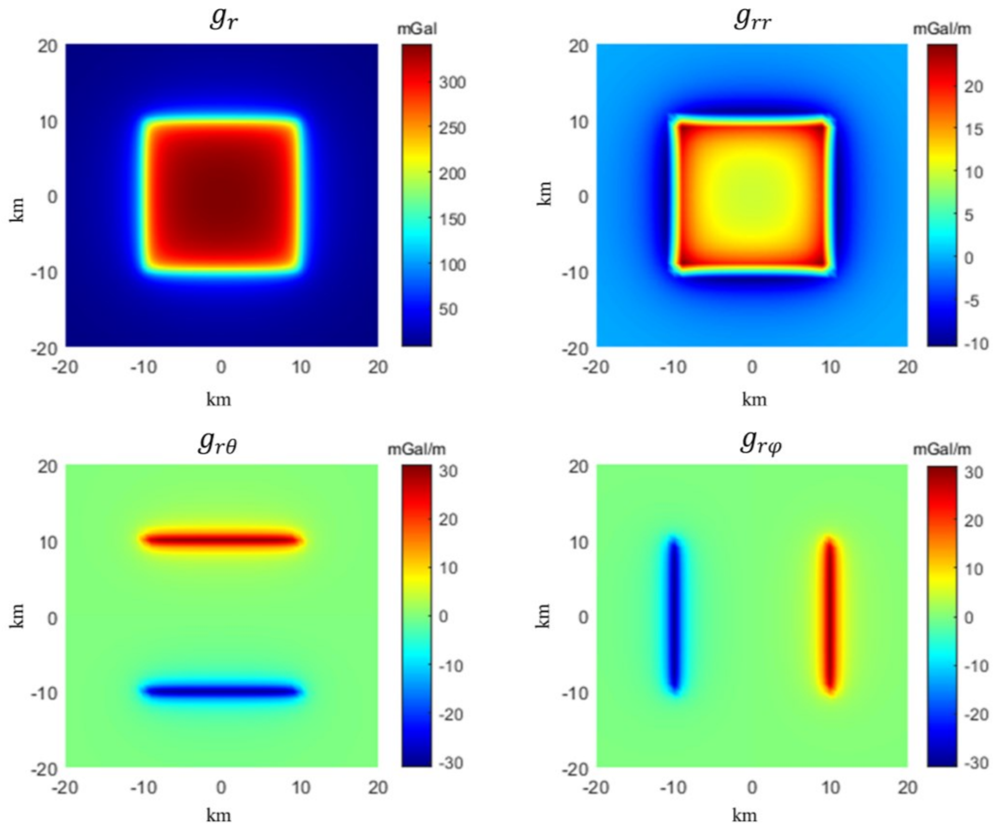

Figure A2. Example of radial component of the field (g_r) of a tesseroid and its derivatives $g_{rr}, g_{r\theta}, g_{r\varphi}$ in spherical coordinates.

Airy isostatic gravity anomalies

This section reports and partly expands the supplementary materials of the paper Buoninfante et al. (2023).

Here I explain the method used to calculate the isostatic anomalies based on the Airy-Heiskanen compensation model (Rummel et al., 1988), adapted to Mercury. In the Airy-Heiskanen model, isostatic compensation is assumed to occur locally in vertical columns with homogeneous density above the compensation surface. Consequently, the depth of the compensation surface is directly related to the topography and the spatial resolution of the Airy-Heiskanen compensation model is identical to the resolution of the topography model.

According to Hirt et al. (2012), assuming the Airy-Heiskanen compensation model, the coefficients of the topographic and isostatic effect can be obtained with a third-order series expansion:

$$\begin{Bmatrix}\bar{C}_{lm}\\ \bar{S}_{lm}\end{Bmatrix} = \frac{3}{2l+1}\frac{\rho}{\bar{\rho}}\left[\left[1-\left(\frac{R-T}{R}\right)^{l}\right]\begin{Bmatrix}\overline{HC1}_{lm}\\ \overline{HS1}_{lm}\end{Bmatrix} + \frac{l+2}{2}\left[1+\frac{\rho}{\rho_m-\rho}\left(\frac{R-T}{R}\right)^{l-3}\right]\begin{Bmatrix}\overline{HC2}_{lm}\\ \overline{HS2}_{lm}\end{Bmatrix} + \right.$$

$$\left.\frac{(l+2)(l+1)}{6}\left[1-\left(\frac{\rho}{\rho_m-\rho}\right)^{2}\left(\frac{R-T}{R}\right)^{l-6}\right]\begin{Bmatrix}\overline{HC3}_{lm}\\ \overline{HS3}_{lm}\end{Bmatrix}\right], \tag{A.26}$$

where T is the mean compensation depth, ρ_m is the mantle density, ρ is the mean topography density, $\bar{\rho}$ is the mean planet density, R is the planet's equatorial radius. $\overline{HC1}_{lm}$ and $\overline{HS1}_{lm}$ are the spherical harmonic coefficients of the dimensionless surface functions H/R:

$$\frac{H}{R} = \sum_{l=0}^{lmax}\sum_{m=0}^{l}(\overline{HC1}_{lm}\cos m\varphi + \overline{HS1}_{lm}\sin m\varphi)\,\bar{P}_{lm}(\cos\theta). \tag{A.27}$$

$\overline{HC2}_{lm}$ and $\overline{HS2}_{lm}$ are the coefficients of the surface function $\left(\frac{H}{R}\right)^2$:

$$\left(\frac{H}{R}\right)^2 = \sum_{l=0}^{lmax}\sum_{m=0}^{l}(\overline{HC2}_{lm}\cos m\varphi + \overline{HS2}_{lm}\sin m\varphi)\,\bar{P}_{lm}(\cos\theta). \tag{A.28}$$

$\overline{HC3}_{lm}$ and $\overline{HS3}_{lm}$ identify the coefficients of surface function $\left(\frac{H}{R}\right)^3$:

$$\left(\frac{H}{R}\right)^3 = \sum_{l=0}^{lmax}\sum_{m=0}^{l}(\overline{HC3}_{lm}\cos m\varphi + \overline{HS3}_{lm}\sin m\varphi)\,\bar{P}_{lm}(\cos\theta). \tag{A.29}$$

The calculated coefficients $\bar{C}_{lm}$ and $\bar{S}_{lm}$ contain both the effect of topography and the isostatic effect.

For the application of the Airy-Heiskanen compensation model to Mercury, I considered the following parameters: T= 35 km, ρ= 2800 kg/m^3, ρ_m= 3200 kg/m^3, and $\bar{\rho}$= 5427 kg/m^3.

Crust-mantle interface sensitivity

This section derives from the Methods section of the paper Buoninfante et al. (2023).

The sensitivity on the estimated crust-mantle interface depth is:

$$S = \frac{(CMI1 - CMI2)}{CMI}, \tag{A.30}$$

where $CMI1$ is the estimated crust-mantle interface depth obtained by using the topography model summed of an estimated average error equal to 9.5% of the coefficients values; $CMI2$ is the estimated crust-mantle interface depth obtained by using the topography model subtracted of an estimated average error equal to 9.5% of the coefficients values; and CMI is the estimated crust-mantle interface depth.

Data availability, software and fundings

Data availability

All basemaps data are publicly available from NASA's Planetary Data System (https://pds-imaging.jpl.nasa.gov/portal/). MESSENGER MDIS data (Monochrome basemaps, Color mosaic, Enhanced Color mosaics and DEM) are downloaded from Planetary Data System (PDS) archive.

Mercury MESS160A and GTMES_150v05 models can be downloaded from the NASA' s Planetary Data System Geosciences Node at https://pds-geosciences.wustl.edu/messenger/mess-h-rss_mla-5-sdp-v1/messrs_1001/data/shadr/.

Moon GRAIL and LRO products are available from the NASA' s Planetary Data System Geosciences Node (https://pds-geosciences.wustl.edu/dataserv/moon.html). The GRGM1200B gravity field model can be downloaded from the NASA' s PDS Geosciences Node at https://pds-geosciences.wustl.edu/grail/grail-l-lgrs-5-rdr-v1/grail_1001/shadr/.

MoonTopo2600p model can be downloaded from https://doi.org/10.5281/zenodo.3870924 (Wieczorek, 2015b).

Mars GMM-3 gravity field model is available at the NASA's PDS Geosciences Node (https://pds-geosciences.wustl.edu/mro/mro-m-rss-5-sdp-v1/mrors_1xxx/data/shadr/).

InSight Crustal Thickness can be downloaded from InSight Crustal Thickness Archive https://zenodo.org/records/6477509 (Wieczorek, 2022).

Software

In this thesis, I used ArcGIS Pro 3.2.2. Geographic Information System software to produce geological maps. I also used MATLAB R2019b and SHTOOLS (Wieczorek and Meschede, 2018) to produce gravity anomaly maps, to model Mercury's crust-mantle interface, to compute THD and EHD, and to estimate basin sizes.

Fundings

I acknowledge funding from the Italian Space Agency (ASI) under ASI-INAF agreements 2017-47-H.0 and 2024-18-HH.0. This research was also supported by INAF through RSN3 Mini-Grant "Investigation of Mercury's Tectonics (iMeT).

Acknowledgements

First, I want to thank my supervisors Luigi, Valentina, Maurizio and Pasquale for their patience, for believing in me, and for the time they dedicated to me in these three years.

I thank all my colleagues, friends, and the entire DiSTAR department, whom I have known for many years, and with whom I have shared and continue to share wonderful moments.

I also thank all the INAF people who I had the pleasure of meeting and with whom I shared pleasant moments especially during the last year.

My thanks go to the OU and IPGP people, who welcomed me with such kindness and availability in their institutes during my stays abroad. I am very grateful to have met new colleagues and especially friends. I would like to thank in particular Prof. David A. Rothery at Open University (Milton Keynes) and Mark A. Wieczorek at Institut de Physique du Globe (Paris) for welcoming me and for the time they dedicated to me during my working period abroad. I hope that in the near future I will have the opportunity to come back to Milton Keynes and Paris to remember the good times and meet up with friends.

I must also thank Prof. Fedi, who has always followed and supported me since my bachelor's degree and without whom perhaps I would never have begun this journey into the "planetary" world.

References

Airy, G. B. (1855). On the computations of the effect of the attraction of mountain masses. Philosophical Transactions of the Royal Society of London 145, 101-104.

Allmendinger, R. (1998). Inverse and forward numerical modeling of trishear fault-propagation folds. Tectonics, 17 (4), 640–656.

Anderson, B. J., Johnson, C. L., Korth, H., Purucker, M. E., Winslow, R. M., Slavin, J. A., Solomon, S. C., McNutt Jr, R. L., Raines, J. M. & Zurbuchen, T. H. (2011). The global magnetic field of Mercury from MESSENGER orbital observations. Science, 333(6051), 1859-1862. https://doi.org/10.1126/science.1211001

Andrews-Hanna, J. C., Asmar, S. W., Head III, J. W., Kiefer, W. S., Konopliv, A. S., Lemoine, F. G., et al. (2013). Ancient igneous intrusions and early expansion of the Moon revealed by GRAIL gravity gradiometry. Science, 339(6120), 675-678. https://doi.org/10.1126/science.1231753

Asmar, S. W., Konopliv, A. S., Watkins, M. M., Williams, J. G., Park, R. S., Kruizinga, G., Paik, M., Yuan, D.-N., Fahnestock, E., Strekalov, D., Harvey, N., Lu, W., Kahan, D., Oudrhiri, K., Smith, D. E., & Zuber, M. T. (2013). The scientific measurement system of the Gravity Recovery and Interior Laboratory (GRAIL) Mission. Space Science Reviews, 178(1), 25–55. https://doi.org/10.1007/s11214-013-9962-0

Baker D. M. H. (2016). Updated Catalogs of Peak-Ring Basins and Protobasins on Mars. 47th Lunar and Planetary Science Conference.

Baker, D. M., Head, J. W., Schon, S. C., Ernst, C. M., Prockter, L. M., Murchie, S. L., Denevi, B. W., Solomon, S. C. & Strom, R. G. (2011a). The transition from complex crater to peak-ring basin on Mercury: New observations from MESSENGER flyby data and constraints on basin formation models. Planetary and Space Science, 59(15), 1932-1948. https://doi.org/10.1016/j.pss.2011.05.010

Baker, D. M., Head, J. W., Fassett, C. I., Kadish, S. J., Smith, D. E., Zuber, M. T., & Neumann, G. A. (2011b). The transition from complex crater to peak-ring basin on the Moon: New observations from the Lunar Orbiter Laser Altimeter (LOLA) instrument. Icarus, 214(2), 377-393. https://doi.org/10.1016/j.icarus.2011.05.030

Barthelmes, F. (2013). Definition of functionals of the geopotential and their calculation from spherical harmonic models: theory and formulas used by the calculation service of the International Centre for Global Earth Models (ICGEM) (revised Edition). Helmholtz Centre Postdam, Postdam. https://doi.org/10.2312/GFZ.b103-0902-26

Barzaghi R., Migliaccio F., Reguzzoni M., Albertella A. (2015). The Earth gravity field in the time of satellites. Geodesy and geomatics to the edge. Rend. Fis. Acc. Lincei, 26 (Suppl 1), pp. S13-S23. doi: 10.1007/s12210-015-0382-9

Becker, K. J., Robinson, M. S., Becker, T. L., Weller, L. A., Edmundson, K. L., Neumann, G. A., Perry, M. E., & Solomon, S. C. (2016). First global digital elevation model of mercury. In 47th lunar and planetary science conference (p. 2959). Abstract No. 1903.

Benkhoff, J., et al. (2021). BepiColombo-mission overview and science goals. Space science reviews, 217(8), 90. https://doi.org/10.1007/s11214-021-00861-4

Benz, W., Slattery, W. L., & Cameron, A. G. W. (1988). Collisional stripping of Mercury's mantle. Icarus, 74(3), 516-528.

Besse, S., Doressoundiram, A., Barraud, O., Griton, L., Cornet, T., Munoz, C., Varatharajan, I., and Helbert, J. (2020). Spectral properties and physical extent of pyroclastic deposits on Mercury: Variability within selected deposits and implications for explosive volcanism. Journal of Geophysical Research: Planets, 125. https://doi.org/10.1029/2018JE005879

Beuthe, M., Charlier, B., Namur, O., Rivoldini, A. & Van Hoolst, T. (2020). Mercury's crustal thickness correlates with lateral variations in mantle melt production. Geophys. Res. Lett. 47, https://doi.org/10.1029/2020GL087261

Blakely R. J. (1996). Potential Theory in Gravity & Magnetic Applications. Cambridge University Press.

Blewett, D. T., Chabot, N. L., Denevi, B. W., Ernst, C. M., Head, J. W., Izenberg, N. R. et al. (2011). Hollows on Mercury: MESSENGER evidence for geologically recent volatile-related activity. Science, 333(6051), 1856–1859. doi:10.1126/science.1211681

Bouman, J. (2000). Quality Assessment of Satellite-Based Global Gravity Field Models. Netherlands Geodetic Commission, Delft.

Breuer, D., & Moore, W. B. (2007). In Planets and Moons. Treatise on Geophysics, ed. G. Schubert, Elsevier, 10, 299-348 (Amsterdam, 2007).

Broquet, A. & Wieczorek, M.A. (2019). The gravitational signature of Martian volcanoes. J. Geophys. Res. Planet 124 (8), 2054–2086. https://doi.org/10.1029/2019JE005959

Buoninfante, S., Milano, M., Negri, B., Plainaki, C., Sindoni, G., & Fedi, M. (2023). Gravity evidence for a heterogeneous crust of Mercury. Scientific Reports, 13(1). https://doi.org/10.1038/s41598-023-46081-4

Buoninfante, S., Wieczorek, M. A., Galluzzi, V., Ferranti, L., Milano, M. & Palumbo, P. (2024). Quantifying the size of impact basins on the Moon and Mars. In Europlanet Science Congress 2024, EPSC2024-484, 17. https://doi.org/10.5194/epsc2024-484

Byrne, P. K., Klimczak, C., Şengör, A. C., Solomon, S. C., Watters, T. R., Hauck S. A. (2014). Mercury’s global contraction much greater than earlier estimates. Nature Geoscience, 7 (4), pp. 301-307. https://doi.org/10.1038/ngeo2097

Byrne, P. K., Klimczak, C., & Celâl Şengör, A. M. (2018). The tectonic character of Mercury. In S. C. Solomon, L. R. Nittler, & B. J. Anderson (Eds.), Mercury: The view after

MESSENGER (pp. 249–286). Cambridge University Press. https://doi.org/10.1017/9781316650684.011

Byrne, P.K., Ostrach, L.R., Fassett, C.I., Chapman, C.R., Denevi, B.W., Evans, A.J. & Solomon, S.C. (2016). Widespread effusive volcanism on Mercury likely ended by about 3.5Ga. Geophysical Research Letters, 43(14), 7408–7416. https://doi.org/10.1002/2016GL069412

Cameron, A. G. W. (1985). The partial volatilization of Mercury. Icarus, 64(2), 285-294.

Canale, M., Wright, J. & Rothery, D.A. (2024). A hybrid geological map of Sibelius Crater on Mercury, and its associated ejecta and impact melt deposits. Geological Society, London, Special Publications, 541(1), 153-180. https://doi.org/10.1144/SP541-2022-29

Cartier, C., Namur, O., Nittler, L. R., Weider, S. Z., Crapster-Pregont, E., Vorburger, A., Frank, E. A., Charlier, B. (2020). No FeS layer in Mercury? Evidence from Ti/Al measured by MESSENGER. Earth and Planetary Science Letters, 534 (116108), pp. 1-11. https://doi.org/10.1016/j.epsl.2020.116108

Cavanaugh, J. F., Smith, J. C., Sun, X., Bartels, A. E., Ramos-Izquierdo, L., Krebs, D. J., et al. (2007). The Mercury Laser Altimeter instrument for the MESSENGER mission. Space Science Reviews, 131, 451-479. https://doi.org/10.1007/s11214-007-9273-4

Cella, F., Fedi, M., & Florio, G. (2009). Toward a full multiscale approach to interpret potential fields. Geophysical Prospecting, 57(4), 543-557. https://doi.org/10.1111/j.1365-2478.2009.00808.x

Chahine, M. T., A'Hearn, M. F., & Rahe, J. H. (2013). Comparative Planetology with an Earth Perspective: Proceedings of the First International Conference Held in Pasadena, California, June 6–8, 1994. Springer Science & Business Media.

Chappaz, L. et al. (2017). Evidence of large empty lava tubes on the Moon using GRAIL gravity. Geophys. Res. Lett. 44, 105-112 https://doi.org/10.1002/2016GL071588

Collins, G. S., Melosh, H. J., Morgan, J. V., & Warner, M. R. (2002). Hydrocode simulations of Chicxulub crater collapse and peak-ring formation. Icarus, 157(1), 24-33. https://doi.org/10.1006/icar.2002.6822

Colombo, G. & Shapiro, I. I. (1966). The rotation of the planet Mercury. Astrophys. J. 145, 295–307. https://doi.org/10.1086/148762

Cook, A. C., & Robinson, M. S. (2000). Mariner 10 stereo image coverage of Mercury. Journal of Geophysical Research: Planets, 105(E4), 9429-9443. https://doi.org/10.1029/1999JE001135

Cooper, G. R. J., & Cowan, D. R. (2006). Enhancing potential field data using filters based on the local phase. Computers & Geosciences, 32(10), 1585-1591. https://doi.org/10.1016/j.cageo.2006.02.016

Cordell L. (1979). Gravimetric expression of graben faulting in Santa Fe Country and the Espanola Basin, New Mexico. Geological Society Guidebook, 30th Field Conference, New Mexico, 59–64. https://doi.org/10.56577/FFC-30.59

Correia, A. C., & Laskar, J. (2004). Mercury's capture into the 3/2 spin-orbit resonance as a result of its chaotic dynamics. Nature, 429(6994), 848-850. https://doi.org/10.1038/nature02609

Crameri, F. (2018). Scientific colour maps. Zenodo. http://doi.org/10.5281/zenodo.1243862

Crane, K. T., & Klimczak, C. (2017). Timing and rate of global contraction on Mercury. Geophysical Research Letters, 44(7), 3082-3089. https://doi.org/10.1002/2017GL072711

Crane, K. T. & Klimczak, C. (2019). Tectonic patterns of shortening landforms in Mercury's Northern Smooth Plains, Icarus, 317, 66–80. https://doi.org/10.1016/j.icarus.2018.05.034

Cremonese, G., Capaccioni, F., Capria, M. T., Doressoundiram, A., Palumbo, P., Vincendon, M., et al. (2020). SIMBIO-SYS: scientific cameras and spectrometer for the BepiColombo mission. Space science reviews, 216, 1-78. https://doi.org/10.1007/s11214-020-00704-8

Davies, M. E., Dornik, S. E., Gault, D. E. & Strom, R. G. (1978). Atlas of Mercury. NASA Special Publication, 423.

De Marchi, F., Cappuccio, P., Mitri, G., & Iess, L. (2022). Frequency-dependent Ganymede's tidal Love number k2 detection by JUICE's 3GM experiment and implications for the subsurface ocean thickness. Icarus, 386, 115150. https://doi.org/10.1016/j.icarus.2022.115150

DeHon, R. A., Scott, D. H., & Underwood, J. R. (1981). Geologic Map of the Kuiper Quadrangle of Mercury.

Denevi, B. W., Chabot, N. L., Murchie, S. L., Becker, K. J., Blewett, D. T., Domingue, D. L., Ernst, C. M., Hash, C. D., Hawkins, S. E., Keller, M. R., & Laslo, N. R. (2018). Calibration, projection, and final image products of MESSENGER's mercury dual imaging system. Space Science Reviews, 214(1), 1–52. https://doi.org/10.1007/s11214-017-0440-y

Denevi, B. W., Ernst, C. M., Meyer, H. M., Robinson, M. S., Murchie, S. L., Whitten, J. L., Head, J. W., Watters, T. R., Solomon, S. C., Ostrach, L. R., Chapman, C. R., Byrne, P. K., Klimczak, C., Peplowski, P. N. (2013). The distribution and origin of smooth plains on Mercury. Journal of Geophysical Research: Planets, 118(5), pp. 891-907. https://doi.org/10.1002/jrge.20075

Denevi, B. W., Robinson, M. S., Solomon, S. C., Murchie, S. L., Blewett, D. T., Domingue, D. L., McCoy, T. J., Ernst, C. M., Head, J. W., Watters, T. R., & Chabot, N. L. (2009). The evolution of Mercury's crust: A global perspective from MESSENGER. Science, 324(5927), 613–618. https://doi.org/10.1126/science.1172226

Di Achille, G., Popa, C., Massironi, M., Mazzotta Epifani, E., Zusi, M., Cremonese, G. & Palumbo, P. (2012). Mercury's radius change estimates revisited using MESSENGER data. Icarus, 221 (1), 456–460. DOI: 10.1016/j.icarus.2012.07.005.

Ding, M., Soderblom, J. M., Bierson, C. J. & Zuber, M. T. (2021). Investigating the influences of crustal thickness and temperature on the uplift of mantle materials beneath large impact craters on the Moon. J. Geophys. Res. Planets 126, https://doi.org/10.1029/2020JE006533

Dollfus, A., Chapman, C. R., Davies, M. E., Gingerich, O., Goldstein, R., Guest, J., Morrison, D. and Smith, B. A. (1978). IAU Nomenclature for Albedo Features on the Planet Mercury. Icarus, 34, 210-214.

Dombard, A. J. & Hauck, S. A. (2008). Despinning plus global contraction and the orientation of lobate scarps on Mercury: Predictions for MESSENGER. Icarus 198, 274-276 https://doi.org/10.1016/j.icarus.2008.06.008

Dzurisin, D. (1978). The tectonic and volcanic history of Mercury as inferred from studies of scarps, ridges, troughs, and other lineaments. Journal of Geophysical Research: Solid Earth (1978–2012), 83 (B10), 4883–4906, DOI: 10.1029/JB083iB10p04883.

Ebbing, J., Haas, P., Ferraccioli, F. et al. (2018). Earth tectonics as seen by GOCE - Enhanced satellite gravity gradient imaging. Sci. Rep. 8, 16356 https://doi.org/10.1038/s41598-018-34733-9

Ebbing, J., Bouman, J., Fuchs, M., Lieb, V., Haagmans, R., Meekes, J. A. C., & Fattah, R. A. (2013). Advancements in satellite gravity gradient data for crustal studies. The leading edge, 32(8), 900-906. https://doi.org/10.1190/tle32080900.1

Edmundson, K. L., Cook, D. A., Thomas, O. H., Archinal, B. A., & Kirk, R. L. (2012). Jigsaw: The ISIS3 bundle adjustment for extraterrestrial photogrammetry. ISPRS Annals of the Photogrammetry, Remote Sensing and Spatial Information Sciences, 1, 203-208.

Elgner, S., Stark, A., Oberst, J., Perry, M. E., Zuber, M. T., Robinson, M. S., & Solomon, S. C. (2014). Mercury′ s global shape and topography from MESSENGER limb images. Planetary and Space Science, 103, 299-308. https://doi.org/10.1016/j.pss.2014.07.019

Erslev, E., (1991). Trishear fault-propagation folding. Geology,19, 617–620.

Evans, A. J., Brown, S. M. and Solomon S. C. (2015). Characteristics of early mantle convection and melting on Mercury, in Proc. 45th Lunar Planet. Sci. Conf., vol. 45, LPI Contribution 2414, Woodlands, Tex.

Evjen H.M. (1936). The place of the vertical gradient in gravitational interpretations. Geophysics 1, 127-136.

Fassett, C. I. et al. (2012). Large impact basins on Mercury: Global distribution, characteristics, and modification history from MESSENGER orbital data. J. Geophys. Res. Planets 117, https://doi.org/10.1029/2012JE004154

Fedi, M. (2002a). Multiscale derivative analysis: A new tool to enhance detection of gravity source boundaries at various scales. Geophysical Research Letters, 29(2), 16-1. https://doi.org/10.1029/2001GL013866

Fedi, M. (2002b). Correction to "Multiscale derivative analysis: A new tool to enhance detection of gravity source boundaries at various scales" by Maurizio Fedi. Geophysical Research Letters, 29(18), 8-1. https://doi.org/10.1029/2002GL015644

Fedi, M. & Florio, G. (2001). Detection of potential fields source boundaries by enhanced horizontal derivative method. Geophysical Prospecting, 49, 40-58. https://doi.org/10.1046/j.1365-2478.2001.00235.x

Fedi, M. & Florio, G. (2002). A stable downward continuation by using the ISVD method. Geophys. J. Int. 151, 146-156 https://doi.org/10.1046/j.1365-246X.2002.01767.x

Fegan, E. R., Rothery, D. A., Marchi, S., Massironi, M., Conway, S. J., & Anand, M. (2017). Late movement of basin-edge lobate scarps on Mercury. Icarus, 288, 226-234. https://doi.org/10.1016/j.icarus.2017.01.005

Frank, E. A., Potter, R. W., Abramov, O., James, P. B., Klima, R. L., Mojzsis, S. J., & Nittler, L. R. (2017). Evaluating an impact origin for Mercury's high‐magnesium region. Journal of Geophysical Research: Planets, 122(3), 614-632. https://doi.org/10.1002/2016JE005244

Galiano, A., Capaccioni, F., Filacchione, G., & Carli, C. (2022). Spectral identification of pyroclastic deposits on Mercury with MASCS/MESSENGER data. Icarus, 388, 115233.

Galluzzi, V., Ferranti, L., Massironi, M., Giacomini, L., Guzzetta, L., & Palumbo, P. (2019). Structural analysis of the Victoria quadrangle fault systems on Mercury: Timing, geometries, kinematics, and relationship with the high‐Mg region. Journal of Geophysical Research: Planets, 124(10), 2543-2562. https://doi.org/10.1029/2019JE005953

Galluzzi, V., Guzzetta, L. G., Ferranti, L., Di Achille, G., Rothery, D. A., & Palumbo, P. (2016). Geology of the Victoria quadrangle (H02), Mercury. Journal of Maps, 12, 227–238. https://doi.org/10.1080/17445647.2016.1193777

Galluzzi, V. (2019). Multi-mapper projects: Collaborative Mercury mapping. In H. Hargitai (Ed.), Planetary Cartography and GIS, Lecture Notes in Geoinformation and Cartography (pp. 207–218). https://doi.org/10.1007/978-3-319-62849-3_9

Galluzzi, V., Rothery, D. A., Blance, A., Buoninfante, S., Giacomini, L., Guzzetta, L., Lennox, A. R., Man, B., Sepe, A., Tognon, G., Wright, J., Massironi, M., Ferranti, L. (2024). Update on the Quadrangle Geological Map Series of Mercury. Abstract Booklet, Mercury 2024, Kyoto, Japan.

Gaposchkin E.G., (1974). Earth's gravity field to the eighteenth degree and geocentric coordinates for 104 stations from satellite and terrestrial data. J. Geophys. Res., 79, pp. 5377-5411.

Gault, D. E., Guest, J. E., Murray, J. B., Dzurisin, D., & Malin, M. C. (1975). Some comparisons of impact craters on Mercury and the Moon. Journal of Geophysical Research, 80(17), 2444-2460.

Gault, D.E., Quaide, W.L., Oberbeck, V.R. (1968). Impact cratering mechanics and structures. In: French, B.M., Short, N.M. (Eds.), Shock Metamorphism in Natural Materials. Mono Book Corp., Baltimore, 87-99.

Genova, A., Goossens, S., Lemoine, F. G., Mazarico, E., Neumann, G. A., Smith, D. E., & Zuber, M. T. (2016). Seasonal and static gravity field of Mars from MGS, Mars Odyssey and MRO radio science. Icarus, 272, 228-245. https://doi.org/10.1016/j.icarus.2016.02.050

Genova, A. et al. (2019). Geodetic evidence that Mercury has a solid inner core. Geophys. Res. Lett. 46, 3625-3633 https://doi.org/10.1029/2018GL081135.

Genova, A., Hussmann, H., Van Hoolst, T. et al. (2021). Geodesy, Geophysics and Fundamental Physics Investigations of the BepiColombo Mission. Space science reviews 217, 31. https://doi.org/10.1007/s11214-021-00808-9

Genova, A. et al. (2023). Regional variations of Mercury's crustal density and porosity from MESSENGER gravity data. Icarus 391, https://doi.org/10.1016/j.icarus.2022.115332

Giacomini, L., Galluzzi, V., Massironi, M., Ferranti, L., & Palumbo, P. (2022). Geology of the Kuiper quadrangle (H06), Mercury. Journal of Maps, 18, 246–257. https://doi.org/10.1080/17445647.2022.2035268

Glazner, A. F., & Bartley, J. M. (1994). Eruption of alkali basalts during crustal shortening in southern California. Tectonics, 13(2), 493-498. https://doi.org/10.1029/93TC03491

Goossens, S., Genova, A., James, P. B. & Mazarico E. (2022). Estimation of crust and lithospheric properties for Mercury from high-resolution gravity and topography. Planet. Sci. J. 3, https://doi.org/10.3847/PSJ/ac703f

Goossens, S., Lemoine, F. G., Sabaka, T. J., Nicholas, J. B., Mazarico, E., Rowlands, D. D., Loomis, B. D., Chinn, D. S., Neumann, G. A., Smith, D. E., & Zuber, M. T. (2016). A Global Degree and Order 1200 Model of the Lunar Gravity Field Using GRAIL Mission Data. In 47th Lunar and Planetary Science Conference, abstract 1484, The Woodlands, Texas, USA.

Goossens, S., Sabaka, T. J., Genova, A., Mazarico, E., Nicholas, J. B., Neumann, A. A. (2017). Evidence for a low bulk crustal density for Mars from gravity and topography. Geophys. Res. Lett. 44, 7686–7694 https://doi.irg/10.1002/2017GL074172

Goossens, S., Sabaka, T. J., Wieczorek, M. A., Neumann, G. A., Mazarico, E., Lemoine, F. G., Nicholas, J. B., Smith, D. E. & Zuber, M. T. (2020). High-resolution gravity field models from GRAIL data and implications for models of the density structure of the Moon's crust. Journal of Geophysical Research: Planets, 125(2), e2019JE006086. https://doi.org/10.1029/2019JE006086

Grolier, M. J., & Boyce, J. M. (1984). Geologic map of the Borealis region (H-1) of Mercury. USGS Miscellaneous Investigations Series Map I–1660 1–1.

Grombein T., Seitz K., Heck B. (2013). Optimized formulas for the gravitational field of a tesseroid. J. Geod., 87, pp. 645-660. doi: 10.1007/s00190-013-0636-1.

Grott, M. & Wieczorek, M.A. (2012). Density and lithospheric structure at Tyrrhena Patera, Mars, from gravity and topography data. Icarus 221, 43-52 https://doi.org/10.1016/j.icarus.2012.07.008

Guest, J. E., & Greeley, R. (1983). Geologic Map of the Shakespeare Quadrangle of Mercury.

Gulick, S. P. S., Christeson, G. L., Barton, P. J., Grieve, R. A. F., Morgan, J. V., & Urrutia-Fucugauchi, J. (2013). Geophysical characterization of the Chicxulub impact crater. Reviews of Geophysics, 51(1), 31-52. https://doi.org/10.1002/rog.20007

Guzzetta, L. G., Galluzzi, V., Ferranti, L., & Palumbo, P. (2017). Geology of the Shakespeare quadrangle (H03), Mercury. Journal of Maps, 13, 227–238. https://doi.org/10.1080/17445647.2017.1290556

Hall, G. P., Martindale, A., Bridges, J. C., Nittler, L. R., & Bunce, E. J. (2021). The Distribution of Peak-Ring Basins on Mercury and Their Correlation With the High-Mg/Si Terrane. Journal of Geophysical Research: Planets, 126(9), e2021JE006839.

Hauber, E., Naß, A., Skinner, J. A., & Huff, A. (2020). Planetary Geologic Mapping. https://doi.org/10.1007/978-3-319-62849-3_5

Hauck, S. A., Dombard, A. J., Phillips, R. J. & Solomon, S. C. (2004). Internal and tectonic evolution of Mercury. Earth Planet. Sci. Lett. 222, 713-728. https://doi.org/10.1016/j.epsl.2004.03.037

Hauck, S. A., II et al. (2013), The curious case of Mercury's internal structure, J. Geophys. Res. Planets, 118, 1204–1220, doi:10.1002/jgre.20091.

Hawkins, S. E., Boldt, J. D., Darlington, E. H., Espiritu, R., Gold, R. E., Gotwols, B., Grey, M. P., Hash, C. D., Hayes, J. R., Jaskulek, S. E., Kardian, C. J. et al. (2007). The Mercury dual imaging system on the MESSENGER spacecraft. Space Science Reviews, 131(1), 247–338. https://doi.org/10.1007/s11214-007-9266-3

Head, J. W. et al. (2009). Evidence for intrusive activity on Mercury from the first MESSENGER flyby. Earth Planet. Sci. Lett. 285, 251-262 https://doi.org/10.1016/j.epsl.2009.03.008

Head III, J. W., Fassett, C. I., Kadish, S. J., Smith, D. E., Zuber, M. T., Neumann, G. A., & Mazarico, E. (2010). Global distribution of large lunar craters: Implications for resurfacing and impactor populations. Science, 329(5998), 1504-1507. https://doi.org/10.1126/science.1195050

Herrero-Gil, A., Ruiz, J., & Romeo, I. (2020). 3D modeling of planetary lobate scarps: The case of Ogygis Rupes, Mars. Earth and Planetary Science Letters, 532, 116004. https://doi.org/10.1016/j.epsl.2019.116004

Hirt, C., Kuhn M., Featherstone, W. E. & Göttl, F. (2012). Topographic/isostatic evaluation of new-generation GOCE gravity field models. J. Geophys. Res. Solid Earth 117, B05407, 1-16 https://doi.org/10.1029/2011JB008878

Hofmann-Wellenhof B. & Moritz H. (2005). Physical geodesy. Springer – Verlag Wien, Austria.

Hsu S., Coppens D. and Shyu C. (1998). Depth to magnetic source using the generalized analytic signal. Geophysics 63, 1947-1957.

Hsu S., Sibuet J.C. and Shyu C. (1996). High-resolution detection of geologic boundaries from potential field anomalies: an enhanced analytic signal technique. Geophysics 61, 373-386.

Hubbard, A. (2014). Explaining Mercury's density through magnetic erosion. Icarus, 241, 329-335. https://doi.org/10.1016/j.icarus.2014.06.032

Iess, L., & Boscagli, G. (2001). Advanced radio science instrumentation for the mission BepiColombo to Mercury. Planetary and Space Science, 49(14-15), 1597-1608. https://doi.org/10.1016/S0032-0633(01)00096-4

Iess, L., Asmar, S. W., Cappuccio, P., Cascioli, G., De Marchi, F., Di Stefano, I., et al. (2021). Gravity, geodesy and fundamental physics with BepiColombo's MORE investigation. Space Science Reviews, 217(1), 21. https://doi.org/10.1007/s11214-021-00800-3

James, P. B. (2013). Geophysical insights into the histories of Venus, Mercury, and the Moon (Ph. D. Thesis). Massachusetts Institute of Technology.

James, P. B., Zuber, M. T., Phillips, R. J. & Solomon S. C. (2015). Support of long-wavelength topography on Mercury inferred from MESSENGER measurements of gravity and topography. J. Geophys. Res. Planets 120, 287–310 https://doi.org/10.1002/2014JE004713

James, P. B., Phillips, R. J., Grott, M., Hauck, S. A. & Solomon, S. C. (2016). The thickness of Mercury's lithosphere inferred from MESSENGER gravity and topography. In 47th Lunar and Planetary Science Conference.

Jet Propulsion Laboratory (JPL), (1976). MVM '73 stereo data package user guide, Pasadena, California.

Johnson, C. L. et al. (2000). Lithospheric loading by the Northern Polar Cap on Mars. Icarus 144, 313-328 https://doi.org/10.1006/icar.1999.6310

Jozwiak, L. M., Head, J. W., Wilson, L. (2018). Explosive volcanism on Mercury: Analysis of vent and deposit morphology and modes of eruption. Icarus, 302, 191-212. https://doi.org/10.1016/j.icarus.2017.11.011

Kaku, T. et al. (2017). Detection of intact lava tubes at Marius Hills on the Moon by SELENE (Kaguya) Lunar Radar Sounder. Geophys. Res. Lett. 44, 10,155-10,161 https://doi.org/10.1002/2017GL074998

Kenkmann, T., Poelchau, M. H., & Wulf, G. (2014). Structural geology of impact craters. Journal of Structural Geology, 62, 156-182.

Kennedy, M., & Kopp, S. (2004). Understanding Map Projections GIS by ESRI, in: GIS by ESRI. Environmental Systems Research Institute, Inc., pp. 1–116.

Killen, R. M., & Ip, W. H. (1999). The surface-bounded atmospheres of Mercury and the Moon. Reviews of Geophysics, 37(3), 361-406. https://doi.org/10.1029/1999RG900001

Kinczyk, M. J., Prockter, L. M., Byrne, P. K., Denevi, B. W., Ostrach, L. R., & Skinner, J. A. (2018). A global geological map of Mercury. Mercury: Current and future science of the innermost planet, Columbia, Maryland, p. Abstract #6123.

Kinczyk, M. J., Prockter, L. M., Byrne, P. K., Denevi, B. W., Buczkowski, D. L., Ostrach, L. R., & Miller, E. B. (2019). The first global geological map of Mercury. EPSC-DPS Joint Meeting, 13, 1045.

Kinczyk, M. J., Prockter, L. M., Byrne, P. K., Susorney, H. C., & Chapman, C. R. (2020). A morphological evaluation of crater degradation on Mercury: Revisiting crater classification with MESSENGER data. Icarus, 341, 113637. https://doi.org/10.1016/j.icarus.2020.113637

King, S. D. (2008). Pattern of lobate scarps on Mercury's surface reproduced by a model of mantle convection, Nat. Geosci., 1, 229–232. https://doi.org/10.1038/ngeo152

King, J. S., & Scott, D. H. (1990). Geologic Map of the Beethoven Quadrangle of Mercury.

Klima, R. L., Denevi, B. W., Ernst, C. M., Murchie, S. L., & Peplowski, P. N. (2018). Global distribution and spectral properties of low-reflectance material on Mercury. Geophysical Research Letters, 45(7), 2945-2953.

Klimczak, C., Watters, T. R., Ernst, C. M., Freed, A. M., Byrne, P. K., Solomon, S. C., Blair, D. M., & Head, J. W. (2012). Deformation associated with ghost craters and basins in volcanic smooth plains on Mercury: Strain analysis and implications for plains evolution. Journal of Geophysical Research: Planets, 117(E12). https://doi.org/10.1029/2012JE004100

Klimczak, C. et al. (2013). Insights into the subsurface of the Caloris basin, Mercury, from assessing of mechanical layering and changes in long-wavelength topography. J. Geophys. Res. Planets, 118, 2030-2044 https://doi.org/10.1002/jgre.20157

Klimczak, C., Byrne, P. K., & Solomon, S. C. (2015). A rock-mechanical assessment of Mercury's global tectonic fabric. Earth and Planetary Science Letters, 416, 82–90, DOI: 10.1016/j.epsl.2015.02.003.

Klipstein, W., Arnold, B., Enzer, D., Ruiz, A., Tien, J., Wang, R., & Dunn, C. (2013). The lunar Gravity Ranging System for the Gravity Recovery and Interior Laboratory (GRAIL) Mission. Space Science Reviews, 178(1), 57–76. https://doi.org/10.1007/s11214-013-9973-x

Konopliv, A. S., Banerdt, W. B. & Sjogren, W. L. (1999). Venus Gravity: 180th degree and order model. Icarus 139, 3-18.

Konopliv, A. S., Park, R. S. & Ermakov, E. I. (2020). The Mercury gravity field, orientation, love number, and ephemeris from the MESSENGER radiometric tracking data. Icarus 335, https://doi.org/10.1016/j.icarus.2019.07.020

Konopliv, A. S., Park, R. S., Yuan, D.-N., Asmar, S. W., Watkins, M. M., Williams, J. G., Fahnestock, E., Kruizinga, G., Paik, M., Strekalov, D., Harvey, N., Smith, D. E., & Zuber, M. T. (2013). The JPL lunar gravity field to spherical harmonic degree 660 from the GRAIL Primary Mission. Journal of Geophysical Research: Planets, 118, 1415–1434. https://doi.org/10.1002/jgre.20097

Konopliv, A. S., Park, R. S., Yuan, D.-N., Asmar, S. W., Watkins, M. M., Williams, J. G., Fahnestock, E., Kruizinga, G., Paik, M., Strekalov, D., Harvey, N., Smith, D. E., & Zuber, M. T. (2014). High-resolution lunar gravity fields from the GRAIL Primary and Extended Missions. Geophysical Research Letters, 41, 1452–1458. https://doi.org/10.1002/2013GL059066

Kring, D. A., Tikoo, S. M., Schmieder, M., Riller, U., Rebolledo-Vieyra, M., Simpson, S. L. et al. (2020). Probing the hydrothermal system of the Chicxulub impact crater. Science Advances, 6(22), eaaz3053. https://doi.org/10.1126/sciadv.aaz3053

Lemoine, F. G., Goossens, S., Sabaka, T. J., Nicholas, J. B., Mazarico, E., Rowlands, D. D., Loomis, B. D., Chinn, D. S., Caprette, D. S., Neumann, G. A., Smith, D. E., & Zuber, M. T. (2013). High-degree gravity models from GRAIL primary mission data. Journal of Geophysical Research: Planets, 118, 1676–1698. https://doi.org/10.1002/jgre.20118

Lemoine, F. G., Goossens, S., Sabaka, T. J., Nicholas, J. B., Mazarico, E., Rowlands, D. D., Loomis, B. D., Chinn, D. S., Neumann, G. A., Smith, D. E., & Zuber, M. T. (2014). GRGM900C: A degree-900 lunar gravity model from GRAIL primary and extended mission data. Geophysical Research Letters, 41, 3382–3389. https://doi.org/10.1002/2014GL060027

Lewang, A. M., Hiesinger, H., Bernhardt, H., Galluzzi, V., Guzzetta, L., & Massironi, M. (2018). Preliminary geologic map of the Beethoven basin, Mercury. In 49th Annual Lunar and Planetary Science Conference (No. 2083, p. 1846).

Loveless, S. R., Klimczak, C., McCullough, L. R., Crane, K. T., Holland, S. M., & Byrne, P. K. (2024). A statistical evaluation of the morphological variability of shortening landforms on Mercury. Icarus, 416, 116106. https://doi.org/10.1016/j.icarus.2024.116106

Lowrie, W. (2007). Fundamental of Geophysics (Second Edition). Cambridge Univ. Press, Cambridge.

Lucchetti, A., et al. (2018). Mercury Hollows as Remnants of Original Bedrock Materials and Devolatilization Processes: A Spectral Clustering and Geomorphological Analysis. JGR: Planets 123, Issue 9, 2365-2379. https://doi.org/10.1029/2018JE005722

Ma, G., & Li, L. (2012). Edge detection in potential fields with the normalized total horizontal derivative. Computers & Geosciences, 41, 83-87. https://doi.org/10.1016/j.cageo.2011.08.016

Malliband, C. C., Rothery, D. A., Balme, M. R., Conway, S. J., Pegg, D. L., & Wright, J. (2023). Geology of the Derain quadrangle (H10), Mercury. Journal of Maps, 1–10. https://doi.org/10.1080/17445647.2022.2112774

Man, B., Rothery, D. A., Balme, M. R., Conway, S. J., & Wright, J. (2023a). Widespread small grabens consistent with recent tectonism on Mercury. Nature Geoscience, 16(10), 856-862. https://doi.org/10.1038/s41561-023-01281-5

Man, B., Rothery, D. A., Balme, M. R., Conway, S. J., Wright, J., Pegg, D L., Lennox, A. R. & Buoninfante, S. (2023b). Geology of the Neruda quadrangle (H13), Mercury, Journal of Maps, 19:1, DOI: 10.1080/17445647.2023.2256353.

Mancinelli, P., Minelli, F., Pauselli, C., & Federico, C. (2016). Geology of the Raditladi quadrangle, Mercury (H04). Journal of Maps, 12, 190–202. https://doi.org/10.1080/17445647.2016.1191384

Manheim, M. R. et al. (2022). High-resolution regional digital elevation models and derived products from MESSENGER MDIS images. Remote Sens. 14, 3564 https://doi.org/10.3390/rs14153564

Marchi, S., Chapman, C. R., Fassett, C. I., Head, J. W., Bottke, W. F., & Strom, R. G. (2013). Global resurfacing of Mercury 4.0-4.1 billion years ago by heavy bombardment and volcanism. Nature, 499, 59–61.

Marchi, S., Mottola, S., Cremonese, G., Massironi, M., & Martellato, E. (2009). A new chronology for the Moon and Mercury. The Astronomical Journal, 137(6), 4936. DOI:10.1088/0004-6256/137/6/4936

Margot, J. L., Peale, S. J., Jurgens, R. F., Slade, M. A., Holin, I. V. (2007). Large longitude libration of Mercury reveals a molten core. Science, 316 (5825), pp. 710-714. https://doi.org/10.1126/science.1140514.

Massironi, M., Cremonese, G., Marchi, S., Martellato, E., Mottola, S., Wagner, R. J. (2009). Mercury's geochronology revised by applying Model Production Function to Mariner 10 data: Geological implications. Geophysical Research Letter, 36, L21204. doi:10.1029/2009GL040353

Massironi, M., & Byrne, P. K. (2015). High-relief ridge. In H. Hargitai & Á. Kereszturi (Eds.), Encyclopedia of planetary landforms (pp. 932–934). New York: Springer. doi:10.1007/978-1-4614-3134-3

Massironi, M., Byrne, P. K., & van der Bogert, C. H. (2015). Lobate scarp. In H. Hargitai & Á. Kereszturi (Eds.), Encyclopedia of planetary landforms (pp. 1255–1262). New York: Springer. doi:10.1007/978-1-4614-3134-3

Matsuyama, I. & Nimmo, F. (2009). Gravity and tectonic patterns of Mercury: Effect of tidal deformation, spin-orbit resonance, nonzero eccentricity, despinning, and reorientation. Journal of Geophysical Research: Planets (1991–2012), 114 (E1), DOI: 10.1029/2008JE003252.

Mazarico, E. et al. (2014). The gravity field, orientation, and ephemeris of Mercury from MESSENGER observations after three years in orbit. J. Geophys. Res. Planets 119, https://doi.org/10.1002/2014JE004675.

Mazarico, E. et al. (2016). The gravity field of Mercury after MESSENGER. In 47th Lunar and Planetary Science Conference, no. 1903, p. 2022.

Mccauley, J. F., Guest, J. E., Schaber, G. G., Trask, N. J., & Greeley, R. (1981). Stratigraphy of the Caloris basin, Mercury. Icarus, 47(2), 184-202.

McGill, G. E., & King, E. A. (1983). Geologic Map of the Victoria Quadrangle of Mercury.

Melosh, H. J. (1989). Impact cratering: A geologic process. New York: Oxford University Press; Oxford: Clarendon Press.

Melosh, H J. (1996). Impact Cratering: A Geologic Process. Oxford Monographs on Geology and Geophysics 11.

Melosh, H. J. (1977). Global tectonics of a despun planet. Icarus, 31 (2), 221–243, DOI: 10.1016/0019-1035(77)90035-5.

Melosh, H. J. & Dzurisin, D. (1978). Mercurian global tectonics: A consequence of tidal despinning?. Icarus, 35 (2), 227–236, DOI: 10.1016/0019-1035(78)90007-6.

Michel, N. C., Hauck, S. A., Solomon, S. C., et al. (2013). Thermal evolution of Mercury as constrained by MESSENGER observations. J. Geophys. Res. Planets 118, 1033-104 https://doi.org/10.1002/jgre.20049

Milani, A., Rossi, A., Vokrouhlický, D., Villani, D., & Bonanno, C. (2001). Gravity field and rotation state of Mercury from the BepiColombo Radio Science Experiments. Planetary and Space Science, 49(14-15), 1579-1596. https://doi.org/10.1016/S0032-0633(01)00095-2

Miller, H. G., & Singh, V. (1994). Potential field tilt—a new concept for location of potential field sources. Journal of applied Geophysics, 32(2-3), 213-217. https://doi.org/10.1016/0926-9851(94)90022-1

Molodensky M., Eremeev V., Yurkina M. (1962). Methods for study of the external gravitational field and figure of the Earth. Transl. from Russian (1960), Israel Program for Scientific Translations.

Montanari, D., Minissale, A., Doveri, M., Gola, G., Trumpy, E., Santilano, A., & Manzella, A. (2017). Geothermal resources within carbonate reservoirs in western Sicily (Italy): A review. Earth-Science Reviews, 169, 180-201. https://doi.org/10.1016/j.earscirev.2017.04.016

Murchie, S. L., Watters, T. R., Robinson, M. S., Head, J. W., Strom, R. G., Chapman, C. R., Solomon, S. C., McClintock, W. E., Prockter, L. M., Domingue, D. L. & Blewett, D. T. (2008). Geology of the Caloris basin, Mercury: A view from MESSENGER. Science, 321 (5885), 73–76, DOI: 10.1126/science.1159261.

Murchie, S. L., Mick, A., Prockter, L. M., Rivkin, A., Guinness, E., & Ward, J. (2017). MDIS CDR/RDR SOFTWARE INTERFACE SPECIFICATION.

Murray, B. C. (1975). The Mariner 10 pictures of Mercury: An overview. Journal of Geophysical Research, 80(17), 2342-2344. https://doi.org/10.1029/JB080i017p02342

Nabighian M.N. (1984). Toward a three-dimensional automatic interpretation of potential field data via generalized Hilbert transforms: fundamental relations. Geophysics 49, 780-786.

Namur, O., & Charlier, B. (2017). Silicate mineralogy at the surface of Mercury. Nature Geoscience, 10, 9–13. https://doi.org/10.1038/ngeo2860

Naranjo, J. A., Villa, V., Ramírez, C., & Pérez de Arce, C. (2018). Volcanism and tectonism in the southern Central Andes: Tempo, styles, and relationships. Geosphere, 14(2), 626-641. https://doi.org/10.1130/GES01350.1

Neukum, G., Oberst, J., Hoffmann, H., Wagner, R., & Ivanov, B.A. (2001). Geologic evolution and cratering history of Mercury. Planetary and Space Science, 49(14-15), 1507–1521. https://doi.org/10.1016/S0032-0633(01)00089-7

Neumann, G. A., Zuber, M. T., Wieczorek, M. A., Head, J. W., Baker, D. M., Solomon, S. C. et al. (2015). Lunar impact basins revealed by Gravity Recovery and Interior Laboratory measurements. Science advances, 1(9), e1500852. https://doi.org/10.1126/sciadv.1500852

Neumann, G. A. et al. (2016). Mercury shape model from laser altimetry and planetary comparisons. In 47th Lunar and Planetary Science Conference, no. 1903, p. 2087. Retrieved from https://www.hou.usra.edu/meetings/lpsc2016/pdf/2087.pdf.

Nimmo, F. & Watters, T. R. (2004). Depth of faulting on Mercury: implications for heat flux and crustal and effective elastic thickness. Geophys. Res. Lett. 31, https://doi.org/10.1029/2003GL018847

Nittler, L. R., Starr, R. D., Weider, S. Z., McCoy, T. J., Boynton, W. V., Ebel, D. S., Ernst, C. M., Evans, L. G., Goldsten, J. O., Hamara, D. K., Lawrence, D. J., McNutt, R. L., Schlemm, C. E., Solomon, S. C., Sprague, A. L. (2011). The major-element composition of Mercury's surface from MESSENGER X-ray spectrometry. Science, 333 (6051), pp. 1847-1850. https://doi.org/10.1126/science.1211567.

Nittler, L. R. et al. (2020). Global major-element maps of Mercury from four years of MESSENGER X-ray spectrometer observations. Icarus, 345, https://doi.org/10.1016/j.icarus.2020.113716

Oberst, J., Preusker, F., Phillips, R. J., Watters, T. R., Head, J. W., Zuber, M. T., & Solomon, S. C. (2010). The morphology of Mercury's Caloris basin as seen in MESSENGER stereo topographic models. Icarus, 209(1), 230-238. https://doi.org/10.1016/j.icarus.2010.03.009

Oberst, J., Preusker, F., Stark, A., Matz, K. D., Gwinner, K., & Roatsch, T. (2017). High-resolution topography from MESSENGER orbital stereo imaging—the H7 quadrangle "Beethoven". Lunar Planet. Sci, 48, 1442.

Orgel, C., Fassett, C. I., Michael, G., Riedel, C., van der Bogert C. H., & Hiesinger, H. (2020). Re-examination of the population, stratigraphy, and sequence of Mercurian basins:

Implications for Mercury's early impact history and comparison with the Moon. Journal of Geophysical Research: Planets, 125. https://doi.org/10.1029/2019JE006212

Osinski, G. R. & Spray, J. G. (2005). Tectonics of complex crater formation as revealed by the Haughton impact structure, Devon Island, Canadian High Arctic. Meteoritics & Planetary Science 40, 12, 1813–1834.

Ostrach, L. R., Robinson, M. S., Whitten, J. L., Fassett, C. I., Strom, R. G., Head, J. W., & Solomon, S. C. (2015). Extent, age, and resurfacing history of the northern smooth plains on Mercury from MESSENGER observations. Icarus, 250, 602–622.

Padovan, S., Margot, J.-L., Hauck, S. A., Moore, W. B., & Solomon, S. C. (2014). The tides of Mercury and possible implications for its interior structure. J. Geophys. Res. Planets 119, 850-866 https://doi.org/10.1002/2013JE004459

Padovan, S., Wieczorek, M. A., Margot, J.-L., Tosi, N., & Solomon, S. C. (2015). Thickness of the crust of Mercury from geoid-to-topography ratios. Geophysical Research Letters, 42, 1029–1038. https://doi.org/10.1002/2014GL062487

Padovan, S., Tosi, N., Plesa, A.-C., & Ruedas, T. (2017). Impact-induced changes in source depth and volume of magmatism on Mercury and their observational signatures. Nature Communications, 8, 1945. https://doi.org/10.1038/s41467-017-01692-0

Pappa, F., Ebbing, J., Ferraccioli, F., & van der Wal, W. (2019). Modeling satellite gravity gradient data to derive density, temperature, and viscosity structure of the antarctic lithosphere. Journal of Geophysical Research: Solid Earth, 124, 12053–12076

Park, R. S., Konopliv, A. S., Yuan, D.-N., Asmar, S. W., Watkins, M. M., Williams, J. G., Smith, D. E., & Zuber, M. T. (2015). A high-resolution spherical harmonic degree 1500 lunar gravity field from the GRAIL mission. In American Geophysical Union Fall Meeting,San Francisco, California, USA. Paper 67307, abstract G41B-01.

Pegg, D. L., Rothery, D. A., Balme, M. R., Conway, S. J., Malliband, C. C., & Man, B. (2021a). Geology of the Debussy quadrangle (H14), Mercury. Journal of Maps, 17, 718–729. https://doi.org/10.1080/17445647.2021.1996478

Pegg, D. L., Rothery, D. A., Balme, M. R., & Conway, S. J. (2021b). Explosive vent sites on Mercury: Commonplace multiple eruptions and their implications. Icarus, 365, 114510. https://doi.org/10.1016/j.icarus.2021.114510

Perry, M. E. et al. (2015). The low-degree shape of Mercury. Geophys. Res. Lett. 42, 6951-6958 https://doi.org/10.1002/2015GL065101

Phillips, R. J. et al. (2018). Mercury's crust and lithosphere: structure and mechanics, in Mercury: The view after MESSENGER (eds Solomon, S. C., L. R. Nittler, L. R. & B. J. Anderson, B. J.), vol. 21, 52–84, (Cambridge Univ. Press, Cambridge).

Phipps Morgan, J. & Blackman, D.K. (1993). Inversion of combined gravity and bathymetry data for crustal structure: A prescription for downward continuation. Earth Planet. Sci. Lett. 119, 167–179 https://doi.org/10.1016/0012-821X(93)90014-Z

Pike, R.J. (1988). Geomorphology of impact craters on Mercury. In: Vilas, F., Chapman, C.R., Matthews, M.S. (Eds.), Mercury. University of Arizona Press, Tucson, Arizona, 165–273.

Plattner, A. M. & Johnson, C. L. (2021). Mercury's Northern Rise core field magnetic anomaly. Geophys. Res. Lett. 48, https://doi.org/10.1029/2021GL094695

Pratt, J. H. (1855). On the attraction of the Himalaya Mountains and of the elevated regions beyond upon the plumb-line in India. Transactions of the Royal Society of London, B 145.

Preusker, F., Oberst, J., Head, J. W., Watters, T. R., Robinson, M. S., Zuber, M. T., & Solomon, S. C. (2011). Stereo topographic models of Mercury after three MESSENGER flybys. Planetary and Space Science, 59(15), 1910-1917. https://doi.org/10.1016/j.pss.2011.07.005

Preusker, F., Stark, A., Oberst, J., Matz, K. D., Gwinner, K., Roatsch, T., & Watters, T. R. (2017a). Toward high-resolution global topography of Mercury from MESSENGER orbital stereo imaging: A prototype model for the H6 (Kuiper) quadrangle. Planetary and Space Science, 142, 26-37. https://doi.org/10.1016/j.pss.2017.04.012

Preusker, F., Oberst, J., Stark, A., Matz, K. D., Gwinner, K., & Roatsch, T. (2017b). High-resolution topography from MESSENGER orbital stereo imaging—the H3 quadrangle “Shakespeare”. Lunar Planet. Sci, 48, 1441.

Preusker, F., Oberst, J., Stark, A., & Burmeister, S. (2018). High-resolution topography of Mercury from MESSENGER orbital stereo imaging–the southern hemisphere quadrangles. The International Archives of the Photogrammetry, Remote Sensing and Spatial Information Sciences, 42, 1389-1394.

Qingyun, D., Fei, L., Jianguo, Y., Zhiyong, X. & Rodriguez, J. A. P. (2018). Buried impact features on Mercury as revealed by gravity data. J. Geophys. Res. Planets 123, 3005–3019. https://doi.org/10.1029/2018JE005801

Regan R. D., Marsh J. G., Vincent S. (1979). The application of satellite data to potential field studies. Geoexploration, 17, pp. 185-204.

Reid A.B., Allsop J.M., Granser H., Millett A.J. and Somerton I.W. (1990). Magnetic interpretation in three dimensions using Euler deconvolution. Geophysics 55, 80-91.

Reigber, C. (2005). Gravity field recovery from satellite tracking data. In Theory of satellite geodesy and gravity field determination (pp. 197-234). Berlin, Heidelberg: Springer Berlin Heidelberg.

Ritzer, J. A., Hauck, S. A. II, Barnouin, O. S., Solomon, S. C., Watters, T. R. (2010). Mechanical Structure of Mercury’s Lithosphere from MESSENGER Observations of Lobate Scarps. 41st Lunar and Planetary Science Conference.

Rivera-Valentin, E. G., and Barr, A. C. (2014). Estimating the size of late veneer impactors from impact-induced mixing on Mercury, Astrophys. J. Lett., 782, L8, doi:10.1088/2041-8205/782/1/L8.

Robinson, M. S., Murchie, S. L., Blewett, D. T., Domingue, D. L., Hawkins, S. E. III, Head, J. W., Holsclaw, G. M., McClintock, W. E., McCoy, T. J., McNutt, R. L. Jr., Prockter, L. M., Solomon, S. C., Watters, T. R. (2008). Reflectance and Color Variations on Mercury: Regolith Processes and Compositional Heterogeneity. Science 321, 66-69. doi:10.1126/science.1160080

Rodriguez, J. A. P., Domingue, D., Travis, B., Kargel, J. S., Abramov, O., Zarroca, M., Banks, M. E., Weirich, J., Lopez, A., Castle, N., Jianguo, Y. & Chuang, F. (2023). Mercury's Hidden Past: Revealing a Volatile-dominated Layer through Glacier-like Features and Chaotic Terrains. The Planetary Science Journal, 4(11), 219. DOI: 10.3847/PSJ/acf219

Roest W.R., Verhoef J. and Pilkington M. (1992). Magnetic interpretation using the 3-D analytic signal. Geophysics 57, 116-125.

Rothery, D. A. (2015). Planet Mercury: from pale pink dot to dynamic world. Springer. https://doi.org/10.1007/978-3-319-12117-8.

Rothery, D. A., & Massironi, M. (2010). Beagle Rupes–Evidence for a basal decollement of regional extent in Mercury's lithosphere. Icarus, 209(1), 256-261. https://doi.org/10.1016/j.icarus.2009.12.009

Rothery, D. A., Massironi, M., Alemanno, G., Barraud, O., Besse, S., Bott, N., et al. (2020). Rationale for BepiColombo studies of Mercury's surface and composition. Space science reviews, 216, 1-46. https://doi.org/10.1007/s11214-020-00694-7

Rummel R., Rapp R. H., Sunkel H., Tacherning C. C. (1988). Comparisons of Global Topographic/Isostatic Models to the Earth's Observed Gravity Field. Report No. 388, Department of Geodetic Science and Surveying, Ohio.

Sauro, F. et al. (2020). Lava tubes on Earth, Moon and Mars: a review on their size and morphology revealed by comparative planetology. Earth Sci. Rev. 209, 103288, https://doi.org/10.1016/j.earscirev.2020.103288

Schaber, G. G., & McCauley, J. F. (1980). Geologic Map of the Tolstoj Quadrangle of Mercury.

Schlemm, C. E., Starr, R. D., Ho, G. C., Bechtold, K. E., Hamilton, S. A., Boldt, J. D., et al. (2007). The X-Ray Spectrometer on the MESSENGER spacecraft. The Messenger Mission to Mercury, 393-415. https://doi.org/10.1007/978-0-387-77214-1_11

Sepe, A., Ferranti, L., Galluzzi, V., Schmidt, G. W., Buoninfante, S., and Palumbo, P. (2024). Tectonic influence of multi-ring basins: The case of Mercury's Discovery Quadrangle and the Andal-Coleridge basin., Europlanet Science Congress 2024, Berlin, Germany, 8–13 Sep 2024, EPSC2024-1106. https://doi.org/10.5194/epsc2024-1106

Skinner, J. A., Huff, A. E., Black, S. R., Buban, H. C., Fortezzo, C. M., Gaither, T. A., Hare, T. M., & Hunter, M. A. (2022). Planetary Geologic Mapping Protocol 2022: U.S. Geological Survey Techniques and Methods 11-B13.

Smith, D. E. et al. (2012). Gravity field and internal structure of Mercury from MESSENGER. Science 336, 214-217. https://doi.org/10.1126/science.1218809

Solomon, S. C. (1976). Some aspects of core formation in Mercury. Icarus, 28 (4), 509–521, DOI: 10.1016/0019-1035(76)90124-X.

Solomon, S. C. et al. (2001). The MESSENGER mission to Mercury: scientific objectives and implementation. Planet. Space Sci. 49, 1445-1465 https://doi.org/10.1016/S0032-0633(01)00085-X

Solomon, S. C., McNutt, R. L., Gold, R. E., Domingue, D. L. (2007). MESSENGER Mission Overview. Space Sci. Rev., 131, pp. 3-39. https://doi.org/10.1007/s11214-007-9247-6

Solomon, S. C. & Anderson, B. J. (2018). The MESSENGER mission: science and implementation overview, in Mercury: the view after MESSENGER (eds Solomon, S. C., Nittler, L. R. & Anderson, B. J.), vol. 21, 1-29, (Cambridge Univ. Press, Cambridge, 2018).

Sori, M. M. (2018). A thin, dense crust for Mercury. Earth Planet. Sci. Lett. 489, 92–99 https://doi.org/10.1016/j.epsl.2018.02.033

Sprague, A. L. (1990). A diffusion source for sodium and potassium in the atmospheres of Mercury and the Moon. Icarus, 84(1), 93-105. https://doi.org/10.1016/0019-1035(90)90160-B

Spudis, P. D., & Guest, J. E. (1988). Stratigraphy and geologic history of Mercury. Mercury, 118–164. U.S. Geological Survey.

Spudis, P. D., & Prosser, J. G. (1984). Geologic Map of the Michelangelo Quadrangle of Mercury. U.S. Geological Survey.

Srinivasan, D. K., Perry, M. E., Fielhauer, K. B., Smith, D. E., & Zuber, M. T. (2007). The radio frequency subsystem and radio science on the MESSENGER mission. Space Science Reviews, 131, 557-571. https://doi.org/10.1007/s11214-007-9270-7

Stark, A., Preusker, F., Oberst, J., Matz, K. D., Gwinner, K., & Roatsch, T. (2017). High-Resolution Topography from MESSENGER Orbital Stereo Imaging-The H5 Quadrangle" Hokusai". Lunar and planetary science, 48, 2287.

Stevenson, D. J. (2012). Mercury's mysteries start to unfold. Nature, 485, pp. 52-53. https://doi.org/10.1038/485052a

Stewart, S. T., Leinhardt, Z. M., & Humayun, M. (2013, March). Giant impacts, volatile loss, and the K/Th ratios on the Moon, Earth, and Mercury. In 44th Annual Lunar and Planetary Science Conference (No. 1719, p. 2306).

Strom, R. G. (1997). Mercury: an overview. Adv. Space Res. 19, 1471-1485 https://doi.org/10.1016/S0273-1177(97)00346-3

Strom, R. G., Malin, M. C., Leake, M. A., & Kozak, R. (1990). Geologic Map of The Bach (H-15) Quadrangle.

Strom, R. G., Trask, N. J., & Guest, J. E. (1975). Tectonism and volcanism on Mercury. Journal of Geophysical Research, 80(17), 2478–2507. doi:10.1029/JB080i017p02478

Szczech, C. C., Oberst, J., Stark, A., Hussmann, H., & Preusker, F. (2024). Impact structures on Mercury from MESSENGER data: Implications on their formation processes and crustal structure. Icarus, 116244. https://doi.org/10.1016/j.icarus.2024.116244

Tanaka, K. L., Skinner Jr., J. A., & Hare, T. M. (2011). Planetary geologic mappers handbook. USGS Astrogeology Science Center. Retrieved from http://astrogeology.usgs.gov/search/details/Docs/Mappers/PGM_Handbook_2011/pdf

Tenthoff, M, Wohlfarth, K. & Wöhler, C. (2020). High resolution digital terrain models of Mercury. Remote Sens. 12, 3989, https://doi.org/10.3390/rs12233989

Tenzer R., Foroughi I., Hirt C., Novak P., Pitonak M. (2019). How to Calculate Bouguer Gravity Data in Planetary Studies. Surveys in Geophysics, 40, pp. 107-132. https://doi.org/10.1007/s10712-018-9504-0

Tesauro, M., Kaban, M. K., & Cloetingh, S. A. (2012). Global strength and elastic thickness of the lithosphere. Global and Planetary Change, 90, 51-57. https://doi.org/10.1016/j.gloplacha.2011.12.003

Thomas, P. G., Masson, P., & Fleitout, L. (1982). Global volcanism and tectonism on Mercury: comparison with the Moon. Earth and Planetary Science Letters, 58(1), 95-103.

Thomas, R. J., Rothery, D. A., Conway, S. J., & Anand, M. (2014a). Hollows on Mercury: Materials and mechanisms involved in their formation. Icarus, 229, 221-235. https://doi.org/10.1016/j.icarus.2013.11.018

Thomas, R. J., Rothery, D. A., Conway, S. J., & Anand, M. (2014b). Mechanisms of explosive volcanism on Mercury: Implications from its global distribution and morphology, J. Geophys. Res. Planets, 119, 2239–2254. https://doi.org/10.1002/2014JE004692

Thomas, R. J., Rothery, D. A., Conway, S. J. & Anand, M. (2015). Explosive volcanism in complex impact craters on Mercury and the Moon: influence of tectonic regime on depth of magmatic intrusion. Earth Planet. Sci. Lett. 431, 164-172 https://doi.org/10.1016/j.epsl.2015.09.029

Thompson D.T. (1982). EULDPH: a new technique for making computer-assisted depth estimates from magnetic data. Geophysics 47, 31-37.

Thurston J.B. and Smith R.S. (1997). Automatic conversion of magnetic data to depth, dip and susceptibility contrast using the SPI method. Geophysics 62, 807-813.

Tibaldi, A., Pasquarè, F., & Tormey, D. (2010). Volcanism in reverse and strike-slip fault settings. In New frontiers in integrated solid earth sciences (pp. 315-348). Springer, Dordrecht. https://doi.org/10.1007/978-90-481-2737-5

Tobler, W. (1987). Measuring spatial resolution. Land Resources Information Systems Conference, 12–16.

Tosi, N., Grott, M., Plesa, A.-C and Breuer, D. (2013). Thermochemical evolution of Mercury's interior, J. Geophys. Res. Planets, 118, 2474–2487, doi:10.1002/jgre.20168.

Tosi, N. et al. (2015). Mercury's low-degree geoid and topography controlled by insolation-driven elastic deformation. Geophys. Res. Lett. 42, 7327–7335 https://doi.org/10.1002/2015GL065314

Trask, N. J., & Dzurisin, D. (1984). Geologic Map of the Discovery Quadrangle of Mercury.

Trask, N. J., & Guest, J. E. (1975). Preliminary geologic terrain map of Mercury. Journal of Geophysical Research, 80(17), 2461–2477. https://doi.org/10.1029/JB080i017p02461

Turcotte, D. L., Willemann, R. J., Haxby, W. F. & Norberry, J. (1981). Role of membrane stresses in the support of planetary topography. J. Geophys. Res. 86, B5, 3951-3959.

Turcotte, D. L., & Schubert, G. (2002). Geodynamics. Cambridge University Press. (New York).

Uieda L., Barbosa V. C. F., Braitenberg C. (2015). Tesseroids: Forward-modeling gravitational fields in spherical coordinates. Geophysics, 81, no. 5, pp. F41-F48. doi:10.1190/GEO2015-0204.1.

Vening Meinesz, F. A. (1931). Une nouvelle méthode pour la réduction isostatique régionale de l'intensité de la pesanteur. Bullettin Geodesique 29, 33-51.

Verduzco, B., Fairhead, J. D., Green, C. M., & MacKenzie, C. (2004). New insights into magnetic derivatives for structural mapping. The leading edge, 23(2), 116-119. https://doi.org/10.1190/1.1651454

Verma, A. K. & Margot, J. L. (2016). Mercury's gravity, tides, and spin from MESSENGER radio science data. J. Geophys. Res. Planets 121, 1627-1640 https://doi.org/10.1002/2016JE005037

Watters, T. R., Cook, A. C., & Robinson, M. S. (2001). Large-scale lobate scarps in the southern hemisphere of Mercury. Planetary and Space Science, 49(14-15), 1523-1530. https://doi.org/10.1016/S0032-0633(01)00090-3

Watters, T. R., James, P. B. & Selvans, M. M. (2021). Mercury's crustal thickness and contractional strain. Geophys. Res. Lett. 48, https://doi.org/10.1029/2021GL093528

Watters, T. R., and Nimmo, F. (2010). The tectonics of Mercury, in Planetary Tectonics, edited by T. R. Watters and R. A. Schultz, pp. 15–80, Cambridge Univ. Press, Cambridge.

Watters, T. R., Robinson, M. S. and Cook, A. C. (1998), Topography of lobate scarps on Mercury: New constraints on the planet's contraction, Geology, 26, 991–994.

Watters, T. R., Schultz, R. A., Robinson, M. S. & Cook, A. C. (2002). The mechanical and thermal structure of Mercury's early lithosphere. Geophys. Res. Lett. 29, https://doi.org/10.1029/2001GL014308

Watters, T. R., Selvans, M. M., Banks, M. E., Hauck, S. A., Becker, K. J., & Robinson, M. S. (2015). Distribution of large-scale contractional tectonic landforms on Mercury: Implications for the origin of global stresses. Geophysical Research Letters, 42(10), 3755-3763. https://doi.org/10.1002/2015GL063570

Watters, T. R., Solomon, S. C., Robinson, M. S., Head, J. W., André, S. L., Hauck II, S. A. & Murchie, S. L. (2009). The tectonics of Mercury: The view after MESSENGER's first flyby. Earth and Planetary Science Letters, 285 (3), 283–296, DOI: 10.1016/j.epsl.2009.01.025.

Watts, A. B. (2010). Crust and lithosphere dynamics. Treatise on Geophysics (ed Gerald Schubert), vol. 6.

Watts, A. B. & Moore, J. D. P. (2017). Flexural isostasy: constraints from gravity and topography power spectra. J. Geophys. Res. Solid Earth 122, 8417–8430 https://doi.org/10.1002/2017JB014571

Weider, S. Z., Nittler, L. R., Starr, R. D., McCoy, T. J., Stockstill-Cahill, K. R., Byrne, P. K., Denevi, B. W., Head, J. W., & Solomon, S. C. (2012). Chemical heterogeneity on Mercury's surface revealed by the MESSENGER X-Ray Spectrometer. Journal of Geophysical Research: Planets, 117(E12). https://doi.org/10.1029/2012JE004153

Weider, S. Z., Nittler, L. R., Starr, R. D., Crapster-Pregont, E. J., Peplowski, P. N., Denevi, B. W., Head, J. W. et al. (2015). Evidence for geochemical terranes on Mercury: Global mapping of major elements with MESSENGER's X-Ray Spectrometer. Earth and Planetary Science Letters, 416, 109-120. https://doi.org/10.1016/j.epsl.2015.01.023

Whitten, J. L., Head, J. W., Denevi, B. W., & Solomon, S. C. (2014). Intercrater plains on Mercury: Insights into unit definition, characterization, and origin from MESSENGER datasets. Icarus, 241, 97–113.

Wieczorek, M. A. (2015a). Gravity and Topography of the Terrestrial Planets. Treatise on Geophysics (Second Edition) 10, 153-193 https://doi.org/10.1016/B978-0-444-53802-4.00169-X

Wieczorek, M. A. (2015b). Spherical harmonic model of the shape of Earth's Moon: MoonTopo2600p [Dataset]. Zenodo. https://doi.org/10.5281/zenodo.3870924

Wieczorek, M. A. (2022). Insight crustal thickness archive [Data Set]. Zenodo. https://doi.org/10.5281/zenodo.6477509

Wieczorek, M. A., Broquet, A., McLennan, S. M., Rivoldini, A., Golombek, M., Antonangeli, D., et al. (2022). InSight constraints on the global character of the Martian crust. Journal of Geophysical Research: Planets, 127, e2022JE007298. https://doi.org/10.1029/2022JE007298

Wieczorek, M. A. & Meschede, M. (2018). SHTools – Tools for working with spherical harmonics. Geochem. Geophys. Geosystems 19, 2574-2592 https://doi.org/10.1029/2018GC007529

Wieczorek, M. A., Neumann, G. A., Nimmo, F., Kiefer, W. S., Taylor, G. J., Melosh, H. J. et al. (2013). The crust of the Moon as seen by GRAIL. Science, 339(6120), 671-675. https://doi.org/10.1126/science.1231530

Wieczorek M.A. & Phillips R. J. (1998). Potential anomalies on a sphere: Applications to the thickness of the lunar crust. Journal of Geophysical Research, 103, no. E1, pp.1715-1724.

Wieczorek, M. A. & Simons, F. J. (2005). Localized spectral analysis on the sphere. Geophys. J. Int. 162, 655-675. https://doi.org/10.1111/j.1365-246X.2005.02687.x

Wijns, C., Perez, C., & Kowalczyk, P. (2005). Theta map: Edge detection in magnetic data. Geophysics, 70(4), L39-L43. https://doi.org/10.1190/1.1988184

Wright, J., Rothery, D. A., Balme, M. R., & Conway, S. J. (2019). Geology of the Hokusai quadrangle (H05), Mercury. Journal of Maps, 15, 509–520. https://doi.org/10.1080/17445647.2019.1625821

Zuber, M. T. et al. (2012). Topography of the northern hemisphere of Mercury from MESSENGER Laser Altimetry. Science 336, 217-220. https://doi.org/10.1126/science.1218805

Zuber, M. T., Smith, D. E., Watkins, M. M., Asmar, S. W., Konopliv, A. S., Lemoine, F. G., Melosh, H. J., Neumann, G. A., Phillips, R. J., Solomon, S. C., Williams, J. G., Goossens, S. J., Kruizinga, G., Mazarico, E., Park, R. S., & Yuan, D.-N. (2013). Gravity Field of the Moon from the Gravity Recovery and Interior Laboratory (GRAIL) Mission. Science, 339, 668–671. https://doi.org/10.1126/science.1231507